MODEL BASED DESIGN OF BARRIER COATINGS FOR PAPER BASED MATERIALS

A thesis presented in partial fulfilment of the requirements for the degree of Doctor of Philosophy in Bioprocess Engineering

at Massey University, Manawatū Campus

New Zealand

Gonzalo Andrés Martínez-Hermosilla

2015

ABSTRACT

Paper based materials have limited vapour barrier properties. Several techniques have been developed to overcome this limitation. One of such technique is the use of barrier dispersion coatings. These barriers are continuous and solid layers normally applied on the surface of paper materials. Dispersion coatings are normally composed of two materials; a latex binder and filler particles. The interaction between these materials creates tortuous pathways that reduce the diffusion of the permeant. The main objective of this study was to develop an understanding of how the dispersion coatings can be designed to optimise the barrier properties of paper materials. In particular, the aim was to comprehend the effect of fillers added into dispersion coatings on the permeability with the purpose of developing of a model for predicting permeability.

A number of models have been developed to predict the permeability of barrier films such as thermoplastic composites but none have been applied or developed for use on barrier dispersion coatings. These models are normally based on idealised geometries, where the fillers are arranged in either oriented or random ways. The heterogeneous characteristics of the barrier dispersion coatings, such as uneven coating thickness, particle size and the lower elongation of the fillers used in dispersion coatings limit the use of the existing models for the prediction of dispersion coating barrier performance.

To develop a predictive model, the characterisation of aspects such as shape, size distribution and volume fraction of fillers in barrier coatings and their effect on the barrier performance were studied. The analysis of the geometry of fillers was carried out by image analysis from microscopy (scanning electron and light microscopes). This was carried out on three types of kaolin clays. The shapes, Feret diameters, and thicknesses of the clays were characterised. The filler shapes were elongated with an average ratio between the major and minor diameter being no larger than two. The Fourier series descriptor approximates the filler shape at the second harmonic. The Feret diameter and thickness were fitted to distribution curves. These distributions were used to define the fillers for generation of particle populations required for modelling. The particle populations can be based on either assuming representative filler shapes such as rectangular or elliptical plates or by the Fourier series descriptor.

Characterisation of dispersion coatings were also carried out. The dispersion coatings were formulated by styrene-butadiene latex and mixed with the selected clays at several filler volume fractions and applied on 160 $g \cdot m^{-2}$ linerboards. The characterisation was based on the measurement of water vapour transmission rate (WVTR) and oxygen transmission rate (O_2TR).

The coating thickness was also measured by scanning electron microscopy image analysis. The WVTR and O_2TR were shown to be sensitive to the type of filler, volume fraction of filler, and thickness of the coatings. Both the WVTR and O_2TR tended to be lower as the filler size, filler volume fraction, and coating thickness increased. The thickness of the coating was found to be dependent on the coating process (coated rod), coating formulation, and its variability on the linerboard topography.

The proposed model predicted the relative permeability based on the estimation of permeant flux by the Fick's first law through three dimensional coating geometries. The coatings were filled with rectangular plates randomly located. These plates were defined by distribution curves of maximum Feret diameter, elongation, and thickness of the selected clays. The amount of fillers in the coating was determined by part of filler volume fractions used for measurements of WVTR and O_2TR. The sizes of the geometries were defined by the representative elemental volume estimated from the filler volume fraction and the variation of the predictions. The geometries were generated by programming in Matlab under particular conditions of coating formulation and exposure.

The mathematical solution of the model was carried out by finite element method and solved by Comsol Multiphysics. As expected from the experimental characterisation of the coatings, the predictions indicated that the relative permeability reduced as the volume fraction of filler and the size of the clay increased; however, overestimation of the barrier properties were predicted. To understand the reasons for the discrepancy, several factors, that were not included in the conceptual model, were analysed. It was observed that the filler agglomeration and uncoated areas was the most significant factor that may affect the prediction of the relative permeability. Other factors such the uniformity of coating profile, and filler shape were found to have an effect on the prediction. Despite the discrepancy, the model was suitable for prediction of how to improve barrier performance trend. Thus, it was possible to evaluate different factors related to the barrier performance to find their best combination.

In order to optimise the formulation of barrier dispersion coatings, sensitivity analyses were carried out based on factors that affect the permeability. Filler settling in the coating or coatings with two layers were found to provide a reduction of relative permeability. This technique also may reduce the material used for coating preparation and the occurrence of uncoated areas. However, these effects were smaller than the effect of filler agglomeration on the barrier performance. For this reason, future studies should be focused on the improvement of dispersion of fillers in the coating binder. The application of the model in other coating formulations must consider the definitions of the concepts used in the study in order to apply the correct

information for running simulations.

Because this model was the first approach developed for dispersion coatings, several aspects were fully not explored in this study. In future research may be focused on the improvement of filler geometry characterisation, dispersion of fillers in the coating binder, incorporation of coating irregularities in the conceptual model, and incorporation of commercial coatings additives in the model. These points may increase the complexity of the model; however, it is expected that such complexity will be practical to be included in the model in the near future due to advances in computing capability for FEM simulations.

ACKNOWLEDGEMENT

I would like to express my sincere thanks to the people and organisations (or variables if I use modelling nomenclature) that made this project possible. I would like to begin by thanking to my chief supervisors Prof. John E. Bronlund. Thanks for the kindly and supportive guidance during the long marathon that a PhD is. Thanks to believe in me even when I thought that everything went wrong. Thanks to look at me as a peer giving to me the freedom to do what I though was right (which normally was wrong) but also encourage me to be critical and proactive. And thanks to look after me during the last 5 and half years. Also, I am sincerely thanks to my co-supervisors Dr. Behudin (Beko) Mesic and Mr. Tom E. Robertson for their knowledge, support and guidance during the project. I deeply appreciate all that you did for this project.

I would like to express my sincere gratitude to Massey University. In particular, the School of Engineering and Advanced Technology and its staff that always was there to kindly help me. Special acknowledge to Mrs. Ann-Marie Jackson for proving equipment, materials and facilities for running experiments and to Mr. Nick Look for IT support. Also, my sincere thanks to Mrs. Glenda Rosoman, Ms. Gayle Leader, and Mrs. Linda Lowe for the administrate support. My gratitude is also for the Institute of Food, Nutrition and Human Health to facilitate materials and equipment at the postharvest laboratory and its manager Mrs. Sue Nicholson to guide and advise me during measurement of coating performance. My sincere thanks are also for the Manawatū Microscopy and Imaging Centre, based at the Institute of Fundamental Science, and its SEM manager Mr. Doug Hopcroft to advise me for specimen preparation and capture of SEM images to characterise coating and fillers.

This project would not have been possible without the financial and technical support from Scion Research. My gratitude to Scion and its technical staff, Mrs. Donna Smith and Mr. Robin Parr for helping to prepare and evaluate coating trails. Also, thanks to Dr. Lloyd Donaldson and Dr. Alan Dickson to advise me in the preparation of specimens and operation of SEM. A special acknowledge to the Packaging Research Team headed by Ms. Lou Sherman.

Life without friends is very difficult. For this reason, I would like to sincere acknowledgement to all my friends that I met in New Zealand. My deepest gratitude to Mrs. Jenny and Mr. Doug Elliott who looked after me during the first years of my life in New Zealand. Thank you very much for the friendship and patience that you always have had to me. Also, thanks to Dr. Ximena Trejo-Araya to be always there to talk about life. Thank you very much to the other PhD students at the university (well, some of them are already doctors); Daw, Sadia, Pei and

Tawan. Also thank you very much to all my friends that make the trips to grab coffee more interesting; Eli, Colin, Jacky and many others that always were there to give me a friendly conversation and advice.

Also, I would like to express my sincere thanks to my friends in Chile. I wish to express my deepest appreciation to Assoc. Prof. Juan A. Cañumir Veas. He was the first person who believed in my skills to develop researching from the beginning of my career as an engineering student. In some way, without his motivation I would not have written this thesis. Also, all my friends that always supported me during this period of my life (particularly for welcomes and farewells).

The most important support that I had during this time was my family. They always were there to listen to me how awful is the life of a PhD student. Always there to listen to me about how good life in New Zealand is. Always there to listen how difficult is life so far away. But also they were always there to give me their love that was the main driving force (another modelling nomenclature) to keep working until finish this project. Thank you very much Mom, Dad, Beñita, Felipe y Josefina!

Para mi familia en cariño:

El soporte más importante que tuve todo este tiempo fueron ustedes. Ustedes siempre estuvieron ahí para escucharme decir lo horrible que era la vida de un estudiante de doctorado. También ustedes siempre estuvieron ahí para escucharme decir lo increíble que es Nueva Zelanda. Ustedes también estuvieron ahí para escucharme decir lo difícil que es vivir tan lejos. Pero ustedes siempre estuvieron ahí para darme su cariño y apoyo que fueron la principal fuerza propulsora (otro concepto de modelación) que me permitió llegar al final de este proyecto. Muchas gracias Mamá, Papá, Beñita, Felipe y Josefina!

Gonzalo A. Martínez Hermosilla, November 2014

TABLE OF CONTENT

LIST OF NOMENCLATURE

$\left(\frac{P_f}{P_u}\right)_{pinhole}$: Relative permeability of coating with one representative pinhole

$TR_f\big|_{z=0}$: Transmission rate of the coating at $z = 0\ \mu m$

$TR_f\big|_{z=K}$: Transmission rate of the coating at $z = K\ \mu m$

$\frac{P_f}{P_u}$: Relative permeability from simulation with even coating profile (normal simulations)

$Pf/Pu_{\alpha E}$: Relative permeability across the third dimensional aspect ratio

$\dot{m}_{N_2}$: Mass flow rate of nitrogen in the inlet ($g \cdot min^{-1}$)

$\dot{m}_{air_{in}}$: Mass flow rate of air in the inlet ($g \cdot min^{-1}$)

$\frac{\sigma_x}{\sigma_{N_2}}$: Ratio of the collision diameter of the permeant and nitrogen

$\emptyset_{F_1}$: Volume fraction of the first layer of the coating

$\emptyset_{F_2}$: Volume fraction of the second layer of the coating

$\emptyset_{F_{final}}$: Final volume fraction of coating formed by two layers

$\emptyset_F$: Volume fraction of fillers

Δp_f: Partial pressure of permeant for filled coatings (Pa)

Δp_u: Partial pressure of permeant for unfilled coating (Pa)

A_{O_2TR}: Area of permeability for O_2TR (m^2)

A_{f_i}: Surface area of the fillers assuming a regular shape

A_{f_i}: Surface area of fillers assuming a regular shape

A_{WVTR}: Area of permeability for WVTR (m^2)

A_d: Area of filler

$A_{exposure}$: Exposure area (m^2)

$A_{reference}$: Reference area (m^2)

C_{10}: Constant for calculation of partial pressure at saturation of the air

C_{11}: Constant for calculation of partial pressure at saturation of the air

C_{12}: Constant for calculation of partial pressure at saturation of the air

C_{13}: Constant for calculation of partial pressure at saturation of the air

C_8: Constant for calculation of partial pressure at saturation of the air

C_9: Constant for calculation of partial pressure at saturation of the air

D_f: Fractal dimension

D_{filled}: Diffusivity of permeant through the filled coating ($m^2 \cdot s^{-1}$)

$D_{unfilled}$: Diffusivity of permeant through the unfilled coating ($m^2 \cdot s^{-1}$)

E_D: Activation energy of diffusion ($J \cdot mol^{-1}$)

E_i: Elongation of the *i* filler

E_t: Theoretical elongation

F_{N_2}: Flow of oxyfree nitrogen ($mL \cdot min^{-1}$)

J_P: Permeant flux ($mol \cdot s^{-1} \cdot m^{-2}$)

J_{cyl}: Permeant flux through the coating when the cross section shape is assumed as cylinder ($mol \cdot m^{-2} \cdot s^{-1}$)

K_f: Coating thickness for a particular formulation (m)

$K_{layer\,1}$: Thickness of the first layer of the coating

$K_{layer\,2}$: Thickness of the second layer of the coating

$K_{no\,sed}$: Thickness of the unfilled region (m)

K_{sed}: Thickness of the settling region(m)

K_{sv}: Stern-Volmer constant

L_i: Length of the *i* filler (m)

L_i: Maximum Ferert diameter of the *i* filler (m)

P_f: Permeability of filled coatings ($mol \cdot m \cdot m^{-2} \cdot s^{-1} \cdot Pa^{-1}$)

P_u: Permeability of unfilled coating ($mol \cdot m \cdot m^{-2} \cdot s^{-1} \cdot Pa^{-1}$)

RH_{in}: Relative humidity inside of the gravimetric cup

RH_{out}: Relative humidity outside of the gravimetric cup

$RP_{no\,sed}$: Relative permeability of the unfilled region

RP_{obs}: Relative permeability of analysed barrier dispersion coatings

RP_{sed}: Relative permeability of the settling region

$RP_{settling}(\emptyset_F)$: Relative permeability at filler volume fraction $\emptyset_F$

$RP_{settling}$: Relative permeability of a barrier dispersion coating with filler sedimentation

TR_f: Transmission rate of permeant for filled coatings ($mol \cdot m^{-2} \cdot s^{-1}$)

TR_{fk}: Transmission rate of the permeant through the coating for a particular coating formulation and conditions of exposure ($mol \cdot m^{-2} \cdot s^{-1}$)

TR_n: Normalised TR for either WVTR or O_2TR ($mol \cdot m^{-2} \cdot s^{-1}$)

$TR_{pinhole}$: Transmission rate through the pinhole ($mol \cdot m^{-2} \cdot s^{-1}$)

TR_u: Transmission rate of permeant for unfilled coating ($mol \cdot m^{-2} \cdot s^{-1}$)

T_g: Glass transition temperature of the coating ($°C$)

$V_{coating}$: Volume of coating after drying and consolidation of the substrate (mL)

V_{filler}: Volume of fillers (mL)

$V_{latex\,dry}$: Volume of dried latex (mL)

$V_{solid\ part\ binder}$: Volume of solid part of the binder (mL)

$WVTR_{filled}$: Normalised water vapour transmission rate of barrier dispersion coatings filled at different volume fraction of filler

$WVTR_{unfilled}$: Normalised water vapour transmission rate of unfilled barrier dispersion coatings

Xf_{solid}: Solid content of the latex

X_{max}: Maximum average of the relative permeability for the previous five estimations of the relative permeability

X_n: Average of the relative permeability at iteration n

a_n: Magnitude of each harmonic

b_{f_i}: Thickness of fillers assuming a regular shape

b_i: Thickness of the i filler (m)

b_n: Phase of each harmonic

c_{N_2}: Concentration of oxygen of the nitrogen inlet (0%)

c_{N_2/O_2}: Concentration of oxygen in the outlet of the carrier gas chamber (%)

$c_{air_{in}}$: Concentration of oxygen in the air inlet (21 %)

$c_{air_{out}}$: Concentration of oxygen in air inlet (%)

c_{bottom}: Concentration of permeant on the bottom surface of coating $(mol \cdot m^{-3})$

c_{top}: Concentration of permeant on the top surface of coating $(mol \cdot m^{-3})$

c_{wv}: Concentration of water vapour at either bottom or top coating surface $(mol \cdot m^{-3})$

$d_{F_{max}}$: Maximum Feret diameter of the filler

$d_{F_{min}}$: Minimum Feret diameter of the filler

d_F: Statistical diameter defined as the distance between pairs of parallel tangents to the projected outline of the particle in some fixed direction

d_M: Statistical diameter defined as chord length, parallel to some fixed direction, which divides the particle projected outline into two equal area

d_a: Diameter of a circle having the same projected area as the particle in stable orientation

d_c: Diameter of a circle having the same perimeter (P) as the projected outline of the particle

d_p: Diameter of a circle having the same projected area as the particle in random orientation

$d_{pinhole}$: Diameter of the pinhole (m)

d_s: Diameter of a sphere having the same surface (S) as the particle

d_{sv}: Diameter of a sphere having the same external surface to volume ratio as the particle

d_{trial}: Diameter of the coating trial (m)

d_v: Diameter of a sphere having the same volume (V) as the particle

f_{bR}: Bulkiness of fillers

$gsm_{linerboard}$: Grammage of the linerboard $(g \cdot m^{-2})$

gsm_n: Coat weight for normalisation $(g \cdot m^{-2})$

gsm: Coat weight of the coating trials $(g \cdot m^{-2})$

k_e: Shape parameter

$m_{V_{solid\ part\ binder}}$: Mass of the solid part of the binder (g)

m_{perm}: Molecular weight of any permeant gas $(g \cdot mol^{-1})$

m_{WV}: Molecular weight of water vapour $(18.02\ g \cdot mol^{-1})$

m_{filler}: Mass of the fillers (g)

$m_{latex\ dry}$: Mass of the dried latex (g)

m_p: Mass of pycnometer (g)

m_{pf}: Mass of pycnometer and fillers (g)

m_{pf}: Mass of pycnometer and filler sample (g)

m_{pl}: Mass of pycnometer raised with reference liquid (g)

m_{plf}: Mass of pycnometer raised with reference liquid and filler sample (g)

m_{total}: Total mass of filler in a given sample

m_{trial}: Mass of the coating trial sample (g)

nx_i: Initial number of segments of coating grid through x-axis

ny_i: Initial number of segments of coating grid through y-axis

nz_i: Initial number of segments of coating grid through z-axis

p_{atm}: Atmospheric pressure

p_{bottom}: Partial pressure on bottom coating surface (Pa)

p_{sat}: Saturated pressure (Pa)

p_{top}: Partial pressure on top coating surface (Pa)

p_v: Current partial pressure at either bottom or top surface of the coating (Pa)

p_{vs}: Partial pressure at saturation at either bottom or top side of the coating (Pa)

r_1: Radius of the shortest distance between a coating surface and the imaginary centre of the cylinder (projection of the radius) (m)

r_2: Radius of the largest distance between a coating surface and the imaginary centre of the cylinder (projection of the radius) (m)

sd_{max}: Maximum standard deviation of the relative permeability for the previous five

estimations of the relative permeability

sd_n: Standard deviation of the relative permeability at iteration n

x_e: Elongation of the filler

x_f: Thickness of filled coatings (m)

x_f: Length (m) or thickness (m) of the fillers at a particular probability

x_{max}: Maximum length(m) or thickness (m) of the fillers at a particular probability

x_{min}: Minimum length(m) or thickness (m) of the fillers at a particular probability

x_u: Thickness of unfilled coating (m)

$y_{settling}$: Fraction of the coating thickness where the settling occurs

γ_1: Angle formed between the centre of the rotated filler and a corner with the original position as references

γ_2: Angle formed between the centre of the filler and a corner

γ_F: Maximum angle of filler orientation

$\frac{\varepsilon}{k}$: Lennard-Jones temperature (K)

μ_e: Location parameter

μ_e: Location parameter

μ_f: Average of the logarithm of length(m), or thickness (m) of the fillers

μ_f: Average of the logarithm of length or thickness of the fillers

$\rho_{V_{solid\ part\ binder}}$: True density of the solid part of the binder $(g \cdot mL^{-1})$

ρ_{filler}: True density of the filler $(g \cdot mL^{-1})$

ρ_l: Density of the reference liquid $(g \cdot mL^{-1})$

$\rho_{latex\ dry}$: True density of the dried latex $(g \cdot mL^{-1})$

ρ_{latex}: True density of the liquid latex $(g \cdot mL^{-1})$

ρ_{liquid}: True density of liquid part $(g \cdot mL^{-1})$

σ_e: Scale parameter

σ_e: Scale parameter

σ_f: Standard deviation of the logarithm of length(m) or thickness (m) of the fillers

σ_f: Standard deviation of the logarithm of length or thickness of the fillers

τ_0: Fluorescence lifetime at 0% of oxygen

ψ_{Ap}: Circularity of fillers

ψ_s: Sphericity of fillers

ΔH_S: Heat of solution $(J \cdot mol^{-1})$

Δc: Variation in concentration between surfaces $(mol \cdot m^{-3})$

Δm: Variation in mass of the gravimetric cup during time (g)

Δp: Difference in partial pressure of permeant on both sides of the barrier dispersion coating

Δp: Difference of partial pressure between coating trials surfaces (Pa)

c: Concentration of permeant on the surface of the dispersion coating $(mol \cdot m^{-3})$

A: Area of permeability (m^2)

A: Area of the matrix

C: Roundness of fillers

C: Length of fillers in the width direction

D: Diffusivity coefficient $(m^2 \cdot s^{-1})$

E: Elongation of fillers

$F(x_f; \mu_f, \sigma_f)$: Cumulative distribution function of the length, or thickness of fillers

F: Flatness of fillers

J: Length of coating (m)

K: Thickness of coating (m)

L: Length of fillers

M: Width of coating (m)

N: Number of fillers for coating definition

P: Permeability of coating trials of such as WV or O_2 $(mol \cdot m \cdot m^{-2} \cdot s^{-1} \cdot Pa)$

Q: Amount of permeant passing through the barrier coating (g)

$R(\theta)$: Radius generated from Fourier shape descriptor

R: Ideal gas constant $(8.314\ J \cdot mol^{-1} \cdot K^{-1})$

RH: Relative humidity at either bottom or top coating surface

S_{order}: Parameter of order of the Bharadwaj model

TR: Transmission rate of permeant $(mol \cdot m^{-2} \cdot s^{-1})$

a, s: Space between two parallel filler layers and the slit between two filler particles

b: Thickness of fillers

c: Concentration gradient of the gas $(mol \cdot m^{-3})$

$f(x_f; \mu_f, \sigma_f)$: Probability density function of the length or thickness of fillers

n: Number of harmonics

p: Partial pressure of the permeant (Pa)

r: Diagonal (hypotenuse) formed between any corner and the centre of a filler

s: Solubility of the permeant $(mol \cdot m^{-3} \cdot Pa^{-1})$

t: Time of measurement (day)

x: Thickness of the barrier (m)

α: Aspect ratio of fillers

δ: Ratio between A_d and A

θ: Temperature $(°C)$

λ: Linear fraction or the ratio between the thickness of the fillers and the total thickness of the barrier

μ: Mean of the natural logarithm of the Fourier shape descriptor parameters

σ: Standard deviation of the natural logarithm of the Fourier shape descriptor parameters

τ: Fluorescence lifetime of the sample

LIST OF FIGURES

LIST OF TABLES

xxx

Chapter 1

INTRODUCTION

1.1. Project Background

Paper based materials have been widely used to protect goods against ambient conditions. Paper consists of a porous cellulose structure made of microfibrils of long-chain cellulose molecules in a crystalline state with amorphous regions regularly disrupting the crystalline structure (Khwaldia, Arab-Tehrany, & Desobry, 2010). The interaction of the cellulose fibres generates a matrix structure and as a result a porous media (Alava & Niskanen, 2006), which limits the barrier performance of paper based materials (Khwaldia, et al., 2010; Robertson, 2013). Consequently, barrier coatings are normally applied on the surface of paper based materials to improve their barrier properties. Barrier dispersion coatings have been considered for improvement of barrier properties due to their compostable and repulpable characteristics that could become an environmentally friendly replacement for conventional extruded barrier coatings such as polyethylene (Andersson, Ernstsson, & Järnström, 2002).

A barrier dispersion coating is a continuous layer applied as an aqueous dispersion (such as latex) which forms a solid and non-porous layer after drying (Kimpimäki & Savolainen, 1997; Lepoutre, 1989). During coating preparation, fillers and other additives are included in the coating formulation to achieve the required level of barrier properties (Kimpimäki & Savolainen, 1997). The combination of fillers and binder creates a network structure with tortuous paths that reduce the diffusive flow of permeant through the coated substrate (Andersson, et al., 2002). The effectiveness of the fillers in improving barrier properties is related to their geometrical characteristics, chemical nature, and interaction with the binder (Rissa, Lepisto, Vaha-Nissi, & Savolainen, 2000). From the above observation, it can be inferred that the permeability of coated material is associated with its final coating structure. Factors such as the amount of fillers in the binder, filler orientation in the binder, adhesion of fillers in the binder, binder distribution, shape of fillers, and size of fillers are directly related to a reduction of permeability (Andersson, 2008; Rissa, et al., 2000; Rissa, Lepistö, & Yrjölä, 2006; Schuman, Karlsson, Larsson, Wikström, & M., 2005).

Several investigations have been carried out to characterise the structure of barrier dispersion coatings and their effect on barrier properties. For measurement of filler orientation in dispersion coatings after consolidation, experiments suggest that large aspect ratio of fillers and

thin coatings could influence the parallel orientation of the fillers (Rissa, et al., 2000; Schuman, Karlsson, et al., 2005). This conclusion is intuitive and some experimental results support it; however, others provide contradictory results (Rissa, et al., 2000). A large sample size is needed in order to achieve some degree of accuracy in these results (Rissa, et al., 2000). The effect of the amount of filler on the reduction of permeability in coating has been studied by several researchers. Ambiguous results across these studies are common. In some cases, findings show that fillers reduce the permeability of coatings (Schuman, Karlsson, et al., 2005). In other studies the effect is not clear and the permeability could be similar for coatings with different amount of fillers (Andersson, et al., 2002). These examples show that the characterisation of the coating structures and their performance as barriers may limit further investigations.

Another way to understand the effect of the coating structure on the permeability of coated materials is by development of models and simulations that describe the phenomenon based on current understanding. From the 1960's onwards, the modelling of barriers has mostly been focused on thermoplastics composites (Choudalakis & Gotsis, 2009). These models predict the relative permeability of filled polymer films based on the geometrical characteristics of fillers and have produced reasonably results. However, the models are only valid across a narrow range of specific cases due to the oversimplification used of modelling variables. These include the use of uniform filler shape, ideal distributions of filler, a limited angle of filler orientation, and a narrow amount of filler in the coating formulation. This presents a restriction for the description of barrier dispersion coating performance.

In the case of simulation, advancements of technologies and computer software have driven its use in research. Computers and their current capability allow simulations with more realistic conditions in a reasonable computation time. Thus, combining state of the art technology with current knowledge about barrier films could contribute to understanding the mechanisms of how dispersion coatings improve barrier properties. As a result barrier dispersion coating formulations could be optimised in order to produce the best barrier properties for particular conditions. Models developed for barrier dispersion coatings could be used to guide the formulation of dispersion coating to achieve required performance.

1.2. Research aim

The aim of this research was to develop an understanding of how barrier dispersion coating formulations can be designed in order to optimise barrier properties in paper and paperboard based on both modelling and simulation. Specifically, the aim was to analyse the effect of adding fillers added to coatings on the permeability. With the purpose of developing model to

predict permeability, variables such as shape, size distribution and volume fraction of fillers were studied. The research represents a substantial contribution to the general packaging industry because it addresses a need of finding optimal formulations for coatings and additionally, a possible application of models in the industry to add value to products.

Chapter 2

LITERATURE REVIEW

The purpose of this chapter was to address the main concepts related to the barrier performance of dispersion coatings applied on paper based materials. This section describes barrier dispersion coatings including the substrates, coating formulation, and coating structure and their influence on barrier properties. In addition, a discussion of modelling approaches reported in the literature to predict relative permeability of filled polymer films will be presented. Finally, the required parameters to develop a model for the prediction of the barrier properties of dispersion coatings will be introduced.

2.1 Paper based materials

Paper is one of the key substrates for dispersion coatings. Paper based materials consist on a porous cellulose structure made of microfibrils of long-chain cellulose molecules in a crystalline state with amorphous regions regularly disrupting the crystalline structure (Khwaldia, et al., 2010). The cellulose is obtained from wood or other similar natural sources (Alava & Niskanen, 2006; Kirwan, 2005). The manufacturing of paper materials is carried out by filtering, pressing, drying and eventual chemical treatment of cellulose fibre suspensions forming sheets or boards (Fellers, 2009; Robertson, 2013). Due to the manufacturing process and the fact that the fibres are much longer than their thickness, their orientation is normally in the plane of the paper sheets rather than the paper thickness direction (Fellers, 2009). This confers different properties according to the direction of the study (anisotropic properties). Due to these reasons, properties are normally characterised in three directions of the papers; machine direction (MD) or the direction of paper which is parallel to the paper manufacturing direction, cross direction (CD) or the direction of paper which is perpendicular to the paper manufacturing direction, and thickness direction (ZD) (Biermann, 1996; Fellers, 2009). As an example, strength usually is greater if measured in the MD than in the CD and both greater than ZD due to the alignment in the paper plane and depending on how long and slender of the fibres (Hubbe, 2005). Other properties such as tensile, fold, or compression are also dependent of the direction (Alava & Niskanen, 2006; Biermann, 1996; Kirwan, 2005).

The structure of the paper can be changed depending how the pulp preparation (process where the raw fibres are converted into a fibrous mass) and paper manufacturing processes are developed according to the requirement of the final product (Bristow, 2009; Fellers, 2009;

Robertson, 2013). Figure 2.1 shows planar views of a linerboard paper and a grease proof paper. The differences between the samples are mostly related to the beating process. This relates to the process where the pulp are treated by swollen, internally delaminated, fibrillated, and sometimes reduced in length to improve strength properties (Biermann, 1996; Hubbe, 2005). In the case of the linerboard sample, the fibres are only slightly beaten giving high compression strength, creep resistance, toughness in converting and delamination resistance. In the case of the greaseproof paper, the fibres are well beaten and as a result the fibres structure is deteriorated making the paper transparent with low opacity (Fellers, 2009).

a) 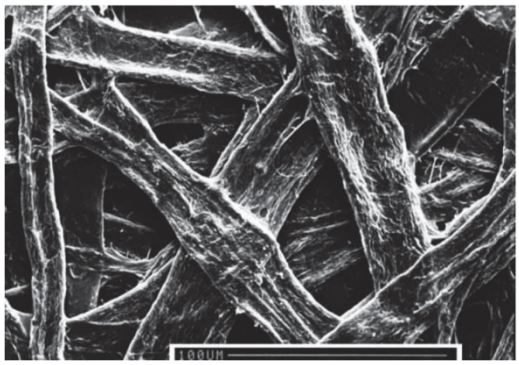 b) 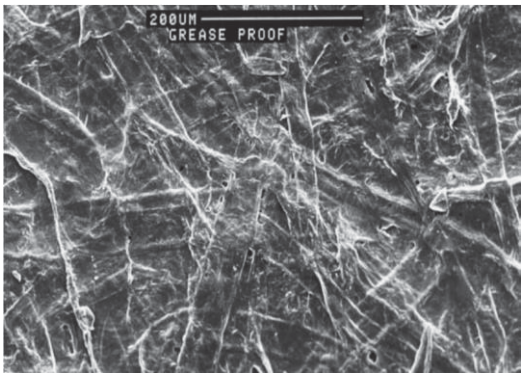

Figure 2.1 Plane view of a) linerboard and b) grease proof paper samples (Fellers, 2009)

As shown in Figure 2.1, the topography of the paper surface varies depending on the treatment of the cellulose fibres. The paper surfaces are normally treated to reduce their natural heterogeneity (Bristow, 2009). This is required to improve mechanical, barrier, or aesthetic properties (Robertson, 2013). For example, by surface sizing the irregularities of the paper surface are filled with particles such as starch, rosin, glues, caseins, synthetics resins or cellulose derivatives to reduce the penetration of liquids (Robertson, 2013; Smook, 1982). Increase on the smoothness and glossiness of the paper can be achieved by calendaring (Robertson, 2013; Vernhes, Dubé, & Bloch, 2010). This treatment reorients the fibres of the surface of the paper by application of pressure.

The lack of barrier performance of uncoated papers is mainly related to the hydrophilic nature of cellulose due to the OH sites in the basic unit of cellulose ($C_6H_{10}O_5$) and the high fibre network porosity (Khwaldia, et al., 2010). For this reason, application of barrier films on the paper surface is required to improve their barrier properties. Polymeric films are widely used as barrier films. Such films include polyvinylidene chloride (PVdC), ethylene vinyl alcohol (EVOH), and organic or inorganic sol-gels to prevent permeation of, for example, oxygen or water vapour (Leonard, 2009). Due to the constant search for environmentally friendly materials, improvement of barrier properties of paper based substrates has been encouraged the

study of no fossil-based, biodegradable, and recyclable materials (Andersson, 2008). Because of their compostable and repulpable characteristics, paper based substrates coated with barrier dispersion coatings have been considered as a potentially good replacement for conventional polymer films (Andersson, et al., 2002; Samyn et al., 2010).

2.2 Barrier dispersion coatings

A barrier dispersion coating is an aqueous dispersion applied as a layer onto substrates. The coating becomes solid and non-porous after drying (Kimpimäki & Savolainen, 1997; Lepoutre, 1989). Its purpose is to improve the barrier properties of the substrate against the transfer or uptake of water vapour, water, grease and oil, various gases, and impurities (Vähä-Nissi, Kervinen, Savolainen, Egolf, & Lau, 2006). In addition, it contributes to the smoothness, roughness, printability, gluability (Vähä-Nissi, et al., 2006). The most commonly used polymers are latexes formed by styrene-butadiene, styrene-n-butyl acrylate, linear vinyl acetate or polyolefins dispersed in water to give an emulsion of small particles, normally from 50 to 300 nm with a solid content from 25% to 70% (Andersson, 2008; Kimpimäki & Savolainen, 1997; Lehtinen, 2000a). As a clarification, other types of coatings are used in the industry; however, their purposes are different than barrier dispersion coating. For example, aqueous pigment coatings are used to improve printing properties of papers (Lehtinen, 2000c).

The latexes provide important barrier properties; however, the demand for better performance has resulted in further improvement through the use of additives in coating formulations. Carboxylic acid can be used to increase the ionizing degree of the polymer. The degree of carboxylation affects the water retention, viscosity, bonding, and the resulting barrier properties. (Kimpimäki & Savolainen, 1997). Thickeners are applied to adjust the viscosity of natural polymers, cellulose derivatives, synthetic polymers and starch to facilitate coating application. Bubbles in the coating are prevented by anti-foamers and surfactants, which are added to ensure dissolution of monomers and the initiation of the polymerization reaction. Styrene or alkyl acrylate provides hydrophobicity. Waxes such as paraffin microcrystals or carnauba wax are used to change the surface energy and the polarity of the coating (Kimpimäki & Savolainen, 1997).

Mineral fillers (sometimes called pigments) are added to dispersion coatings to improve the barrier properties by increasing the length of the diffusion pathway for permeants (Andersson, et al., 2002) as shown in Figure 2.2.

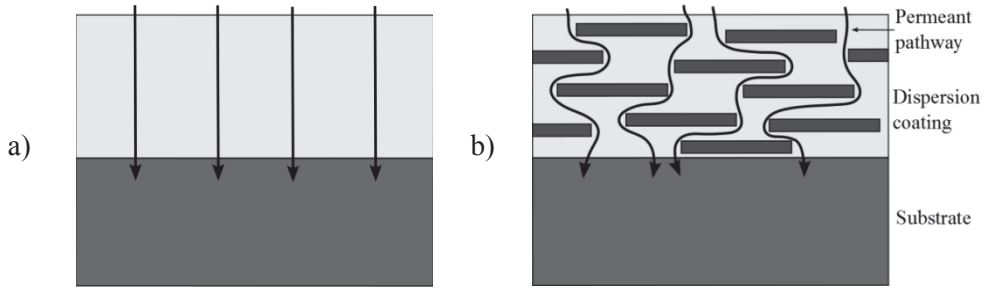

Figure 2.2 Diffusion of permeant through barrier dispersion coatings a) without filler b) with filler

The chemical composition affects the hydrophilic/hydrophobic character of the fillers. The hydrophobicity in talc or some clays usually contribute to the reduction of moisture permeability in barrier coatings for paper (Schuman, Karlsson, et al., 2005). However, their hydrophobic nature results in difficulties in dispersing them in water during coating formulation and require the use of dispersants (Mesic, Kugge, & Järnström, 2010).

The increase in the length of the permeant pathway can be characterised as the tortuosity, which is defined as the ratio between the distance that a permeant molecule must travel to get through the barrier and the thickness of the barrier (Nielsen, 1967). The tortuosity is mostly governed by the geometrical characteristics of the fillers, such as length or diameter, surface area, shape, the filler volume fraction and their spatial distribution in the polymer phase (Choudalakis & Gotsis, 2009). Narrow filler size distribution and plate shaped fillers with a high ratio between length and thickness, such as kaolin clay and talc have a positive effect on the barrier properties because they maximise the permeant diffusion pathway length (Kugge & Johnson, 2008; Schuman, Karlsson, et al., 2005).

To provide low permeability, the quantity of the fillers in coatings has to be as high as possible; however, it must be lower than the critical pigment (filler) volume concentration (CPVC). This parameter represents the concentration of binder (polymer) that is just enough to coat all the filler and fill the intervening spaces (Braunshausen, Baltrus, & De Bolt, 1992; Keddie, 1997). The CPVC depends on the packing characteristics of the fillers, type of binder and the type and amount of special additives (Asbeck & Van Loo, 1949). At higher concentration, issues such as agglomeration and voids between fillers occur that compromises the coating performance (Asbeck & Van Loo, 1949). For good flexibility, low blocking tendency and good barrier properties, the quantity of fillers normally used is from 40% to 50% of volume concentration (Andersson, 2008; Andersson, et al., 2002). Table 2.1 shows some characteristics of fillers normally used for barrier dispersion coating formulation.

Table 2.1 Characteristics of fillers used in barrier dispersion coatings

Fillers	Equivalent diameter (μm)	Shape	Aspect ratio	Surface area ($m^2 \cdot g^{-1}$)	Density ($g \cdot mL^{-1}$)	Ref*
Kaolin clay	0.3-5	Hexagonal plate	10-80	67-72	2.58	a, b
Talc	0.3-5	Plate	30	67-70	2.70	a, b, c
Plastic fillers						
Solid	0.1-0.5	Spherical	1	--	1.05	a, b
Hollow	0.4-1.0	Spherical	1	--	0.6-0.9	a, b
Calcined kaolin	0.7 (median)	Aggregate plate	4.8- 7.4	14-22	2.69	a, b, d
Alumina trihydrate	0.2-2	Plate	--	5-90	2.42	a, b

* a: Bundy& Ishley (1991) , b: Lehtinen (2000b), c: Schuman et al.(2005), d: Andrady (2008)

For practical proposes, the amount of materials (latex, fillers, additives, etc.) are measured in terms of mass. The mass of the materials can be easily estimated by precision scales reaching high level of accuracy. However, the effect of the fillers in the reduction of permeability is related to the volume that they fill in comparison to the total coating volume. Thus, it is required to transform the mass units into volume. In this case, the total coating volume refers to the dispersion coating after drying and consolidation on the substrate. Based on the density of solid part of binder and fillers it is possible to convert the units as shown in Equations 2.1, 2.2, and 2.3.

$$V_{coating} = V_{filler} + V_{solid\ part\ binder} \tag{2.1}$$

$$V_{filler} = \frac{m_{filler}}{\rho_{filler}} \tag{2.2}$$

$$V_{solid\ part\ binder} = \frac{m_{V_{solid\ part\ binder}}}{\rho_{V_{solid\ part\ binder}}} \tag{2.3}$$

where

$V_{coating}$: Volume of coating after drying and consolidation of the substrate (mL)

V_{filler}: Volume of fillers (mL)

m_{filler}: Mass of the fillers (g)

ρ_{filler}: True density of the filler ($g \cdot mL^{-1}$)

$V_{solid\ part\ binder}$: Volume of solid part of the binder (mL)

$m_{V_{solid\ part\ binder}}$: Mass of the solid part of the binder (g)

$\rho_{V_{solid\ part\ binder}}$: True density of the solid part of the binder ($g \cdot mL^{-1}$)

Better barrier properties can be achieved when the fillers are oriented parallel to the substrate surface. Variations in the angle of orientation could affect the pathway length for the permeant,

reducing the effectiveness of the fillers to improve the barrier properties (Schuman, Karlsson, et al., 2005). Uneven topography of the substrate gives less pronounced orientation of the fillers to the coated specimen (Schuman, Karlsson, et al., 2005) as shown Figure 2.3. However, high filler content and thin thickness of the barrier dispersion impose partial parallel orientation of the fillers (Chinga, Helle, & Johnse, 2000). Rissa, et al. (2000) investigated this effect using both X-ray diffraction and scanning electron microscopy (SEM) with X-ray supporting this conclusion but SEM showed no clear indication of this. This may be explained by the low number of fillers analysed. Bollström et al. (2013) indicated that kaolin clays with high aspect ratio generally have higher alignment at high volume fraction; however, this is not significant for fine kaolin.

The parallel orientation of the fillers may improve when finishing processes are applied on the barrier dispersion coating such as calendering where, as well as paper manufacturing, the roughness is reduced by pressing the coating surface at a certain temperature (Rissa, et al., 2000; Schuman, Adolfsson, Wikström, & Rigdahl, 2005).

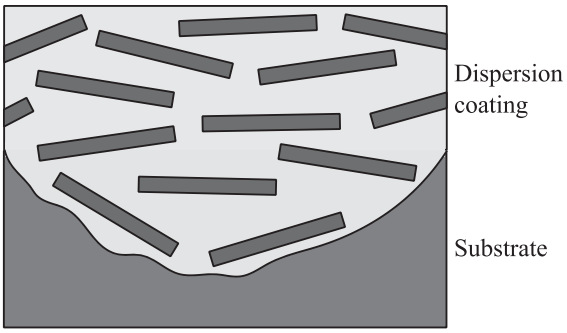

Figure 2.3 Effect of the substrate surface on the orientation of pigments in barrier dispersion coatings

During the coating consolidation, the water of the coating is removed, forming a rigid three-dimensional structure (Eksi & Bousfield, 1997). This process affects the distribution of the polymer phase, filler orientation, air space around fillers and the polymer phase or final thickness of the coating and therefore influences many properties of the coating such as porosity and gloss (Eksi & Bousfield, 1997; Lepoutre, 1989). The thickness of a normal and single wet coating layer, including polymer phase, fillers and additives, is between 5 and 20 μm, roughly equivalent to a wet coat weight from 5 to 20 $g \cdot m^{-2}$. After the dewatering and drying processes, the thickness and dry coat weight is reduced and, depending on the solid content of the coating, the reduction could be relatively high. The final coating thickness can be about a half or less of the original thickness after drying.

Another important aspect that affects the performance of dispersion coatings as barriers is the coating layer structure. The process of coating formation is normally divided into three main parts; shrinkage of the inter particle distance due to drying; coalescence of polymer particles and the possible further inter diffusion of polymer chains of adjacent particles as shown in Figure 2.4 (Kimpimäki & Savolainen, 1997). These processes start as soon as the coating is applied on the paper sheet (Bertrand, Gange, Desaulniers, Vidal, & Hayes, 2004). the formation of the coating, many forces act simultaneously in opposite directions. These factors are affected by particle size and distribution, rheological properties, water evaporation rate, drying temperature and the chemical composition of the latex (Kimpimäki & Savolainen, 1997).

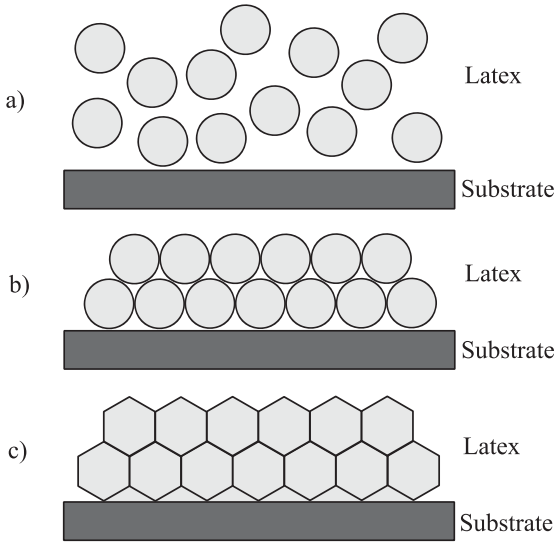

Figure 2.4 Schematic diagram of different steps for coating formation of latex particles: a) shrinkage of interparticle distance; b) coalescence of polymer particles; c) inter diffusion of polymer chains of adjacent particles (Kimpimäki & Savolainen, 1997)

It is important to note that the uniformity of the coating thickness is affected by the surface of the substrate as shown in Figure 2.3 (Allem, 1998). Uneven substrates require filling of all irregularities to reduce the occurrence of uncovered areas (Allem, 1998; Kimpimäki & Savolainen, 1997). It is common to treat the substrate surface with a pre coating to smooth the surface and as a result homogenise the thickness of the coating to avoid uncoated areas (Schuman, Wikström, & Rigdahl, 2004b).

2.3 Characterisation of the size and shape of fillers

In general, the geometry of particles is traditionally represented by attributes such as size or shape. For spherical shaped particles, a single dimension can be used to define size. However, in the case of non-spherical or irregular shaped particles more than one dimension is required

(Allen, 1997). These particles are normally compared with standard reference shapes, for instance, circles or ellipsoids measuring the size of special features within that reference shape (Kanit, Forest, Galliet, Mounoury, & Jeulin, 2003). The size can also be defined based on a reference with a given direction, for example, parallel and opposite tangents lines or bisecting the surface area of the particle (Allen, 1997). This type of approach is called statistical diameter (Allen, 1997; Masuda, Higashitani, & Yoshida, 2006). Table 2.2 below shows a list of typical definitions of particle diameters.

Table 2.2 Typical definitions of particle diameters presented in the literature (Allen, 1997; Masuda, et al., 2006)

Symbol	Description	Equation
d_v	Diameter of a sphere having the same volume (V) as the particle	$d_v = \sqrt[3]{\frac{6 \cdot V}{\pi}}$ (2.4)
d_s	Diameter of a sphere having the same surface (S) as the particle	$d_s = \sqrt{\frac{S}{\pi}}$ (2.5)
d_{sv}	Diameter of a sphere having the same external surface to volume ratio as the particle	$d_{sv} = \frac{{d_v}^3}{{d_s}^2}$ (2.6)
d_a	Diameter of a circle having the same projected area as the particle in stable orientation	$d_a = \sqrt{\frac{4 \cdot A}{\pi}}$ (2.7)
d_p	Diameter of a circle having the same projected area as the particle in random orientation	$d_p = \sqrt{\frac{4 \cdot A}{\pi}}$ (2.8)
d_c	Diameter of a circle having the same perimeter (P) as the projected outline of the particle	$d_c = \frac{P}{\pi}$ (2.9)
d_F	Statistical diameter defined as the distance between pairs of parallel tangents to the projected outline of the particle in some fixed direction (Feret diameter)	
d_M	Statistical diameter defined as chord length, parallel to some fixed direction, which divides the particle projected outline into two equal area (Martin diameter)	

Due to the range of directions that can be assumed for estimation of d_F and d_M, they are often defined in several ways. In Figure 2.5 some d_F and d_M definitions are presented (Hentschel & Page, 2003).

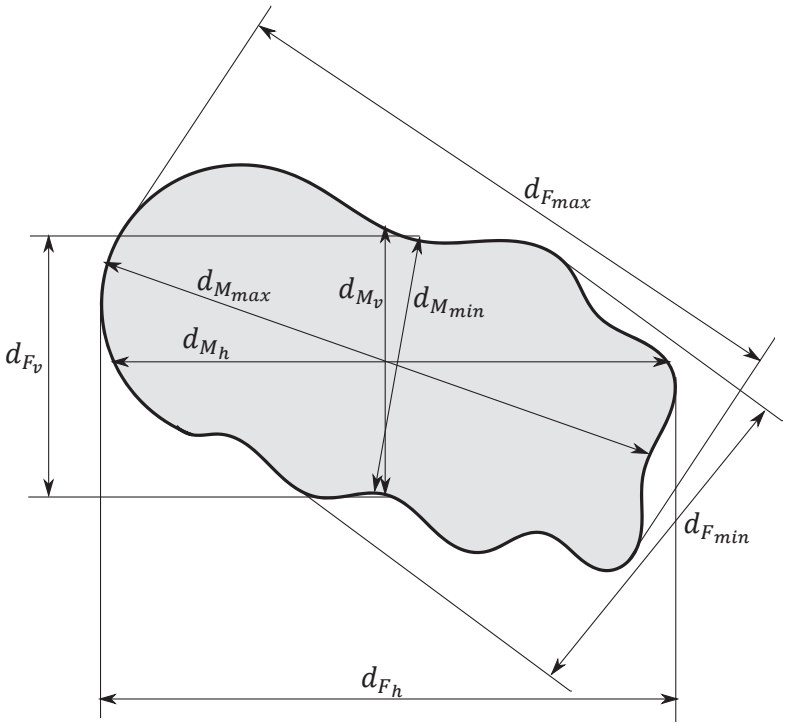

Figure 2.5 Definition of the filler dimensions where $d_{F_{max}}$ and $d_{F_{min}}$ are the largest and the smallest Feret diameter at any angle of orientation, $d_{M_{max}}$ and $d_{M_{min}}$ are the largest and the smallest Martin diameter at any angle of orientation, d_{F_h} and d_{F_v} are the Feret diameter between right and left-most external point and bottom and top most external point, and d_{M_h} and d_{M_v} are the Martin diameter between right and left-most external point and bottom and top most external point

The sizes of particles are most simply expressed in terms of a single, linear dimension. However, in reality they are not normally monodispersed (Djamarani & Clark, 1997). As such the size of a specific type of particle is represented by distribution curves such as Arithmetic-normal, Log-normal, or Rosin-Rammler distributions (Allen, 1997; Bowman, Soga, & Drummond, 2001; Djamarani & Clark, 1997; Masuda, et al., 2006).

As particle size is defined assuming simplified geometry, it is important to characterise the real shape or to quantify how close the filler shapes are compared to a known geometry. To do this, several descriptors have been widely used to characterise both size and shapes of fillers (Bowman, et al., 2001; Hentschel & Page, 2003; Masuda, et al., 2006; Podczeck, 1997). These descriptors represents the filler geometry in terms of ratios between different dimensions, similarities with a known shape, or characteristics of filler surface such as roughness or texture (Masuda, et al., 2006). Normally the descriptors are used to broadly define the geometry of fillers. Thus, more than one descriptor is normally needed to represent a particular filler size or shape (Hentschel & Page, 2003). A list of the most common shape descriptors is given in Table 2.3 below.

Table 2.3 Some common shape descriptors presented in the literature

Shape descriptor	Equation		Ref*
Aspect ratio: Ratio between the maximum diameter and the thickness of the particle	$\alpha = \frac{d_{Fmax}}{b}$	(2.10)	A
Elongation: Ratio between maximum and minimum diameters of a particle	$E = \frac{d_{Fmax}}{d_{Fmin}}$	(2.11)	b, c, d
Flatness: Ratio between the minimum diameter and the thickness of the particle	$F = \frac{d_{Fmin}}{b}$	(2.12)	b
Circularity: Ratio of the perimeter of a circle (P_c) with the same projected area of the particle (P_{filler})	$\psi_{Ap} = \frac{P_c}{P_{filler}}$	(2.13)	e, b
Sphericity: Ratio of the surface area of a sphere (s_s) with the same volume of the particle (s_{filler})	$\psi_s = \frac{s_s}{s_{filler}}$	(2.14)	e, b
Bulkiness: Ratio between the area of a circumscribed rectangle or circled (A_{ref}) of the image and that of the particle (A_{filler})	$f_{bR} = \frac{A_{ref}}{A_{filler}}$	(2.15)	b
Roundness: The reciprocal of ψ_{Ap}	$C = \frac{{P_{filler}}^2}{4 \cdot \pi \cdot A_{filler}}$	(2.16)	d, b
Fractal dimension: Roughness parameter (D_f) that indicates the irregularities of surfaces at intervals of the perimeter	$log(P_{filler}) = (1 - D_f) log\eta + c$	(2.17)	e, b
Fourier series descriptor: Radius of the filler from the centre of gravity at different angle of orientation $R(\theta)$ where a_0, a_n, and b_n are the Fourier series parameters	$R(\theta) = a_0 + \sum_{n=1}^{N} [a_n \cos(n\theta) + b_n \sin(n\theta)]$	(2.18)	f, g

* a: Luo & Daniel (2003), b: Masuda, et al. (2006), c: Podczeck (1997), d: Hentschel & Page (2003), e: Allen (1997), f: Ehrlich & Weinberg (1970), g: Bowman, et al. (2001)

The above descriptors represent particular attributes of the fillers relating to different dimension of the fillers. Descriptors such as aspect ratio, elongation, or others that are calculated as ratios between particular properties have the advantage to be simple to estimate. However, it is not possible to reconstruct the fillers from that information (Hentschel & Page, 2003). In addition, the descriptors can show similar values for fillers that are evidently different (Russ, 1990). Thus, these descriptors may be more suitable for measurement of average shape or summary statistics. However, the Fourier series descriptor represents the shape of the fillers based on a mathematical expression and, as a result, the shapes can be reconstructed (Ehrlich & Weinberg, 1970). The level of details for the shape representation increases as the number of harmonics (or n in Equation 2.18) used for the calculation is larger.

2.4 Use of microscopy for characterisation of geometry of fillers and barrier dispersion coatings

Of the numerous methods that can be used to study the size of fillers, such as sieving, sedimentation, or laser diffraction, microscopy is the only method that can be considered absolute because it allows analysis and measurement of the individual particles (Allen, 1997; Masuda, et al., 2006). Optical microscopy is most often used for examination of individual particles with sizes from about 3 μm to 150 μm (Allen, 1997) although it is possible to observe details below 1 μm (Michler, 2008). At the smaller scale, electron microscopy can be considered. Using electron microscopy, it is possible to visualise objects down to 0.2-0.3 nm in the case of transmission electron microscopy and down to 0.7 nm for scanning electron microscopy (Allen, 1997). From these techniques it is also possible to obtain information about the morphology or shape of particles (Masuda, et al., 2006). During observations, images of the samples are captured and digitalised for further extraction of the information by image processing and analysis.

Microscopy is also used to characterise the structure of coatings. Scanning electron microscopy has been widely used to investigate the morphology of thin films and coatings (Lehtinen, 2000b). The study of coating structure, roughness, thickness (Chinga, et al., 2000; Kugge, Craig, & Daicic, 2004; Y. Li & He, 2012; Rissa, et al., 2006), porosity (Pöhler, Juvonen, & Sneck, 2006), and distribution of fillers in coatings (Rissa, et al., 2000; Rissa, et al., 2006) has been carried out by observation of cross section samples of coated papers. Microscopy of the surface of coated paper samples help in the description of coating topography, detection of imperfections, and distribution of fillers (Kugge, et al., 2004; Y. Li & He, 2012).

2.5 Measurement of transmission rate in barrier dispersion coating

In general, the process of gas transfer through barriers can be described by the Fick's law (Choudalakis & Gotsis, 2009; Comyn, 1985; Crank, 1956; Robertson, 2013). In particular, the Fick's law for steady state diffusion (or the first Fick's law) describes the transport of permeant in the barrier due to the gradient in permeant concentration at a constant rate (Comyn, 1985; Robertson, 2013). The unidirectional flux of permeant under steady state condition is represented by Equation 2.19.

$$J_p = -D\frac{\partial c}{\partial x} \tag{2.19}$$

where

J_p: Permeant flux ($mol \cdot s^{-1} \cdot m^{-2}$)

D: Diffusivity coefficient ($m^2 \cdot s^{-1}$)

c: Concentration gradient of the gas ($mol \cdot m^{-3}$)

x: Thickness of the barrier (m)

The heterogeneity of the coatings or interaction between permeant and the coating are not considered in the Fick's law (Robertson, 2013). For this reason, the barrier performance of dispersion coatings is often evaluated by measurement of the transmission rate (TR) of permeants. TR represents the resistance of barrier dispersion coatings to diffusion of substances such as gases, flavour, or aroma compounds (Robertson, 2013). The following expression represents TR.

$$TR = \frac{Q}{A \cdot t} \tag{2.20}$$

where

Q: Amount of permeant passing through the barrier coating (g)

A: Area of permeability (m^2)

t: Time of exposition (day)

Normally the measurement of TR is carried out by exposing the barriers to gas phases where the concentration of permeant is different across the barrier (Figure 2.6) (Lee, Yam, & Piergiovanni, 2008). This condition creates a driving force that induces a flux of permeant from the high concentration side to the low concentration side of the dispersion coating. It is common to measure the permeant flux when it becomes constant or also called steady state diffusion. This is explained, in part, due to the transient period to reach the steady state diffusion being much shorter than the self-life of the dispersion coatings or other barriers (Lee, et al., 2008).

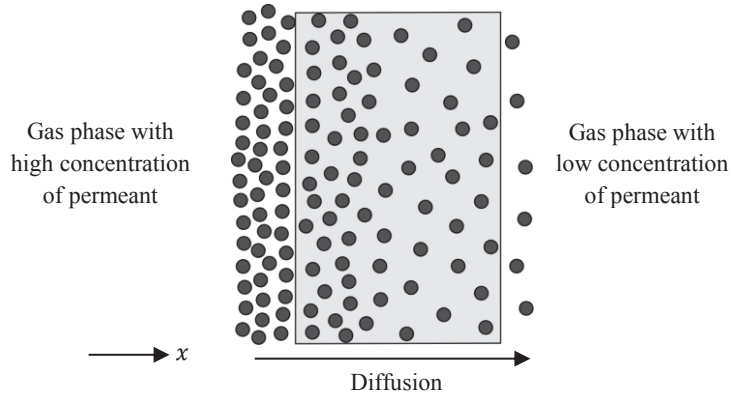

Figure 2.6 Diffusion of permeant through barriers

The factors that affect the TR of any permeant through barriers are related to the nature of the coatings. For example polymer molecular size, polymer additives; permeants and their molecular size and capability of interaction with the barrier, and environmental factors such as temperature and relative humidity, all affect performance (Finnigan, 2009; Krochta, 2010; Robertson, 2013). For dispersion coating testing, the permeants are selected based on the final use for the coated paper materials. In this way, water vapour (WVTR), oxygen (O_2TR), and carbon dioxide (CO_2TR) transmission rates are often required (Krochta, 2010).

It is important to note that the diffusion is affected by factors such as temperature or relative humidity. Thus, proper control of these factors during measurement is required (Johnson & Demorest, 2009). As an example, in the case of WVTR the measurements are normally carried out at either 50% RH and 23°C, 75% and 25°C, or 90% and 38°C (Kimpimäki & Savolainen, 1997). The most common standards for measurement of performance of barrier materials are ASTM E96-95 (1995), ASTM F2622-08 (2008), ASTM F1927-07 (2007), ASTM D3985-05 (2010), ASTM F2476-05 (2006), TAPPI T448 om-09 (2009), TAPPI/ANSI T464 om-12 (2012).

The permeability (P, mol.m.m^{-2}.s^{-1}.Pa^{-1}) of a coating formulation allows characterisation of the barrier properties discounting independent of its thickness. Equation 2.21 shows that P is a function of D and the solubility (S) of the permeant in the barrier. Diffusivity (D) represents a kinetic term which reflects the dynamics of the permeant and the barrier and S represents a thermodynamic term which depends on the interaction between the permeant and the barrier (Robertson, 2013).

$$P = D \cdot S \tag{2.21}$$

where

S: Solubility coefficient of the permeant in the barrier ($mol \cdot m^{-3} \cdot Pa^{-1}$)

If the barrier has a polymer phase, this may contain impermeable crystalline regions that reduce the cross sectional area for diffusion. The diffusion across the polymer phase can be modelled as a function of the permeability through the amorphous phase (non-crystalline region), volume fraction of the amorphous phase and a crystalline structure factor (Solovyov & Goldman, 2008). By using Equation 2.21, P can be calculated redefining S as a function of the solubility and the volume fraction of the amorphous phase (Michaels & Bixler, 1961).

Equation 2.20 is a different way to express the Fick's law, the thickness of the barrier is implicitly included and it has an effect on the value of TR. To represents P in terms of TR, Equation 2.22 can be applied (Robertson, 2013).

$$P = TR \cdot \frac{x}{\Delta p} \tag{2.22}$$

where

Δp: Difference in partial pressure of permeant on both sides of the barrier dispersion coating (Pa)

Based on *SI*, TR can be expressed in terms of $mol \cdot m^{-2} \cdot s^{-1}$ and P in terms of $mol \cdot m \cdot m^{-2} \cdot s^{-1} \cdot Pa^{-1}$. However, these units are normally transformed into many correct combinations presented in the literature such as $g \cdot m^{-2} \cdot day^{-1}$ or $mL \cdot m^{-2} \cdot day^{-1}$ in the case of $WVTR$ or O_2TR respectively (Finnigan, 2009; Robertson, 2013). A suggestion for standard units of gas exchange measurement has been proposed by Banks, et al. (1995).

2.6 Modelling of performance for barrier films

From an experimental point of view, it is a great challenge to optimise the structure of barrier coatings in order to improve their barrier properties (Zeng, Yu, & Lu, 2008). Modelling and simulations can be used to help to describe the properties of required materials and guide experiments to get the best barrier properties. The study of the interaction between fillers and polymer has been mostly developed for thermoplastic composites resulting in a high level of understanding. Numerous models to predict permeability as a function of filler shape and volume fraction have been developed during the last five decades (Choudalakis & Gotsis, 2009; Solovyov & Goldman, 2008).

The mechanisms of permeability reduction for thermoplastics composites is similar to barrier dispersion coatings where fillers are added in the polymer structure to lengthen the permeant pathway and, as a result, increase the tortuosity (Arora & Padua, 2010; de Azeredo, 2009; Park, Lee, Park, Cho, & Ha, 2003; Sinha Ray & Okamoto, 2003; Solovyov & Goldman, 2008). The process to convert polymers into thermoplastic barrier composites normally begins with plastic pellets which are melted and extruded (Lee, et al., 2008; Osborn & Jenkins, 1992). During the extrusion, additives can be used to achieve efficient and uniform composition of the melting (Osborn & Jenkins, 1992). To complete the process, the melt is filtered to remove any impurities and then formed into plastic sheets, films (Osborn & Jenkins, 1992; Robertson, 2013) or applied as extrusion coatings on different substrates thus forming the thermoplastic layer.

The investigation of barrier properties of thermoplastic composites have been focused on clay fillers due to their availability, platelet morphology, and high cation exchange capacities (Arora & Padua, 2010; Park, et al., 2003; Sinha Ray & Okamoto, 2003; Solovyov & Goldman, 2008). As an example, particle elongation from 40 to 1000 and surface areas around 750 $m^2 \cdot g^{-1}$ are commonly found for montmorillonite, saponite, or hectolite clays (Andrady, 2008; Hussain & Mehdi, 2006; Lehtinen, 2000d). Low concentrations of fillers (0.5 to 5 wt %) are normally required to significantly reduce the permeability of thermoplastic composites by up to four orders of magnitude (Andersson, 2008; Lange & Wyser, 2003; LeBaron, Wang, & Pinnivaia, 1999). It is important to note that a larger quantity of fillers in thermoplastic composites increases the chances of agglomeration of the fillers, and viscosity of the composites (Andersson, 2008). All these factors affect the dispersion of the fillers in the matrix and as a consequence their effectiveness in reducing permeability.

The permeability of thermoplastic composite films is modelled representing the effect of hypothetically impermeable and uniformly sized fillers in a binder in terms of the relative permeability (P_f/P_u). In general, this representation can be defined as a relationship between the volume fraction of fillers ($\emptyset_F$) in the thermoplastic composite and the tortuosity (τ) (Equation 2.23). The different types of fillers are represented by combinations of aspect ratio and shape of the fillers.

$$\frac{P_f}{P_u} = \frac{1 - \emptyset_F}{\tau} \tag{2.23}$$

where

P_f : Permeability of a filled thermoplastic composite

P_u : Permeability of a unfilled thermoplastic composite

The initial modelling approaches were based on oriented arrangements of the fillers which were equally distanced to each other, forming parallel layers. Normally the fillers were assumed to be rectangular shaped fillers with infinite depth and known height and length forming a two-dimensional geometry (Figure 2.7).

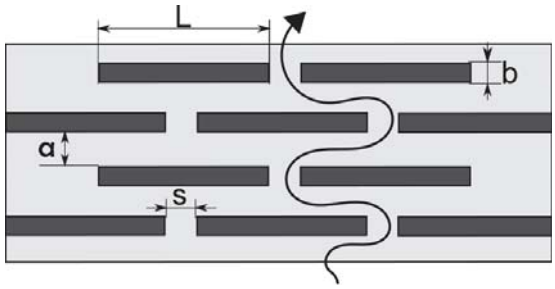

Figure 2.7 Geometry of the dispersion assuming oriented arrangement of the fillers. Where L is the second largest dimension of the filler particles, b is the filler particle thickness, a and s are the distance between filler particles in the thickness and width directions respectively.

One of the first models to predict relative permeability in polymers filled to dilute composites ($\alpha \cdot \emptyset_F \ll 1$, where α is the aspect ratio of the fillers) with oriented fillers was developed by Nielsen (1967). The author indicated that the relative permeability of thermoplastic composites is inversely proportional to the tortuosity, which is affected by the distance of the permeant pathway. Nielsen assumed that the pathway of the permeant is exactly through the middle of the gaps between fillers (Figure 2.7). Under this assumption, the model predicts the maximum possible tortuosity and consequently is the best scenario for barrier films with this assumed geometry (in reality some permeant will take a shorter path).

Similarly Cussler et al. (1988) studied the effect of the oriented arrangement of the fillers for semi dilute regimes ($\alpha \cdot \emptyset_F \gg 1$), including not only the effect of the resistance generated by fillers; but also the resistance of the space between fillers in the coating width direction (s) against the flux of permeant (Figure 2.7). Comparisons between experimental data and predictions indicate that the Nielsen and Cussler et al. models are more appropriate for films with $\emptyset_F$ lower than 10% when applied to different types of coating materials and fillers evaluated for several gases (Choudalakis & Gotsis, 2009; C. Lu & Mai, 2007; Nazarenko, Meneghetti, Julmon, Olson, & Qutubuddin, 2007; Wang, Wang, Qi, Zhang, & Zhang, 2005).

The Cussler et al. (1988) model was developed as a simplification of an earlier model created by Wakeham and Mason (1979). Assuming a single, perforated layer, the diffusion was further extended to account for the constriction (s) and the resistance related to the length of the pores in the width direction (Choudalakis & Gotsis, 2009; Falla, Mulski, & Cussler, 1996). Also, analogous to the Wakeham-Mason model, Aris (1986) developed a model by defining the same factors described above. However, in the case of Wakeham-Mason, the definition of the constriction resistance was independent of aspect ratio where for the Aris definition it is not (Choudalakis & Gotsis, 2009; Solovyov & Goldman, 2008).

The oriented arrangement of the fillers represents the best scenario that filled films could achieve for a given volume fraction. In many cases this assumption oversimplifies the structure of real coatings because the fillers tend to be randomly located. For this reason, other authors have included the random arrangement of the fillers during model development (Figure 2.8).

a)  b) 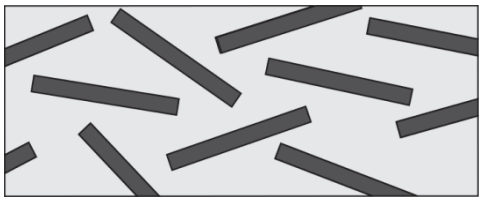

Figure 2.8 Random arrangement of the fillers into the coating with a) parallel orientation and b) non parallel orientation.

Lape et al. (2004) developed a model for composites filled with monodispersed flakes with random orientation as shown Figure 2.8a. The permeant pathway is determined by considering the probability of the permeant to pass through the shortest and the longest pathway around fillers. This compensation reduces the pathway distance to 2/3 of the path length that the fillers create in the case of the oriented arrangement.

Sun et al. (2008) indicated that the fillers tend to have parallel orientation when $\emptyset_F$ is high (Figure 2.8a), supporting the assumption presented by Lape et al. (2004); however, at low $\emptyset_F$ it is possible to observe fillers with different angles of orientation (Figure 2.8b). The random arrangement of the fillers with non-parallel angles of orientation into the films was analysed by Bharadwaj (2001) based on a modification of the Nielsen model. Completely dispersed fillers reduce the distance of the permeant pathway, deteriorating the barrier properties of the films. This reduction is directly associated to the angle of the fillers compared to the direction of the permeant flux. Based on the above observation, Bharadwaj counteracted the reduction of tortuosity by adding a parameter of order (S_{order}) defined by Tsvetkov (1942).

Other authors have developed models assuming flakes or disk shaped fillers. This assumption changes the perspective of the model to three-dimensional geometries. Fredrickson and Bicereno (1999) and Gusev and Lusti (2001) considered randomly located disk shaped fillers. The model of Fredrickson-Bicereno is based on multiple scattering theory for semi dilute regimes ($\alpha \cdot \emptyset_F \gg 1$). In the case of Gusev-Lusti, a finite element method simulation was used to solve the Laplace's equation for the local chemical potential. Despite the same assumptions being used in both models, the Fredrickson-Bicenaro model predicted a higher relative permeability than the Gusev-Lusti model particularly at relatively high $\emptyset_F$ and α (Choudalakis & Gotsis, 2009; Gusev & Lusti, 2001). These differences could be more than one order of

magnitude in cases of $\emptyset_F$ > 5% and α > 1,000 (Gusev & Lusti, 2001). More recently Minelli, Baschetti and Doghieri (2011) proposed a model valid for both two and three dimensional hexagonal, square, circular and octagonal plates randomly dispersed in a binder. This model was developed based on finite volume elements.

Assuming an oriented arrangement of hexagons, Moggridge et al. (2003) developed a model based on the previous work carried out by Cussler et al. (1988). The structure supposes three layers of hexagonally shaped fillers to avoid direct diffusion through the film. As used in the Fredrickson and Bicenaro model, a shape factor of 2/27 was included to correct the prediction under this scenario.

Zwon and Zumbrunnen (2003) proposed a different way to describe the effect of the fillers on the barrier performance of thermoplastic composites. They defined two parameters for this purpose; the linear fraction (λ) or the ratio between the thickness of the fillers and the total thickness of the barrier and the area fraction (δ) or the ratio between the area of filler (A_d) and the matrix (A) that faces the permeant. The product of λ and δ is equivalent to $\emptyset_F$. The model defines the randomness of the filler orientation by adapting the value of δ up to 1, when the fillers are oriented in serial or transversal orientation with respect to the permeant flux, forming layers of fillers in the thermoplastic profile. Under this scenario and assuming that the fillers are completely impermeable, the relative permeability of the thermoplastic composites becomes 0.

Nagy and Duxbury (2002) presented a model that describes the effect of the high aspect ratio of particles (from 100 to 2000) on barrier properties of thermoplastic composites. By assuming rectangular plates, two and three dimensional geometries were created and simulations were carried out. From the simulations, fitting parameters were found to describe the relative permeability according to the dimensionality of the geometries.

It is important to note that other types of models have also been developed to describe the transport across barriers. Similar to the effect of the filler in polymers, the permeability of uniformly distributed binary blends of polymers has been studied. The models are adaptations of thermal/conductivity models that assume spherical particles as the minor phase. A review of these models and their application on mixed matrix membranes is presented by Pal (2008). None of these models were analysed in this thesis because they significantly differ to the type of barrier and fillers that are analysed in the following chapters.

A summary of the models described above and their performance are presented in Table 2.4 and Figure 2.9 respectively.

Table 2.4 Summary of the presented models

Pigment arrangement	Model	Equation	Parameters		Shape	Dimension
	Nielsen (1967)	$\frac{P_f}{P_u} = \frac{1-\emptyset_F}{1+\alpha\emptyset_F}$	$\alpha = \frac{L}{2b}$	(2.24)	Circular, rectangular	Two
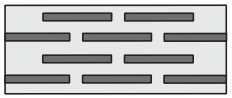	Cussler, et al.(1988)	$\frac{P_f}{P_u} = \left(1+\frac{\alpha^2{\emptyset_F}^2}{1-\emptyset_F}\right)^{-1}$	$\alpha = \frac{L+s}{2b}$ $s \ll L$	(2.25)	Rectangular	Two
	Wakeham-Mason (1979)	$\frac{P_f}{P_u} = \left(1+\frac{\alpha^2{\emptyset_F}^2}{1-\emptyset_F}+\frac{\alpha\emptyset_F}{\sigma}+2(1-\emptyset_F)ln\left(\frac{1-\emptyset_F}{2\sigma\emptyset_F}\right)\right)^{-1}$	$\alpha = \frac{L+s}{2b}$ $\sigma = \frac{s}{2b}$	(2.26)	Rectangular	Two
	Aris (1986)	$\frac{P_f}{P_u} = \left[1+\frac{\alpha^2{\emptyset_F}^2}{1-\emptyset_F}+\frac{\alpha\emptyset_F}{\sigma}+\frac{4}{\pi}\frac{\alpha\emptyset_F}{1-\emptyset_F}ln\left(\frac{\pi\alpha^2\emptyset_F}{\sigma(1-\emptyset_F)}\right)\right]^{-1}$	$\alpha = \frac{L+s}{2b}$ $\sigma = \frac{s}{2b}$	(2.27)	Rectangular	Two
	Lape, et al.(2004)	$\frac{P_f}{P_u} = \frac{1-\emptyset_F}{\left(1+\frac{2}{3}\alpha\emptyset_F\right)^2}$	$\alpha = \frac{L}{2b}$	(2.28)	Rectangular	Two
	Bharadwaj (2001)	$\frac{P_f}{P_u} = \frac{1-\emptyset_F}{1+\alpha\emptyset_F\frac{2}{3}\left(S_{order}+\frac{1}{2}\right)}$	$\alpha = \frac{L}{2b}$ $S_{order} = 0$	(2.29)	Rectangular	Two
	Kwon -Zumbrunnen (2003)*	$\frac{P_f}{P_u} = \frac{1-\delta}{1-\delta+\emptyset_F}$	$\delta = \frac{A_d}{A}$	(2.30)	Rectangular	Two
	Fredickson & Bicerano (1999)	$\frac{P_f}{P_u} \approx F_m\left(\frac{\pi}{ln\alpha}\alpha\emptyset_F\right)$ $F_m(x) = \left(\frac{1}{m}\sum_{j=1}^{m}\frac{1}{1+a_j x}\right)^2$	$\alpha = \frac{L}{2b}$	(2.31)	Circular	Three
	Gusev- Lusti (2001)	$\frac{P_f}{P_u} = exp\left[-\left(\alpha\frac{\emptyset_F}{x_0}\right)^{\beta}\right]$	$\alpha = \frac{L}{b}$ $\beta = 0.71$ $x_0 = 3.47$	(2.32)	Circular	Three
	Minelli et al. (2011)	$\frac{P_f}{P_u} = \left[\frac{\emptyset_F}{2}(\alpha+2)+\frac{2\emptyset_F}{\pi\alpha}(\alpha+2)^2 ln\left(\frac{1}{\pi}(\alpha+2)\right)\right]^{-1}$ $r \le 1$ $\frac{P_f}{P_u} = \left[1+\frac{\emptyset_F}{2}(\alpha+2)^2+\frac{2\emptyset_F(\alpha+2)^4}{4\left(\alpha^2-\alpha\emptyset_F(\alpha+2)\right)}+\frac{2}{\pi}(\alpha+2)^2 ln\left(\frac{2}{\pi}\left(\frac{\alpha}{\emptyset_F(\alpha+2)}+1\right)\right)\right]^{-1}$ $r \ge 1$	$r = \frac{2[\alpha-\emptyset_F(\alpha+2)]}{\emptyset_F(\alpha+2)^2}$ $\alpha = \frac{L}{2b}$	(2.33)	Circular, Squares, Hexagonal, Octagonal	Two, three
	Moggridge et al (2003)	$\frac{P_f}{P_u} = \left(1+\frac{2}{27}\frac{\alpha^2{\emptyset_F}^2}{1-\emptyset_F}\right)^{-1}$	$\alpha = \frac{L}{2b}$	(2.34)	Hexagonal	Three
	Nagy- Duxbury (2002)	$\frac{P_f}{P_u} = \frac{1}{1+c_1\alpha\emptyset_F+c_2(\alpha\emptyset_F)^2}$	$c_1^{2D} = 0.46 \pm 0.01$ $c_2^{2D} = 0.165 \pm 0.01$ $c_1^{3D} = 0.44 \pm 0.03$ $c_2^{3D} = 0.050 \pm 0.01$ $\alpha = \frac{L}{b}$	(2.35)	Square	Two, Three

*: Adapted for prediction of relative permeability for thermoplastics composites with impermeable filler

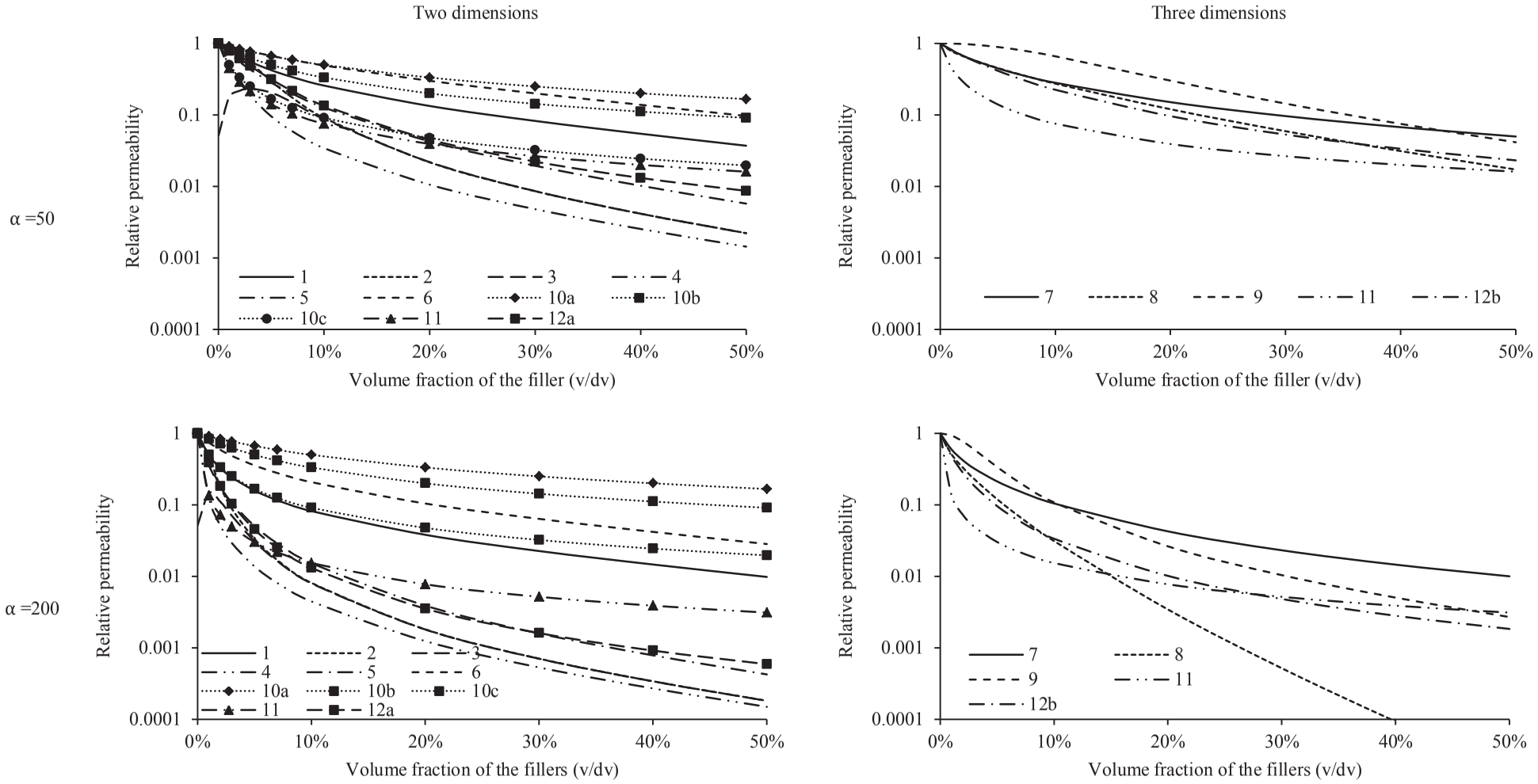

Figure 2.9 Relative permeability of filled films with α =50 and α =200 as a function of the volume fraction of the fillers. The models are 1: Nielsen (1967), 2: Cussler et al. (1988), 3: Wakeham-Mason (1979), 4: Aris (1986), 5: Lape et al. (2004), 6: Bharadwaj (2001), 7: Fredickson-Bicerano (1999), 8: Gusev-Lusti (2001), 9: Moggridge et al. (2003), 10a: Kwon-Zumbrunnen (2003) at β=0.9, 10b: Kwon-Zumbrunnen (2003) at β=0.95, 10c: Kwon-Zumbrunnen (2003) at β=0.999, 11: Minelli et al. (2011), 12a: 2D Nagy-Duxbury (2002), 12b: 3D Nagy-Duxbury (2002)

As shown in Figure 2.9 all models are very sensitive to changes in the volume fraction of fillers. Based on these models, it is possible to achieve reduction of up to three orders of magnitude in the relative permeability for barriers with 50% volume fraction of fillers, and even higher if the aspect ratio of fillers increases. However, similar models predict different relative permeabilities. As expected, the Nielsen (1967) model predicts higher relative permeability of the barrier compared with the Cussler et al. (1988), the Wakeham-Mason (1979) and the Aris (1986) models due to the effect of slit constriction that these three models assumed. Despite the similarities between the Aris (1986) and the Minelli et al. (2011) models, the predictions showed more pronounced reduction of the relative permeability using the Aris model.

The Lape et al. (2004) and the Bharadwaj (2001) models predict higher relative permeability than models with oriented arrangement due to the shorter diffusion pathway produced by the random arrangement of the fillers. The Bharadwaj model (2001) predicted higher relative permeability than the Lape et al. model (2004) because of the reduction of barrier properties caused by the angle of orientation.

At low aspect ratio, the Fredickson-Bicerano (1999) and the Gusev-Lusti (2001) models predict similar performance for the barriers; however, the Moggridge et al. model (2003) estimated better barrier properties because the regular arrangement of the fillers creates an overlapping structure reducing the spaces between fillers. Interestingly the Gusev-Lusti model (2001) is more sensitive to changes in the aspect ratio of the fillers than the other models. The reduction in the predicted relative permeability was several orders of magnitude at high aspect ratio. The prediction from the two dimensional Nagy-Duxbury (2002) model was always higher than its three dimensional version. Both model predictions were always lower than the Fredickson-Bicenaro model (1999).

In the case of the Kwon – Zumbrunnen model (2003), the results shown that the prediction was very sensitive to δ, particularly when it is close to 1 where the fillers tend to be parallel oriented. It is important to mention that high accuracy in the calculation of δ is required due to the sensitivity of the model to this parameter. This seems to be a difficult task because it is required to know the area of filler (A_d) that faces the permeant.

2.7 The applicability of literature models on the prediction of barrier performance of dispersion coatings

As the literature has shown, upon increasing the volume fraction of the fillers, the barrier properties of both barrier dispersion coatings and thermoplastic composites improve. In Table 2.4, there are a number of models that could potentially be applied to dispersion coatings. These

differ with respect to amount of fillers, orientation of fillers, and filler particle elongation. These factors must be considered in selecting which models are most appropriate for barrier dispersion coatings.

In the coating, the fillers are spatially arranged randomly and, depending on the coating conditions, can have non-parallel orientation. Thermoplastic composites are more susceptible to distribution of the filler with non-parallel orientation due to the low volume fraction of the fillers normally used and the relative high film thickness compared to barrier dispersion coatings. The opposite is found in barrier dispersion coatings where the freedom of rotation of fillers is limited by the large amount of fillers and reduced coating thickness. In assuming oriented arrangement of the fillers with parallel orientation (Figure 2.7), the possibility for rotation of them is limited by the length of the fillers and the spaces between the layers of fillers (Figure 2.10). In this way, the maximum angle of orientation for fillers can be calculated by the following geometric considerations:

$$\gamma_F = \gamma_1 - \gamma_2 \tag{2.36}$$

$$\gamma_1 = \sin^{-1}\left[\frac{1}{r}\cdot\left(a+\frac{b}{2}\right)\right] \tag{2.37}$$

$$\gamma_2 = \sin^{-1}\left(\frac{b}{2\cdot r}\right) \tag{2.38}$$

$$r = \frac{1}{2}\sqrt{L^2+b^2} \tag{2.39}$$

$$\emptyset_F = \frac{L\cdot b}{(L+s)\cdot(a+b)} \tag{2.40}$$

where

γ_F: Maximum angle of filler orientation

γ_1: Angle formed between the centre of the rotated filler and a corner with the original position as references

γ_2: Angle formed between the centre of the filler and a corner

L: Length of the fillers

b: Thickness of the fillers

r: Diagonal (hypotenuse) formed between any corner and the centre of a filler

a, s: Space between two parallel filler layers and the slit between two filler particles.

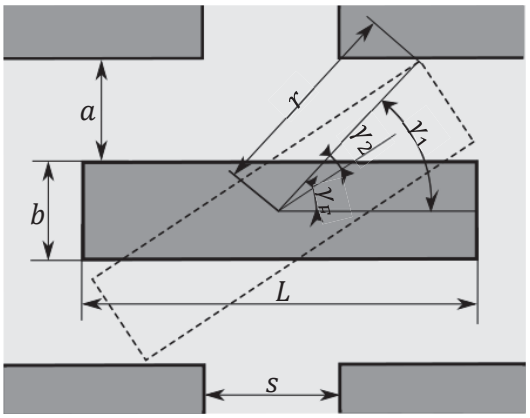

Figure 2.10 Maximum angle of orientation for fillers with oriented arrangement

As shown in Figure 2.11, the possible angle of orientation decreases if the volume fraction and the aspect ratio of the fillers increase. In the case of barrier dispersion coatings, the angle of filler orientation is much reduced due to the large $\emptyset_F$ and the thin coating thickness. Even for low volume fraction, the angle of orientation is not high enough to justify the need for models that include the random orientation of the fillers. It is important to note that the above results are valid for areas where the substrate surface does not affect the orientation of the fillers such as for pre-coated substrates.

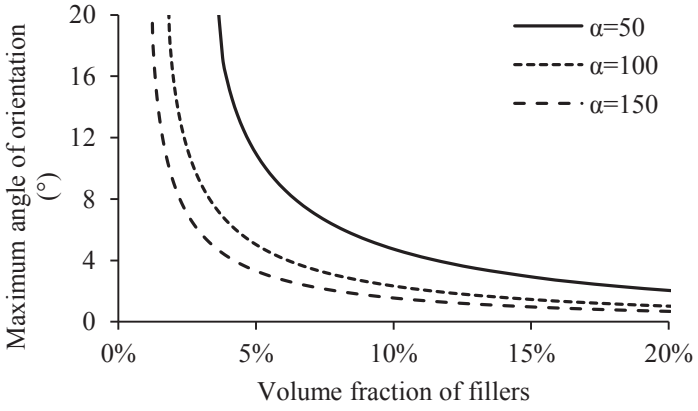

Figure 2.11 Theoretical maximum angle of pigment orientation for three fillers aspect ratio (α) estimated from the centre of the fillers.

The majority of the presented models assume the elongation ratio (E) is infinite (i.e. The Nielsen (1967), Cussler et al. (1988), Wakeham-Mason (1979), etc). This makes them more applicable for fillers with a large E. Based on Equation 2.24, approximation of the error of assuming two dimensions can be estimated from Equation 2.41, where the relative permeability for the third dimensional aspect ratio (αE) is compared to the relative permeability ignoring the third dimensional effect.

$$\frac{Pf/Pu_{\alpha E}}{Pf/Pu} = \frac{1 + \frac{C}{2 \cdot b} \cdot \emptyset_F}{1 + \frac{L}{2 \cdot b} \cdot \emptyset_F} \tag{2.41}$$

where

$Pf/Pu_{\alpha E}$: Relative permeability across the third dimensional aspect ratio

C: Length of fillers in the width direction

According to Figure 2.12, if the elongation is very large, the approximation of the error (Equation 2.38) tends to zero and the two dimensional models are valid. It can be seen that an elongation of 10 would result in approximately a 10% error in the prediction of relative permeability for various amounts of fillers. For elongation ratios higher than 10, the two dimensional models are likely to be suitable. The fillers used for both thermoplastic composites and barrier dispersion coatings are normally plate or flake shaped where the length and width are relatively similar (E≈ 1) (Gelinas & Vidal, 2010; Holik, 2006; Lehtinen, 2000d). Because of these particle shape factors, the most appropriate models to predict relative permeability of barrier dispersion coatings are those that assume three-dimensional geometries and parallel orientation of the fillers.

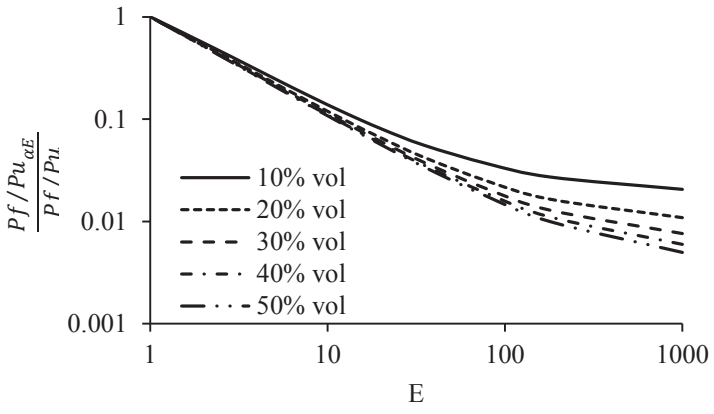

Figure 2.12 Relative permeability of length coating direction and width coating direction using the Nielson model (Nielsen, 1967) as a function of the elongation (E) of the fillers for five volume fractions.

From the above discussion, the models that closer represent the structure of dispersion coatings are those that assumed parallel orientation of three dimensional fillers such as the Fredickson-Bicenaro (1999), the Gusev-Lusti (2001), the Moggridge et al. (2003), the Minelli et al. (2011), and the Nagy-Duxbury (2002) models. These models assume good dispersion of filler particles. In thermoplastic composites, this is generally true because of the low volume fraction and for this reason these models are applied for volume fractions lower than 20% (Bharadwaj, 2001;

Solovyov & Goldman, 2008). The quantity of fillers required for barrier dispersion coatings is several times higher than that used for thermoplastic composites due to the relatively small aspect ratio and surface area of the fillers. This indicates that the preparation of barrier dispersion coatings may be sensitive to agglomeration, particularly around the critical pigment volume concentration (CPVC), which effectively reduces the already relatively low aspect ratio of the fillers (Table 2.1). The CPVC varies depending on the filler properties but ranges from 50% vol to 55% of volume concentration. When agglomeration occurs, higher permeability will occur, although industrial coating application would avoid agglomeration. The models can be used to demonstrate this increase in permeability by decreasing the aspect ratio (α).

Figure 2.13 shows the effect of the decreasing aspect ratio on relative permeability at volume fraction in the expected CPVC range using the Moggridge et al. model (2003). The relative permeability can increase if the aspect ratio of filler is reduced particularly in cases where the original aspect ratio is lower than 15. This effect is stronger if the volume fraction of the filler increases.

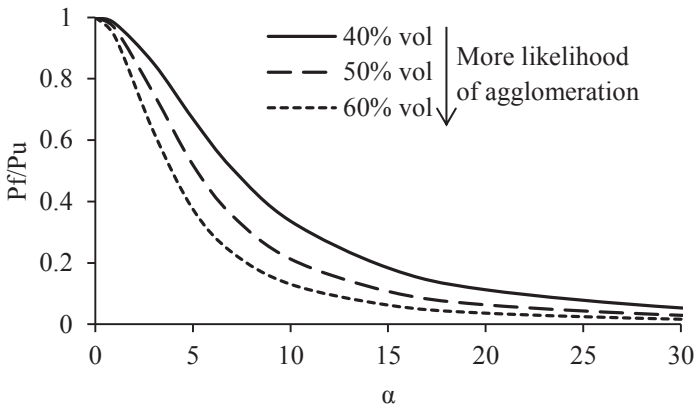

Figure 2.13 Effect of aspect ratio (α) on the reduction of relative permeability for a filled coating using the Moggridge et al. (2003) model for three volume fractions of fillers.

In all the models proposed in the literature, the characteristics of the continuous polymer phase are not included and the models just predict the changes of the final diffusivity of filled barriers with respect to the diffusivity of unfilled barriers. Likewise, the conditions that the barriers are exposed to, do not play any role in the relative permeability. Under this scenario, for proving that the models work properly for barrier dispersion coatings, the characteristics of unfilled and filled coatings, such as known coating thickness or polymer diffusivity are required. Unfortunately this is a very challenging task, difficult even under laboratory scale conditions.

There is little experimental data for dispersion coating with varying filler volume fractions and

/or aspect ratio, which is suitable to validate the use of the models. Zhu et al. (2013) presented WVTR results for a number of dispersion coatings, formulated with styrene-butadiene with six types of fillers and an evaluation of six models presented in Equations 2.24, 2.25, 2.28, 2.29, and 2.34. However, the validation was carried out over a very limited range of volume fraction and aspect ratios (around 60% mass fraction and 6.0 of aspect ratio). In addition, the investigation showed the amount of the fillers in terms of mass fraction and did not explain how it was transformed into volume fraction as it is required to evaluate the models. Bollström et al. (2013) studied the barrier properties of dispersion coatings prepared with platy and fine kaolin clays dispersed in styrene-butadiene and styrene-acrytelate latexes. The dispersion coatings were formulated at 40% and 57% of volume fraction of fillers. This information allows partial validation of the models in a limited region of volume fraction but not against lower filler volumes fractions. Schuman et al. (2005) reported barrier coating performance with a larger range of volume fraction of fillers. Their experimental data were for a kaolin clay/latex system including two different volume fractions (about 10% and 37%) and one filler particle aspect ratio. They found that the Moggridge et al model fitted the trend although they had to dramatically reduce the aspect ratio of the fillers from 45 in the experiment to 12 for the model input. These data are not sufficient to evaluate the effectiveness of the models for prediction of permeability through barrier dispersion coatings. However, they suggested that other factors may be required to predict permeability of the barrier dispersion coatings such as the dispersion of fillers in the coating, fillers thickness, filler size distribution, or the structure of the barrier dispersion coating. For these reasons, further investigation is required to evaluate how the conditions of the structure impact on the barrier performance of dispersion coatings. Based on this understanding, models and simulation could be developed to predict performance of barrier dispersion coatings.

2.8 Development of models and simulation based on particles dispersion of other type of systems

As well as thermoplastic composites and dispersion coatings, the problem of how to populate an area or volume with a certain number of particles has been studied in diverse fields. The studies cover areas as different as mechanical properties of metal composites (Shen & Lissenden, 2002; Wu, Zhang, Yang, & Huang, 2014) or clustered particle (Deng & Chawla, 2006), shape analysis of railway ballast (M. Lu & McDowell, 2007), permeability of dispersed nanotubes in polymer matrix (Gusev & Guseva, 2007), projectile penetration testing (Fang & Zhang, 2014), spheres packing (Baranau, Hlushkou, Khirevich, & Tallarek, 2013), and several others mentioned in the literature. Examples of two different studies where particles were modelled are presented in Figure 2.14.

a) b)

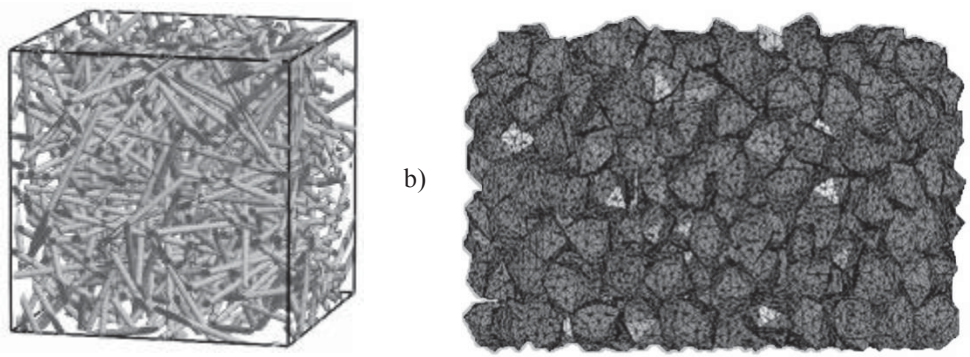

Figure 2.14 a) Analysis of permeability of nanotubes in a polymer matrix (Gusev & Guseva, 2007), b) rubber-rubble overlay used for projectile penetration testing (Fang & Zhang, 2014)

Common considerations are normally seen between the cases. For example, the definition of particles is normally carried out by assuming shapes. This assumption can vary from simply two dimensional shapes such as circles to more complex shapes like irregular particles in three dimensions such as irregular octahedra. The particles can be regularly or randomly distributed in the studied volume. In the case of sphere packing it is expected that all the particles are together. However, in the case of modelling of composites for example, the particles are normally dispersed in the volume. In both cases it is necessary to avoid overlapping between particles to create realistic scenarios. The detection of overlapping is straightforward for simple geometries such as spheres; however, this could become more complex if the particle shapes are more irregular (Nolan & Kavanagh, 1995). This suggests that the methodology for overlapping detection may have a relation with the specific conditions of the models.

It is also normal to assume periodic boundary conditions in some or all the boundaries (surfaces) of the studied volume. This refers to the continuity of the solution between opposite boundaries reducing the required number of particles and the size of the studied volume (Euston, Costello, Naser, & Nicolasai, 2007; Goodyer & Bunge, 2009).

The mathematical formulation of the models is usually resolved by finite element method (FEM). The FEM is a technique that models systems by division of their geometries into discrete components or elements, often simple shapes, whose behaviour is readily understood by a finite number of parameters and where differential and integral equations can be solved (Liu & Quek, 2013; Reddy & Gartling, 2010; Zienkiewicz, Taylor, & Zhu, 2005). The solution of the complete system is obtained by association of the calculation for each element by a procedure of establishing local equilibrium at common points between elements or nodes (Zienkiewicz, et al., 2005). This process leads to the establishment of governing equations for each element based on physical and mathematical principles and a set of lineal algebraic

simultaneous equations for the entire geometry to describe the solution of the system (Liu & Quek, 2013). The FEM has been used as a tool to simulate and analyse designs in different areas of engineering (Chandrupatla & Belegundu, 2012; Liu & Quek, 2013).

Due to the random nature of many variables in these problems such as location of the particles into the studied volume, it is also common to use the Monte Carlo simulation to define those variables. The main idea of this method is to run a number of simulations based on random sampling (Thomopoulos, 2013). The system inputs of the simulations are randomly defined and as a consequence the outcome results are different between simulations. To achieve a proper representation of the phenomenon that has being studied, normally a large number of simulations is required. This is applied for the location of the particles in the studied volume, but according to the main definition of the Monte Carlo simulations, it seems to be valid for other variables such as particle length, thickness, aspect ratio, elongation or any other factors that may be defined randomly.

From the above discussion, the development of a model to predict barrier performance of dispersion coatings may be possible. The model can be developed by taking the considerations of previous works and adapting them to the specific conditions required for dispersion coatings modelling. A model with these characteristics would be useful to evaluate different parameters that affect the permeability of dispersion coatings and as a result optimise the formulation of the dispersion coating.

2.9 Discussion and conclusion

The literature review highlighted that the structure and composition of barrier dispersion coatings influence their barrier properties. The addition of fillers in the binder increases the tortuosity of pathways, allowing a reduction of the permeability. In addition, the chemical properties of fillers and their interaction with the coating binder is also a factor to consider for analysis of barrier performance of barrier dispersion coatings. As such, the final structure of the dispersion coating affects the reduction of permeability. This understanding could help in the formulation of dispersion coatings for particular requirements. However, from the experimental point of view, it is a great challenge to optimise the structure or manipulate the fabrication of barriers with the best barrier properties. Modelling and simulation can be used to help describe the properties of materials required and guide experiments to get the best barrier properties.

A number of models have been developed to predict the permeability of barrier films such as thermoplastic composites but none have been applied or developed for use on barrier

dispersion coatings. The models are normally based on idealised geometries, where the fillers are arranged in either an oriented or random way. Specific filler shapes are assumed that create, in most cases, a two dimensional geometry of the barrier films. The heterogeneous characteristics of the barrier dispersion coatings such as uneven coating thickness, particle size and lower elongation of the fillers limit the use of the presented models for the prediction of dispersion coating barrier performance. For thermoplastic composite, the models are valid for only low volume fraction of the fillers ($\emptyset_F$< 10%) as at higher levels, filler agglomeration occurs. The amount of fillers used for barrier dispersion coatings is much higher (40- 50%) before agglomeration occurs ($\emptyset_F$> CPVC) and therefore the models are potentially applicable to up to this range.

Those models that assumed plate shaped fillers are the most suitable to predict relative permeability of barrier dispersion coatings (the Fredickson-Bicenaro (1999), the Gusev-Lusti (2001) and the Moggridge et al. (2003) models). These models assumed parallel three-dimensional fillers with circular or hexagonal shaped filler particles. The conditions are consistent with the characteristics of barrier dispersion coatings. Normally, the fillers used in barrier dispersion coatings such as clay or talc are defined as plate shaped fillers and they tend to be parallel to the substrate due to the high volume fraction and low thickness of the coatings. Very little data for dispersion coatings with variables α and $\emptyset_F$ have been reported in the literature. However, the discrepancy between experimental data and predicted results suggested that other factors may need to be considered to predict permeability of the barrier dispersion coatings such as dispersion of fillers in coating, filler thickness, filler size distribution, or the structure of the barrier dispersion coating. For these reasons, further investigation is required to evaluate how the conditions of the barrier dispersion structure impacts on the barrier performance of dispersion coatings. Based on this understanding, models and simulations could be developed to predict barrier performance of barrier dispersion coatings.

Based on this analysis, the development of models for barrier dispersion coatings have to focus on three-dimensional geometries. For this reason, characterisation of filler geometry and coating structure are required.

The current level of the computer tools (such as FEM) allows development of complex models and the simulation of three-dimensional geometries including all the aspects needed to properly characterise barrier dispersion coatings.

Chapter 3

GEOMETRICAL CHARACTERISATION OF FILLERS USED FOR DISPERSION COATINGS

The objective of this chapter was to develop a quantitative analysis of the geometry of fillers used in dispersion coatings. The development of mathematical models of barrier dispersion coatings requires characterisation of the geometry of the fillers used. The characterisation would ideally allow the representative reproduction of their key aspects when generating model based geometries. In terms of filler geometry it is likely that the fillers used are non-uniform and therefore measurement of the distribution of size and shape is required. Depending of the complexity of the shape selected for subsequent modelling, a number of different approaches for filler characterisation were highlighted in the literature. This chapter aimed at exploring these methods to allow the application of mathematical modelling of varying complexity in later chapters.

3.1. Selected fillers for further analysis

Three pre-dispersed kaolin clay fillers widely used in the coating industry were selected for further analysis. In this thesis, the clays were identified as Clay A, Clay B, and Clay C. The names of the companies that produce the clays were not identified due to intellectual property considerations. These clays were the same used in coating formulations analysed in the following chapters. The characterisation of the representative size and shape of the filler was based on the analysis of images from light microscopy. Table 3.1 shows the available data of the selected clays

Table 3.1 Available information of selected clays

Filler	Aspect ratio (Shape factor)	Particle size (%<2 μm)
Clay A	100	-
Clay B	60	-
Clay C	-	97

To guide the understanding of the measurements, the parameters that were measured are presented in Figure 3.1.

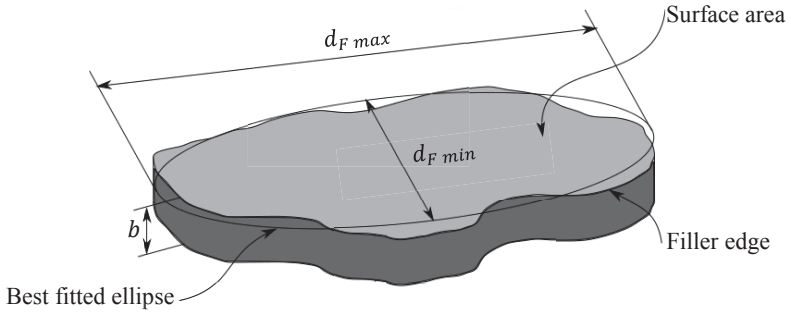

Figure 3.1 Scheme of a filler and the dimension measured where $d_{F_{max}}$ is the maximum Feret diameter of the filler, $d_{F_{min}}$ is the minimum Feret diameter of the filler, and b is the filler thickness

3.2. Calculation of true density of the selected fillers

The true density can be defined as the ratio between the mass and the volume of the fillers, not including the volume between filler gaps (Allen, 1997). By relating the volume of the fillers and the volume surrounding them, it is possible to measure the true density. It is common to use the pycnometer to obtain accurate measurement of the true density. The pycnometer (or gravity bottle) is a flask with a capillarity tube that allows constant volume of the reference liquid. This liquid is used to estimate both the volume of fillers and the volume surrounding them by changes of weight in the pycnometer (Allen, 1997; Masuda, et al., 2006).

In this experiment, about $2\,g$ of fillers were put into the pycnometer and its weight was measured. Then, the pycnometer with fillers was filled with distilled water (reference liquid), agitated for a few minutes and weighted. The pycnometer also was filled with only distilled water. Also, the weight of the pycnometer was determined to be discounted to the above measurements. From the above information, the true density can be estimated by Equation 3.1 (Masuda, et al., 2006).

$$\rho_{filler} = \frac{\rho_l \cdot (m_{pf} - m_p)}{(m_{pl} - m_p) - (m_{plf} - m_{pf})} \tag{3.1}$$

where

ρ_{filler}: True density of the fillers $(g \cdot mL^{-1})$

ρ_l: Density of the reference liquid $(g \cdot mL^{-1})$

m_{pf}: Mass of pycnometer and fillers (g)

m_p: Mass of pycnometer (g)

m_{pl}: Mass of pycnometer raised with reference liquid (g)

m_{plf}: Mass of pycnometer raised with reference liquid and filler sample (g)

m_{pf}: Mass of pycnometer and filler sample (g)

To improve the estimation, the moisture content of the fillers was estimated by gravimetric method ($24h$ at $105°C$) and discounted of m_{pf}. For each type of clay, three replicates were taken. The average and standard deviation of the measurements are presented in Table 3.2.

Table 3.2 Results of true density measured by pycnometer method for the selected fillers

	Clay A	**Clay B**	**Clay C**
Average density $(g \cdot mL^{-1})$	2.158	2.501	2.354
Standard deviation density $(g \cdot mL^{-1})$	0.074	0.036	0.047

3.3. Filler surface characterisation

Light microscopy was used to observe the surface of the fillers. For this, filler samples were diluted in deionised water at 0.3 wt%. This mixture was agitated for 15 min with a 45° inclined blade turbine (25 mm diameter) at 700 rpm in a 325 mL beaker with 4 baffles. The pH of each dilution was adjusted to 8-9 by adding drops of 0.5M NaOH to improve the dispersion of the fillers in the solution. After mixing, three samples of each suspension were taken by immersing microscope glass slides into the liquid. The surfaces of the slides were treated prior with a surfactant solution to reduce the surface tension of the dispersion allowing better distribution of the fillers on the slides. The slides were then dried on a hot plate for a few seconds at about $100°C$. Finally, the slides were stained with methylene blue to improve the contrast of the filler particle edges. Because of the plate-like structure of the clay particles, in this sample preparation method the fillers lay flat, presenting the largest surface area of each particle. This method was based on Gelinas and Vidal (2010).

An Olympus BX53 light microscope with an integrated camera was used to observe the surface area of the fillers placed on the glass slides. 736x626 pixels images were captured at different points on the glass slides using 40 X magnification with no colour filters. The images were enhanced to differentiate the fillers and the background using ImageJ. The enhancement started by converting the images into 8-bit black and white. From these images, threshold was applied to differentiate the fillers and image background. This process relates to the selection of pixels that are in a given range of brightness to differentiate different objects in the images. The threshold range was based on the brightness of the fillers in each image. Once the threshold was applied, the images were converted into binary images by giving two levels of pixel colour; white for the background and black for the fillers. It is important to mention that some images required further enhancement due to the presence of noise. For example, those isolated pixels that are not related to the fillers (this is commonly called salt and pepper noise) were discarded

by median filters. The median filters replace the value of the isolated pixels by the median values of the pixels in their neighbourhoods (Fisher et al., 2014). Despite the low concentration of the dilution used to prepare the samples (condition that facilitates the good dispersion of the fillers on the glass slides), some cases presented filler agglomeration or overlapped fillers. In these cases, watershed was applied to digitally separate and individualise fillers. Figure 3.2 shows an example of the image processing from the original image to the final binary image after enhancement.

a) b)

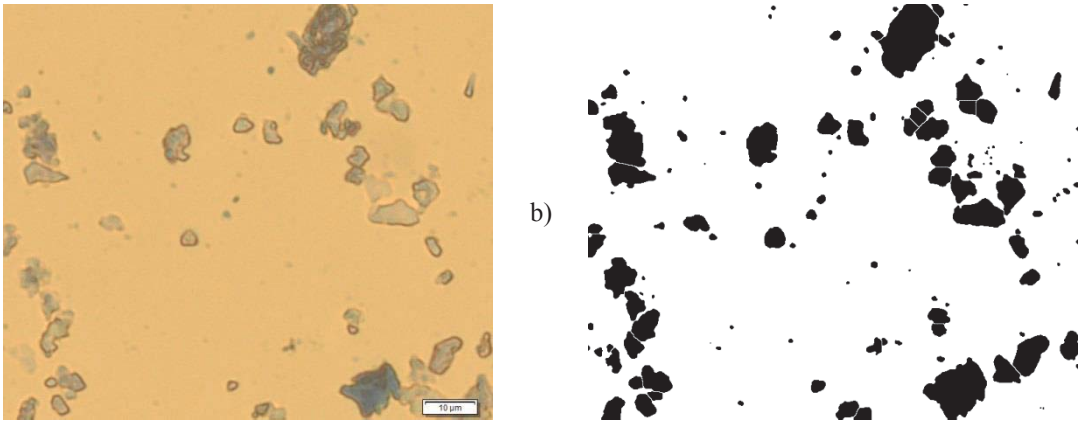

Figure 3.2 Light microscope image captured for filler characterisation of Clay A; a) original image, and b) image after enhancement

Nine images were analysed for each type of clay reaching a total number of measured fillers of 3150, 2215, 2241 for Clay A, B, and C respectively. The fillers were then analysed in two ways. Firstly by estimation of the surface area and secondly by fitting the best ellipse on the filler contour based on the least squares fitting methodology. The surface area of the fillers was calculated by counting pixels of the filler projection and transforming them into area units based on the image scale. The best fitted ellipse was used to determine the maximum ($d_{F_{max}}$) and minimum ($d_{F_{min}}$) Feret diameters represented by the major and minor semi axes of the ellipse respectively. Based on a discretisation of the filler edge in a group of points, the fitting allows representation of the filler shape by a mathematical curve (Fitzgibbon, Pilu, & Fisher, 1999; Gander, Golub, & Strebel, 1994). This method is used as the reference needed for measurement of the Feret diameters. To find the best fit, least square of the distance between points in the fitted ellipse and the edge of the filler has to be reached (Fitzgibbon, et al., 1999; Pratt, 1987).

Both measurements, the Feret diameters and surface area of fillers, were estimated by ImageJ and the probability distributions of them were defined by Matlab. To reduce bias from experimental error, all of those fillers that showed elongation equal to 1 or fillers represented by less than 0.5 μm of the maximum Feret diameter were not considered for the analysis. In the

same way, those fillers that were excessively large were rejected for further analysis. Table 3.3 shows the results of length and area for the selected fillers.

Table 3.3 Maximum Feret diameter ($d_{F_{max}}$) at different cumulative probability and average surface area of the selected fillers

	$d_{F_{max}}$ (μm)					Surface area
	10%	**25%**	**50%**	**75%**	**90%**	**(μm^2)**
Clay A	1.33	2.27	3.76	3.15	8.51	11.48
Clay B	1.31	2.20	3.67	2.10	7.79	9.47
Clay C	1.14	1.98	3.33	2.24	6.93	9.47

In terms of the maximum Feret diameter, the differences found between types of fillers were as expected. Clay A was the longest followed by Clay B and C respectively. This trend was also shown for diameters at different particle size classes where at a given percentage of filler size distribution, Clay A was longer than Clay B, and Clay B was longer than Clay C. The literature indicates that most particles of kaolin clays are between 0.3 μm and 5 μm (Holik, 2006). This range was coincident with the observed diameters where the majority of the fillers were smaller than 10μm. The surface area for the largest of each filler particles was approximately 120 μm^2 where Clay A presented the largest average surface area of 11.48 μm^2 in comparison with Clay B and Clay C. Figure 3.3 shows distributions of filler size parameters measured from the surface area of the fillers. For both maximum Feret diameter and surface area, the experimental data fitted well with the log-normal distribution. This distribution is commonly used as a good descriptor of size for any type of particle (Allen, 1997; Bowman, et al., 2001; Djamarani & Clark, 1997; Masuda, et al., 2006). Equations 3.2 and 3.3 show the cumulative distribution and probability density function of the Log-normal distribution.

$$F(x_f;\mu_f,\sigma_f) = \int_{x_{min}}^{x_{max}} f(x_f;\mu_f,\sigma_f)dx_f \tag{3.2}$$

$$f(x_f;\mu_f,\sigma_f) = \frac{1}{x_f \cdot \sigma_f \cdot \sqrt{2\pi}} \cdot exp\left[-\frac{(\ln x_f - \mu_f)^2}{2 \cdot \sigma_f^2}\right] \quad , \qquad x_f > 0 \tag{3.3}$$

where

μ_f: Average of the logarithm of length (m) or surface area (m^2) of the fillers

σ_f: Standard deviation of the logarithm of length (m) or surface area (m^2) of the fillers

x_f: Length (m) or surface area (m^2) of the fillers at a particular probability

$F(x_f;\mu_f,\sigma_f)$: Cumulative distribution function of the length or surface area of fillers

$f(x_f; \mu_f, \sigma_f)$: Probability density function of the length or surface area of fillers

x_{max}: Maximum length (m) or surface area (m^2) of the fillers at a particular probability

x_{min}: Minimum length (m) or surface area (m^2) of the fillers at a particular probability

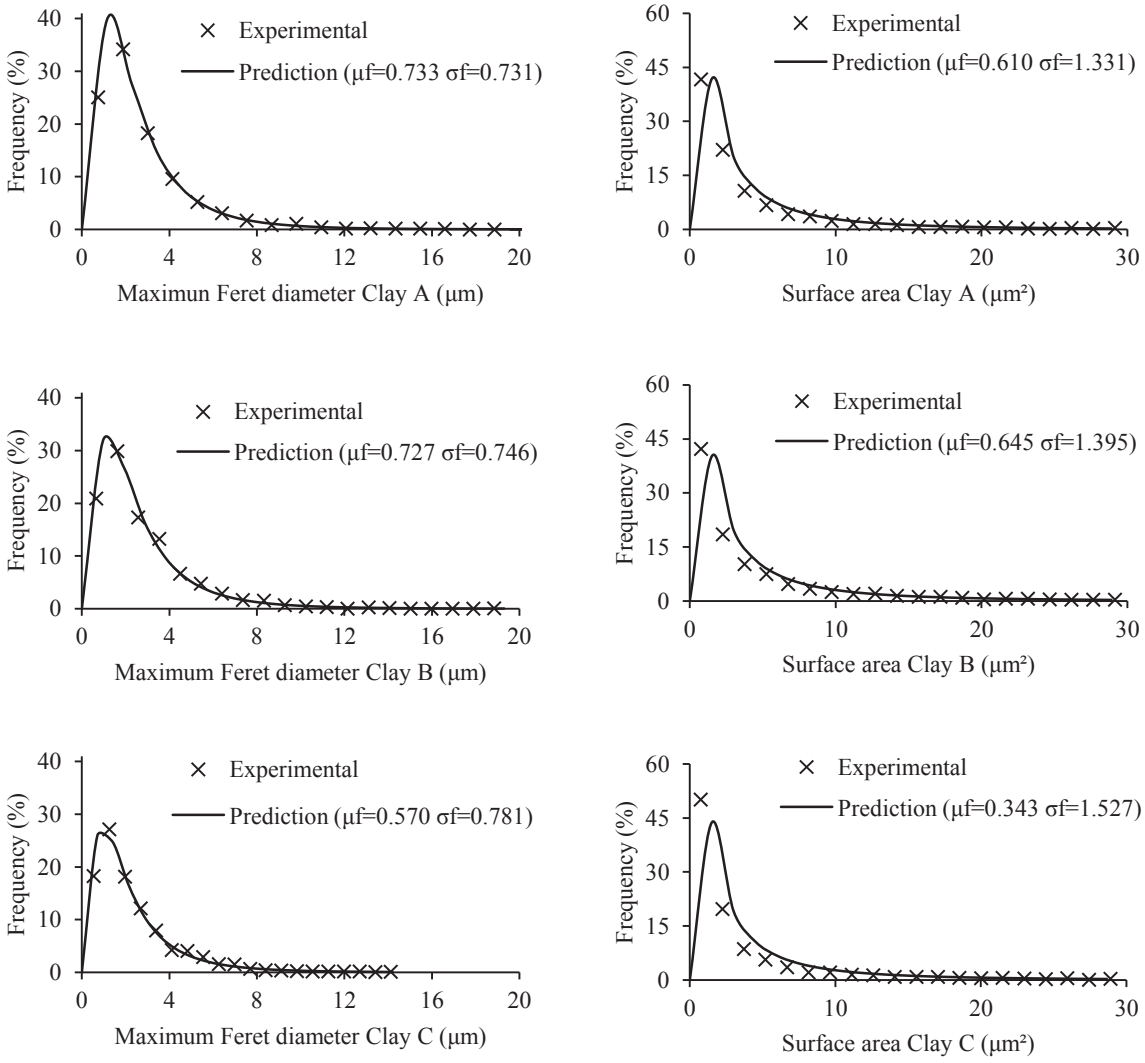

Figure 3.3 Maximum Feret diameter and surface area of the selected clays where μ_f and σ_f are the mean and standard deviation of the maximum Feret and surface area natural logarithm respectively required to define the lognormal distribution

Figure 3.4 shows a comparison between surface area and the maximum Feret diameter for the selected fillers. The surface area was selected as reference for comparison due to their properties of clays being dominated by their surface area (Velde, 1995). The trend indicated a positive linear correlation between the maximum Feret diameter and surface area; 0.94, 0.84, and 0.93 for Clay A, B, and C respectively. Higher variation of the results was found as the fillers

became larger. Figure 3.4 also compared the results with theoretical elongation calculated by assuming elliptical shaped fillers. The elongation represents the ratio between the maximum and the minimum Feret diameters for each of the fillers. The theoretical elongation of most of the fillers varied between one (or circular shape) and three.

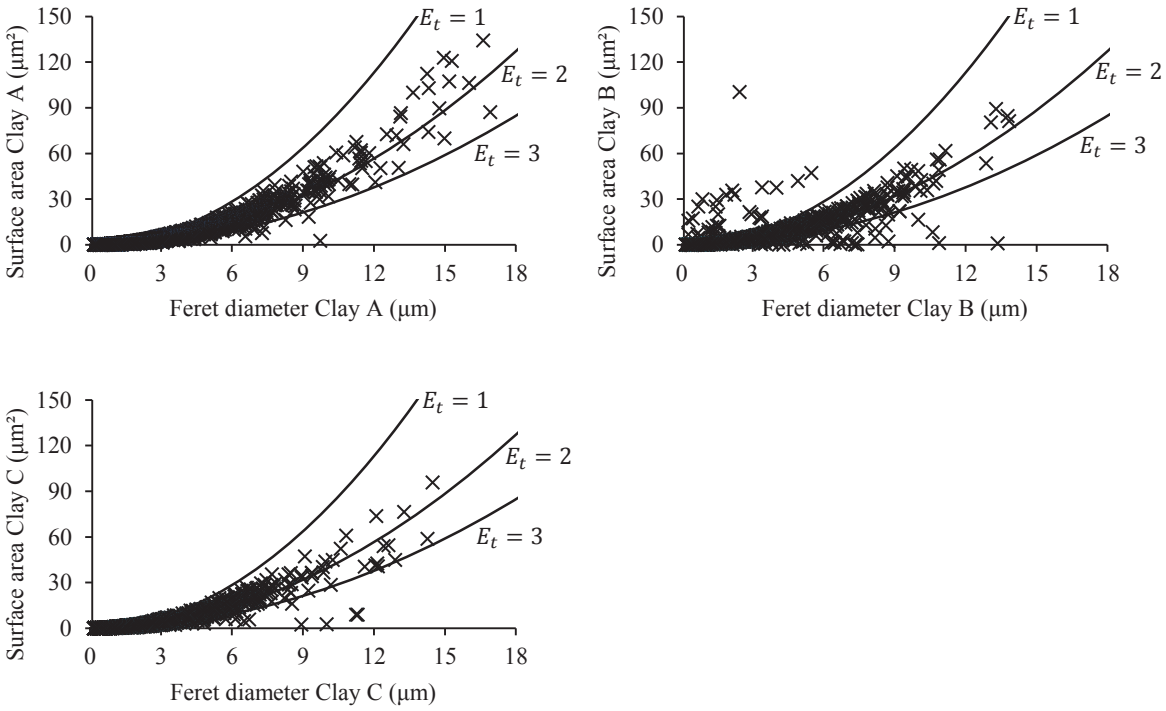

Figure 3.4 Relation between Feret diameter and surface area observed in Clay A, B, and C where $\boldsymbol{E_t}$ is the theoretical elongation calculated assuming elliptical shaped fillers

Measurements of elongation are presented in Figure 3.5. The average elongation was found to be very similar between fillers reaching values of 1.63, 1.55 and 1.68 for Clay A, Clay, and Clay C. The results indicate that the differences between the minor and major filler length is not large supporting the idea that fillers were circular-oval. These results also coincided with the previous estimation presented in Figure 3.4. The generalised extreme value distribution was found as the best to represent this parameter. This distribution is used to predict conditions in the future particularly when the extreme values are important such as the level of sea, wind speed, hydrology, structural design and others (Ayyub & McCuen, 2011; Hosking, Wallis, & Wood, 1985). The distribution combines the Gumbel, Frechet, and Weibull maximum extreme value distributions and it is defined by three parameters; the shape k, the scale σ, and the location μ parameters (Embrechts, Klüppelberg, & Mikosch, 1997). It is important to mention that there seems to be no precedence in the measurement of elongation for kaolin clay, so it is not possible to compare that parameter with other published data. Equations 3.4 and 3.5 showed that expression in terms of cumulative and density functions respectively.

$$F(x_E;\mu_E,\sigma_E,k_E) = exp\left\{-\left[1+k_E\cdot\left(\frac{x_E-\mu_E}{\sigma_E}\right)\right]^{-1/k_E}\right\},\quad 1+\frac{k_E\cdot(x_E-\mu_E)}{\sigma_E}>0 \tag{3.4}$$

$$f(x_E;\mu_E,\sigma_E,k_E) = \frac{1}{\sigma_E}\cdot\left[1+k_E\cdot\left(\frac{x_E-\mu_E}{\sigma_E}\right)\right]^{(-1/k_E)-1} exp\left\{-\left[1+k_E\cdot\left(\frac{x_E-\mu_E}{\sigma_E}\right)\right]^{-1/k_E}\right\} \tag{3.5}$$

where

x_E: Elongation of the filler

μ_E: Location parameter

σ_E: Scale parameter

k_E: Shape parameter

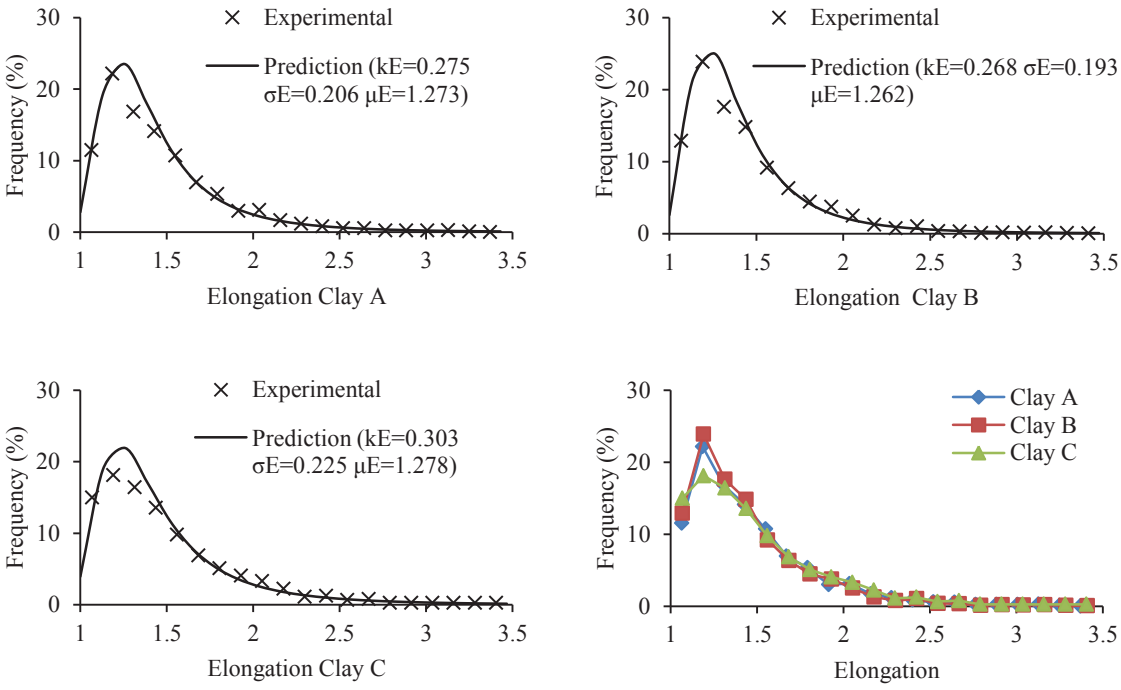

Figure 3.5 Elongation distributions estimated for the selected fillers where k_E is the shape parameter, $\boldsymbol{\sigma_E}$ is the scale parameter, and μ_E is the location parameter of the generalised extreme value distribution

The measured elongation showed no correlation with the maximum Feret diameter and surface area in any of the selected clays. In the case of the maximum Feret diameter, the correlation coefficients were 0.24, 0.23, and 0.14 for Clay A, B, and C respectively. The correlation was even lower in the case of surface area reaching values of 0.08, 0.08, and -0.01 for Clay A, B, and C respectively. Figure 3.6 shows the comparison between the elongation with the surface area and the maximum Feret diameter for the selected clays.

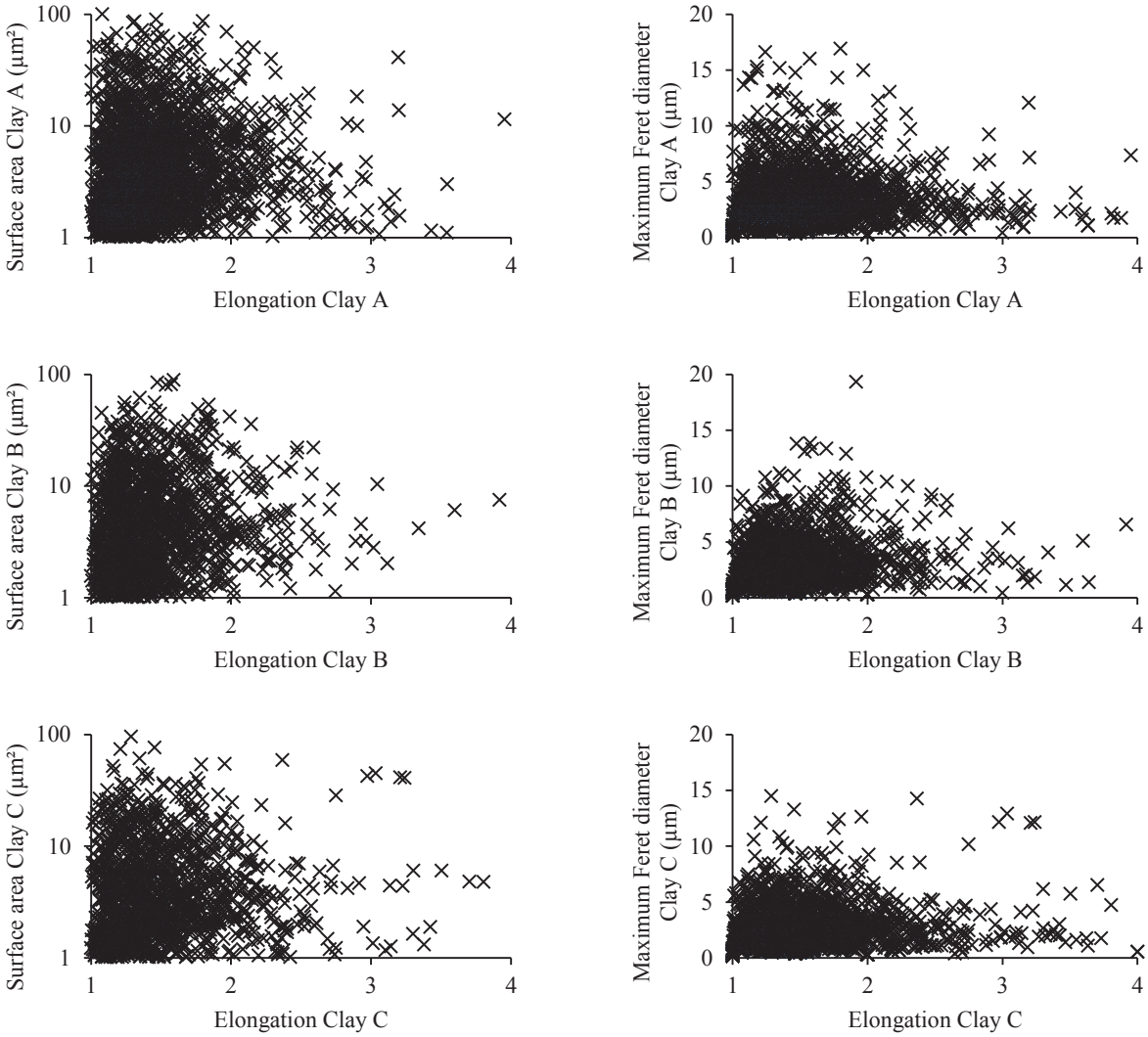

Figure 3.6 Comparison between surface area, maximum Feret diameter, and elongation for Clay A, B, and C

In order to characterise the filler shape, the circularity (ψ_{Ap}), roundness (C), and fractal dimension (D_f) were estimated. Those descriptors were selected because each of them covers an aspect of the filler shape. The circularity represents the ratio between the squared perimeter of the filler and the measured surface area (Hentschel & Page, 2003). If the circularity is equal to 1, it means that the filler shape is a circle. The roundness describes the degree that the particle shape is a circle. Unlike the circularity, the roundness is the ratio of the surface area of the fillers and the squared perimeter of an equivalent circle defined by the surface area of the particle (Z. Li et al., 2002). The fractal dimension quantifies the silhouette of particles in terms of how smooth or irregular the particle silhouettes are. The fractal dimension is in the range from 1, where the shape is completely smooth, to 2, where the shape is completely irregular (Masuda, et al., 2006).

The average circularity of Clay A, Clay B, and Clay C were equal to 0.68, 0.73, and 0.66 respectively. In the case of roundness, the values reached 0.69, 0.70, and 0.69 for Clay A, Clay B, and Clay C respectively. These results suggest that the shape of the filler is closer to being circles/ovals than rectangular. In terms of the silhouette, Clay A, Clay B, and Clay C were shown to have average fractal dimensions equal to 1.87, 1.88, and 1.86 respectively. This indicated that the fillers have a degree of irregularities on their edges. In general, these shape descriptors indicated that the shape of the fillers were very similar to each other. The above observation was also reinforced with the relative low elongation estimated (Figure 3.5). Correlations between area and shape descriptors were found (Figure 3.7). As the area increases, the circulatory decreases and the fractal dimension increases meaning that the silhouette of the fillers becomes more complex as the fillers size increases. No correlations were found between roundness and area for the selected fillers.

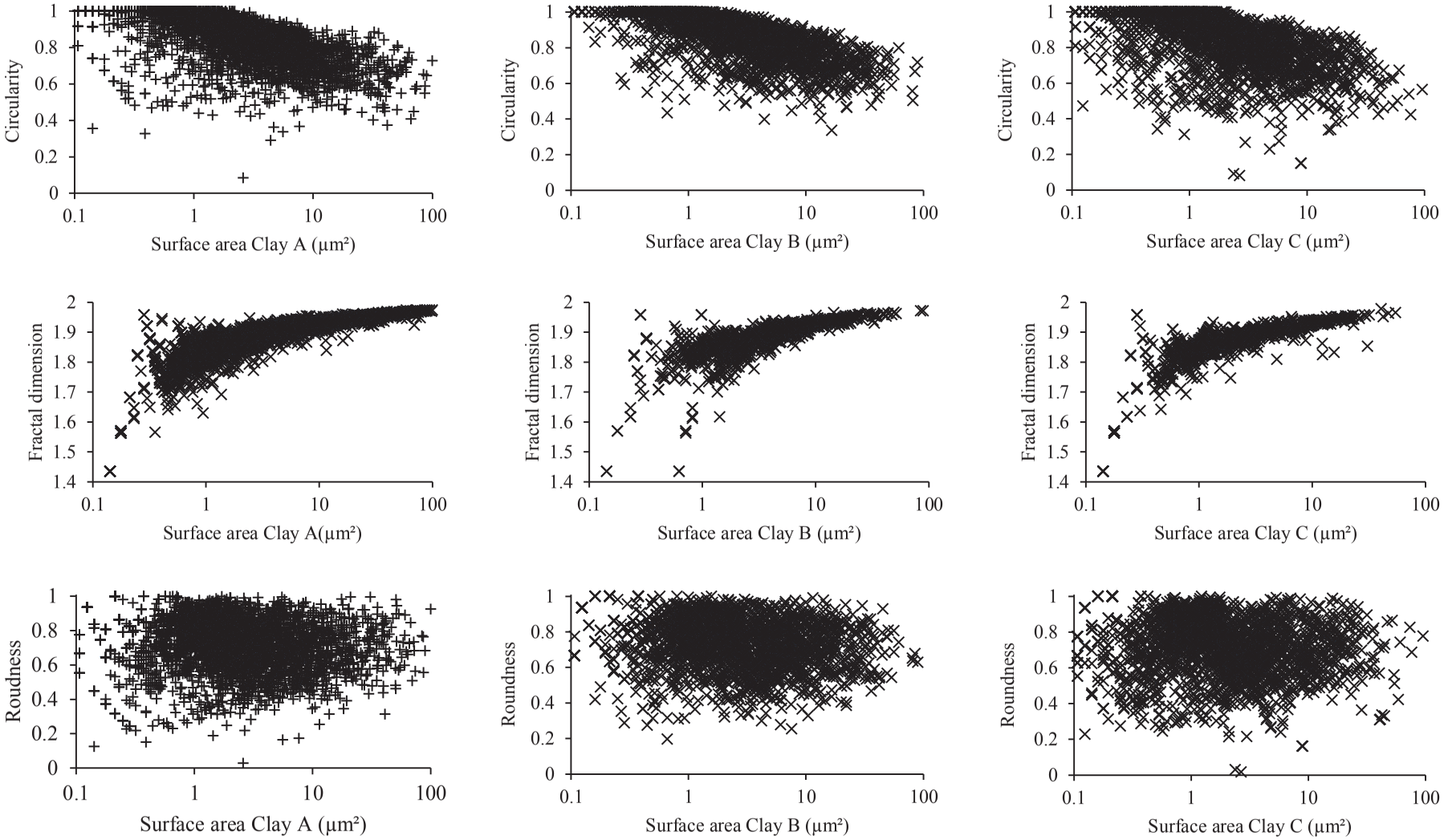

Figure 3.7 Correlation between circularity, fractal dimension, and roundness with respect to the area for filler samples of Clay A, B, and C

The Fourier descriptor method defines the shape of particles based on the radius formed from the centre of gravity to the edge of the filler $R(\theta)$ at different angle of rotation θ as shown in Figure 3.8 (Hawkins, 1990). Unlike the above descriptors, this method allows reconstruction of the filler shapes from quantitative information.

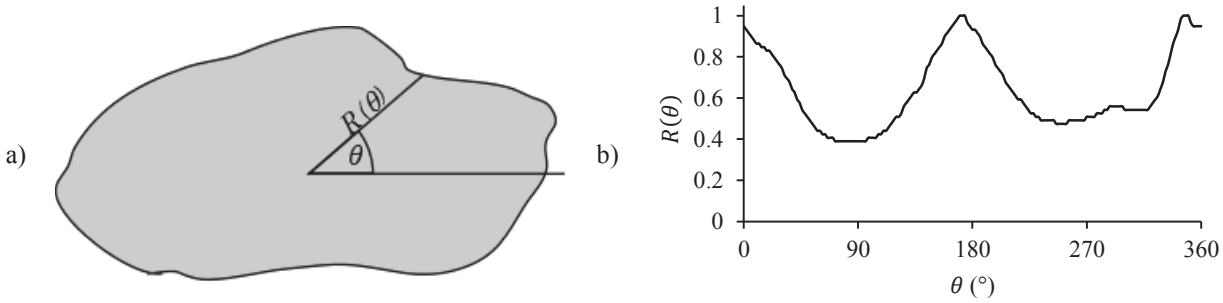

Figure 3.8 Representation of the Fourier descriptor a) radius at a particular angle of rotation on a filler b) plot of the radius as a function of the angle of rotation

The plot of $R(\theta)$ against the angle of rotation θ generates an oscillatory curve which can be represented by the Fourier series. Thus, a particular filler shape can be characterised by finding the parameters of the Fourier series. As presented in Table 1.3, the basic form of the Fourier descriptor equation is expressed below (Ehrlich & Weinberg, 1970).

$$R(\theta) = a_0 + \sum_{n=1}^{N} [a_n \cos(n\theta) + b_n \sin(n\theta)] \tag{2.16}$$

where

$R(\theta)$: Radius from the centre of gravity to the edge of the pigment at an angle θ

N: Total number of harmonics

n: Harmonic number

a: Magnitude of each harmonic

b: Phase of each harmonic

The number of harmonics in the series represents the particular shape and the magnitude of each harmonic represents the silhouette of each filler shape (Hawkins, 1990). The harmonic magnitudes can be calculated by the following expressions (Ehrlich & Weinberg, 1970).

$$a_0 = \frac{1}{2\pi}\int_0^{2\pi} R(\theta)d\theta \tag{3.6}$$

$$a_n = \frac{1}{\pi}\int_0^{2\pi} R(\theta)\cdot cos(n\theta)d\theta \tag{3.7}$$

$$b_n = \frac{1}{\pi}\int_0^{2\pi} R(\theta)\cdot sin(n\theta)d\theta \tag{3.8}$$

To calculate the parameters for definition of the Fourier descriptor, the edges and the centre of gravity of the fillers were identified on the enhanced images. The distance between the centre of gravity and the edge were measured at every 15° providing 24 radii for each filler. This angle of rotation gives the lowest error in the representation of filler shape. The calculation of this is presented in Appendix C. Russ (2011) suggested that this level of shape discretisation gives enough information to fit the Fourier descriptor for most particles. Incomplete fillers, such as those located at the edges of the images, were omitted for calculation. Because each filler has different dimensions, the measured radii were converted into relative radius to enable comparison between all the fillers. The relative radius was defined as the ratio of the observed radius and the longest radius of the fillers. From this, the parameters of the Fourier series were estimated following Equations 3.6, 3.7, and 3.8 to define Equation 2.16. The program to estimate the Fourier descriptor is presented in Appendix A. Figure 3.9 below shows a diagram of the calculation process.

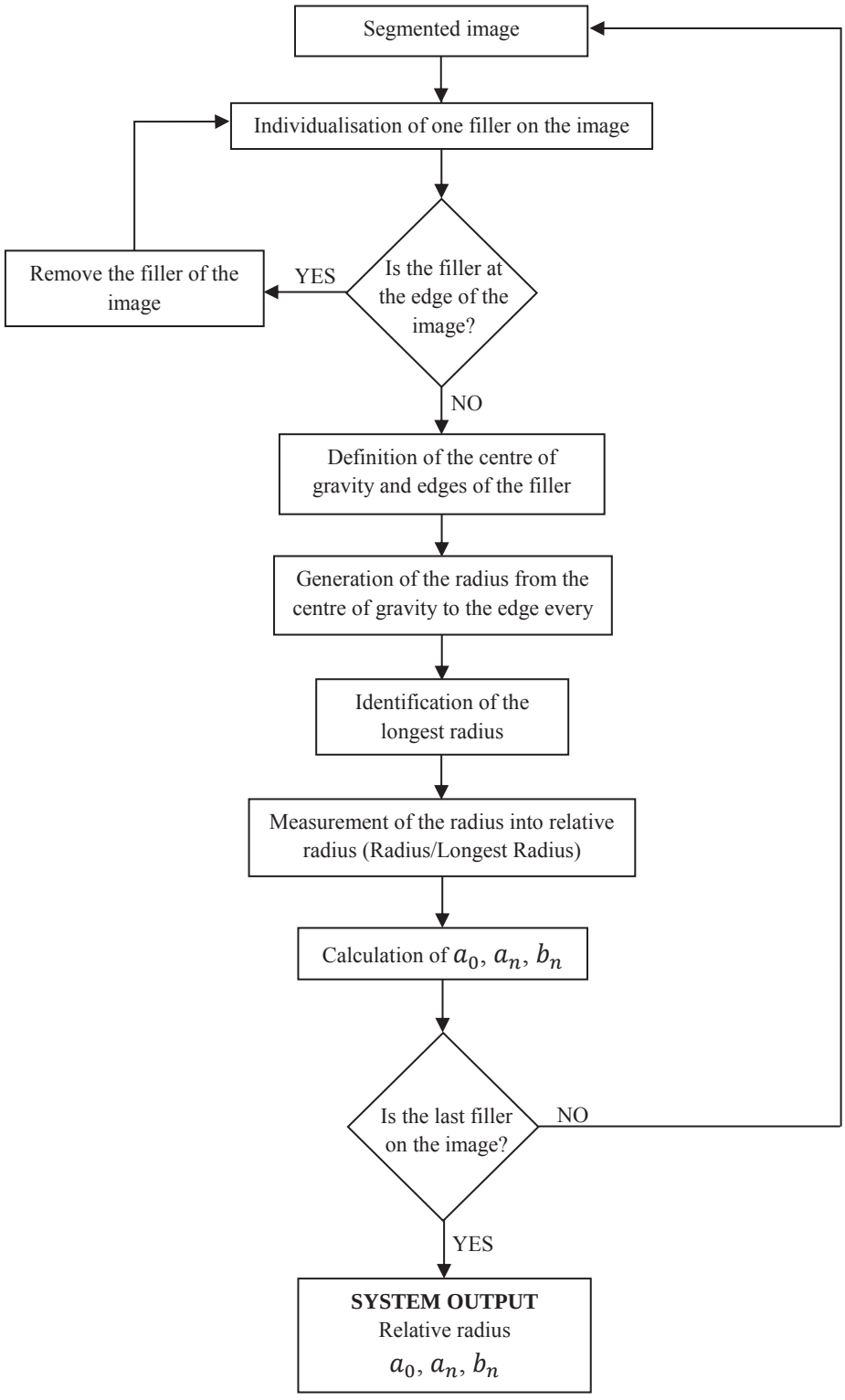

Figure 3.9 Scheme of the calculation of Fourier series for description of filler shape

Figure 3.10 is an example of the images taken for clay samples with the radii generated to calculate the Fourier descriptors.

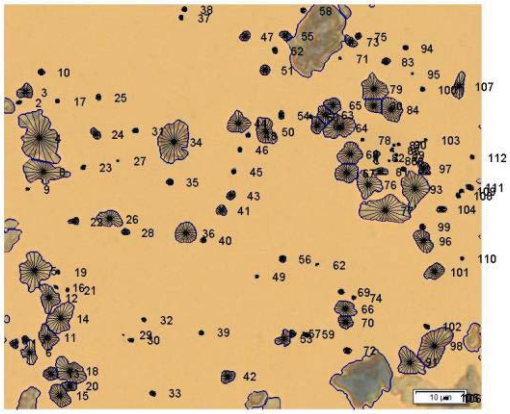

Figure 3.10 Radius of filler for calculation of Fourier descriptor for a sample of Clay A

Figure 3.11 shows that the largest relative lengths were located at 0° (360°) and 180° and the smallest at about 90° and 270° for all the selected fillers. As expected, this means that the fillers were elongated. The minimum relative lengths were 0.675, 0.680, and 0.655 of the largest length for Clay A, Clay, and Clay C respectively. This represents an estimated average elongation of about 1.5 for each type of clay. This result coincides with those presented in previous sections. Figure 3.11 also shows that the variation of the average increases as the angle of rotation is closer to 90° and 270°. This observation suggests that the shape of the fillers is more intricate than the average representation.

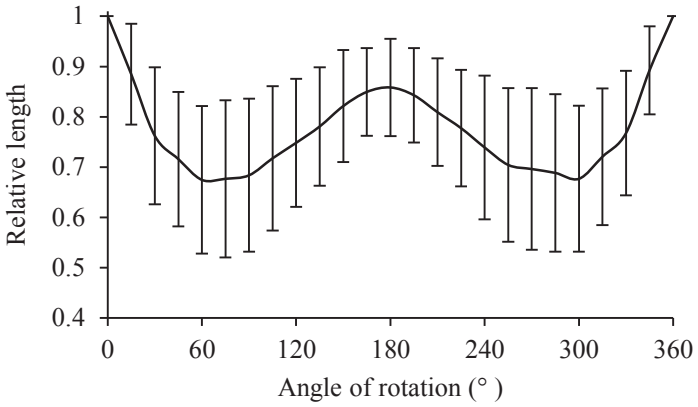

Figure 3.11 Characterisation of the filler shape by Fourier descriptor for Clay A (the error bars represent standard deviation).

To characterise all the irregularities of the silhouette of the fillers, the Fourier series parameters had to be defined. The parameter a_0 was estimated as 0.782 ± 0.08, 0.786 ± 0.08, and 0.770 ± 0.09 for Clay A, B, and C, respectively. The a_0 represents approximately the average of the relative length of fillers (Ehrlich & Weinberg, 1970). These results coincided with those shown

in Figure 3.11, where the average length of the fillers was about 0.8. In the case of a_n and b_n, the values depend on the number of harmonics that it is used for modelling. As the number of harmonics increases, the representation of the filler silhouette is closer to the real filler shape. This can be observed by comparing the radii lengths generated by the Fourier descriptor and the observed radii at different values of harmonics and angle of rotation (Figure 3.12).

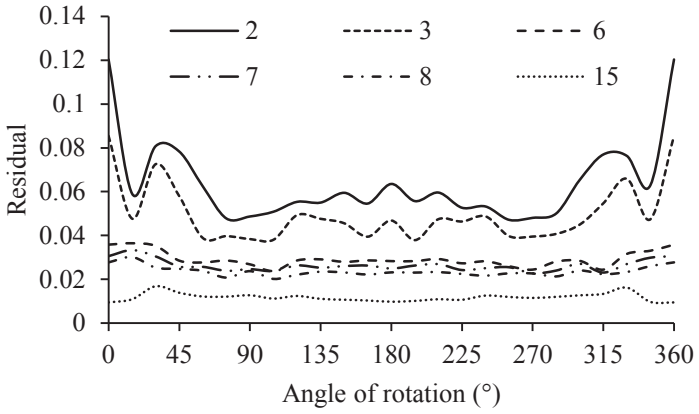

Figure 3.12 Residual plot (difference between predicted and observed filler radius) at different angle of rotation for different number of harmonics in an image of Clay A

The largest differences were observed at 0° and 360°. From 90° to 270°, a decrease was observed until a relatively constant residual was reached. For the definition of fillers based on 2 harmonics, the magnitude of the residual reached 12%. The differences decreased down to 4% by increasing the number of harmonics up to 6. Under these conditions, the differences were relatively constant at any angle of rotation. In terms of representation of shape, the ideal is to define the shape using the minimum number of parameters with no loss of accuracy. Thus, in this investigation the number of harmonics was assumed as 7 due to the low error in the representation of filler shape.

Figure 3.13 and Figure 3.14 show the average values of a_n and b_n, for each selected filler

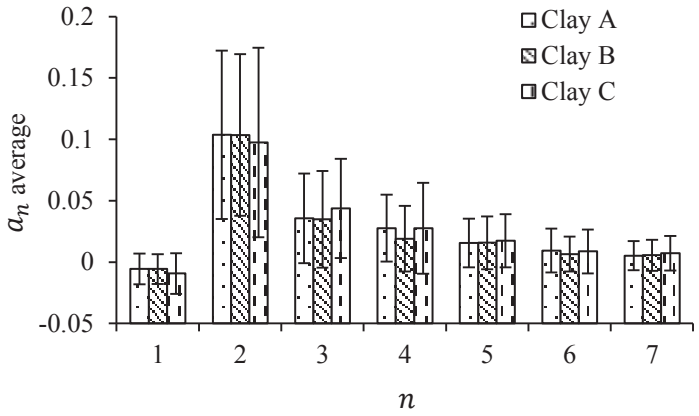

Figure 3.13 Average value of a_n for the selected fillers at different values of harmonics (n) (the error bars represent standard deviation)

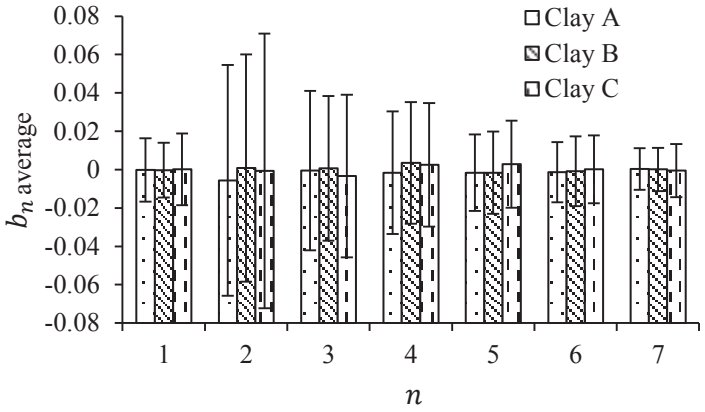

Figure 3.14 Average value of b_n for the selected fillers at different values of harmonics (n) (the error bars represent standard deviation)

In all the cases the value of a_2 was observed as the highest reaching values of about 0.1 for all the selected fillers. The values of b_n remained relatively constant at 0 for all the harmonics; however, larger variability was observed for b_2 compared to other values of b_n. This could be explained due to the first harmonics (1 to 3) describe most of the shape of the fillers and the others (4 to 7) define particular areas of the silhouette (Hawkins, 1990; Russ, 2011). It is important to note that the harmonics are equivalent to the periods on the sinusoidal curve in a complete rotation. Each period represents an interval of the curve where the changes in radius length occur and are not repeated. As shown in Figure 3.11, there are mainly two intervals of changes of radius length; one from the largest radius to the smallest radius and then the largest radius from 0° to 180° and the same sequence from 180° to 360°. This means that the required number of periods to represent these fluctuations has to be at least two. This can be seen in Figure 3.15 where only two harmonics (n) represented most of the characteristic shape of two given fillers.

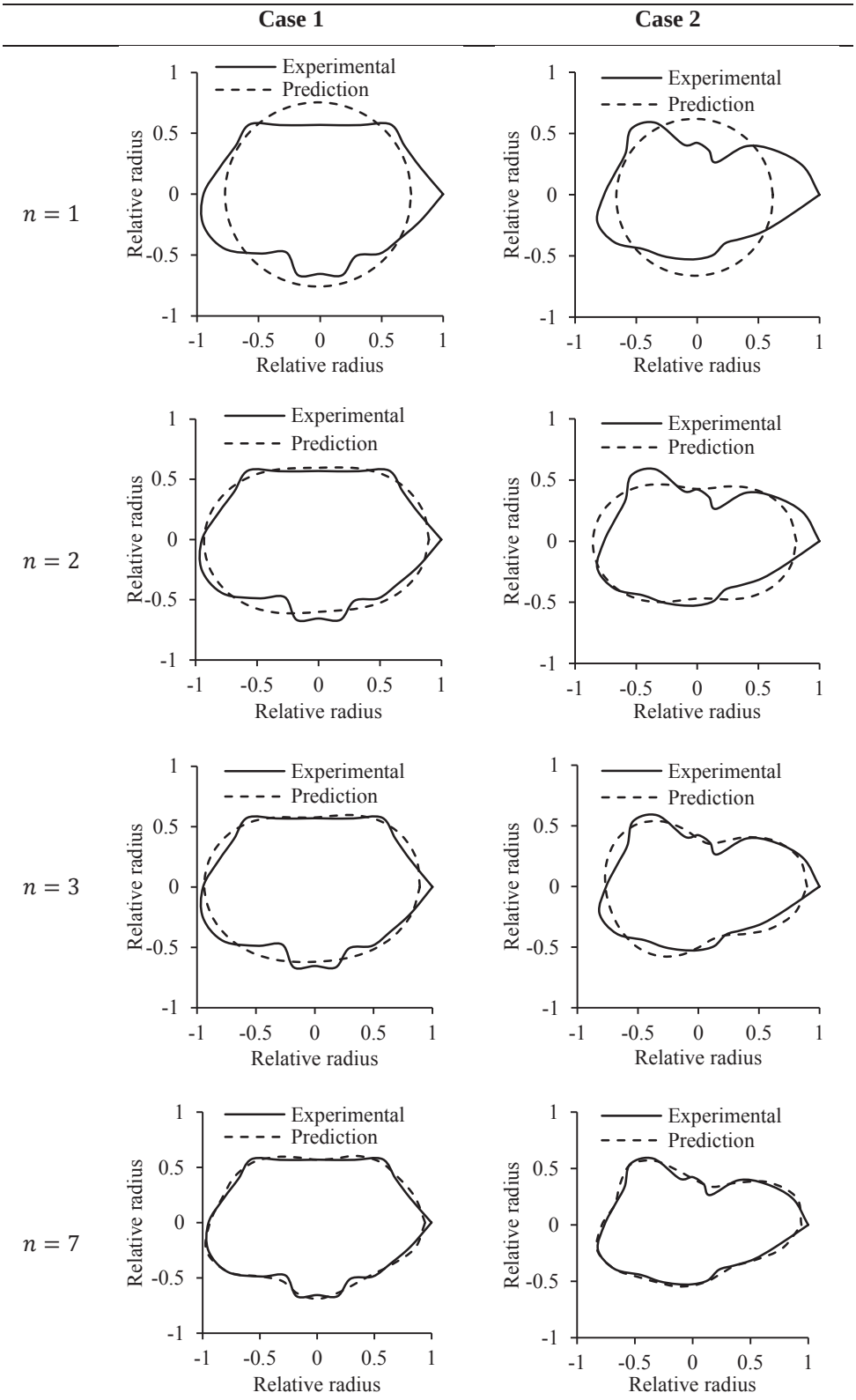

Figure 3.15 Two cases of generation of filler shape by Fourier shapes descriptor at different number of harmonics (***n***) and comparison with observed shapes

Table 3.4 and Table 3.5 show distribution parameters of a_n and b_n. The Weibull distribution was found appropriate to characterise a_0 and a_1. From a_2 to a_7 the log-normal distribution was

suitable to describe the filler shape. In the case of b_n, almost all of these parameters fitted to the logistic distribution. Only b_2 fitted with the normal distribution. It is important to mention that a_n can fluctuate reaching negative values. This limits the suitable number of distributions able to describe these parameters. However, by including a location parameter γ that makes the data positive, it is possible to use the Weibull, or Log-logistic distributions. If γ is equal to 0, the distributions represent their basic forms. The cumulative distributions and the probability density functions fitted with the Fourier descriptor parameters are presented below for the; the Weibull (Equations 3.9 and 3.10), the Normal (Equations 3.11 and 3.12), and the Logistic distributions (Equations 3.13 and 3.14). The Log-normal distribution was presented previously (Equation 3.2 and 3.3)

$$F(x) = 1 - exp\left(-\left(\frac{x-\gamma}{\beta}\right)^{\alpha}\right) \tag{3.9}$$

$$f(x) = \frac{\alpha}{\beta} \cdot \left(\frac{x-\gamma}{\beta}\right)^{\alpha-1} exp\left(-\left(\frac{x-\gamma}{\beta}\right)^{\alpha}\right) \tag{3.10}$$

$$F(x) = \frac{1}{2}\left[1 + erf\left(\frac{x}{\sqrt{2}}\right)\right], \quad erf(x) = \frac{1}{\sqrt{\pi}}\int_{-\infty}^{\infty} exp(-t^2)dt \tag{3.11}$$

$$f(x) = (2\pi \cdot \sigma^2)^{-1/2} \cdot exp\left[-\frac{(x-\mu)^2}{2\sigma^2}\right] \tag{3.12}$$

$$F(x) = \left[1 + exp\left(-\frac{x-\mu_{logistic}}{\sigma_{logistic}}\right)\right]^{-1} \tag{3.13}$$

$$f(x) = exp\left(-\frac{x-\mu_{logistic}}{s}\right) \cdot \left[\sigma \cdot \left(1 + exp\left(-\frac{x-\mu_{logistic}}{\sigma_{logistic}}\right)\right)\right]^{-1} \tag{3.14}$$

where

$F(x)$: Cumulative distribution of the distributions

$f(x)$: Probability density function of the distributions

x: Parameter of the Fourier series descriptor

γ: Location parameter of the Weibull and the Log-normal distributions

β: Shape parameter of the Weibull distribution

α: Scale parameter of the Weibull distribution

μ: Mean of the Normal distribution

σ: Standard deviation of the Normal distribution

$\mu_{logistic}$: Location parameter of the Logistic distributions

$\sigma_{logistic}$: Scale parameter of the Logistic distributions

An example of the distributions can be seen in Figure 3.16.

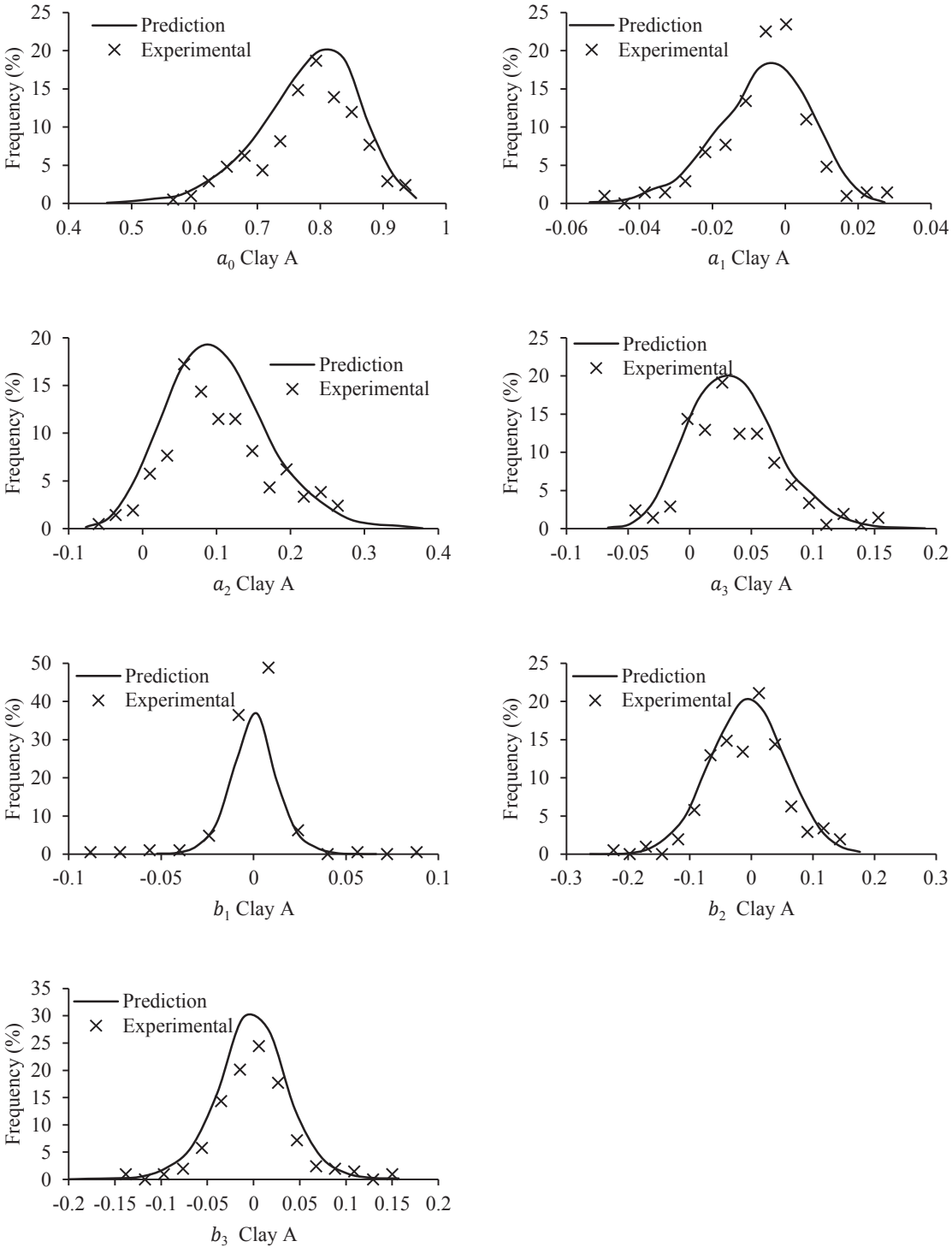

Figure 3.16 Distribution of Fourier shape descriptor of Clay A

Table 3.4 Parameters of distributions for a_n where α is the scale parameter and β is the shape parameter of the Weibull distribution. μ and σ are the mean and standard deviation of the natural logarithm to define the Log-normal distribution. γ is the location parameter for both distributions

Parameter	Distribution	Clay A	Clay B	Clay C
a_0	Weibull	$\alpha = 0.815$	$\alpha = 0.823$	$\alpha = 0.809$
		$\beta = 12.146$	$\beta = 11.392$	$\beta = 10.156$
a_1	Weibull	$\alpha = 0.075$	$\alpha = 0.081$	$\alpha = 0.091$
		$\beta = 6.257$	$\beta = 7.278$	$\beta = 8.510$
		γ = -0.075	γ = -0.082	γ = -0.093
a_2	Log-normal	μ = -0.845	μ = -0.570	μ =-0.938
		$\sigma = 0.157$	$\sigma = 0.115$	$\sigma = 0.193$
		γ =-0.331	γ =-0.466	γ =-0.301
a_3	Log-normal	μ = -1.456	μ = -1.121	μ =-2.053
		$\sigma = 0.153$	$\sigma = 0.117$	$\sigma = 0.297$
		γ =-0.200	γ =-0.294	γ =-0.090
a_4	Log-normal	μ = -1.377	μ = -0.356	μ =-1.530
		$\sigma = 0.108$	$\sigma = 0.038$	$\sigma = 0.166$
		γ =-0.226	γ =-0.682	γ =-0.192
a_5	Log-normal	μ = -1.106	μ = -1.725	μ =-2.136
		$\sigma = 0.059$	$\sigma =$ 0.117	$\sigma = 0.180$
		γ =-0.316	γ =-0.164	γ =-0.103
a_6	Log-normal	μ = -2.798	μ = -2.210	μ =-1.605
		$\sigma = 0.260$	$\sigma = 0.130$	$\sigma = 0.087$
		γ =-0.054	γ =-0.104	γ =-0.193
a_7	Log-normal	μ = -1.224	= -1.098	μ =-1.843
		$\sigma = 0.040$	$\sigma = 0.380$	$\sigma = 0.088$
		γ =-0.289	γ =-0.328	γ =-0.152

Table 3.5 Parameters of distributions for b_n where $\mu_{logistic}$ is the location parameter and $\sigma_{logistic}$ is the scale parameter of the Logistic distributions and μ is the mean and σ of the Normal distribution

Parameter	Distribution	Clay A	Clay B	Clay C
b_1	Logistic	$\mu_{logistic}$ =3.372×10^{-04}	$\mu_{logistic}$ =-2.557×10^{-04}	$\mu_{logistic}$ =-7.638×10^{-05}
		$\sigma_{logistic}$ = 7.163×10^{-03}	$\sigma_{logistic}$ = 4.990×10^{-03}	$\sigma_{logistic}$ = 8.382×10^{-03}
b_2	Normal	μ =-5.607×10^{-03}	μ =1.046×10^{-04}	μ =-6.976×10^{-04}
		σ =6.017×10^{-02}	σ =5.985×10^{-02}	σ =7.157×10^{-02}
b_3	Logistic	$\mu_{logistic}$ =-1.025×10^{-03}	$\mu_{logistic}$ =3.292×10^{-04}	$\mu_{logistic}$ =-2.282×10^{-03}
		$\sigma_{logistic}$ =2.188×10^{-02}	$\sigma_{logistic}$ =1.926×10^{-02}	$\sigma_{logistic}$ =2.146×10^{-02}
b_4	Logistic	$\mu_{logistic}$ =-3.811×10^{-05}	$\mu_{logistic}$ =2.078×10^{-03}	$\mu_{logistic}$ =1.803×10^{-03}
		$\sigma_{logistic}$ =1.526×10^{-02}	$\sigma_{logistic}$ =1.533×10^{-02}	$\sigma_{logistic}$ =1.560×10^{-02}
b_5	Logistic	$\mu_{logistic}$ =-1.132×10^{-03}	$\mu_{logistic}$ =-9.735×10^{-04}	$\mu_{logistic}$ =2.048×10^{-03}
		$\sigma_{logistic}$ =1.087×10^{-02}	$\sigma_{logistic}$ =1.098×10^{-02}	$\sigma_{logistic}$ =1.175×10^{-02}
b_6	Logistic	$\mu_{logistic}$ =-1.294×10^{-03}	$\mu_{logistic}$ =-3.293×10^{-04}	$\mu_{logistic}$ =-2.560×10^{-04}
		$\sigma_{logistic}$ =7.905×10^{-03}	$\sigma_{logistic}$ =9.609×10^{-03}	$\sigma_{logistic}$ =9.240×10^{-03}
b_7	Logistic	$\mu_{logistic}$ =1.119×10^{-04}	$\mu_{logistic}$ =-3.543×10^{-04}	$\mu_{logistic}$ =-8.955×10^{-04}
		$\sigma_{logistic}$ =6.189×10^{-03}	$\sigma_{logistic}$ =6.215×10^{-03}	$\sigma_{logistic}$ =7.294×10^{-03}

It is interesting that the average values of both a_n and b_n were similar between clays if the comparison is done at the same harmonic level (Figure 3.13 Figure 3.14).This may suggest that the clays were similar. However, the small variations in the parameters of the distribution curves may have relevance when a population of fillers is required as is carried out for modelling of coating geometries. Thus, it is not suitable to simplify the clay geometry as one general shape for all the filler types and it is needed to define the Fourier descriptor parameters for each selected clays.

To prove that the generated filler shapes are in concordance with those observed experimentally, a comparison based on surface area and elongation of fillers was carried out. For this, values of a_0, a_n and b_n were randomly selected according to their distributions. Then, by Equation 2.16 the shapes where defined. 10,000 iterations per clay were used to define the curves and the results were presented in Figure 3.17. No clear results were achieved by using the distributions of the Fourier shape descriptor parameters. In the case of Clay A, the elongation was underestimated; however, for the other clays the predictions were to some degree better. In terms of surface area, the predictions tended to be overestimated compared to the experimental data.

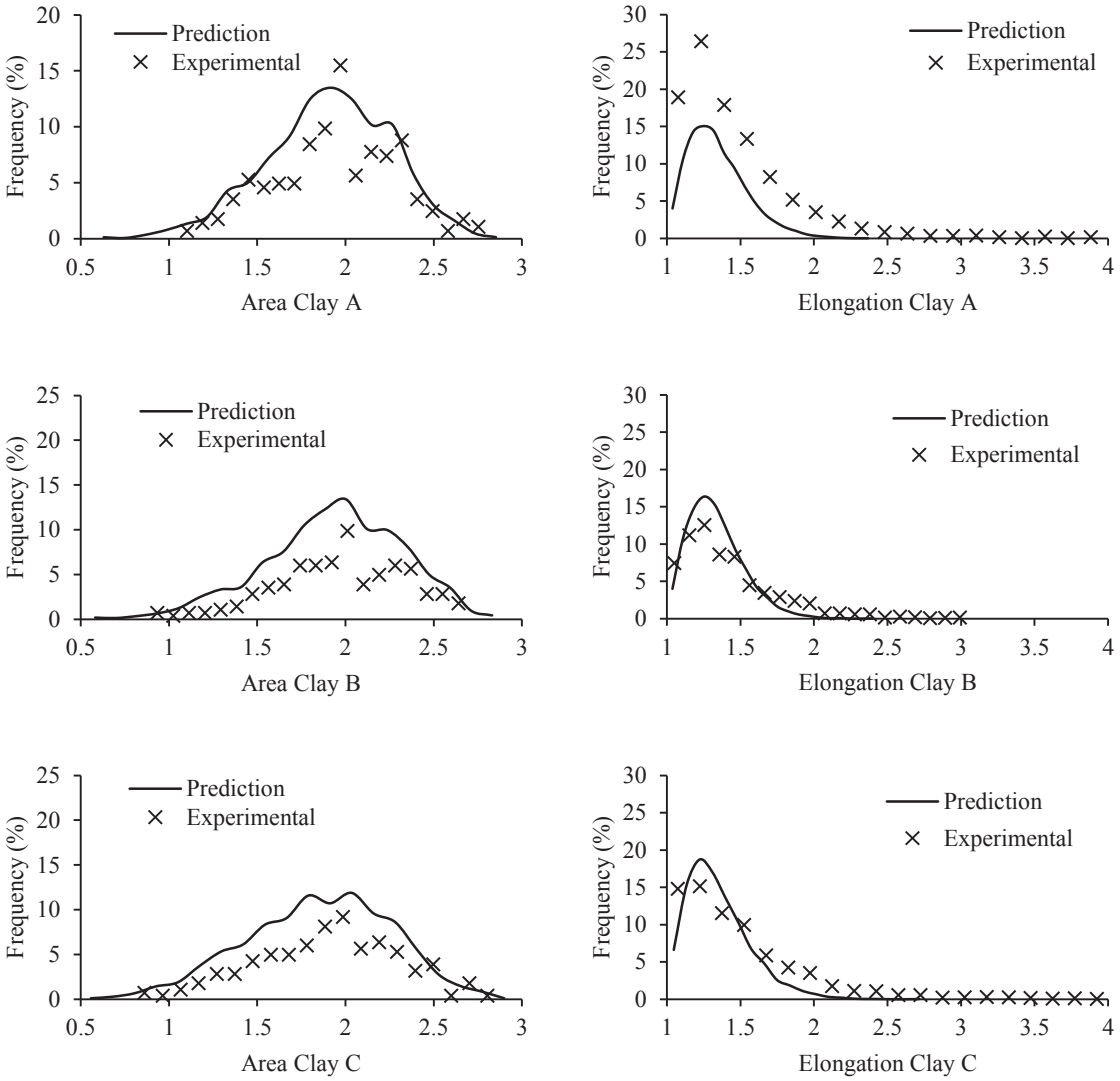

Figure 3.17 Comparison between prediction and experimental data of surface area and elongation for the selected clays

A reason for this discrepancy may be related to correlations between Fourier shape descriptor parameters. Negative and positives correlations between a_1, a_n and b_n parameters at 1, 2, or 3 harmonics were observed (Table 3.6). This may suggest that it is not recommended to predict the shape of fillers by random definition of a_n and b_n to estimate the Fourier series. Instead, a potential solution is to propose a list of representative values a_n and b_n that can be used to define a number of shapes. A list of Fourier descriptor parameters is given in Appendix B.

Table 3.6 Example of correlation table of Fourier series for Clay A

	a_0	a_1	a_2	a_3	a_4	b_1	b_2	b_3	b_4
a_0	1.000	**0.415**	**-0.766**	-0.250	-0.254	-0.093	0.088	0.091	-0.033
a_1		1.000	-0.219	**-0.465**	-0.046	0.064	0.170	0.099	-0.075
a_2			1.000	0.046	-0.034	0.057	-0.091	-0.041	0.133
a_3				1.000	-0.199	-0.027	0.076	0.067	0.025
a_4					1.000	0.113	0.013	-0.039	-0.201
b_1						1.000	**0.393**	**-0.539**	-0.098
b_2							1.000	-0.050	0.007
b_3								1.000	0.019
b_4									1.000

Table 3.7 Example of correlation table of Fourier series for Clay B

	a_0	a_1	a_2	a_3	a_4	b_1	b_2	b_3	b_4
a_0	1.000	**0.475**	**-0.748**	-0.254	-0.209	0.136	0.173	-0.020	0.045
a_1		1.000	-0.329	**-0.492**	-0.183	0.203	0.215	-0.084	-0.001
a_2			1.000	-0.037	-0.033	-0.097	-0.109	0.093	-0.079
a_3				1.000	-0.073	-0.130	-0.023	0.161	-0.017
a_4					1.000	0.007	-0.091	-0.003	0.145
b_1						1.000	**0.359**	**-0.488**	-0.005
b_2							1.000	-0.055	0.088
b_3								1.000	-0.081
b_4									1.000

Table 3.8 Example of correlation table of Fourier series for Clay C

	a_0	a_1	a_2	a_3	a_4	b_1	b_2	b_3	b_4
a_0	1.000	**0.652**	**-0.635**	-0.453	-0.195	-0.092	-0.075	0.062	-0.041
a_1		1.000	-0.353	**-0.583**	-0.176	-0.111	0.019	0.078	-0.015
a_2			1.000	0.091	-0.261	0.050	-0.026	0.042	0.000
a_3				1.000	-0.005	0.056	0.056	-0.028	0.048
a_4					1.000	-0.078	-0.042	-0.083	-0.019
b_1						1.000	**0.455**	**-0.437**	0.009
b_2							1.000	-0.058	0.086
b_3								1.000	0.095
b_4									1.000

3.4. Measurement of filler thickness

The measurement of filler thickness was carried out by the processing and analysis of scanning electron microscopy (SEM) images. The SEM generates the images by probing the specimen

with a focused high-energy beam of electrons that is scanned across the specimen in a raster scan pattern (Schatten, 2013). In particle analysis, the SEM has been widely used due to its capability to focus particles down to 5 to 7 nm (Allen, 1997). The observations were carried out using a FEI Quanta 200 environmental scanning electron microscope available at the Manawatu Microscopy and Imaging Centre, New Zealand. To be able to measure the filler thickness by SEM, it was required to prepare samples of fillers. From this point, the samples of fillers for SEM will be called filler specimens which is the common name in this field. The specimens were prepared based on a dilution of fillers in ethanol (1% vol/vol). This suspension was mixed for 30 min in a 50 mL beaker with a magnetic mixer at 700 rpm. Drops of the suspension were taken and placed on coverslips. The coverslips were dried at room temperature and then broken into small pieces for preparation of SEM specimens. The specimens were sputter coated with carbon and images were taken using a secondary electron detector at 20 kV and magnification from 20,000 X to 50,000 X. Because of the flat surface of the coverslip, the fillers settled down parallel to it during drying (Figure 3.18). The beam of the detector was horizontally situated to point to the thinner side of the fillers. In the case of the filler thickness, the measurements were directly measured from the captured scanning electron microscopy images on 30 fillers per type of clay at 10 points on each of the observed filler.

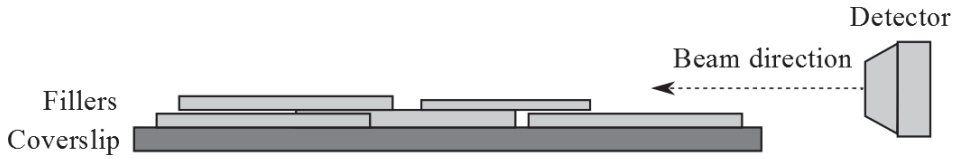

Figure 3.18 Scheme of specimen for measurement of filler thickness by SEM

Figure 3.19 below shows a sample image obtained by SEM of one of the selected Clay A filler specimens.

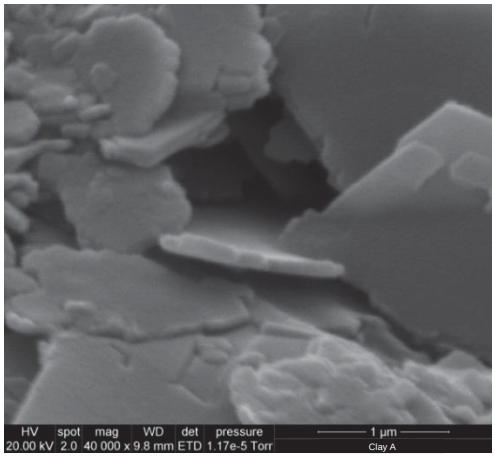

Figure 3.19 Image captured by SEM for calculation of filler thickness of Clay A

The range of filler thickness was observed from 0.068 μm to 0.228 μm. The thickest filler was observed for Clay B reaching an average thickness of 0.141 μm followed by Clay A at 0.130 μm and Clay C with 0.111 μm respectively. Overall, the measurements indicated that the thickness of the fillers is about one order of magnitude smaller than the Feret diameter for all the selected fillers. Gelinas, & Vidal (2010) measured the thicknesses of ten different clays by atomic force microscopy from Brazil and Georgia, US, finding a variation from 0.030 μm to 0.120 μm with a maximum of about 0.200 μm for all the samples. In the same way, Bundy & Ishley (1991) presented measurement of average thicknesses from 0.050 μm to 0.390 μm for six different Georgia kaolin clays used for filling and coating of papers. The Log-normal distribution was adequate to describe the thicknesses of the fillers analysed in this work. The Log-normal distribution was presented previously (Equation 3.2 and 3.3).

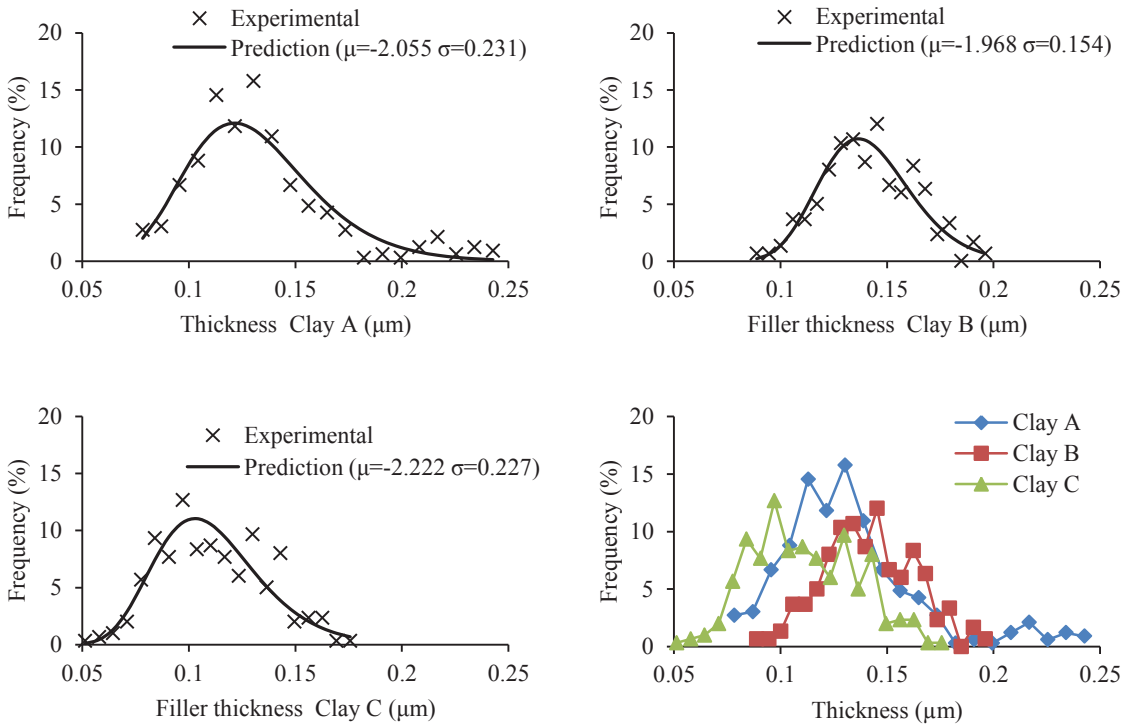

Figure 3.20 Distribution of thickness of selected fillers where μ and σ are the mean and standard deviation of the natural logarithm of the thickness to define the lognormal distribution

The variation of the thickness of each filler is presented in Figure 3.21. This corresponds to the standard deviation of the 10 thicknesses measured in each filler. The results show that the thickness in each filler varies about 0.013 μm in average for all the selected clays with a minimum of 0.005 μm and a maximum of 0.023 μm. Because the standard deviation within each particle is an order of magnitude lower than the thickness of the particles, it is appropriate to assume that each particle has uniform thickness.

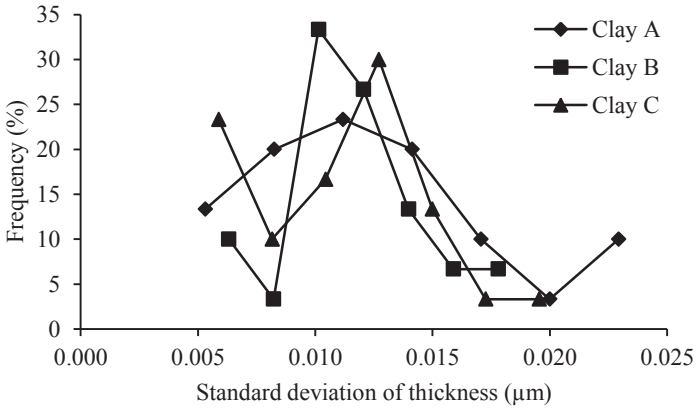

Figure 3.21 Standard deviation of thickness in each filler for the three type of selected clay

Because the measurement of Feret diameter and thickness of fillers were carried out in two different experiments, the distribution of aspect ratio can only be estimated by using a mathematical approach. Monte Carlo simulation was used to predict the aspect ratio of the fillers based on the length and thickness distributions of selected fillers. The estimation of the aspect ratio for the selected fillers was based on the Feret diameter and thickness distribution for selected fillers. 20,000 fillers were defined for each filler type using the Feret diameter and thickness distribution saving the information as datasets. From these datasets and using Monte Carlo simulation, 2,000 fillers were randomly selected and defined to calculate the aspect ratio distribution for the fillers as the ratio between the length and the thickness. The estimation of aspect ratio is presented in Figure 3.22. The mean aspect ratio predicted was 21.0, 19.2, and 23.0 for Clay A, Clay B, and Clay C respectively with dispersion of the estimation from 1 to 100 for all the type of fillers. Publication of physical properties of Brazilian kaolin indicates that the aspect ratio of this type of clay is the range between 10 and 25 (Lehtinen, 2000d). Aspect ratios between 6 and 20 are mostly found in the case of kaolin from Georgian deposits (Drage & Tamms, 2000). The predicted aspect ratio was shown to follow the log normal distribution.

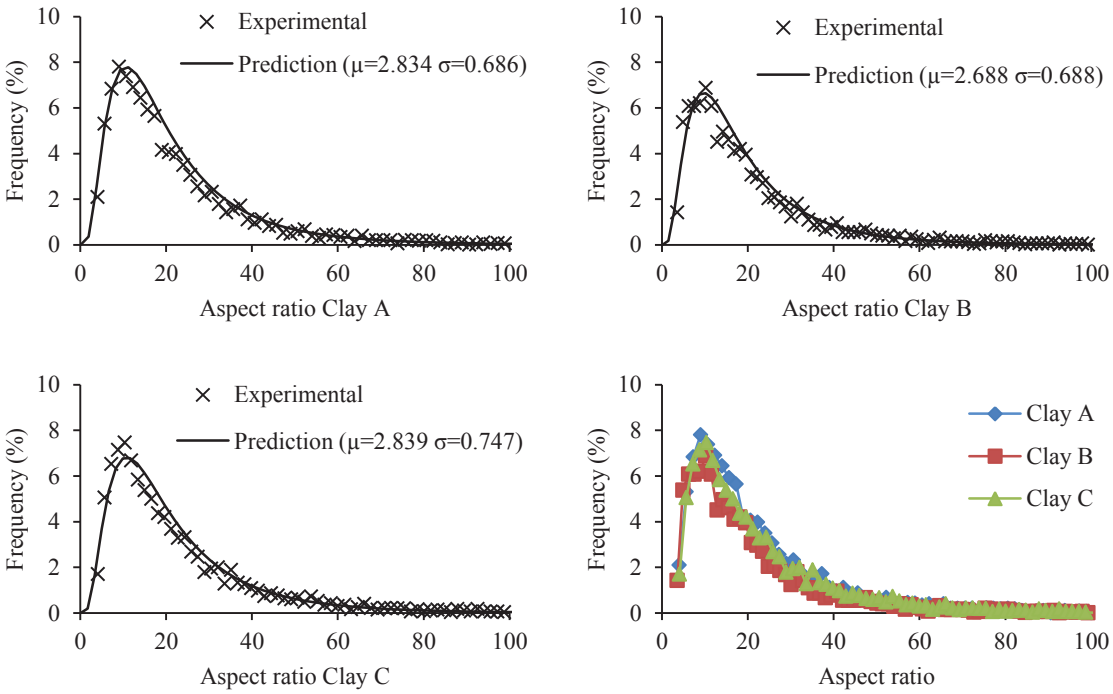

Figure 3.22 Estimation of aspect ratio for the selected clays based on Monte Carlo simulation where μ and $\sigma$are the mean and standard deviation of the natural logarithm of the aspect ratio to define the lognormal distribution

Due to the Monte Carlo simulation, it is implicitly assumed that the length and thickness of the fillers have no correlation to each other. The processing and origin of the clays seems to suggest that the length and thickness of clays are independently defined. The extraction of the clay from the rock is carried out by breaking the granite matrix into small pieces. This process makes particles about 53 μm in size and then, according to the final use of the clay, the particles are refined becoming smaller (Drage & Tamms, 2000). Also, the kaolin as a mineral deposit is presented as a group of layers that makes its characteristic plated shape (Bergaya & Lagaly, 2013; Grim, 1968). Some results suggest that the thickness and Feret diameter of kaolin clay particles may be related (Gelinas & Vidal, 2010; Vaz, Herrmann, & Crestana, 2002); however, the analysis of those results cannot suggest that this correlation is valid for fillers with a length larger than 0.3 μm.

3.5. Comparison between predictions to estimate the best way to characterise filler shape

A number of possible simplified shapes could be selected in model geometry construction. The assumed shapes will; however, have an impact on the resulting surface area and potentiality the predicted barrier performance of a coating. To test this, an evaluation was carried out in two ways; by assuming regular shapes and by Fourier shape descriptor. Circles, squares, ellipses, and rectangles were assumed in the case of regular shapes. Based on the distributions previously

presented, the length and elongation of the fillers were defined based on Monte Carlo simulation by choosing random values of length and elongation. The surface area (A_{f_i}) of the filler was calculated by Equations 3.15, 3.16, 3.17, and 3.18 according to the assumed shape; square, rectangular, circular, and elliptical shape respectively.

$$A_{f_i} = {d_{F_{max}}}^2 \tag{3.15}$$

$$A_{f_i} = \frac{{d_{F_{max}}}^2}{E} \tag{3.16}$$

$$A_{f_i} = \frac{\pi}{4} \cdot {d_{F_{max}}}^2 \tag{3.17}$$

$$A_{f_i} = \frac{\pi}{4} \cdot \frac{{d_{F_{max}}}^2}{E} \tag{3.18}$$

For the Fourier descriptor, the estimated series parameters (a_0, a_n, and b_n) were used to define relative radii (ratio between the estimated radius and the largest radius) in intervals of 15°. The relative radii were then transformed into length from the distributions defined in Section 3.3. Figure 3.23 shows the distribution of surface area of individual fillers based on different regular shapes, Fourier shape descriptor, and the measured area for all the selected clays.

In general, the results showed that the majority of the predictions of surface area were around 1.5 μm^2. Surface areas larger than 10 μm^2 represented less than 5% of all the distributions. All the predictions of area showed similar trends to the areas experimentally measured. As expected the surface area estimated by the Fourier shape descriptor was the closest compared to the area experimentally measured. This is due to the better morphological description of the fillers that this method allows. The shapes that include the elongation as part of shape definition (rectangular and elliptical shapes) presented a better prediction than those which only required length (circular and square shapes). In comparison, closer estimation of the surface area was found by assuming elliptical rather than rectangular filler shapes. It is important to note that the rectangular shapes predicted 21.5% larger surface areas than the elliptical shapes defined by the same value of length and elongation. The square shapes showed the largest prediction of surface area. The differences between square and the other assumed shapes can be important if the elongation is relatively high. For example, assuming an elongation equal to 1.5 the surface area of squared filler is about 48% larger than an ellipse and 33% larger than a rectangle, where both shapes were defined as the same length as the square.

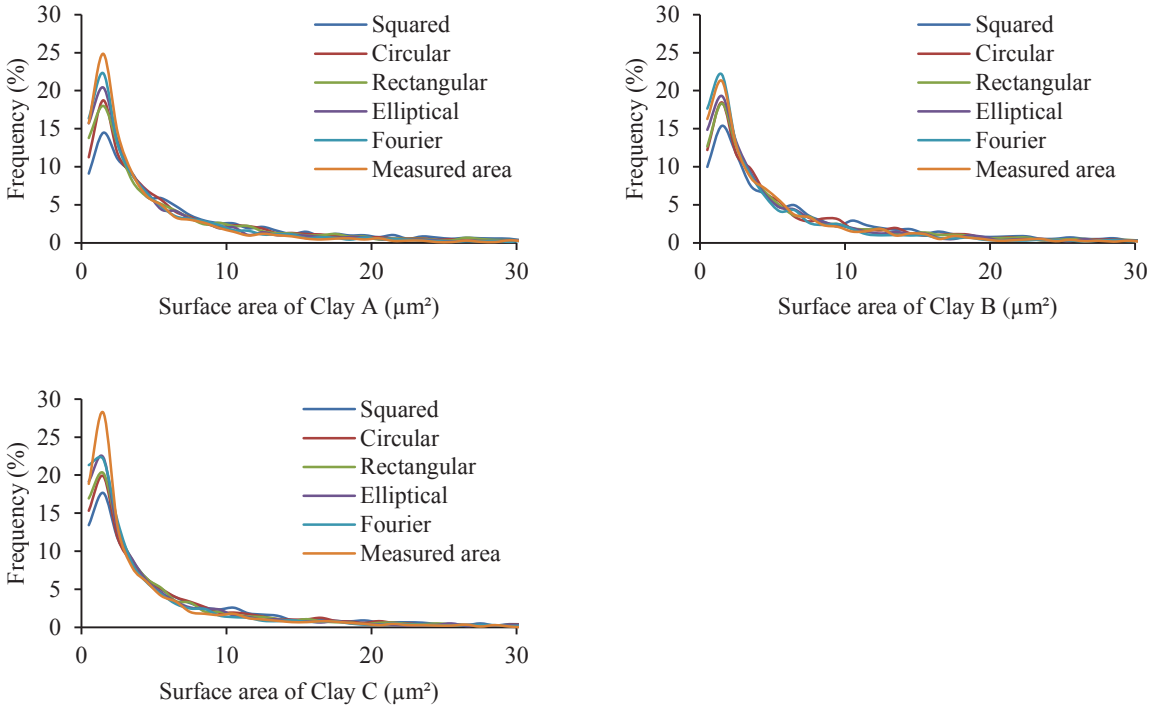

Figure 3.23 Distribution of predictions assuming several filler shapes and measured surface areas for the selected clays

The total number of fillers (N) in a given sample of clay can be related to its density (ρ_{filler}), mass (m_{total}) , surface area (A_{f_i}), and the thickness (b_{f_i}) as shown in Equation 3.19.

$$m_{total} = \rho_{filler} \cdot \sum_{i=1}^{N} A_{f_i} \cdot b_{f_i} \tag{3.19}$$

Equation 3.19 can be used to calculate the total surface area available in a given sample of clay. Table 3.9 shows above calculation based on the fillers shapes previously assumed and the Fourier shape descriptor and compared with the experimental data. This calculation was carried out assuming a filler mass equal to $1 \times 10^{-8}\ g$. In general, the results are in concordance with those presented in previous analysis. The fillers assumed to be circular or squared shapes reached a high difference between the numbers of fillers calculated and those observed experimentally. The prediction improved if this was calculated by the distributions of length, elongation, thickness. Lower differences were observed for elliptical and rectangular shaped fillers. Interestingly, in three cases the estimation based on average values are lower than those calculated by distribution of parameters. The elliptical filler shape was found to be closest to the experimental data. In this case, the differences assuming distribution of length, elongation, and thickness were between 9.1% and 9.5% according to the clay. The Fourier shape descriptor was shown to be very close to the real filler shapes, achieving almost no differences when the

distribution of length, elongation, and thickness are applied. This result is curious because the Fourier shape descriptor parameters did not adequately follow their defined distribution curves (Figure 3.17). The filler thickness variations may reduce the error produced by the distribution of the parameters. Despite this result, it is recommended to use the parameters calculated from the experiments rather than those estimated by distribution curves. These observations are important to the generation of filler populations for simulations of dispersion coating performance.

Table 3.9 Difference between total surface area of fillers calculated by assuming several shapes and the Fourier shape distribution based on average and distribution values of maximum Feret diameter, elongation, thickness, and Fourier shape descriptor parameters

	Parameter	Circle	Square	Ellipse	Rectangle	Fourier
Clay A	**Average**	41.5%	54.0%	4.6%	25.1%	4.0%
	Distribution	26.7%	36.7%	9.4%	22.5%	0.3%
Clay B	**Average**	38.3%	51.5%	4.3%	24.8%	0.1%
	Distribution	25.6%	35.8%	9.1%	22.2%	0.6%
Clay C	**Average**	31.9%	46.5%	14.4%	10.2%	15.4%
	Distribution	25.8%	35.7%	9.5%	21.6%	0.5%

3.6. Discussion and conclusions

The investigation showed a further analysis of the geometry of fillers used for the formulation of barrier dispersion coatings. The analysis indicated that the characterisation of the fillers based on image analysis is possible. The characterisation of the selected clays showed that Clay A is the largest filler followed by Clay B and Clay C respectively. This observation is based on the maximum Feret diameter and surface area. All the shape descriptors demonstrated that the filler shapes were elongated with an average ratio between the major and minor diameter being no larger than two. The shape descriptor also indicated that the fillers tend to have irregular silhouettes. The Fourier series descriptor approximates to the filler shape at the second harmonic which may be due to the regular filler silhouettes. By increasing the number of harmonics more details of the filler silhouettes can be included in the equation. For the selected fillers, it was concluded that 7 harmonics can accurately represent all the selected clays. The thickest fillers were found to be in Clay B, followed by and Clay A and C in that respective order.

It was possible to fit information related to size and shape of fillers into known distribution curves. This reduces the information needed to the parameters that define the distributions. The curves can be used to define the size of the fillers based on the parameters of each particular fitting. Due to the geometry generation of dispersion coatings being based on Monte Carlo

simulation, the size and shape parameters do not have to be related to each other. For example, combinations such as maximum Feret diameter and area may not be used. In the case of the Fourier, the analysis suggested that this method may be defined by experimental data and no Monte Carlo simulation may be applied. However, further improvement in the algorithm for representation of shape by Fourier series descriptor may be carried out to include, for example, correlation between Fourier series parameters.

To simplify the filler shape, the investigation concluded that the shapes can be represented by geometries which include both length and elongation in the definition of surface area. In this way, the best approximation was achieved by elliptical shapes. Analysis of elliptical shaped fillers showed to be similar to the experimental observation.

Chapter 4

CHARACTERISATION OF DISPERSION COATINGS

The development of mathematical models for dispersion coatings requires inputs regarding coating geometries. These inputs allow the generation of representative geometries for different coating formulations. Simulations conducted on these geometries can be used to predict the barrier performance of the coating formulations. However, it is essential to validate the model by comparison between the predictions with experimental measurements. The process of model validation requires characterisation of the barrier properties such as water vapour transmission rate (WVTR) and oxygen transmission rate (O_2TR). As presented in Chapter 2, the main factor that affects the barrier performance is the size and amount of the fillers dispersed in the barrier. Based on this, the formulation of dispersion coatings for model validation should cover these factors. Although a number of research papers present data on barrier properties at different coating formulations, no study could be found where a systematic range of size and amount of fillers has been explored. Only limited experimental data suitable for validating the use of models exists in the literature in relation to dispersion coatings. Schuman et al. (2005), for example, reported a barrier property analysis of a kaolin clay/latex dispersion coating at two different volume fractions and one filler particle aspect ratio. For these reasons, this chapter outlines experimental work to achieve these purposes.

4.1 Preparation of dispersion coating trials

Dispersion coating trials were formulated based on dispersion of the selected clays (Clay A, B, and C) in styrene-butadiene latex DL629 from Dow Chemicals. The styrene-butadiene latex was selected because it has been successfully used in different barrier dispersion coating formulations (Kugge & Johnson, 2008; Mesic, et al., 2010; Schuman, Karlsson, et al., 2005). The properties of the fillers were studied in Chapter 3. The main properties of the latex are presented in Table 4.1.

Table 4.1 Physical properties of the styrene-butadiene latex DL629

Property	Value
Solid content	50 %
Specific gravity	1
pH	6
Minimum film formation temperature (MFFT)	9 $°C$
Glass transition temperature (T_g)	2 $°C$

For analyses carried out in the following sections, the densities of the components of the latex were required. In this way, the latex is composed by two phases; a solid and a liquid part. The liquid part is principally water in which the styrene-butadiene (the solid part) is dispersed. It is well known the density of the water about 1 $g \cdot mL^{-1}$ at room temperature. However, the properties of the solid part are not known. The calculation of the density of the solid part can be based on a similar approach studied in food composites where more than one phase constitutes the structure of the food. The total density of the food composites is related to the density of each phase and its mass fraction in comparison to the total mass (Choi & Okos, 1986). Based on this, the density of the solid part of the latex can be derived as a function of the solid content, total density, and density of the liquid part of the latex (Equation 4.1). The calculation indicated that the density of the solid part of the latex was equal to 1 $g \cdot mL^{-1}$.

$$\rho_{latex\ dry} = \left[\left(\frac{1}{\rho_{latex}} - \frac{1 - Xf_{solid}}{\rho_{liquid}}\right)\frac{1}{Xf_{solid}}\right]^{-1} \tag{4.1}$$

where

ρ_{latex}: True density of the liquid latex ($g \cdot mL^{-1}$)

Xf_{solid}: Solid content of the latex

ρ_{liquid}: True density of liquid part ($g \cdot mL^{-1}$)

To prepare the dispersion coatings, the fillers were pre dispersed in water at 50% mass basis of water and mixed with a stirrer for 30 min at 1,000 rpm to form a slurry. The slurry was then combined with the latex using a high shear mixer for 1 h progressively increasing the rotation speed up to 600 rpm. By mixing the slurry and latex, 300 g of each formulation was made (Table 4.2). As the mass fraction of coating formulations increase, the mass of slurry increased and the mass of latex decreased. Due to both the slurry and the latex being at 50% mass basis of water, the final dried weight of both in the dispersion coating was equal to the half of the original wet weight. In total, five amounts of fillers were used; 10%, 20%, 30%, 40% and 50% as a mass fraction. For checking the coating preparation, the solid content of the slurries and the latex were measured before coating preparation by a moisture balance.

Table 4.2 Wet and dried coating weight of the dispersion coatings at different mass fraction of fillers (w/dw)

Mass fraction	Wet coating weight (g)		Solid part coating weight (g)	
(w/dw)	Slurry	Latex	Slurry	Latex
0%	0	300	0	150
10%	30	270	15	135
20%	60	240	30	120
30%	90	210	45	105
40%	120	180	60	90
50%	150	150	75	75

Before dispersion coating application, pH and viscosity were measured. These parameters can be used as indicators of good dispersion of fillers into the dispersion coating (Drage & Tamms, 2000). It is recommended that the pH during coating application is between 7 and 8 (B. Mesic, personal communication, 30 October, 2012). During the coating preparation, the pH was monitored and adjusted with sodium hydroxide at 0.1M reaching values between 7.2 and 8.1 (Figure 4.1). In the case of viscosity, low values help in the dispersion of the fillers in the coating (Lehtinen, 2000d). The viscosity was measured by Brookfield dial viscometer RV series at 100 rpm with spindle 3. A range between 0.25 and 0.6 $Pa \cdot s$ was observed in all the coating formulations (Figure 4.1). The viscosity for barrier dispersion coating is normally observed to be in the range of 0.05-0.5 $Pa \cdot s$ (Lehtinen, 2000d). Other authors indicate that from 0.5 to 1.0 $Pa \cdot s$ are typically delivered for barrier dispersion coatings (Kimpimäki & Savolainen, 1997).

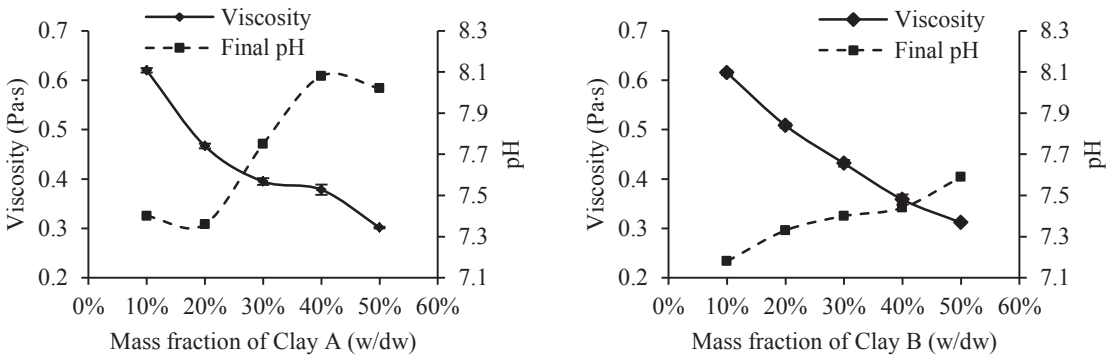

Figure 4.1 pH and viscosity of dispersion coating formulated with Clay A and B as a function of the amount of fillers (the error bars represent standard deviation)

A negative correlation between viscosity and mass fraction of filler was observed (Figure 4.1). This may be related to the larger density of the fillers compared to the solid part of the latex. As a result, the volume of the solid latex part of the dispersion coating decreased as the amount of fillers increased. In turn, the volume of the liquid part remained constant. This difference was quantified in Figure 4.2. As an example, the liquid coating was between 30% and 40% larger

than the dried coating at 50% of filler mass fraction depending of the fillers. In addition, the pH may have some effect. The results showed that the viscosity was lower as the pH increased.

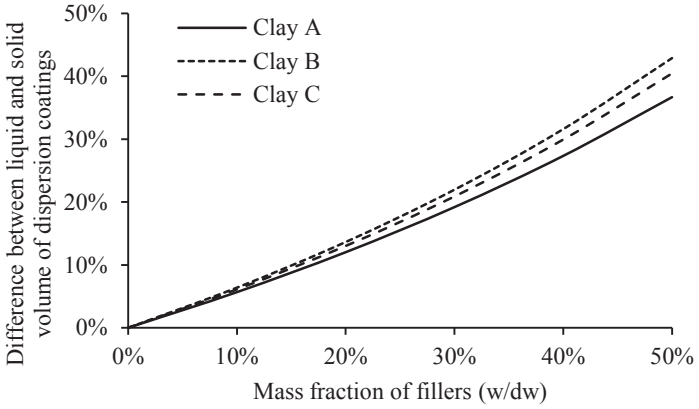

Figure 4.2 Ratio between the liquid volume and the dried volume of coating as a function of the mass fraction of several fillers

The coatings were applied with a drawdown coater Printcoat Instruments model K 202 on 30 $cm \times 30\ cm$ non-calendared and non-sized linerboard papers with grammage equal to 160 $g \cdot m^{-2}$ following the paper machine direction at 8 $cm \cdot s^{-1}$. The drawdown coater is composed of a platform where the linerboard is attached and a rod mounted in linear sliding shafts (Figure 4.3). The rod consists of a stainless steel cylindrical bar that is wound by a stainless steel wire (Dan, Irvin, & Pasquali, 2009). When the rod moves, the wet coating flows through the wire grooves forming the coating layer on the surface of the linerboard. Due to the grooves being dependent on the wire diameters, the wet coating thickness can be adapted by using a rod with a different wire diameter. Immediately after the coating application, the shape of the dispersion coating profile is undulated due to the grooves. However, the surface tension and gravity keep the coating in motion, making the surface even (Dan, et al., 2009).

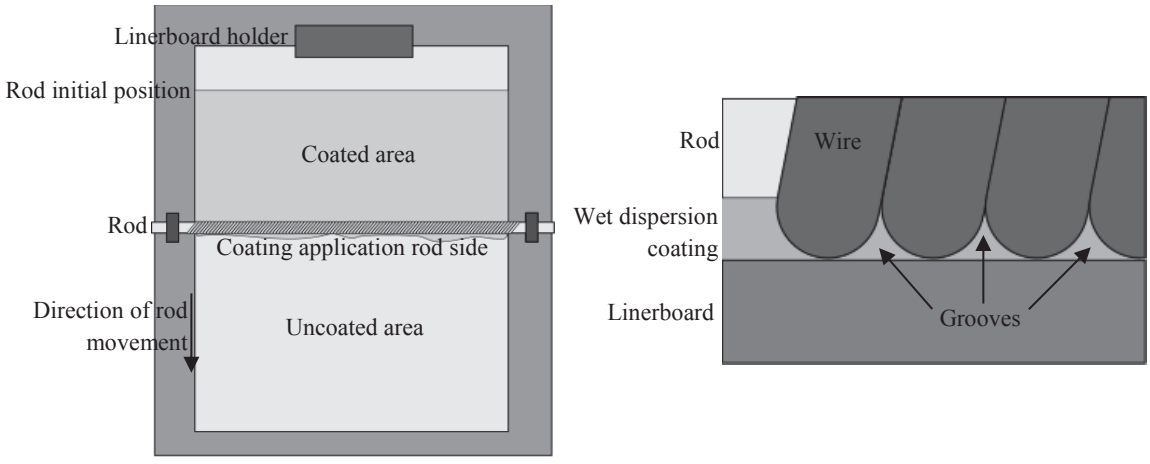

Figure 4.3 Scheme of the drawdown coater with a rod and a closed view of the rod wire

The process of coating application started with placing the rod at the initial position (Figure 4.3). A portion of wet coating was applied on the rod application side forming a line across the linerboard. As the rod moved through the linerboard, the wet coating was evenly distributed on the surface of the linerboard. When the linerboard was completely coated, the rod was disassembled from the drawdown coater, washed with hot water and dishwashing liquid, and dried before application of another coating. In this experiment, rods of sizes 3 (76.2 μm wire diameter) and 4 (101.6 μm wire diameter) were used to achieve two thickness levels. In this thesis, the rods were called "thin rod" and "thick rod" for rod size 3 and 4 respectively. In total, 5 samples per coating formulation were prepared.

After coating application, the trials were kept in frames for 5 min to avoid bending and then dried in an oven at 105°C for 2 min. The coating trials were stored at 23°C and 50% RH for further analysis. In addition, coating trials with only latex were made as references following the same procedure presented previously. All the combinations of formulations, rods, reference coatings, and replicates produced 166 coated samples. A summary of the number of trials is presented in Table 4.3.

Table 4.3 Summary of the number of trials coated for the characterisation of dispersion coatings

	Number of samples	**Cumulative number of samples**
Type of fillers	3	3
Volume fractions	5	15
Rods	2	30
Replicates	5	150
Unfilled dispersion coatings	16	166

Five 90 mm diameter samples of each coating formulation were taken to calculate the weight of the coating per area. The coat weight of the coating formulation after drying ($gsm_{coating}$) was calculated by taking the difference between the coat weight of the coating trial and the grammage of the linerboard (Equation 4.2). The coating trial referred to the dried coating including the linerboard.

$$gsm_{coating} = \frac{m_{trial}}{\frac{\pi}{4} \cdot {d_{trial}}^2} - gsm_{linerboard} \tag{4.2}$$

where

m_{trial}: Mass of the coating trial sample (g)

d_{trial}: Diameter of the coating trial (m)

$gsm_{linerboard}$: Grammage of the linerboard ($g \cdot m^{-2}$)

The final grammage of the dispersion coating formulations are presented in Figure 4.4 and 4.5.

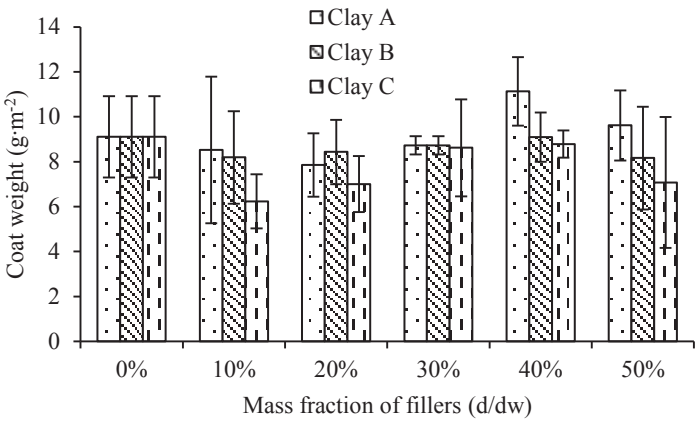

Figure 4.4 Coat weight of the dispersion coating formulation applied with thin rod (the error bars represent standard deviation)

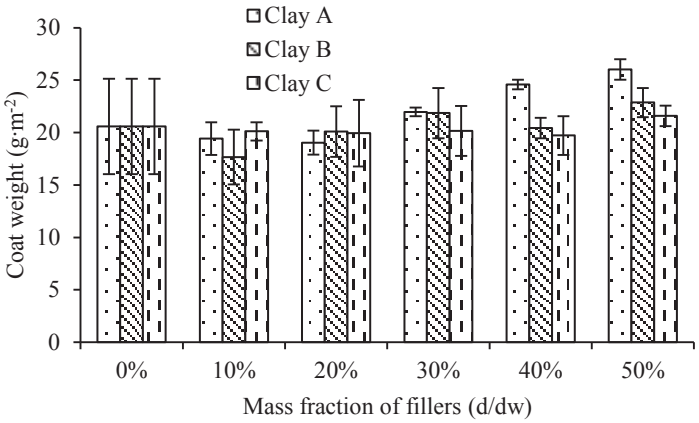

Figure 4.5 Coat weight of the dispersion coating formulation applied with thick rod (the error bars represent standard deviation)

The results indicated that the coat weight varied according to the rod size due to the difference between the applied amounts of coating. The coat weight doubled for the thick rod compared with the same coating formulation made with the thin rod. The coat weight tended to increase as the amount of filler was higher. This is clearer in the case of the thick rod samples. The maximum difference was 5.46 $g \cdot m^{-2}$ between unfilled and 50% mass fraction of coating prepared with Clay A. As a reference, the typical coat weight of a single layer is from 5 to 20 $g \cdot m^{-2}$; however, it could be larger if it is required (Linnonmaa & Trefz, 2000).

A negative correlation was found between the viscosity and the coat weights (Figure 4.6). The correlations were clearer for coatings applied with the thick rod. As well as the comparison

between the amount of filler and the viscosity, this trend may be related to the density of the fillers. As the amount of the filler became larger, the coat weight tended to increase.

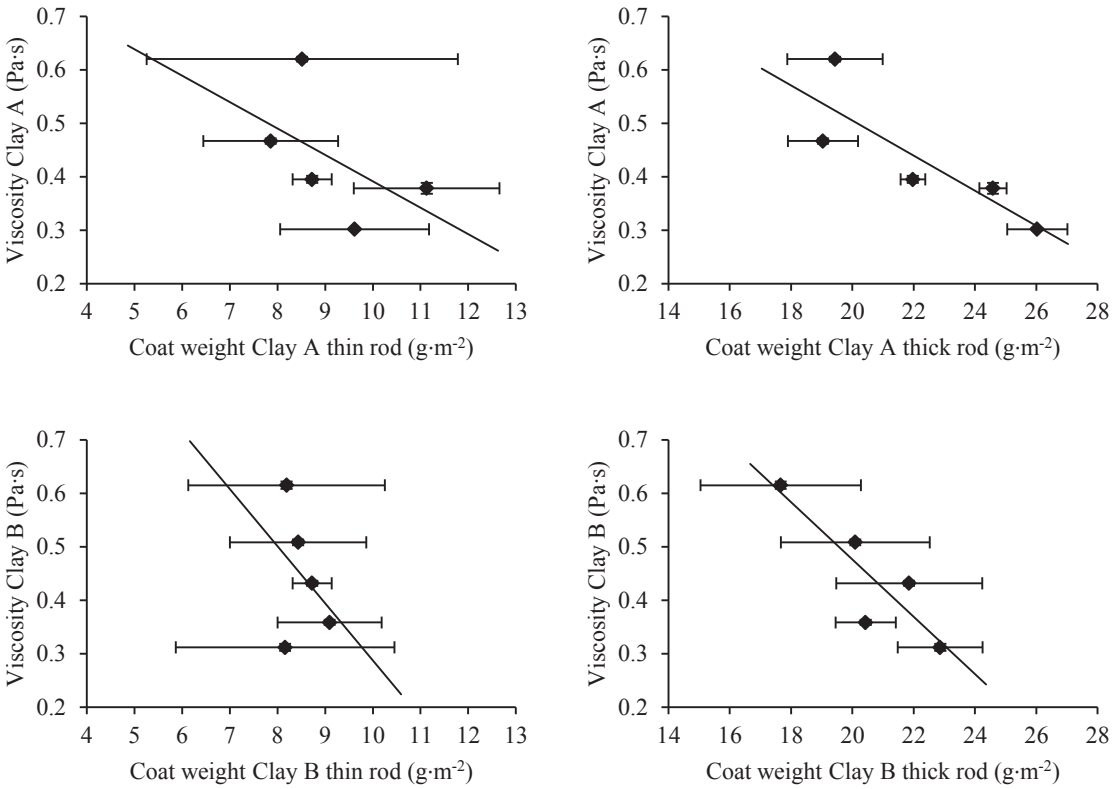

Figure 4.6 Correlation between viscosity and coat weight of dispersion coatings prepared with thin and thick rods (the error bars represent standard deviation)

4.2 Measurement of thickness and profile of the coating

The thicknesses of coatings were measured from images of the cross machine direction section samples taken by scanning electron microscopy (SEM). 2 x 1 cm cross section coating samples were inserted in between the rings of springs keeping the samples vertically oriented (Figure 4.7a). The samples were put into 25 mm diameter silicone rubber moulds and epoxy resin Epofix from Struers was added. The epoxy resin formed a solid block after the curing process. The curing process was carried out at room temperature for 24 h. Then, the top surfaces of the blocks were polished to keep the cross section of the coating trials clean of resin for observation by SEM. To be consistent with nomenclature of SEM technology, from this point the blocks will be called specimens. A polishing machine Mecapol P230 with different grades of sandpaper from coarse to fine were used for polishing the specimen surfaces. During the polishing process, water was used as a lubricant. Diamond suspension and fine sandpaper was used for mirror finishing. In total, two samples per coating formulation coated with the thin rod were mounted as 4 specimens with 8 samples each.

a) 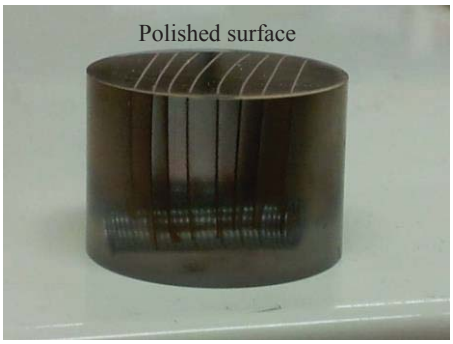

b) 

Figure 4.7 SEM specimens for coating characterisation a) view of sample blocks in the mounting, b) after gold/palladium sputter coating

To prepare the specimens for SEM, a 20 nm thick layer of gold/palladium sputter coating was applied on the polished surfaces to make the area of observation conductive (Figure 4.7b). This is required to avoid surface charging which can distort the capture of the images (Echlin, 2009). The images were captured with a scanning electron microscope Jeol JSM 6700F using both secondary electron image and backscattering electrons detectors at 25 kV of accelerating voltage and 1,000X of magnification. This configuration allowed observation of a length of about 120 μm of dispersion coating. At least 12 images per dispersion coating formulation were analysed. One of the captured images is presented in Figure 4.8.

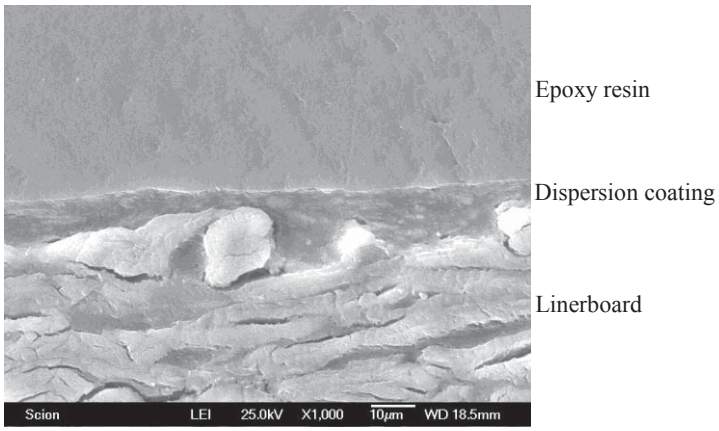

Figure 4.8 Cross section image of barrier dispersion coating at 50% mass fraction of Clay A concentration and coated with the thin rod by secondary electron detector

The image processing and analysis were carried out by Matlab programming. The coating thickness was estimated by measuring the distances between the linerboard and the top coating surface based on a reference line (Figure 4.9). Both surfaces were manually identified by moving the mouse through them. More sophisticated methods such as image analysis were not used due to the similarities of colours between the background and the coating on the images. The reference line was defined by linear regression of coordinates formed by top coating surface pixels. Once the reference line was established, it was displaced to include all the points in the

top surface. From the reference line, perpendicular lines were demarcated and the distance between the dispersion coating surfaces across the perpendicular lines were measured. Using the scale of the SEM images, the distances were transformed from pixels into μm units. The same method was used to estimate surface roughness; however, in this case reference lines were defined for both surfaces and distance between surfaces and their specific reference lines were measured. The measurements were taken every 2.4 μm which is equivalent to 50 points per image. Details of the program for thickness calculation are included in Appendix D.

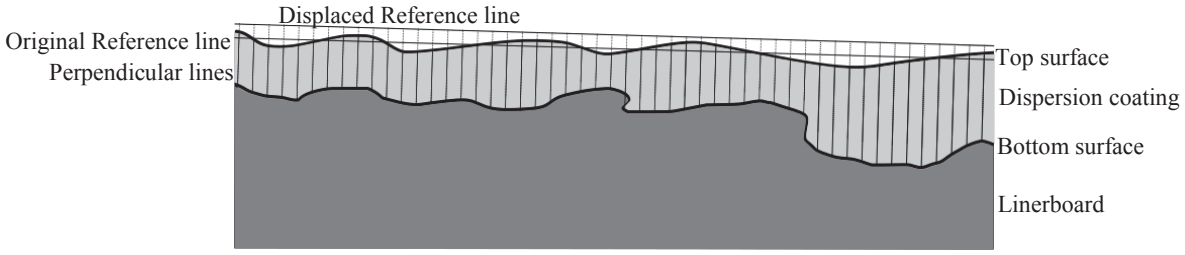

Figure 4.9 Scheme of dispersion coating thickness measurement

The results indicated that the thickness varied according to the coating formulation (Table 4.4). As the volume fraction of the fillers became larger, thinner coatings were obtained. The thickness was also affected by the type of filler. Clay A showed the thickest coating followed by Clay B and C, respectively. The variation of the thickness may have a relation to the difference in densities between the dried latex and the fillers. It is important to note that small variations in the vertical position of the coated samples in the epoxy resin did not affect the measurement. An estimation of the error on the thickness measurement by this factor is shown in Appendix E. The normal distribution was found to be appropriate to represent the dispersion coating thickness for all the formulations (Figure 4.10). The cumulative distribution and probability density function of the Normal distribution were presented in Equations 3.11 and 3.12 respectively.

Table 4.4 Average and standard deviation of the coating thickness at different mass fraction of filler (w/dw) for the three selected fillers including coating thickness with no fillers coated with the thin rod

	Coating thickness average ± standard deviation (μm)					
	0%	**10%**	**20%**	**30%**	**40%**	**50%**
Clay A	13.49 ± 7.12	13.18 ± 5.49	12.81 ± 5.76	12.34 ± 5.41	10.83 ± 4.34	9.90± 4.08
Clay B	13.49 ± 7.12	12.01 ± 4.84	11.86 ± 4.68	10.00 ± 4.32	9.74 ± 4.31	8.88 ± 3.71
Clay C	13.49 ± 7.12	11.07 ± 4.87	9.64 ± 3.80	10.60 ± 5.38	10.00 ± 4.17	10.05 ± 4.80

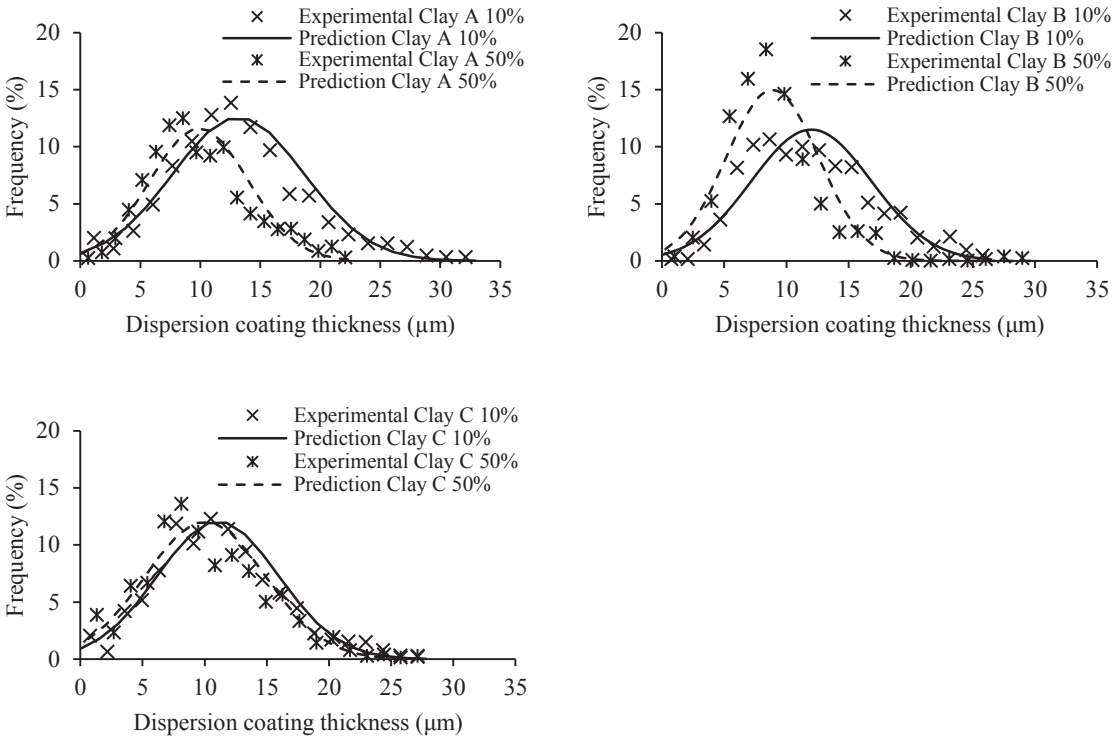

Figure 4.10 Coating thickness density probability for Clay A and Clay C at two filler mass fraction (w/dw)

A positive correlation between viscosity and thickness of coating were observed (Figure 4.11). The thickness may be related to the mass of solids in the liquid coating.

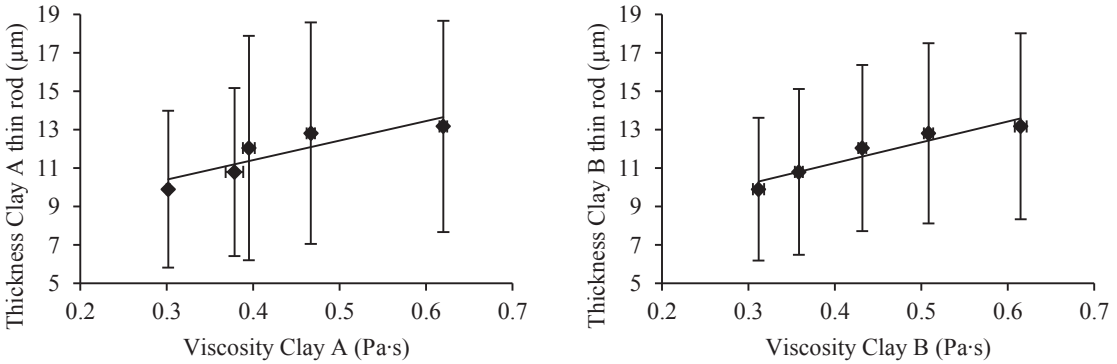

Figure 4.11 Correlation between viscosity and the thickness of the dispersion coating applied with thin rod (the error bars represent standard deviation)

Figure 4.12 shows no clear correlation between the coat weight and the thickness of the coating. With the naked eye, a negative correlation between both factors could be observed. This discrepancy may have relation to the variability of the measurements.

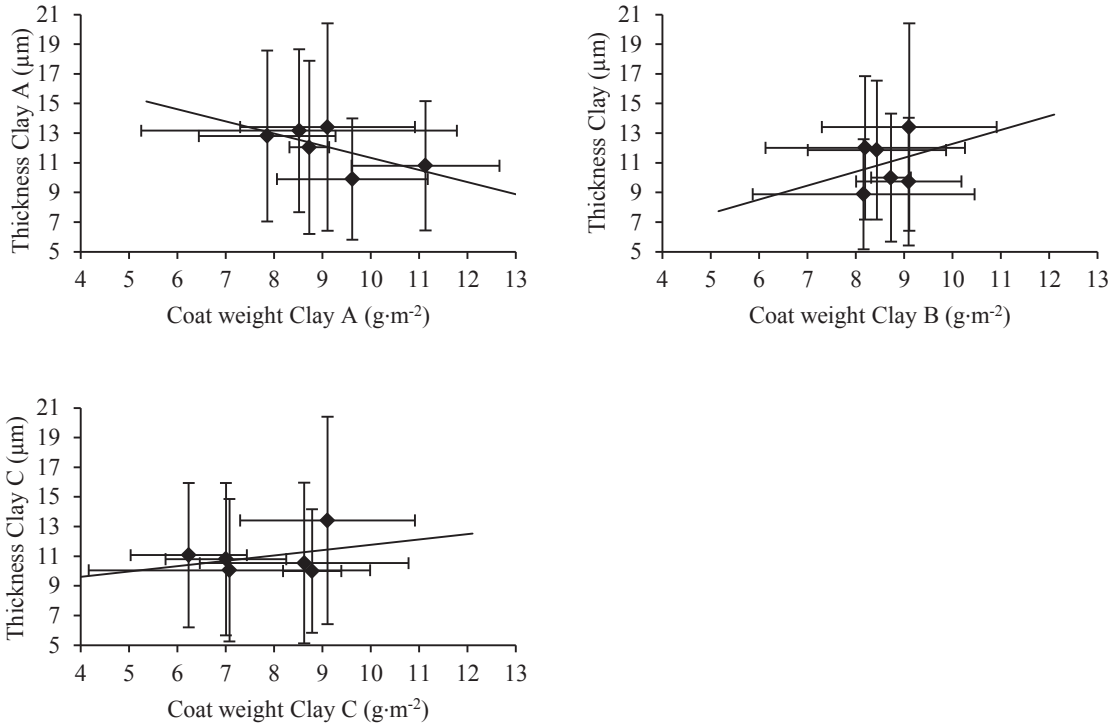

Figure 4.12 Correlation between coat weight and thickness of dispersion coatings prepared with thin rod (the error bars represent standard deviation)

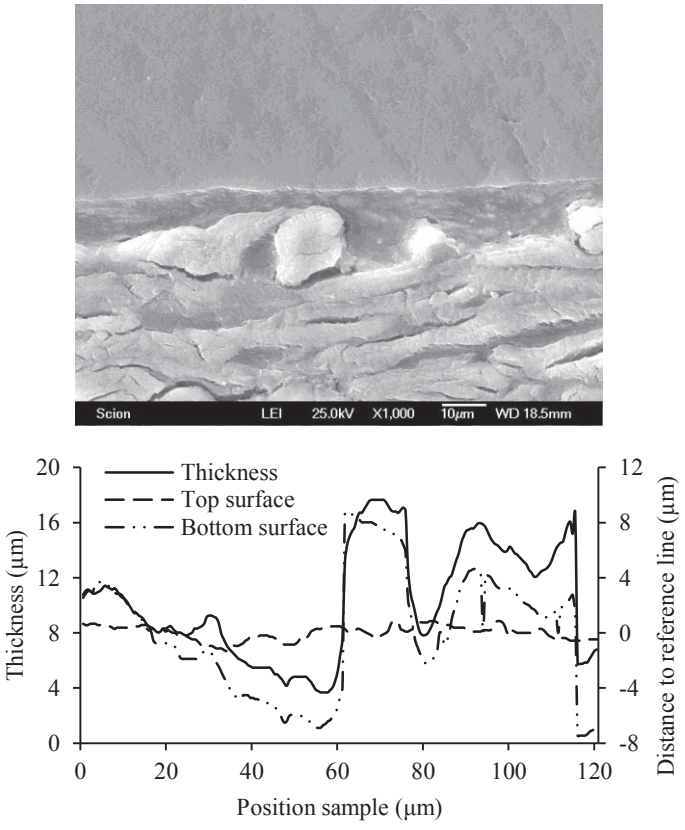

Figure 4.13 SEM dispersion coating image formulated at 10% mass of Clay A coated with the thin rod and its thickness and distance to the reference line of the top and bottom surface

Figure 4.13 shows the thickness of a coating image and its bottom and top surface variations. It is interesting that the thickness mostly followed the trend of the bottom variation curve. This suggested that the thickness profile was governed by the bottom surface of the coating. It is important to mention that the irregularities of that surface depended on the substrate. Thus, the above observation may be valid for all the coating formulations.

The distance between peaks of surface irregularities was measured on 13 images randomly taken from the coating formulations. The results indicated that the average distance was 16.2 μm (Figure 4.14). The distance between peaks followed the Log-normal distribution. Its parameters were μ=2.663 μm and σ=0.502 μm. The cumulative distribution and probability density function of the Log-normal distribution were presented in Equations 3.2 and 3.3 respectively.

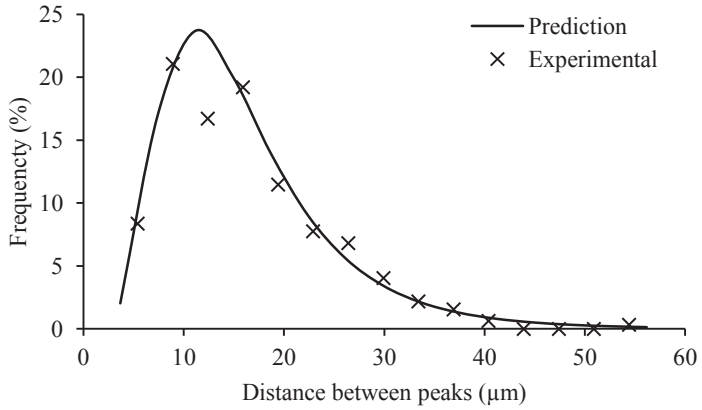

Figure 4.14 Distribution of the distance between peaks of coating surface profile of Clay A 10% dispersion coating made with thin rod (13 images analysed) and log normal distribution fitting (μ=2.663 μm σ=0.502 μm)

The distance between peaks was larger than the thickness of the coating; a ratio between 1.5 and 2.5 (Table 4.5). This suggested that the representation of the coating geometry for modelling had to be within this range. If the range is larger, the irregularities of the coating surface may have to be included.

Table 4.5 Average ratio between the distance between peaks and the thickness for the selected clays at different mass fraction of fillers (w/dw) and coated with the thin rod

Mass fraction	Clay A	Clay B	Clay C
10 %	2.22	1.40	1.46
20 %	2.12	1.39	1.47
30 %	2.47	1.71	2.51
40 %	2.13	1.77	2.83
50 %	1.62	1.70	2.95

The difference in the length between the top and bottom surface was calculated for 30 images selected randomly. On average, a 22.3% larger length was found in the case of the bottom surface. In some cases the difference was about 50% larger. This meant that the surface area of the bottom is larger than the top surface. That difference may influence a drop in the barrier properties of the coating due to the extra area for diffusion. The bend of the surface may promote diffusive flux from different angles and not just vertically from the source of permeant.

4.3 Characterisation of barrier properties of coating trials

The characterisation of barrier properties of coated samples was based on the measurement of water vapour (WVTR) and oxygen (O_2TR) transmission rates. WVTR measurements were carried out based on the Tappi Standard T 448 om-97 (1997). The same samples used for calculation of coat weight were placed in test dishes. The coated side of the trials were exposed to a controlled ambient at 23°C and 50% RH and the uncoated parts faced the inside of the test dishes. Desiccant (calcium chloride) was put inside the test dishes to keep the internal air at 0% RH. The desiccant was about 8 mm deep covering completely the bottom of the test dish. Between 10 and 15 mm of air space separated the coating trial and the desiccant. This condition creates the driving force for the flux of water vapour from outside to inside the test dish. As this occurs, the desiccant gains weight. The gained weight was related to the WVTR ($mol \cdot m^{-2} \cdot s^{-1}$) of the dispersion coatings as shown in Equation 4.3.

$$WVTR = \frac{\Delta m}{A_{WVTR} \cdot t} \cdot \frac{1}{86{,}400} \cdot \frac{1}{m_{WV}} \tag{4.3}$$

where

Δm: Variation in mass of the gravimetric cup during time (g)
A_{WVTR}: Area of permeability for WVTR (m^2)
t: Time of measurement (day)
m_{WV}: Molecular weight of water vapour (18.02 $g \cdot mol^{-1}$)

The test dishes were weighed once every day over five days to ensure a steady permeant flux. Five replicates per dispersion coating formulation were measured. A schematic diagram of the apparatus for measurement of WVTR is presented in Figure 4.15. It is important to note that the edges of the coating trials were excluded in the measurement of WVTR. These areas may have irregular profiles because a larger part of wet coating may remain there after coating application. This may have generated the thickness slightly larger than the other areas of the coating.

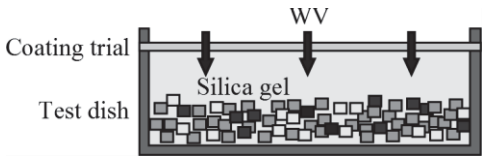

Figure 4.15 Diagram of experimental system used for estimation of WVTR

The estimation of O_2TR was conducted using permeability cells under isostatic conditions at $20°C$ (Figure 4.16). The permeability cells consisted of two stainless steel chambers that were separated by the coated samples. A constant flow of air as a source of oxygen was supplied to the bottom chamber and a flow of oxyfree nitrogen flux (N_2) was supplied in the top chamber. The coated side of the sample was facing the bottom chamber. The coating trial was the only connection between two chambers. Thus, the oxygen that diffuses from the bottom to the top chamber must do it through the sample. As a result, the oxygen in the top chamber can be related to the O_2TR.

180 mm diameter coated samples were exposed to air flux to measure the O_2TR. The flow of air was controlled by a needle valve previously regulated at 200 $mL \cdot min^{-1}$. In the case of N_2, the flow was controlled by a mass flow controller (Aalborg). The measurements were carried out during 4 h at three N_2 flow rates; 100 $mL \cdot min^{-1}$ during 1 h, 75 $mL \cdot min^{-1}$ during the next 1 h, and 50 $mL \cdot min^{-1}$ during the next 2 h. To avoid leaking of gases between the trial and the permeability cell, the edges of the chambers were sealed with rubber rings covered with silicone grease. Three replicates per coating formulation were used for estimation of O_2TR. As with the measurement of WVTR, the edges of the coating sample were not used for the estimation of O_2TR.

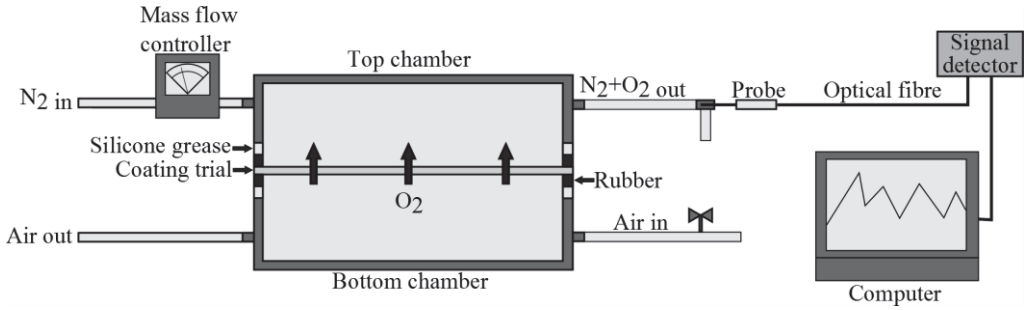

Figure 4.16 Diagram of experimental system used for estimation of O_2TR were O_2 is air, and N_2 is the carrier gas

Two measurements of O_2TR were carried out at the same time with two independent experimental rigs, two permeability cells; one sensed by a Neofox and another sensed by a Tautheta MFPF-100-1 fluorescence lifetime detectors. The detectors sense the fluorescence lifetime of the gas samples and relate it to the amount of O_2 based on the the Stern-Volmer

equation (Mills, 1997). To measure the fluorescence lifetime of the gas sample, the detectors emitted a LED light that runs through optical fibres to the oxygen sensor probes. As the number of detected oxygen molecules increase, the fluorescence signal is quenched. This relationship was represented by Equation 4.4 (Mills, 1997). In this experiment, the fluorescence lifetime was measured every 10 s at the top chamber outlet (N_2+O_2 out) and the data collected by a computer connected to the detectors.

$$c_{N_2/O_2} = \left(\frac{\tau_0}{\tau} - 1\right) \cdot \frac{1}{K_{sv}} \cdot \frac{1}{p_{atm}} \tag{4.4}$$

where

c_{N_2/O_2}: Concentration of oxygen in the outlet of the carrier gas chamber (%)

τ_0: Fluorescence lifetime at 0% of oxygen

τ: Fluorescence lifetime of the sample

K_{sv}: Stern-Volmer constant

p_{atm}: Atmospheric pressure

As shown in Equation 4.4, the concentration of O_2 and fluorescence lifetime is represented by a linear relation where K_{sv} is the slope of the curve. Thus, K_{sv} can be estimated by measuring the fluorescence lifetime of two gas samples where the O_2 is known. For this, Oxyfree Nitrogen was used as a sample with 0% of O_2 and beta standard grade of 20.7% O_2 in N_2 for the other sample.

The conversion of the concentration of oxygen diffused through the dispersion coating into O_2TR $(mol \cdot m^{-2} \cdot s^{-1})$ is shown in Equation 4.5.

$$O_2TR = 1.387 \times 10^{-6} \cdot \frac{F_{N_2} \cdot c_{N_2/O_2}}{A_{O_2TR}} \tag{4.5}$$

where

F_{N_2}: Flow of oxyfree nitrogen $(mL \cdot min^{-1})$

A_{O_2TR}: Area of permeability for O_2TR (m^2)

Because the infiltration of silicone grease from coating sample substrate, A_{O_2TR} becomes irregular and varies between coating trials. Images of the trials were taken after exposure of oxygen to calculate A_{O_2TR} (Figure 4.17). The exposure area was calculated based on a known reference area. The reference was a 25 mm diameter sticker. The images were binarised and the area of the reference and the exposure area was measured in terms of pixels and then

transformed into m^2. Equation 4.6 shows the expression for the above calculation. To extract the information, the images were analysed by a routine developed in ImageJ. On average, the exposure area was 0.022 m^2 for all the dispersion coating formulations. This meant an average of 167 mm diameter of exposure coating area. The diameter of the exposure area was on average 13 mm smaller than the original diameter.

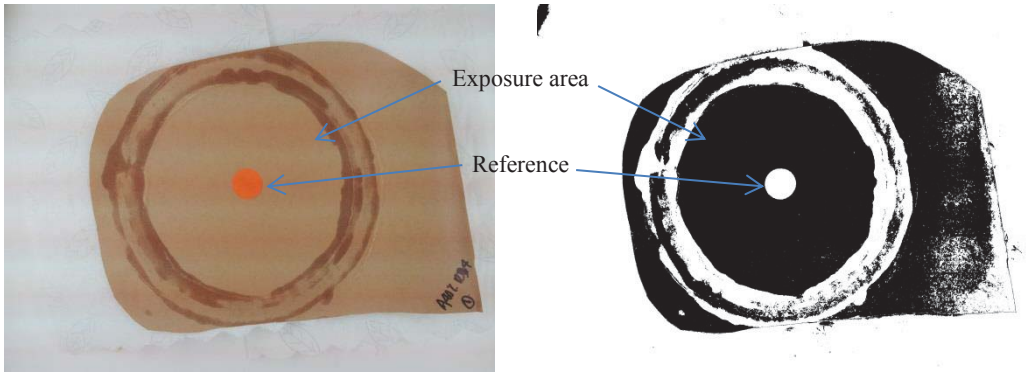

Figure 4.17 Image of the area of oxygen exposure before and after image processing for exposure area calculation of a sample of dispersion coating formulated with Clay A at 10% mass fraction

$$A_{exposure}(m^2) = A_{reference}(m^2) \cdot \frac{A_{exposure}(pixel^2)}{A_{reference}(pixel^2)} \tag{4.6}$$

where

$A_{exposure}$: Exposure area (m^2)

$A_{reference}$: Reference area (m^2)

For comparison between coating formulations, the observed TR were normalised based on the average coat weight of all samples for each coating thickness level (Equation 4.7). This procedure implies the assumption of linear variations of TR as the coat weight changes.

$$TR_n = TR \cdot \frac{gsm_n}{gsm} \tag{4.7}$$

where

TR_n: Normalised TR for either WVTR or O_2TR ($mol \cdot m^{-2} \cdot s^{-1}$)

TR: Either WVTR or O_2TR ($mol \cdot m^{-2} \cdot s^{-1}$)

gsm_n: Coat weight for normalisation ($g \cdot m^{-2}$)

gsm: Coat weight of the coating trials ($g \cdot m^{-2}$)

The WVTR and O_2TR can be transformed into water vapour and oxygen permeability by Equation 4.8 (Robertson, 2013). This estimation allows calculation of the coating performance discounting the effect of the thickness.

$$P = TR \cdot \frac{\Delta x}{\Delta p} \tag{4.8}$$

where

P: Permeability of coating trials of either WV or O_2 ($mol \cdot m \cdot m^{-2} \cdot s^{-1} \cdot Pa$)

Δp: Difference of partial pressure between coating trials surfaces (Pa)

Δx: Thickness of the coated samples (m)

In the case of the water vapour, the partial pressure is a function of the relative humidity and saturated pressure at a particular temperature (Equation 4.9).

$$\Delta p = p_{sat} \cdot (RH_{out} - RH_{in}) \tag{4.9}$$

where

p_{sat}: Saturated pressure (Pa)

RH_{out}: Relative humidity outside of the gravimetric cup

RH_{in}: Relative humidity inside of the gravimetric cup

For oxygen, the partial pressure can be estimated by the relation of the driving force for oxygen permeant and the atmospheric pressure as shown in Equation 4.10.

$$\Delta p = p_{atm} \cdot \left(c_{air_{out}} - c_{N_2/O_2}\right) \tag{4.10}$$

where

$c_{air_{out}}$: Concentration of oxygen in air inlet (%)

c_{N_2/O_2}: Concentration of oxygen in the top chamber outlet (%)

The calculation of $c_{air_{out}}$ was based on a mass balance the oxygen concentration between chambers (Equation 4.11).

$$\dot{m}_{air_{in}} \cdot \left(c_{air_{in}} - c_{air_{out}}\right) = \dot{m}_{N_2} \cdot \left(c_{N_2/O_2} - c_{N_2}\right) \tag{4.11}$$

where

$\dot{m}_{air_{in}}$: Mass flow rate of air in the inlet ($g \cdot min^{-1}$)

$c_{air_{in}}$: Concentration of oxygen in the air inlet (21%)

$\dot{m}_{N_2}$: Mass flow rate of nitrogen in the inlet ($g \cdot min^{-1}$)

c_{N_2}: Concentration of oxygen of the nitrogen inlet (0%)

From Equation 4.11, the $c_{air_{out}}$ is equal to

$$c_{air_{out}} = c_{air_{in}} - \frac{\dot{m}_{N_2\,in}}{\dot{m}_{air_{in}}} \cdot \left(c_{N_2/O_2} - c_{N_2}\right) \tag{4.12}$$

Therefore, the final expression of Equation 4.10 became

$$\Delta p = p_{atm} \cdot \left[c_{air_{in}} - \left(1 + \frac{\dot{m_{N_2 in}}}{\dot{m_{air in}}}\right) \cdot c_{N_2/O_2}\right] \tag{4.13}$$

In previous analysis, the coating formations were defined by the mass fraction of fillers. This made the formulation of the dispersion coating easier. Also, this allowed comparison between results of dispersion coatings with the same mass of fillers. However, the model presented in Chapter 5 was based on volume fraction of fillers. To make the experimental results comparable with the model predictions, transformation of the formulations into volume basis was required. In particular, the amount of fillers with respect to the volume of the dispersion coating was defined as volume fraction. This refers to the ratio between the volume of fillers and the total volume of the dried coating (Equation 4.14). The total volume of dried coating was the sum of the volume of fillers and the dried latex. As presented in Section 2.2 in Chapter 2, by using the density and mass of fillers and dried latex, these volumes can be calculated (Equations 2.2 and 2.3).

$$\emptyset_F = \frac{V_{filler}}{V_{filler} + V_{latex\ dry}} \tag{4.14}$$

$$V_{filler} = \frac{m_{filler}}{\rho_{filler}} \tag{2.2}$$

$$V_{latex\ dry} = \frac{m_{latex\ dry}}{\rho_{latex\ dry}} \tag{2.3}$$

where

$\emptyset_F$: Volume fraction of fillers

V_{filler}: Volume of fillers (mL)

$V_{latex\ dry}$: Volume of dried latex (mL)

m_{filler}: Mass of the fillers (g)

ρ_{filler}: True density of the filler ($g \cdot mL^{-1}$)

$m_{latex\ dry}$: Mass of the dried latex (g)

$\rho_{latex\ dry}$: True density of the dried latex ($g \cdot mL^{-1}$)

The volume fractions of fillers for all the coating formulation are presented in Table 4.6.

Table 4.6 Transformation of the mass fraction of filler (w/dw) of coating formulation into volume fraction of fillers (v/dv)

	Volume fraction of filler (v/dv) per dispersion coating formulation (%)				
Mass fraction	**10%**	**20%**	**30%**	**40%**	**50%**
Clay A	4.9%	10.4%	16.6%	23.6%	31.7%
Clay B	4.3%	9.1%	14.6%	21.0%	28.6%
Clay C	4.5%	9.6%	15.4%	22.0%	29.8%

Figure 4.18 and 4.19 present the measurement of WVTR for all the studied formulations. As expected, the amount of fillers inversely affects the WVTR of the dispersion coatings. For both rods, the lowest WVTR was observed from about 20% of volume fraction of fillers for all the filler types. This reduction was particularly noticeable for the thin coatings where WVTR decreased by almost a half in comparison to unfilled coatings. These results were in the same range as those obtained for barrier properties reported for styrene butadiene/kaolin clay coatings presented in a series of publications written by Schuman et al. (Schuman, Karlsson, et al., 2005; Schuman, et al., 2004b). It is important to note that there are considerable variations in the WVTR measurement at different filler concentrations. Schuman, Wikström, and Rigdahl (2004a) suggested that these variations may be related to the heterogeneity of the coating profile. It has also been reported that uniform coating thickness provides the most effective barrier properties (Andersson, 2008; Krochta, 2010).

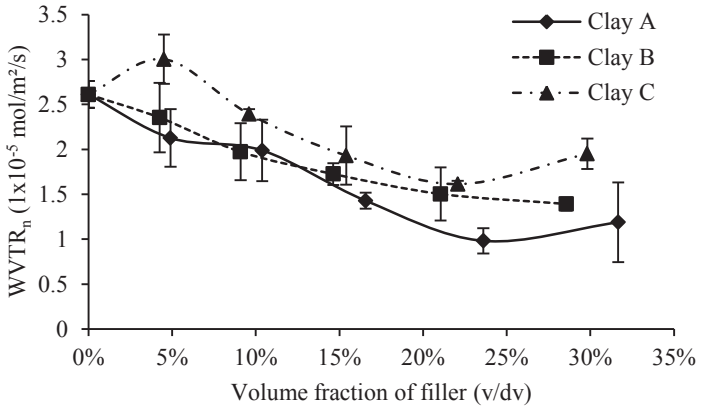

Figure 4.18 Normalised water vapour transmission rate measured for coating formations prepared with the three selected fillers and coated with thin rod ($gsm_n = 8.53\ g \cdot m^{-2}$) (the error bars represent standard deviation)

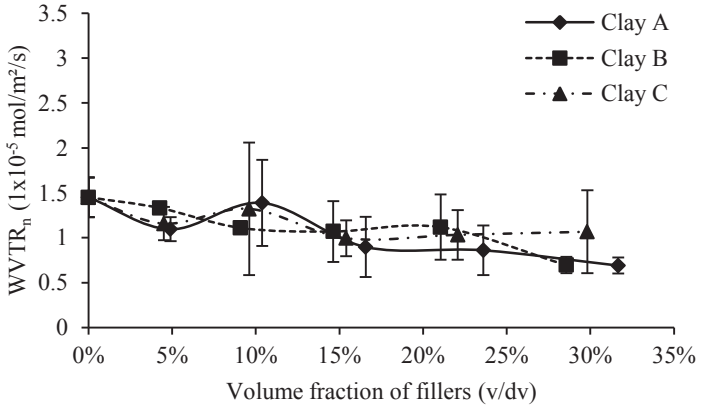

Figure 4.19 Normalised water vapour transmission rate measured for coating formations prepared with the three selected fillers and coated with thick rod ($gsm_n = 20.96\ g \cdot m^{-2}$) (the error bars represent standard deviation)

The reduction in WVTR was also affected by the type of fillers. For those fillers with a large maximum Feret diameter (Clay A), the reduction in WVTR was higher than those of smaller size (such as Clay C) at the same filler concentration. This agreed with findings presented by Rissa et al. (2000) and Schuman, Adolfsson et al. (2005) who concluded that the characteristics of the fillers such as aspect ratio influence the final WVTR of a particular coating formulation.

In the case of the thick coating (Figure 4.19), the results suggested that the WVTR was mostly governed by the thickness of the coating rather than coating formulations. No significant differences were observed between formulations, remaining at about $1 \times 10^{-5}\ mol \cdot m^{-2} \cdot s^{-1}$. This value is similar to the WVTR of the thin coatings at high volume fraction of fillers. The large coating weight of the thick coating makes longer permeant pathways compared to the thin

coating and better barrier properties. It is reported that the WVTR can be reduced by almost a half if the coat weight increases from 10 to 20 $g \cdot m^{-2}$ (Kimpimäki & Savolainen, 1997). In this work, the coat weight were on average in the order of 8.9 $g \cdot m^{-2}$ and 21.0 $g \cdot m^{-2}$ for the thin and thick coatings respectively (Figure 4.4 and 4.5).

It is important to note that the paper substrate only provides support for the settlement of the coating and its barrier properties are minimum (Andersson, 2008; Robertson, 2013). To prove this, measurement of WVTR on 5 samples of uncoated linerboard were carried out at the same conditions as measurement conducted for coating trials. The results indicated that the average WVTR for the linerboard was $2.39 \times 10^{-4}\ mol \cdot m^{-2} \cdot s^{-1}$. Similar results were presented for a commercial 200 $g \cdot m^{-2}$ grammage linerboard. The WVTR in this case was 2.74×10^{-4} $mol \cdot m^{-2} \cdot s^{-1}$ measured at 23°C and 50% RH (Kugge & Johnson, 2008). This was about 10 times larger WVTR than the highest measurement conducted in this experiment. Therefore, this showed that the barrier properties are governed by the coating properties.

Figure 4.20 presents the WVTR with respect to the time of measurement of several coating trials formulated with Clay A at 31.7% and applied with the thick rod. In terms of the measurement of WVTR, this formulation represented the longest expected measurement due to its high barrier properties compared with the others. Therefore, the other formulations should take a shorter time to reach the steady state in WVTR. In this case, the steady state was achieved between 24 h and 48 h of sensing. In some trials no changes of WVTR were observed during the measurement. On average, variation in WVTR between 24 h and 48 h was 4.1%. The standard applied for this measurement indicated that the steady state has been reached when the variation of WVTR in two consecutives measurements is within 5% (Tappi, 1997). The results may suggest that, on average, the steady state of WVTR can be achieved before 24 h.

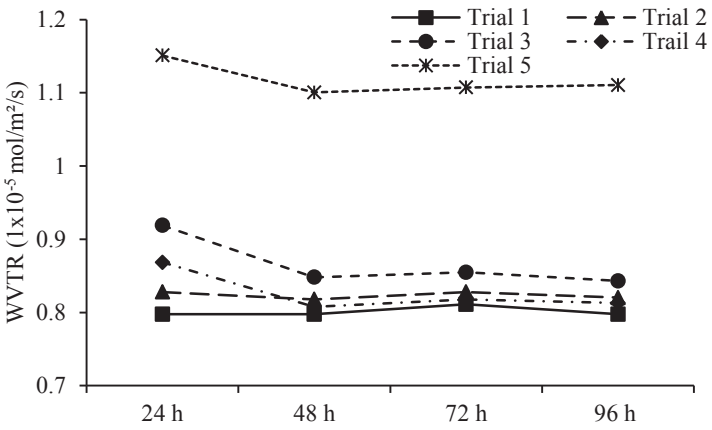

Figure 4.20 WVTR as a function of time of several coatings trials filled with Clay A at 31.7% of volume fraction of fillers (v/dv) and applied with the thick rod

Figure 4.21 and Figure 4.22 show the oxygen transmission rate for coatings formulated with the selected clays and applied with the thin and thick rod. As with the WVTR calculated above, the results were normalised against coat weight to make them comparable to each other. The results indicated similar trends as those presented for WVTR. However, the O_2TR was higher than the WVTR. These differences were more noticeable for coatings prepared with Clay B and C and applied with the thin rod. Depending on the clay, the reduction of O_2TR between rods was between 0.5 and 5 times if the comparison is based on coatings with about 30% volume fraction of filler. Unexpected results were found in the case of dispersion coatings applied with the thick rod. Some measurements indicated that the O_2TR was lower than 0 $mol \cdot m^{-2} \cdot s^{-1}$. This suggested that errors were present during the experiment. Despite the errors, the trend seemed to be similar to those results presented for the WVTR for coating applied with the thick rod. This indicated that no matter the permeant, the barrier performance was governed by the coatings. Perhaps, parameters such as coat weight or thickness may have more importance under those coating conditions.

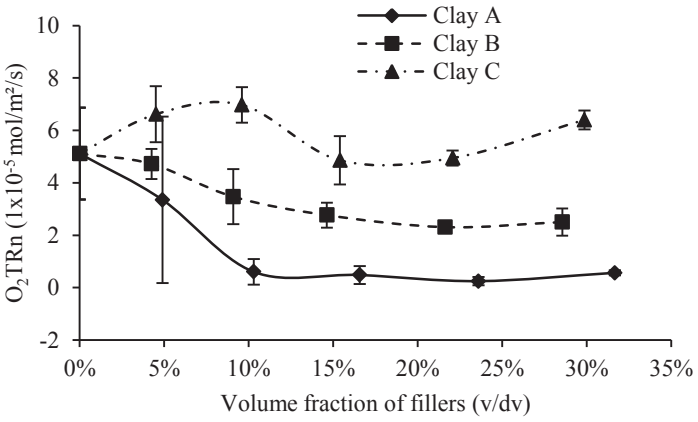

Figure 4.21 Normalised oxygen transmission rate measured for coating formations prepared with the three selected fillers and coated with thin rod ($gsm_n = 8.53\ g \cdot m^{-2}$) (the error bars represent standard deviation)

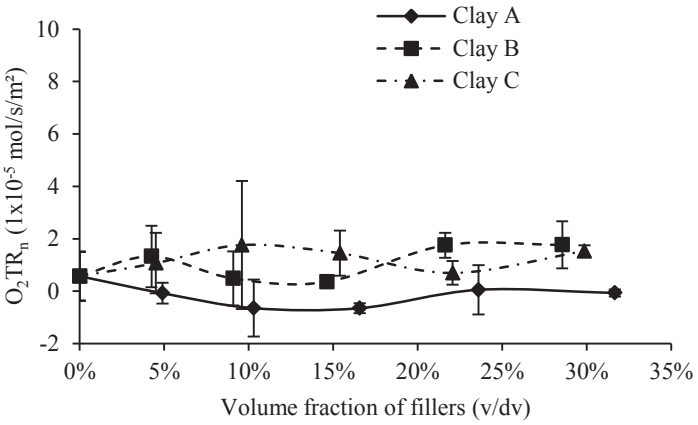

Figure 4.22 Normalised oxygen transmission rate measured for coating formations prepared with the three selected fillers and coated with thick rod ($gsm_n = 20.96\ g \cdot m^{-2}$) (the error bars represent standard deviation)

The permeability of water vapour (WV) and oxygen (O_2) for the coatings applied with the thin rod are presented in Figure 4.23 and 4.24. The WV permeability was one order of magnitude larger than the values for O_2. This may be related to the size of the molecules of permeants and the interaction between permeants and coatings. The size of the permeant molecules affects the permeability in terms of variation of diffusivity. As the permeant molecules are bigger, larger activation energy is required for the diffusion process and as result the diffusivity of the permeant in a given dispersion coating becomes lower (van Krevelen & te Nijenhuis, 2009). This is the case of the permeants used these experiments where the kinetic diameter of the WV and O_2 are 2.65 Å and 3.46 Å respectively (Matteucci, Yampolskii, Freeman, & Pinnau, 2006).

The interaction of the permeant and the coating is represented by the solubility. The solubility of simple permeants such as O_2, H_2, or He is normally low; however, as the permeant-coating

interaction becomes stronger, the solubility significantly increases (Robertson, 2013). This higher interaction may happen when coatings are exposed to permeants such as CO_2 or WV. The average permeability of several permeants across a range of polymers were compared with the permeability of N_2 and published by van Krevelen and te Nijenhuis (2009). The results showed that the permeabilities of O_2 and WV are 3.8 and 550 times larger than N_2 respectively. The difference is mostly because the solubility of WV is 110 times higher than the N_2. In the case of the O_2, the difference is only 2.2 times higher than N_2. This means that the difference of solubility between WV and O_2 is about 50 times.

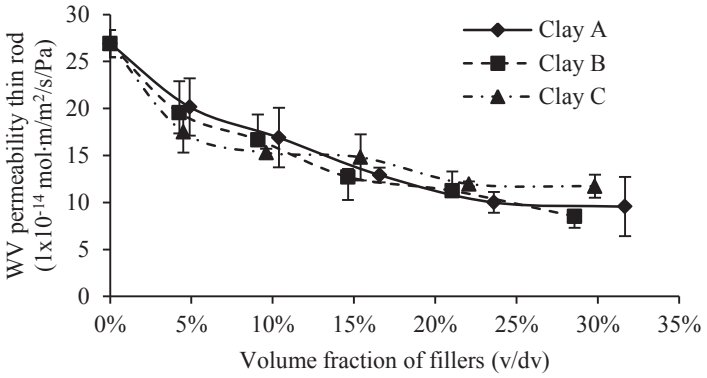

Figure 4.23 Water vapour permeability of coating formulated with the selected clays at different volume fraction of fillers coated with the thin rod (the error bars represent standard deviation)

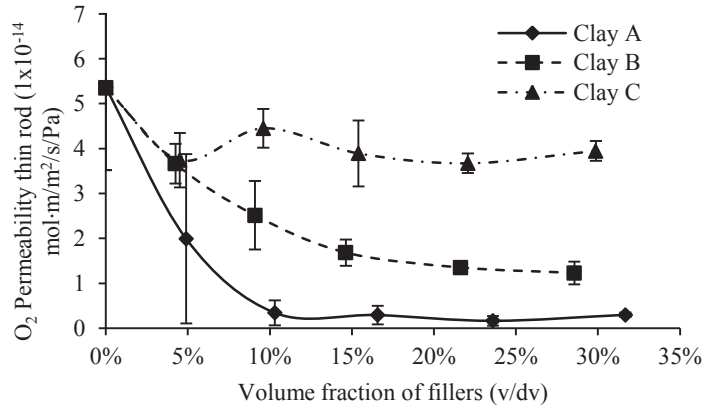

Figure 4.24 Oxygen permeability of coating formulated with the selected clays at different volume fraction of fillers coated with the thin rod (the error bars represent standard deviation)

The relative permeability, based on water vapour and oxygen permeability for coating applied with the thin rod are presented in Figure 4.25. The relative permeability refers to the ratio between the permeabilities of the filled coatings and the unfilled coating. Expected trends were observed; the WV relative permeability increased as the O_2 relative permeability increased.

However, the relative permeability of both permeants should be the same if the only mechanism for permeability reduction is due to the increase in tortuosity. In the case of Clay A and B the WV relative permeability tended to be larger than the O_2TR. The opposite was observed for Clay C. This discrepancy may be related to some degree to errors during TR measurement. The natural variability of the measurement may also influence the results.

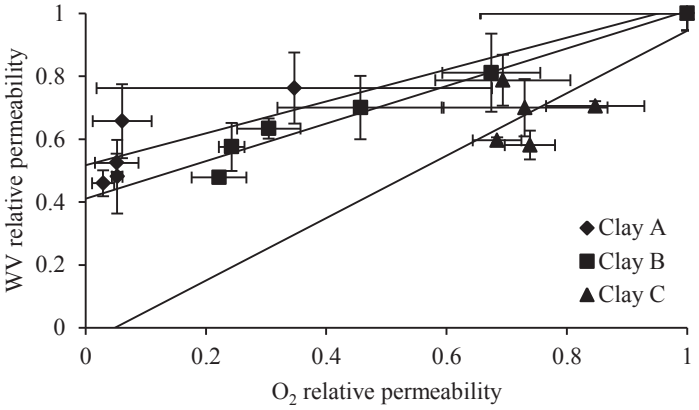

Figure 4.25 Oxygen and water vapour permeability of coatings coating formulated with the selected clays and applied with the thin rod (lines represent the trend of the relative permeability and the error bars represent standard deviation)

4.4 Discussion and conclusion

The presented analysis showed the study of the geometries and barrier performance of a number of different coating formulations. This information is required to both reconstruct representative geometries of dispersion coatings where the model will be applied and to validate the model against experimental data. The geometrical analysis indicated that the thickness of the coatings varied according to their formulations. As the amount of fillers increased, thinner coatings were made. This was due to the increase in liquid volume that the formulation with large amount of filler presented. The coating thickness profile was governed by the coating application and the topography of the linerboard. The peaks of the bottom surface were larger than the thickness of the coating in values from 1.47 to 2.95. Also, the length in the cross machine direction of the bottom surface of the coating was 22.3% larger than the length of the top surface. From this it is possible to infer that the bottom surface area is larger than the top surface. In terms of modelling, the above information can be used as a guide for definition of the representative geometries of dispersion coatings. For example, if the geometries have in-plane dimensions larger than the variations in coating thickness due to the heterogeneity of the bottom surface, irregularities may have to be included. It is important to avoid the incorporation of the irregularities of the coating profile because they increase the complexity of the simulation process.

The barrier properties of the dispersion coatings were affected by the type and amount of fillers. As the literature explains, the transmission rate of gases through barriers is lower as the size and the amount of filler increase. It was noted that the paper does not play any important role in the barrier properties of dispersion coatings. This may allow simplification of the representative geometry of coating trial by representing only the coating geometry and not the linerboard structure. As the coating thickness increases, lower transmission rate is observed. The thickness or weight of the coating seems to impact on the effectiveness of the fillers in terms of TR performance. For thin coatings, the fillers tended to have more importance in reducing TR. In the case of thick coatings, the transmission rate is regulated by the thickness of the coating rather than the coating formulation. Discounting the effect of the thickness on the reduction of TR, the permeability of O_2 was lower than the WV due to the difference between molecular sizes and the stronger interaction between WV and dispersion coatings. This information is considered in the following chapters for validation of the model.

Chapter 5

DEVELOPMENT OF A THREE-DIMENSIONAL MODEL TO PREDICT PERMEABILITY OF DISPERSION COATINGS

This chapter focused on the development of a three dimensional model to predict the permeability through barrier dispersion coatings. The model was developed based on the geometrical characteristics of the barrier dispersion coatings such as coating thickness, the distribution of filler inside the coatings, filler size, and shape. In addition, assumptions based on observations presented in Chapters 3 and 4 to simplify the system to be able to resolve the model. This chapter is focussed on the development and implementation of a model of the system to predict steady state moisture or gas flux through dispersion coatings.

5.1 Conceptual model

Figure 5.1 represents the conceptual model of barrier dispersion coating to be modelled. The system consists of a barrier dispersion coating applied on the surface of linerboard paper. The barrier dispersion coating is formulated by mixing a binder with non-permeable fillers creating a unique, uniform, and nonporous barrier against any type of permeant such as water vapour or oxygen.

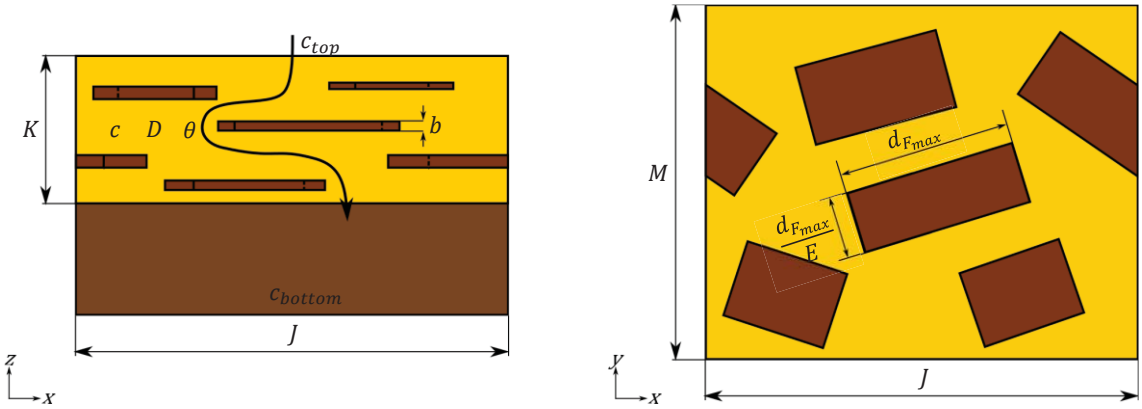

Figure 5.1 Schematic diagram of the conceptualised barrier dispersion coating

The two sides of the barrier dispersion coatings are normally exposed to different concentration of permeant (c_{top} and c_{bottom}), and therefore there is a driving force that creates a diffusive flow though the coating. The temperature of exposure (θ) affects the diffusion flow by changing the diffusivity and solubility properties of the binder. The dynamics for absorption until a steady diffusive flow is typically achieved in a matter of few hours. This was seen in the WVTR

measurements reported in the previous chapter (Figure 4.19). For this reason a steady state model was developed.

The increase in tortuosity of the diffusive flux is based on the geometrical characteristics of the fillers, their amount and distribution in the barrier dispersion. The maximum Feret diameter ($d_{F_{max}}$), elongation (E), and thickness (b) of the fillers vary according to the type of filler used in the coating formulation. The quantity of filler within the coating can be changed from 0% of the total volume of the barrier dispersion coating to the CPVC (refer Chapter 2 for definition).

5.2 Model assumptions

The key assumptions used in the model were based on the mass transfer diffusion mechanisms through the dispersion coatings and, experimental observations of the fillers and coating trial analysed in Chapters 3 and 4. Simplifications of the system through these assumptions are important in order to be able to solve the mathematical formulation of the model.

5.2.1 Mass transfer through the coating

The mechanism of mass transfer was identified as diffusion driven by the permeant concentration gradient. At the beginning of this process, the concentration of permeant is constantly changing across the coating until reaching a balance between the source and the sink of permeant. As previously discussed, this transient period is relatively short compared to the shelf life of the barrier dispersion coating (Finnigan, 2009; Lee, et al., 2008; Robertson, 2013; van Krevelen & te Nijenhuis, 2009; Waack, Alex, Frisch, Stannett, & Szwarc, 1955). For this reason, the model was considered as a steady state mass transfer. Fick's law is generally accepted to describe the transport mechanisms within a polymer matrix (Choudalakis & Gotsis, 2009).

The structure of the linerboard paper can be defined as a cellulose fibre network. This means that direct pathways for diffusive flux exist through the paper structure. As presented in Chapter 4, the WVTR of a linerboard can be 10 times higher than measurements conducted on dispersion coatings with 0% of fillers. For this reason, the resistance to diffusion due to the paper substrate can be considered negligible for modelling. This argument implies that the concentration of permeant at the common surface between the coating and the paper and the bottom surface of the paper is the same.

The edges of the coating were defined with periodic boundary conditions. This assumption allows continuity of the solution on opposite faces of the domain (Goodyer & Bunge, 2009),

and reduction of the number of fillers and the size of coating for simulations (Euston, et al., 2007).

5.2.2 Coating and fillers geometry

Models that use two-dimensional geometries (such as those presented in Table 2.4 in Chapter 2) assume filler particles are infinitely long and as such there is no diffusion in the third direction. As presented in Table 2.1 in Chapter 2, the fillers used for barrier dispersion coatings such as kaolin clay, talc, or calcined kaolin are plate shaped, meaning that their effect on the reduction of permeability is similar in any direction. According to the analysis presented in Chapter 2, the error by assuming two-dimension geometry could be important for fillers with elongation lower than 10, which is the case in this thesis. Therefore, the coatings were defined as three-dimensional geometries.

5.2.3 Rectangular plate as filler shape

The shape assumed for representation of the fillers was rectangular defined by length, elongation, and thickness. As presented in Chapter 2 and 3, the filler geometry can be described as thin plates or hexagons, meaning that their elongations are relatively low and their lengths or equivalent diameters are several times larger than their thicknesses. Thus, the fillers can be modelled as thin plates with curved or even edges (six or more faces). However, more intricate geometry makes it more difficult to mathematically solve the proposed model. To start, regular rectangular geometries were used. This means that the projected surface area of the fillers in the model will be approximately 21.8% higher for a given volume fraction (See Section 3.5 in Chapter 3).

The model will be solved using the Finite Element Method. Therefore, meshing will be required to discretise the geometries into small elements to apply linear or polynomial approximations for permeant concentration across the coating (Pryor, 2012). The elements consist of regular or irregular polygons in the case of two dimensions and tetrahedrons and hexahedrons in three-dimensions (Liu & Quek, 2013). Because the elements have regular shapes with flat sides, the mesh has to be refined for surfaces where curved contours are present (Reddy & Gartling, 2010). Figure 5.2 shows that the mesh for a circular contour has to be refined into smaller elements around the circle edge. The rectangular shape geometry does not require that modification. The number of elements in the case of the circular geometry was notably larger than the geometry with rectangular shape (584 and 482 for circle and square shaped geometry respectively). The increment in the number of elements increases the computing time and could impede the mathematical solution of the simulation. In the case of plates with a large number of

faces, such as hexagonal, the increment in elements is lower; however, complex shapes represent a challenge for programming (e.g. ensuring no overlaps between adjacent fillers).

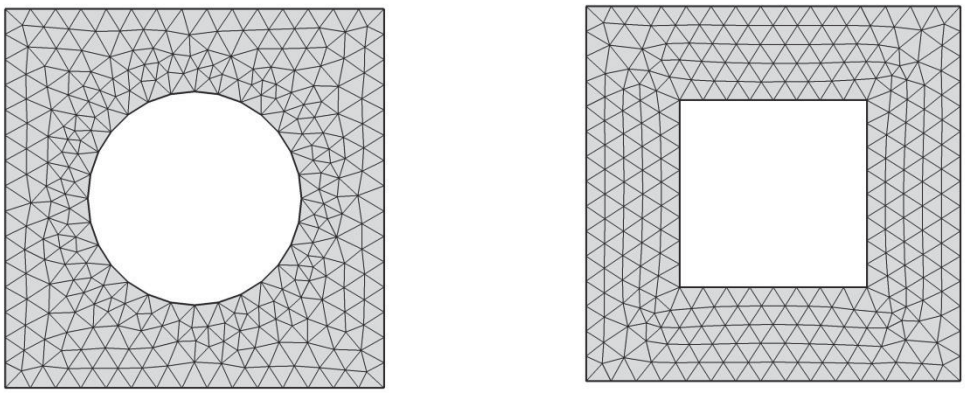

Figure 5.2 Free triangular meshes for circular (584 elements) and rectangular (482 elements) shapes with the same area

5.2.4 Constant coating thickness and even coating surfaces

Barrier dispersion coatings were assumed with even surfaces and constant thicknesses. The reason for these assumptions is related to simplifications of the model. As discussed previously, even geometries are easier to resolve due to the discretisation of the domain which generates a low number of and more regular shaped elements. Taking this into consideration, the calculation of the model is primarily done by relative permeability. In this case, the thickness of the coating does not affect the final results if the coating of both unfilled and filled barriers are the same. After the calculation of the relative permeability and, if it is required, the permeability of the dispersion coating can be calculated based on this calculation and the coating thickness (details of coating thickness in Chapter 4).

5.2.5 Good compatibility between coating binder and fillers

The model assumes that the coating and the fillers are completely compatible. In addition, the properties of coating binder were assumed isotropic. They do not change by the mixing of fillers, only the average properties of the mixing (barrier dispersion coating) change. Coating fillers such as clay, talc calcium carbonate and others are readily compatible with conventional dispersion coatings (Andersson, 2008).

5.2.6 Chemical stability of fillers and non-permeability of the fillers

It was assumed that the fillers are chemically stable and no changes in their properties occur at any stage of the diffusion process. The fillers were assumed to be non-permeable particles and no absorption of permeant is carried out. Kaolin clay, which was used in this study, fulfilled

these assumptions well as it has favourable compatibility with coating binder, low water absorption, and chemical stability (Lehtinen, 2000b).

5.2.7 Perfect dispersion of fillers in the coating:

Complete dispersion of fillers in the coating has been assumed, meaning that the fillers are separated from each other with no agglomeration. This condition is expected in commercial practise to improve the properties of the dispersion coating. It is important to note that the selected fillers are pre-dispersed kaolin clays so as to reduce the risk of agglomeration when they are mixed with the binder. In addition, during the coating preparation stage, the mixing between binder and fillers was agitated long enough to ensure complete dispersion of the fillers. In addition, both the observed pH and viscosity of the dispersion coating before application were consistent with the best laboratory practise for the dispersion of fillers in coating binder and its application on the substrate (Drage & Tamms, 2000; Kimpimäki & Savolainen, 1997).

5.2.8 Parallel orientation of filler with random angle of orientation at the $x - y$ axes

Figure 2.11 of Chapter 2 shows the maximum theoretical angle that fillers can be oriented in a coating formulation. The results indicated that the angle is reduced by increasing the volume fraction and length of the fillers. However, even for low volume fraction of filler and small fillers that angle does not increase significantly. At 5%, which is about the lowest volume fraction for studied coating formulations, the angle is about 15° for fillers with an aspect ratio equal to 50. This angle is reduced to almost a half if the volume fraction is increased up to 10%. Experimentally it is possible to see that the fillers tend to be arranged parallel to the coating surfaces with a slight variation in the angle of orientation between the fillers and the coating surfaces even for low volume fraction of fillers (Figure 5.3). Thus, for simplifying the model development and mathematical solution, the fillers were assumed to be horizontally oriented parallel to the coating surfaces.

When the dispersion coating is applied, a laminar flow is generated due to the low velocity of application and the viscosity of the dispersion. Investigations indicated that the particles, in general, tend to follow the direction of the flow (Bernstein & Shapiro, 1994; Jianzhong, Weifeng, & Zhaosheng, 2004). In dispersion coating this meant that the fillers would be oriented in the coating application direction.

The model assumes that the fillers are located randomly across the coating forming angular orientations from -90º to 90º at the $x - y$ axes. It is possible to see that the fillers are orientated at different angles by observation of the surface of a barrier dispersion coating with a large amount of fillers (Figure 5.4b).

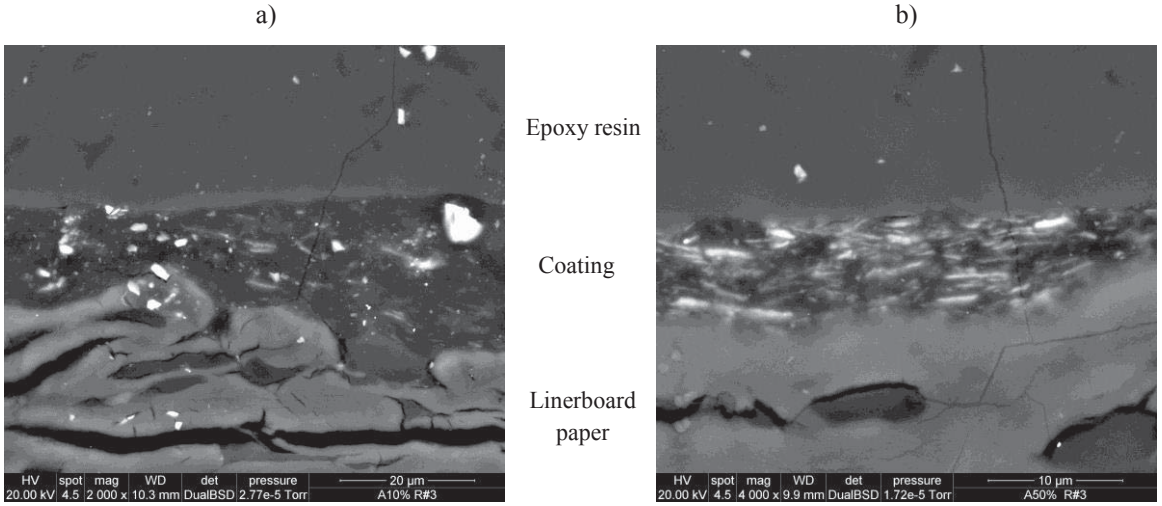

Figure 5.3 SEM cross section images of a barrier dispersion coating filled with Clay A and coated with rod 3 (thin rod) at a) 4.9% and b) 31.7% of volume fraction of fillers (note different scale)

5.2.9 No voids, pinholes and cracks across barrier dispersion coatings

The coating binder was assumed to be continuous with no voids, cracks, or pinholes in its structure. For barrier coatings, the amounts of filler used for all formulations were below the CPVC. Therefore, the volume of coating binder was always larger than the volume of fillers. This condition, in theory, ensures the complete filling of interstitial voids between fillers (Andersson, 2008). From a practical point of view, coating where cracks or pinholes appear are rejected as proper barriers. As shown in Figure 5.3 and Figure 5.4, either for unfilled or filled coatings, no pinholes or cracks were evident. In Figure 5.3 there are vertical cracks; however, these are present in the embedding resin and are not part of the barrier dispersion coatings. It is important to note that Figure 5.4b shows that the surface for coatings filled with Clay A at 31.7% of volume fraction had some bubbles which did not reach the bottom surface of the coating. Thus, these imperfections can be considered as an artefact of sample preparation.

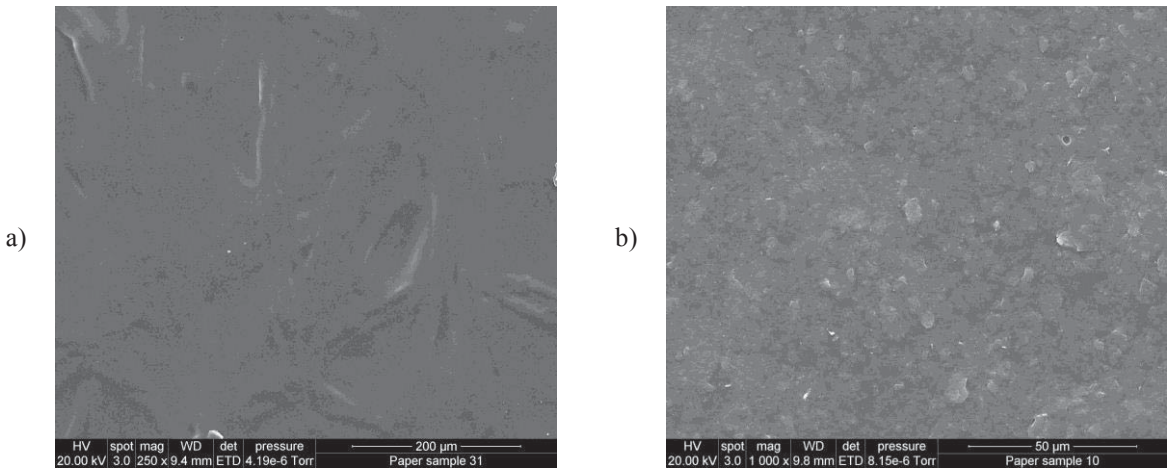

Figure 5.4 SEM images of the top surface of dispersion coatings a) unfilled and b) filled with Clay A at 31.7% of volume fraction of fillers (note different scale)

It is important to note that most of the assumptions such as rectangular shape fillers, horizontal orientation of the fillers, no pores in the coating, non-permeability of fillers and good dispersion of the fillers in the coating describe the best scenario for a barrier dispersion coating. If it is required, the above characteristics can be modified. As an example, agglomeration of the filler in a coating can be represented by increasing the thickness of the fillers.

5.2.10 Independence of the diffusivity to permeant concentration and binder structure

In general, the diffusivity of barriers is considered dependent on the concentration of permeant (Comyn, 1985). In the case of common gases such as N_2, O_2, or CO_2, this dependence can be considered negligible (Robertson, 2013). Other permeants such as organic vapours or more complex molecules such as WV or CO_2 may have stronger interaction with the binder, becoming a permeant concentration dependent process (Robertson, 2013). However, it is reasonable to assume that the concentration dependence of the diffusivity, if it occurs, may be in the same proportion for both filled and unfilled coatings. Therefore, by calculation of the relative permeability (which is the output of this model and its details as presented in the following sections) that effect is cancelled.

As was introduced in the conceptual model (Section 5.1), the coating is represented by a continuous phase with isotropic properties. This depends on the packing of the latex particles after coating formation. If the latex particle packing is different in the coating structure, fluctuations of the diffusivity across the dispersion coating may be observed. Variation of the particle packing may occur at particularly high volume fraction where it is more difficult to encapsulate the fillers and fill void space between them. This may cause deficient contact between latex and fillers and as a result eventual voids around fillers. To simplify mathematical formulation and solution, the model assumed perfect packing of the latex particles and complete contact between latex and the fillers (no voids between latex and fillers).

5.3 Mathematical formulation

As presented in the previous section, the mass transfer occurs in the coating by diffusion and can be defined by Fick's law. Thus, based on the Fick's first law for steady state regimes, it is possible to represent the permeant transfer through the coating for a three-dimensional geometry (Figure 5.1) as shown in Equation 5.1.

$$0 = D \cdot \frac{\partial^2 c}{\partial x^2} + D \cdot \frac{\partial^2 c}{\partial y^2} + \; D \cdot \frac{\partial^2 c}{\partial z^2} \quad , 0 < x < J, \quad 0 < y < M, \quad 0 < x < K \tag{5.1}$$

where

D: Isotropic diffusivity of the coating $(m \cdot s^{-2})$

c: Concentration of the permeant though the coating at (x, y, z) coordinate $(mol \cdot m^{-3})$

J: Length of coating (m)

M: Width of coating (m)

K: Thickness of coating (m)

Because the fillers were assumed to be impermeable particles, there is no diffusive flow through them. Thus, for x, y, x coinciding with the filler, the diffusivity is zero ($D = 0$). Otherwise it is equal to the diffusivity of the binder ($D = D_{binder}$).

To create a driving force for diffusive flux, the concentration of permeant at the top (c_{top}) and the bottom (c_{bottom}) surfaces of the coating were different as shown in Equation 5.2. This results in a diffusive flow from top to bottom surface through the coating.

$$c_{bottom} < c_{top} \quad 0 \leq x \leq J \tag{5.2}$$

$$c = c_{bottom} \quad 0 \leq x \leq J, 0 \leq y \leq M, z = 0 \tag{5.3}$$

$$c = c_{top} \quad 0 \leq x \leq J, 0 \leq y \leq M, z = K \tag{5.4}$$

The edges of the coating were defined with periodic boundary conditions. Thus, the concentration of permeant at a particular edge has to be the same on the opposite edges to maintain the same conditions as above (Equation 5.5 and 5.6)

$$D \cdot \frac{dc}{dx}\Big|_{y=0} = D \cdot \frac{dc}{dx}\Big|_{y=M} \quad 0 \leq z \leq K \tag{5.5}$$

$$D \cdot \frac{dc}{dy}\Big|_{x=0} = D \cdot \frac{dc}{dy}\Big|_{x=J} \quad 0 \leq z \leq K \tag{5.6}$$

The barrier performance of barrier dispersion coatings was calculated as relative permeability based on Equation 2.21 in Chapter 2. This is defined as the ratio between the permeability of a filled coating and the permeability of a reference coating with no fillers (Equation 5.7).

$$\frac{P_f}{P_u} = \frac{TR_f \cdot \frac{x_f}{\Delta p_f}}{TR_u \cdot \frac{x_u}{\Delta p_u}} \tag{5.7}$$

where

P_f: Permeability of filled coatings $\left(mol \cdot m \cdot m^{-2} \cdot s^{-1} \cdot Pa^{-1}\right)$

P_u: Permeability of unfilled coating $(mol \cdot m \cdot m^{-2} \cdot s^{-1} \cdot Pa^{-1})$

TR_f: Transmission rate of permeant for filled coatings $(mol \cdot m^{-2} \cdot s^{-1})$

x_f: Thickness of filled coatings (m)

Δp_f: Partial pressure of permeant for filled coatings (Pa)

TR_u: Transmission rate of permeant for unfilled coating $(mol \cdot m^{-2} \cdot s^{-1})$

x_u: Thickness of unfilled coating (m)

Δp_u: Partial pressure of permeant for unfilled coating (Pa)

The relative permeability does not change if the coating thickness and partial pressure of permeant are equal or different between filled and unfilled coatings. The same coating thickness and partial pressure differences were used for filled and unfilled coatings in model simulations. For this situation, Equation 5.7 can be simplified as the ratio between transmission rates of filled and unfilled coatings (Equation 5.8).

$$\frac{P_f}{P_u} = \frac{TR_f}{TR_u} \tag{5.8}$$

The transmission rate through the filled coating can be calculated by linear integration of the permanent flowrate through the coating at the x-y axis at any z (Equation 5.9). In this work the integration was carried out over the top surface boundary.

$$TR_f = \frac{1}{J \cdot M} \cdot \int_0^M \int_0^J D \cdot \left.\frac{dc}{dz}\right|_{z=K} dx\, dy \tag{5.9}$$

The transmission rate across to the unfilled coating can be directly calculated using the Fick's First Law from the permeant source to the permeant sink in the z axis direction.

$$TR_u = -D \cdot \frac{\left(c_{top} - c_{bottom}\right)}{K} \tag{5.10}$$

To incorporate the effect of the thickness on the barrier properties of coatings, the transmission rate for a particular coating formulation can be calculated using Equation 5.11. This was derived by combination of Equations 5.8 and 5.10.

$$TR_{fk} = \frac{P_f}{P_u} \cdot D \cdot \frac{(c_{top} - c_{bottom})}{K_f} \tag{5.11}$$

where

TR_{fk}: Transmission rate of the permeant through the coating for a particular coating formulation and conditions of exposure ($mol \cdot m^{-2} \cdot s^{-1}$)

K_f: Coating thickness for a particular formulation (m)

The conditions of coating exposure were defined based on the concentration of permeant surround the coating. As was defined in Chapter 4 two permeants were compared; water vapour and oxygen. Water vapour is normally characterised by the relative humidity and not by concentration. However, it is possible to relate the concentration of water vapour and the relative humidity in the ambient at a particular temperature by derivation from the ideal gas law (Equations 5.12).

$$c_{wv} = \frac{p_v}{R \cdot (273.15 + \theta)} \tag{5.12}$$

where

c_{wv}: Concentration of water vapour at either bottom or top coating surface ($mol \cdot m^{-3}$)

p_v: Current partial pressure at either bottom or top surface of the coating (Pa)

R: Ideal gas constant ($8.314\ J \cdot mol^{-1} \cdot K^{-1}$)

θ: Exposure temperature at either bottom or top coating surface ($°C$)

The current partial pressure is proportional to the partial pressure at saturation at a given relative humidity (Equation 5.13).

$$p_v = p_{vs} \cdot RH \tag{5.13}$$

where

p_{vs}: Partial pressure at saturation at either bottom or top side of the coating (Pa)

RH: Relative humidity at either bottom or top coating surface

A number of models have been developed to predict p_{vs} at different ranges of temperature and accuracy (ASHRAE, 2013; Riegel, 1974; Wilhelm, 1976). For this model, the expression

proposed by ASHRAE (2013) was used to determine p_{vs} in a range from 0° to 200 °C (Equation 5.14).

$$p_{vs} = exp\left[\frac{C_8}{(273.15+\theta)} + C_9 + C_{10}\cdot(273.15+\theta) + C_{11}\cdot(273.15+\theta)^2 + C_{12} \cdot(273.15+\theta)^3 + C_{13}\cdot ln(273.15+\theta)\right] \quad (5.14)$$

where

C_8: $-5.800\,220\,6 \times 10^3$

C_9: $1.391\,499\,3$

C_{10}: $-4.864\,023\,9 \times 10^{-2}$

C_{11}: $-4.176\,476\,8 \times 10^{-5}$

C_{12}: $-1.445\,209\,3 \times 10^{-8}$

C_{13}: $-6.545\,967\,3$

Unlike water vapour, the concentration of oxygen is normally well known and expressions for calculation of the amount of oxygen in the ambient are not required. For example, the percentage of oxygen in ambient air is around 21% of the total volume. In the case of experiments, the oxygen is normally supplied by standardised sources where the concentration of the gas has been carefully measured.

5.4 Definition of the dispersion coating geometry

Due to the elongated shape and simplicity for modelling, the fillers were assumed to be rectangular plates. Comparison between shapes and methods to describe the shape of fillers, were presented in Sections 3.3 and 3.5 in Chapter 3. The volume fraction of filler was estimated as the ratio between the volume of fillers in the coating and the total volume of the coating geometry defined based on the relative elemental volume (REV). In the case of the fillers, the estimation of volume can be carried out based on the filler size and shape factors defined in Chapter 3; length, thickness, aspect ratio, elongation and area. The assumption of plates shaped fillers requires the definition of the largest length, the breadth length, and the thickness of the fillers in order to draw the geometry. Because the breadth was not explicitly characterised, it has to be estimated from other shape parameters such as area or elongation. Thus, by using a combination of different shape parameters, the volume of the fillers can be calculated Figure 5.5 shows the distribution of the volume of fillers from different relationships.

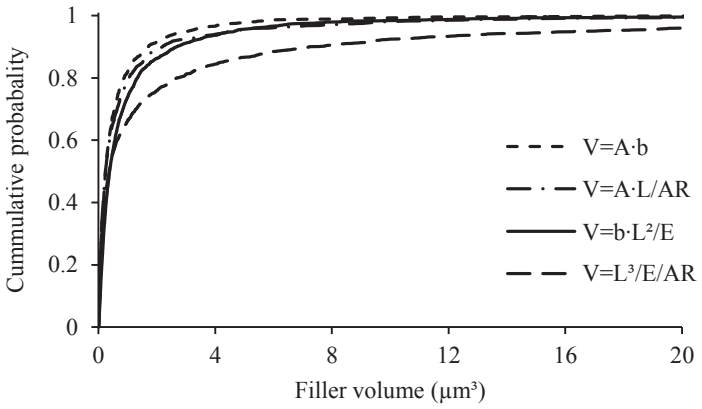

Figure 5.5 Distribution of filler volume (V) calculated by different combination of shape parameters where A is area, b is thickness, L is length, E is elongation, and AR aspect ratio of fillers

The distributions of filler volume indicate that the calculation is affected by how the different shape descriptors were combined to define the volume of the fillers (Figure 5.5). The smallest volume of fillers was observed by the combination of area and thickness of fillers. This is expected because this distribution has been defined by experimental data and the assumption of plate shaped fillers does not interfere with the calculation. However, it is important to note that due to the assumed shape of the fillers for modelling, both the length and thickness of the fillers are required. For this distribution ($V = A \cdot b$), the length can be defined as a combination of area and the elongation of the fillers. Figure 5.6 shows that the estimated filler length by area and elongation is shorter than the observed length distribution. This discrepancy may reduce the volume of the fillers increasing the their number in the coatings.

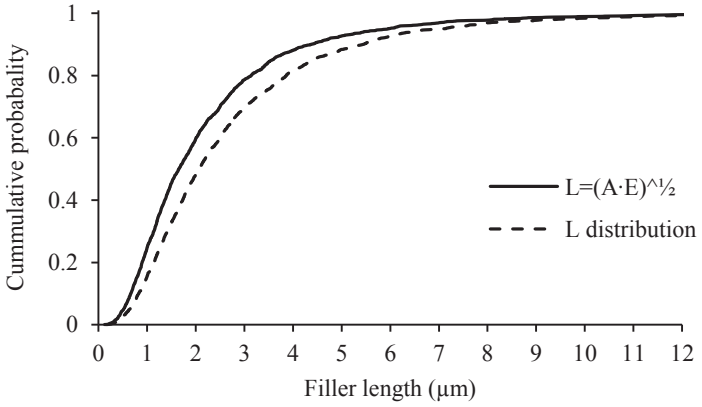

Figure 5.6 Length distribution of fillers experimentally observed (L distribution) and estimated from the area and elongation distributions of fillers

Figure 5.5 also shows that the estimation of filler volume by combinations of area-length-aspect ratio and length-elongation-thickness were similar and the calculation by length-elongation-

aspect ratio was larger than the other estimations. The use of aspect ratio and elongation may explain the large projected volume distribution. These two shape factors were approximated by calculation and not experimentally measured. The aspect ratio was calculated based on measurement of length and thickness from two different experiments. In the case of the elongation, the estimation was based on the ratio between the largest and longest semi-axis of the best fitted ellipse. It is important to note that the calculation of elongation was carried out on each filler particle. As a result this approximation represents a closer reality compared to the aspect ratio which was defined from distributions obtained in two independent experiments.

Based on the discussion above, the fillers were defined as a function of the distributions of length, elongation, and thickness. These parameters were used to generate a database of 20,000 fillers for each of the selected clays. From the databases, a number of fillers were randomly taken to be used for coating geometry generation according to type and volume fraction of the fillers required. The number of fillers had to agree with the following equation.

$$\emptyset_F \leq \frac{1}{J \cdot M \cdot K} \cdot \sum_{i=1}^{N} \frac{L_i^2 \cdot b_i}{E_i} \tag{5.15}$$

where

$\emptyset_F$: Volume fraction of fillers

L_i: Length of the *i* filler (m)

b_i: Thickness of the *i* filler (m)

E_i: Elongation of the *i* filler

N: Number of fillers for coating definition

As presented in Chapter 3, the length and thickness of the fillers follow the Log-normal distribution. Thus, the parameters that define these functions are required for the simulation (Equation 3.2 and 3.3)

$$F(x_f; \mu_f, \sigma_f) = \int_{x_{min}}^{x_{max}} f(x_f; \mu_f, \sigma_f) dx_f \tag{3.2}$$

$$f(x_f; \mu_f, \sigma_f) = \frac{1}{x_f \cdot \sigma_f \cdot \sqrt{2\pi}} \cdot exp\left[-\frac{(\ln x_f - \mu_f)^2}{2 \cdot \sigma_f^2}\right] \quad , \qquad x_f > 0 \tag{3.3}$$

where

μ_f: Average of the logarithm of length(m) or thickness (m) of the fillers

σ_f: Standard deviation of the logarithm of length(m) or thickness (m) of the fillers

x_f: Length (m) or thickness (m) of the fillers at a particular probability

$F(x_f; \mu_f, \sigma_f)$: Cumulative distribution function of the length or thickness of fillers

$f(x_f; \mu_f, \sigma_f)$: Probability density function of the length or thickness of fillers

x_{max}: Maximum length (m) or thickness (m) of the fillers at a particular probability

x_{min}: Minimum length (m) or thickness (m) of the fillers at a particular probability

The generalised extreme value distribution was found to best represent the elongation of fillers (Section 3.3 in Chapter 3). Equations 3.4 and 3.5 showed that expression in terms of cumulative and density functions respectively.

$$F(x_e; \mu_e, \sigma_e, k_e) = exp\left\{-\left[1 + k_e \cdot \left(\frac{x_e - \mu_e}{\sigma_e}\right)\right]^{-1/k_e}\right\}, \quad 1 + \frac{k \cdot (x_e - \mu_e)}{\sigma_e} > 0 \tag{3.4}$$

$$f(x_e; \mu_e, \sigma_e, k_e) = \frac{1}{\sigma_e} \cdot \left[1 + k_e \cdot \left(\frac{x_e - \mu_e}{\sigma_e}\right)\right]^{(-1/k_e)-1} exp\left\{-\left[1 + k_e \cdot \left(\frac{x_e - \mu_e}{\sigma_e}\right)\right]^{-1/k_e}\right\} \tag{3.5}$$

where

x_e: Elongation of the filler

μ_e: Location parameter

σ_e: Scale parameter

k_e: Shape parameter

Uniformly distributed pseudorandom numbers from 0 to 1 were chosen to define the cumulative distribution functions for length, elongation, and thickness of the fillers.

The defined fillers were then located in the coating with parallel orientation to the coating surfaces and random rotation angles at the x-y axis from -90° to 90°. To do this, several factors were considered. The fillers do not cross the top and bottom coating surfaces. Fillers that overlapped the lateral boundaries were copied and located in the opposite edge to keep the required volume fraction and the periodic conditions of the boundaries (Figure 5.7 case 1). For cases where the fillers were located at a corner of the coating, the fillers were copied 3 times and the new fillers were located at the other three corners (Figure 5.7 case 2).

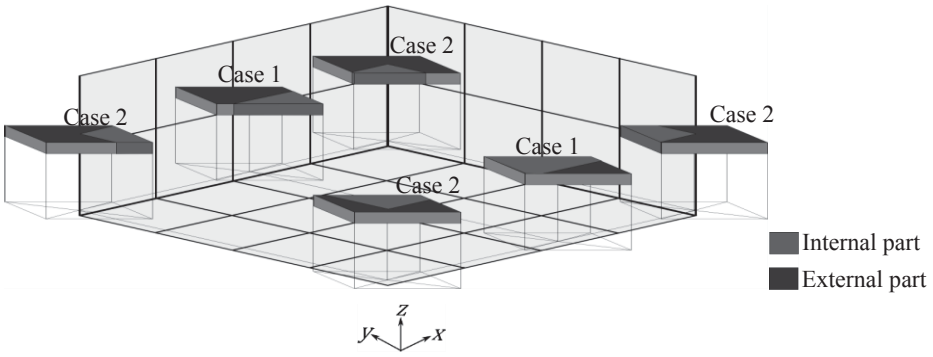

Figure 5.7 Random distribution of fillers in a coating using a grid and example of relocation of fillers into the coating geometry; Case 1: Filler is over an edge; Case 2: Filler is over a corner ($nx_i = 4$, $ny_i = 4$, and $nz_i = 2$)

To ensure, facilitate, and reduce the computing time for a good distribution of fillers, the coatings were divided into grids (Figure 5.7). Inside each grid, the centres of fillers were randomly defined and, from this point, the fillers were drawn. The definition of the grid was based on the number of fillers in the coating binder. In this way, an initial number of elements was assigned based on the division of the coating in equally spaced segments through each axis. The initial number of segments were called nx_i, ny_i, and nz_i for x, y, and z axes respectively. If the initial number of elements was lower than the number of filler (N), the number of segments in the x and y axes was increased one by one unit until a number of elements equal or larger than the number of fillers was achieved (Equation 5.20). For cases where the number of elements was larger than the number of fillers, the elements were randomly chosen leaving the remaining grid element with no fillers.

$$N \geq \sum_{j=0}^{n} (nx_i + j) \cdot (ny_i + j) \cdot nz_i \tag{5.16}$$

To avoid overlapping between fillers, the contour of the fillers was observed from $x - y$ axes, $x - z$ axes, and $y - z$ axes and compared to the other fillers to identify possible overlapping (Figure 5.8a and b). To check for overlapping, the projected faces of the fillers were defined as rectangles. The corners of the observed face were compared with the other faces by dividing the other faces into a number of points (Figure 5.8c). If the observed corner is around some of these points, the face is overlapped to the other. Thus, if the filler overlapped in two or more of the three views, the fillers overlapped and would be relocated randomly into the same grid element. In cases where the filler had been unsuccessfully relocated more than 20 times and empty elements were available, the filler was relocated into another element.

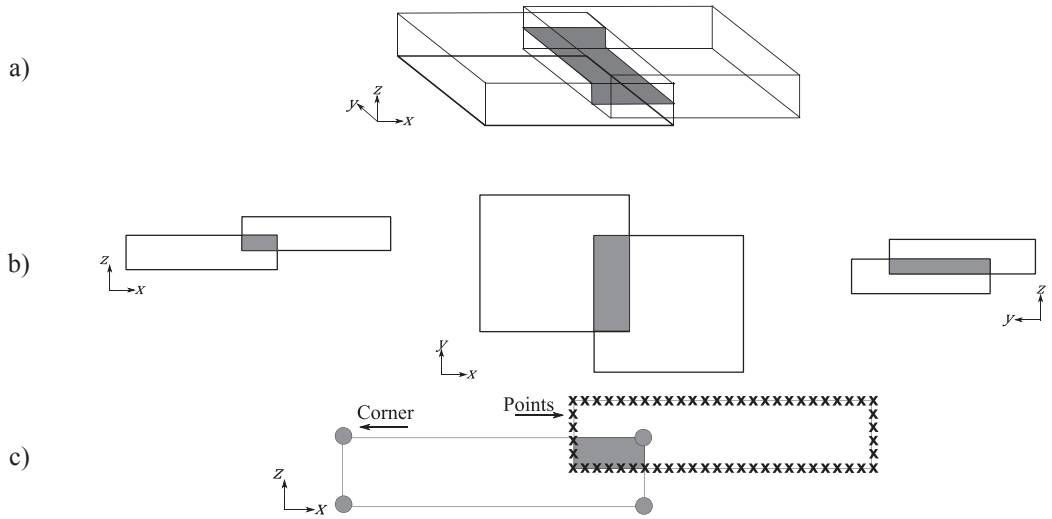

Figure 5.8 Scheme of checking for overlapping of fillers a) two overlapping fillers b) projection of the filler faces, c) discretisation of the filler edges for identification of overlapping

The complete processes of mathematical formulation and generation of barrier dispersion coating geometry were carried out by Matlab programming. The information above was exported into Comsol Multiphysics for mathematical solution by Finite Element Method (FEM). Figure 5.9 shows a final geometry created by Matlab based on the above specifications. Figure 5.10 shows a diagram of how the geometry generation process was carried out. Details of the program operation are included in Appendix F.

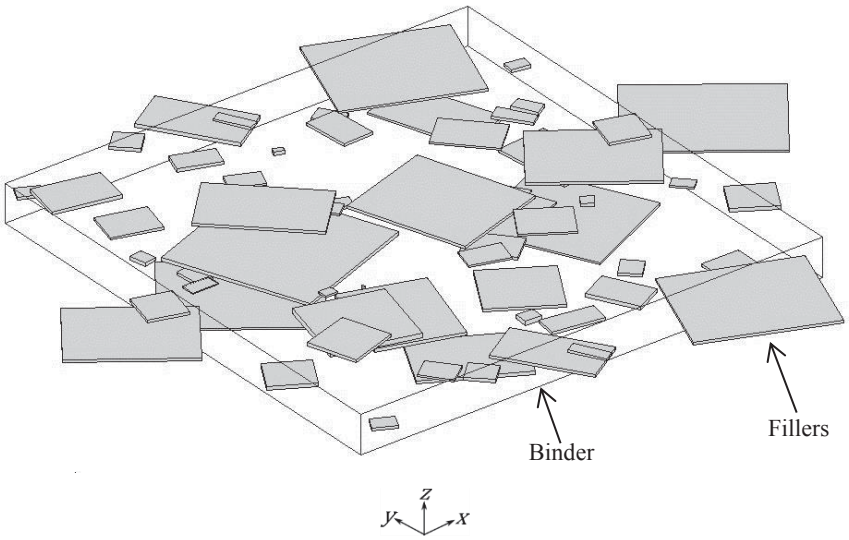

Figure 5.9 Example of a distribution of fillers in the coating binder

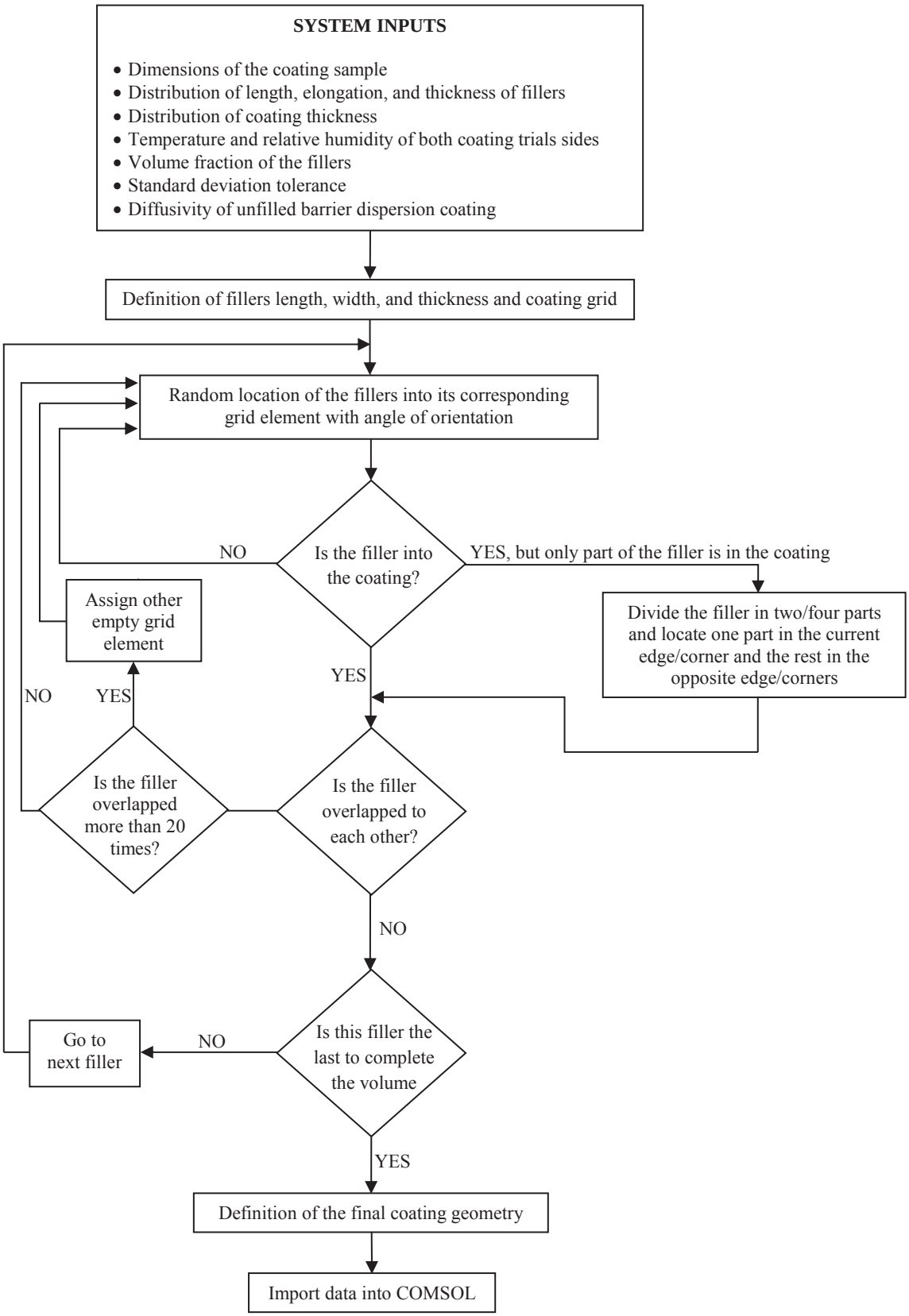

Figure 5.10 Diagram of the Matlab model architecture to predict the permeability of barrier dispersion coatings

5.5 Assigned variables of the model

The variables defined in the model formulation are summarised in Table 5.1

Table 5.1 List of model variables

Symbol	Description	Unit	Class*
c	Concentration of the permeant though the coating at (x, y, z) coordinate	$mol \cdot m^{-3}$	D
D	Isotropic diffusivity of the coating	$m \cdot s^{-2}$	S.I.
J	Length of coating	m	S.I.
M	Width of coating	m	S.I.
K	Thickness of coating	m	S.I.
x	x-axis position	m	I
y	y-axis position	m	I
z	z-axis position	m	I
c_{bottom}	Concentration of permeant at the bottom surface of the paper	$mol \cdot m^{-3}$	C.V.
c_{top}	Concentration of permeant at the top surface of the coating	$mol \cdot m^{-3}$	C.V.
P_f	Permeability of filled coatings	$mol \cdot m \cdot m^{-2} \cdot s^{-1} \cdot Pa^{-1}$	C.V.
P_u	Permeability of unfilled coating	$mol \cdot m \cdot m^{-2} \cdot s^{-1} \cdot Pa^{-1}$	C.V.
TR_f	Transmission rate of permeant for filled coatings	$mol \cdot m^{-2} \cdot s^{-1}$	C.V.
TR_u	Transmission rate of permeant for unfilled coating	$mol \cdot m^{-2} \cdot s^{-1}$	C.V.
TR_f	Transmission rate of the permeant through the coating for a particular coating formulation and conditions of exposure	$mol \cdot m^{-2} \cdot s^{-1}$	C.V.
K_f	Coating thickness for a particular formulation	m	S.I.
c_{wv}	Concentration of water vapour in the ambient	$mol \cdot m^{-3}$	C.V.
p_v	Current partial pressure	Pa	C.V.
p_{vs}	Partial pressure at saturation	Pa	C.V.
C_8	Constant for calculation of partial pressure at saturation of the air		S.I.
C_9	Constant for calculation of partial pressure at saturation of the air		S.I.
C_{10}	Constant for calculation of partial pressure at saturation of the air		S.I.
C_{11}	Constant for calculation of partial pressure at saturation of the air		S.I.
C_{12}	Constant for calculation of partial pressure at saturation of the air		S.I.
C_{13}	Constant for calculation of partial pressure at saturation of the air		S.I.
R	Ideal gas constant	$J \cdot mol^{-1} \cdot K^{-1}$	S.I.

θ	Exposure temperature of the dispersion coatings	$°C$	S.I.
RH	Relative humidity at each sides of the coated paper	%	S.I.
$\emptyset_F$	Volume fraction of fillers		S.I.
N	Number of fillers for coating definition		C.V.
L_i	Length of the *i* filler	m	C.V.
b_i	Thickness of the *i* filler	m	C.V.
E_i	Elongation of the *i* filler		C.V.
$F(x_f; \mu_f, \sigma_f)$	Cumulative probability of length or thickness of the fillers		C.V.
$f(x_f; \mu_f, \sigma_f)$	Density probability of length or thickness of the fillers		C.V.
x_f	Length or thickness of the fillers at a particular probability	m	C.V.
σ_f	Standard deviation of the logarithm of length or thickness of the fillers	m	S.I.
μ_f	Average of the logarithm of length or thickness of the fillers	m	S.I.
x_{max}	Maximum length or thickness of the fillers at a particular probability	m	S.I.
x_{min}	Minimum length or thickness of the fillers at a particular probability	m	S.I.
$F(x_e; \mu_e, \sigma_e, k_e)$	Cumulative probability of the elongation of fillers		C.V.
$f(x_e; \mu_e, \sigma_e, k_e)$	Density probability of the elongation of fillers		C.V.
x_e	Elongation of the filler		S.I.
μ_e	Location parameter		S.I.
σ_e	Scale parameter		S.I.
k_e	Shape parameter		S.I.
nx_i	Initial number of segments of coating grid through x-axis		S.I.
ny_i	Initial number of segments of coating grid through y-axis		S.I.
nz_i	Initial number of segments of coating grid through z-axis		S.I.

* I: independent variable, D: dependent variable, C.V.: consequential variable, S.I.: system input

5.6 Size of the dispersion coating geometry

The generation of the coating geometries for modelling was focused on the coating structure after the drying process. The estimation of the coating dimensions was based on the calculation of a representative elemental volume (REV). The REV is used to describe a volume of a heterogeneous material that is sufficiently large to be representative of the composite, i.e., to effectively include a sampling of all microstructural heterogeneities that occur in the composite (Kanit, et al., 2003). In terms of modelling, the REV is the smallest volume which is sufficiently accurate to model a representative mean constitutive response (Drugan & Willis, 1996).

The definition of the REV was based on three coating geometries larger than the expected REVs. These geometries had the same length and width ($150 \times 150\,\mu m$) and only the thicknesses were different (1 μm, 2 μm and 3 μm for each geometry respectively). From those geometries, small sections were taken and their volume fractions were calculated. The size of the sections was progressively increased until a steady filler volume fraction equal to the original large coating geometries was reached. This size was considered as the REV. The volume fraction was selected as a parameter of comparison because it is one of the main system inputs of the model and also involves the number of fillers in the coating geometry.

The estimation of the REV size was carried out on the worst case scenario for modelling. In this case, coating formulated with Clay A at 4.9% volume fraction was chosen as reference. This combination produces the lowest number of fillers for a given geometry size. Thus, the possibility of different filler arrangement in the coating becomes larger than other coating formulations. From this it is possible to infer that if the REV is representative for the worst case scenario, it is also representative for the other coating formulations.

Figure 5.11 shows the final volume fraction of filler and its standard deviation achieved by REVs. The trend showed that the volume fraction became closer to the reference as the size of the smaller geometries increased. As the size increased, the variation in the results was lower. The major reduction in variation of volume fraction of fillers was observed between 5 and 7.5 μm. From this size range, the average volume fraction of fillers became very close to the expected. The variation of volume fraction from this point seemed to be at a lower rate. It is reasonable to defined the size of the REV by $10 \times 10 \times 2\,\mu m^3$. This size showed to close to the expected volume fraction of filler (4.9%) with low standard deviation. It is important to note that the larger sizes of the geometries are more time consuming and computer demanding. Thus, the reduction in the variability by increasing the size of the geometry may be computationally expensive. It was reasonable to assume that the definition of the geometries size has to be in a balance among low variability, good prediction, and low computer requirement. For this reason, geometry size of 10 μm for J and M was selected.

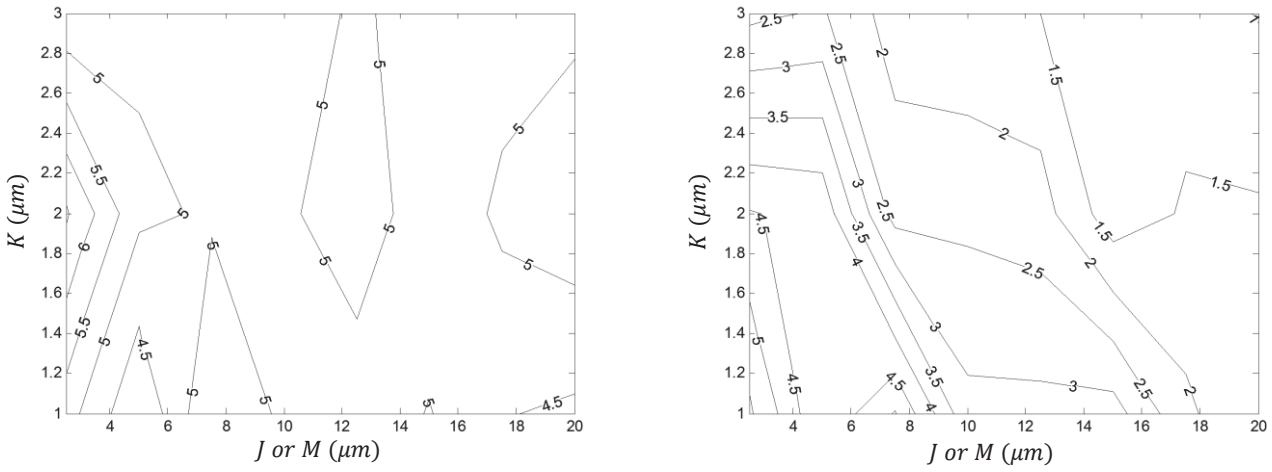

a) b)

Figure 5.11 a) Final volume fraction of fillers (%v/dv) and b) its standard deviation (%v/dv) as a function of the size of the REV filled with Clay A at 4.9% of filler volume fraction (%v/dv)

5.7 Conclusion and discussion

According to the proposed model, the performance of barrier dispersion coating can be modelled based on diffusion as the mechanism of mass transfer. The characteristics of fillers and coatings, and the conditions of coating exposure were the key attributes for the development of the model. A series of assumptions were taken into consideration to simplify and enable the mathematical solution of the model.

The main equation of the mathematical formulation was based on the Fick's First law, to determine the concentration of permeant at any particular coordinates inside the barrier dispersion coating. The calculation of the coating binder dimensions was based on the estimation of REVs. The size of REV should not be smaller than 10 μm of length and width in order to be representative of all the coating formulations. In the case of the fillers, the combination of length, elongation and thickness was the best for characterisation of the filler shape. The fillers were randomly located into the coating based on a grid, where each filler centroid was placed inside a grid element avoiding overlapping with other fillers.

The geometries are generated by programming in Matlab language under particular conditions of coating geometry and exposure. The generated geometries are saved for further mathematical solution. In Chapter 6, a description of how the model was resolved by Finite Element Method in Comsol Multphysics and the results will be validated. In addition, further sensitive analysis of the predictions will be carried out in Chapter 7.

Chapter 6

MATHEMATICAL SOLUTION AND VALIDATION

Chapter 5 outlined the development of a steady state mathematical model for prediction of permeant transport through a three dimensional representation of a barrier coating containing filler particles. Methods to generate geometries based on the distributions of size and characterised in Chapter 3 and 4 were also development using Matlab. This chapter outlines the solution of the model proposed in Chapter 5 by Finite Element Method (FEM). Experiments presented in Chapter 3 were used to define the system inputs related to the filler characterisation. The measurements of WVTR presented in Chapter 4 were used to evaluate the accuracy the model. The model was validated for three different fillers volume fractions for all three of the fillers selected in Chapter 3. Differences between modelling and experimental data were evaluated and possible reasons were proposed.

6.1 Mathematical solution of the model by Finite Element Method (FEM)

The mathematical solution was carried out by FEM and solved by Comsol Multiphysics. Comsol Multiphysics is a solution engine for FEM and partial differential equations or PDEs (Pryor, 2012). A number of modules are available to describe different application areas. These modules include physical and chemical principles with their equations already included for modelling. The software provides different tools to define all the required parameters for FEM modelling such as mesh creation, boundary condition definition, numerical solvers, and analysis of the results. It is also compatible with Matlab, providing an easy way to transfer information regarding the coating geometry written in Matlab code to Comsol Multiphysics for FEM solution.

In this model, the "transport of diluted species" module under steady state conditions was used as the basis of modelling. This module was created to study the evolution of chemical species transported by diffusion, governed by Fick's law (Comsol, 2013). The coating geometry was developed based on an unfilled binder with a fixed thickness (K), length (J), and width (M). The fillers were located randomly inside the binder as presented in Chapter 5. The entire geometry was transformed into an active geometrical space or "domain" where all the calculations were carried out. The domain was created by a Boolean operation of subtraction between the binder and the fillers. The subtraction kept only the binder volume and the fillers were represented as

voids with no permeation through them and, as a result, diffusive flow of permeant occurred only through the binder (Figure 6.1).

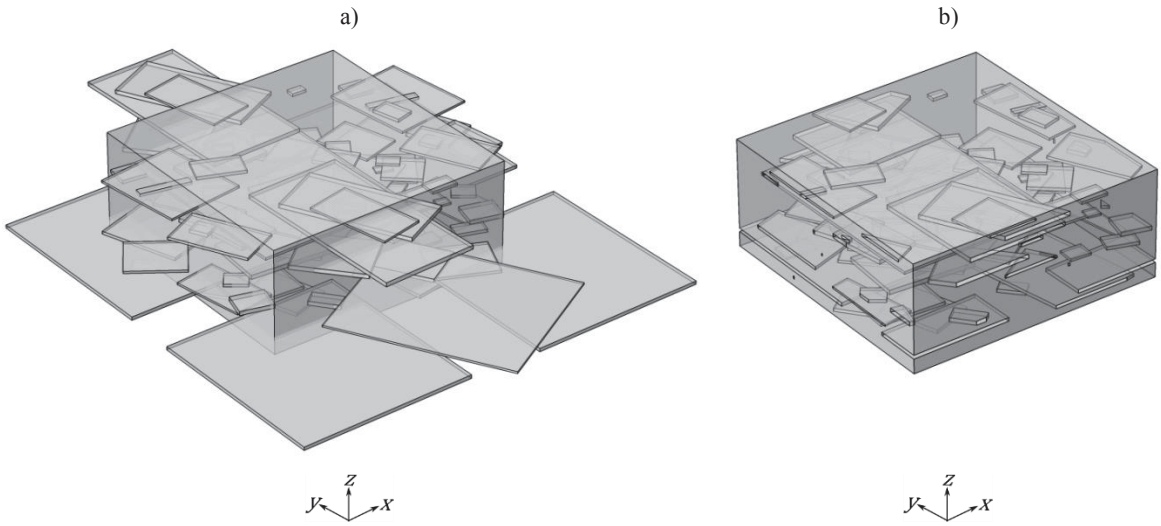

Figure 6.1 Coating geometry a) before and b) after Boolean operation

It is important to note that simulations were not required for the case of unfilled coating. Instead, the permeant flux was estimated directly by Fick's First law (Equation 5.10 in Chapter 5). For this, the same conditions were used as for the simulation of relative the permeability of filled coatings (D, c_{top}, c_{bottom}, K).

From the defined domain, the boundary conditions of the model were established. The temperature of the simulations was assumed to be at 23°C and the relative humidity was considered 0% on the bottom surface of the coating and 50% on the top surface of the coating. The concentration of the permeant on the surface of the dispersion coating can be estimated using Henry's law (Equation 6.1).

$$c = s \cdot p \tag{6.1}$$

where

- c: Concentration of permeant on the surface of the dispersion coating ($mol \cdot m^{-3}$)
- s: Solubility of the permeant ($mol \cdot m^{-3} \cdot Pa^{-1}$)
- p: Partial pressure of the permeant (Pa)

The solubility is a temperature dependent parameter that can be described by an Arrhenius equation. van Krevelen and te Nijenhuis (2009) presented an approximation for calculation of solubility (Equations 6.2, 6.3, and 6.4).

$$\ln\big(s(\theta)\big) = \ln\big(s(25°C)\big) - 0.4343 \cdot \frac{\Delta H_S}{R}\left(\frac{1}{\theta + 273} - \frac{1}{298}\right) \tag{6.2}$$

$$\ln\big(s(25°C)\big) = -7.0 + 0.010 \cdot \frac{\varepsilon}{k} \pm 0.25 \tag{6.3}$$

$$\frac{\Delta H_S}{R} = \left(1.0 - 0.001 \cdot \frac{\varepsilon}{k} \pm 0.5\right) \times 10^{-3} \tag{6.4}$$

where

θ: Temperature ($°C$)

ΔH_S: Heat of solution ($J \cdot mol^{-1}$)

R: Ideal gas constant ($J \cdot mol^{-1} \cdot K^{-1}$)

$\frac{\varepsilon}{k}$: Lennard-Jones temperature (K)

The values of the Lennard-Jones temperature (ε/k) were tabulated in the literature and were 93 K and 809 K for oxygen and water vapour respectively (van Krevelen & te Nijenhuis, 2009). The partial pressure of the permeant can be estimated by Equations 5.13, and 5.14 introduced in Section 5.3 in Chapter 5. As well as the solubility, the diffusivity is dependent on the temperature and the Arrhenius equation can be used to estimate it. The diffusivity can be estimated by the approximation presented in Equations 6.5, 6.6, and 6.7 (van Krevelen & te Nijenhuis, 2009).

$$\ln\big(D(\theta)\big) = \ln\big(D(25°C)\big) - 0.4343 \cdot \frac{E_D}{R}\left(\frac{1}{\theta + 273} - \frac{1}{298}\right) \tag{6.5}$$

$$\ln\big(D(25°C)\big) = -8.0 - 0.457 \times 10^{-3} \cdot \frac{E_D}{R} \tag{6.6}$$

$$\frac{E_D}{R} = \left(\frac{\sigma_x}{\sigma_{N_2}}\right)^2 \cdot \left[6.4 \times 10^3 - 0.16 \cdot \big(25 - T_g\big)^2\right] \pm 1.5 \times 10^3 \tag{6.7}$$

where

D: Diffusivity ($m^2 \cdot s^{-1}$)

E_D: Activation energy of diffusion ($J \cdot mol^{-1}$)

$\frac{\sigma_x}{\sigma_{N_2}}$: Ratio of the collision diameter of the permeant and nitrogen

T_g: Glass transition temperature of the coating ($°C$)

van Krevelen and te Nijenhuis (2009) indicated that the value of $\left(\sigma_x/\sigma_{N_2}\right)^2$ was 0.83 and 0.48 for oxygen and water vapour, respectively. The glass transition temperature of the coating was assumed the same as the pure latex (2 °C in Table 4.1 in Chapter 4). It is important to note that

above the approach is a broad approximation of the diffusivity and solubility of the dispersion coating. However, the accuracy of those parameters was not critical during simulation as they were cancelled during calculation of relative permeability as long as the same boundary conditions (driving force) were applied. A similar process was presented in Chapter 5 Section 5.3.

Periodic boundary conditions were assigned for lateral borders of the coating meaning that the diffusive flow will be the same (but opposite) over the borders at the $y-z$ axes at $x = 0\ \mu m$ and $x = J\ \mu m$ and those at the $x-z$ axes where $y = 0\ \mu m$ and $y = M\ \mu m$.

The domain was meshed, dividing it into sufficiently smaller spaces that approximations can be used as a reasonable analogue of the functional physical behaviour being modelled (Pryor, 2012). Free triangular shaped meshing was used to divide the surfaces of fillers and the coating. The binder was meshed by free tetrahedral shaped meshing. The free meshing generates mesh elements with fixed sizes according to the complexity of the geometry. The mesh elements were finer for the lateral borders of the fillers and for small gaps between filler particles. Coarser mesh elements were defined for the rest of the coating geometry. Refinement of the mesh was carried out during meshing preparation to ensure proper discretisation of the geometry. Figure 6.2 shows the final mesh for the fillers surfaces.

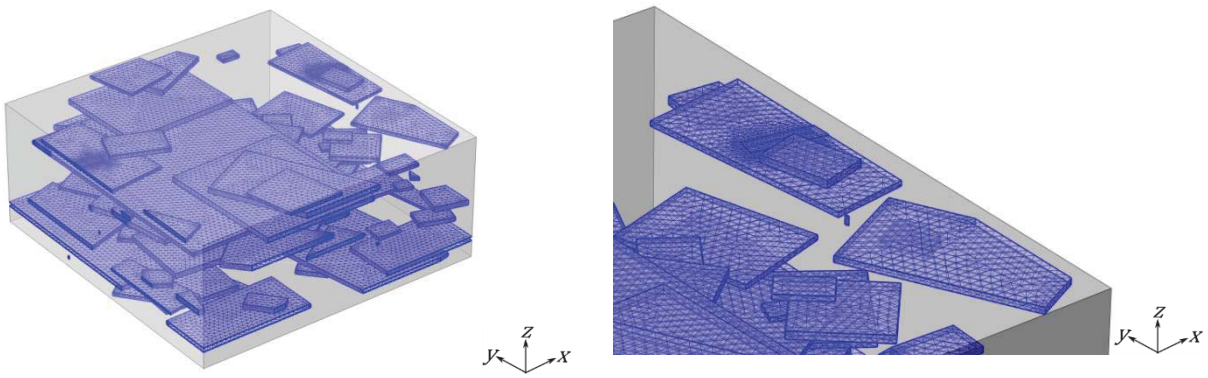

Figure 6.2 Mesh of filler surface including a closer view of the meshing at width of the filler and gap between filler particles

From the above considerations, the concentration of permeant across the coating geometry was predicted based on Equation 5.1 and the diffusive flux was estimated by Equation 5.9, both presented in Chapter 5. The model was solved using Comsol Multiphysics version 4.3b installed in a PC Intel® Core ™ i5-2400 CPU, 3.10 GHz with 16 GB of RAM.

It is important to consider that the number of the elements in the mesh is directly related to the accuracy of the result. A large number of elements however would be computationally expensive (Fagan, 1992; Zimmerman, 2004). To prove that the mesh of the model provided consistent results, the diffusive flow was calculated using the top and bottom coating surfaces and the transmission rate was estimated using both diffusive fluxes. In theory, the diffusive flux at the top and bottom coating surfaces must be the same; however, due to the discretisation of the domain, differences could be found. For this reason, as shown in Equation 6.8, the difference between the transmission rate at the bottom and top coatings surface was kept lower than 1% to keep numerical error low (Goodyer & Bunge, 2009).

$$\frac{\left|TR_f\big|_{z=0} - TR_f\big|_{z=K}\right|}{TR_f\big|_{z=0}} < 1\% \tag{6.8}$$

where

$TR_f\big|_{z=0}$: Transmission rate of the coating at $z = 0\ \mu m$

$TR_f\big|_{z=K}$: Transmission rate of the coating at $z = K\ \mu m$

For cases where the above condition was not achieved, the model mesh was either refined or the geometry was rejected and a new coating was generated. The refinement of the mesh increases the number of elements. As a result, eventually the geometry could not be solved due to limitations of computational resources available.

The relative permeability was calculated as the ratio between the diffusive flux of filled and unfilled coatings (Equation 5.8). The diffusive flux for unfilled coatings was estimated by Equation 5.10 taking into consideration the same conditions for the estimation of diffusive flux for filled coatings.

6.2 Estimation of the required number of geometries to represent barrier dispersion coating performance

Monte Carlo analysis was carried out to predict barrier coating performance. Each simulation used a different geometry with particles chosen from their distributions and randomly placed into to coating. Due to the randomised location of the fillers in the coating geometries, it is possible to achieve different barrier properties between simulations even if the filler concentrations in the geometry of the coating are constant. For this reason, a certain number of geometries were needed to properly represent a particular barrier coating formulation. To satisfy this requirement, the number of geometries had to be enough to keep the average and the

standard deviation of predictions constant and with a maximum variation of 1% compared to the previous five predictions (Equation 6.9 and 6.10).

$$\frac{|sd_n - sd_{max}|}{sd_n} \leq 1\% \tag{6.9}$$

$$\frac{|\overline{X_n} - \overline{X_{max}}|}{\overline{X_n}} \leq 1\% \tag{6.10}$$

where

sd_n: Standard deviation of the relative permeability at iteration n

X_n: Average of the relative permeability at iteration n

sd_{max}: Maximum standard deviation of the relative permeability for the previous five estimations of the relative permeability

X_{max}: Maximum average of the relative permeability for the previous five estimations of the relative permeability

A range of between 30 and 40 iterations was found to be sufficient to meet these criteria for every fillers volume fraction and type of filler simulated.

A summary of the model solution process is presented below.

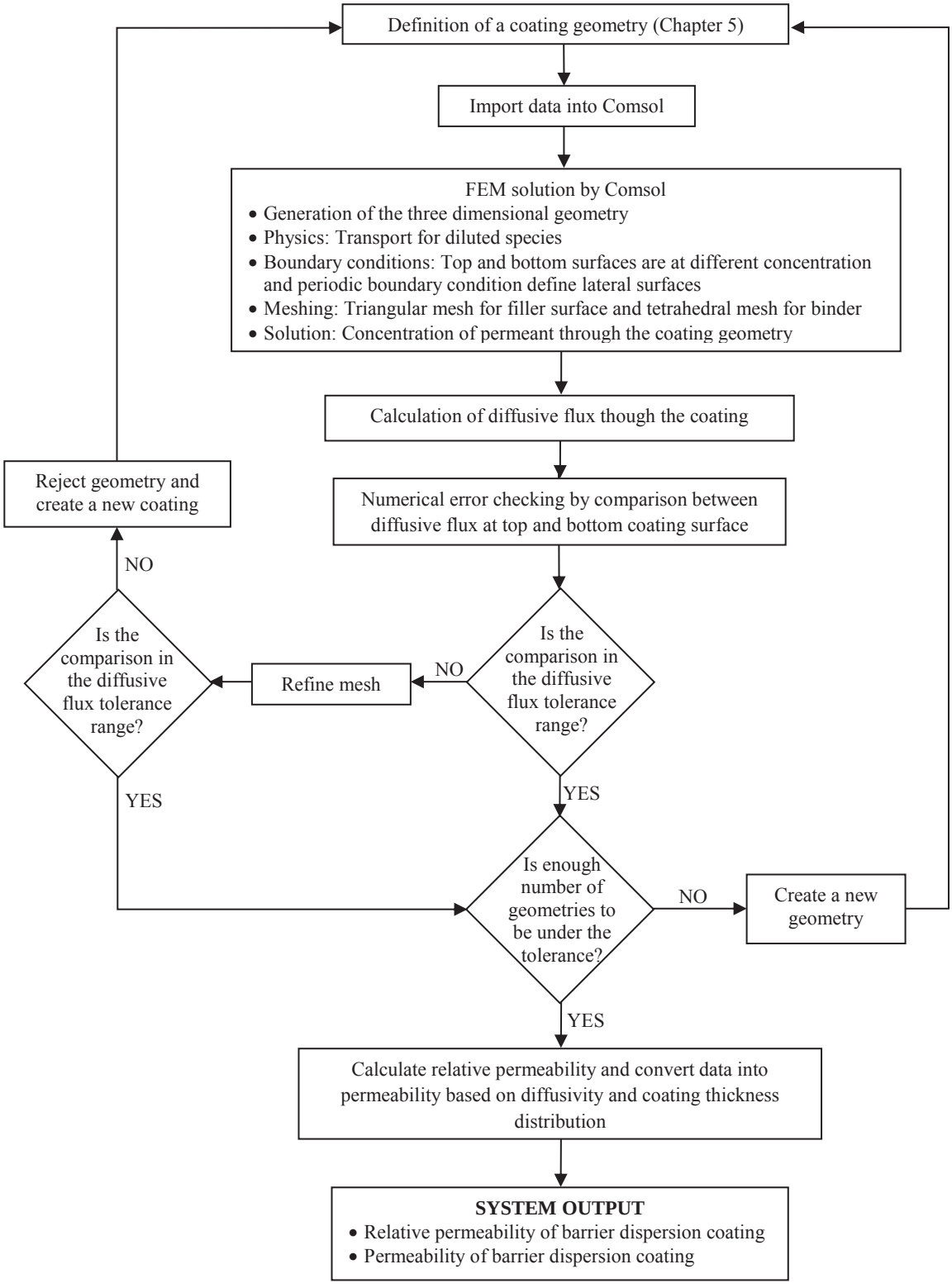

Figure 6.3 Diagram of the mathematical solution of the proposed model to predict permeability of barrier dispersion coatings

6.3 Definition of a representative coating size by estimation of representative elemental volume (REV)

As defined in Chapter 5, the REV represents the smallest volume which is sufficiently accurate to model a representative mean constitutive response (Drugan & Willis, 1996). To find the REV, requires an understanding of how the coating geometry is defined. Figure 6.4 compares the distribution of fillers in coating geometries with different coating thickness at the same volume fraction of fillers. For thin coatings (Figure 6.4a), only a few fillers are needed to achieve the required volume fraction. Thus, the possibility for different filler arrangements is large. This could also create large gaps between fillers for direct diffusion of permeant through the coating. This is even more evident for coatings with large fillers particles because the number of fillers is lower than those coatings with smaller fillers at the same volume fraction. As models generate many arrangements for the fillers, the variation of the prediction of relative permeability increases. A further analysis of this observation was carried out in Chapter 5, Section 5.6. However, when the thickness of the coating increases, the variability becomes lower because the required number of fillers is larger. Under this scenario, the fillers tend to be well dispersed into the coating and the gaps are smaller (Figure 6.4b). Taking these points into consideration, the best clay to define the REV is that which is the largest of all the analysed clays at the lowest volume fraction measured. For these reasons, the conditions to define the REV were based on Clay A at 4.9% volume fraction. These conditions were also used for the preliminary estimation of the REV in Chapter 5, Section 5.6.

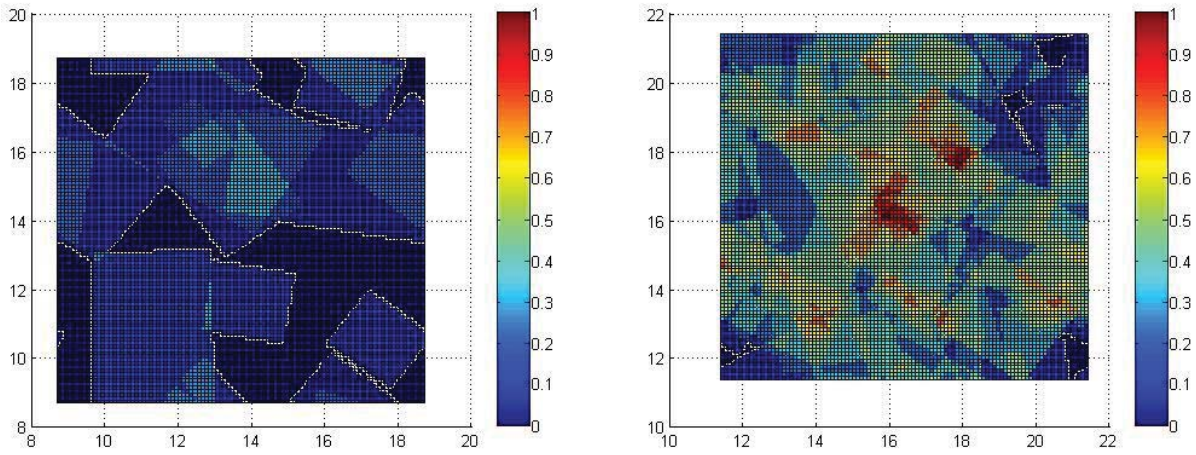

a) b)

Figure 6.4 Distribution of fillers in two coatings with different thickness; a) 2 μm and b) 8 μm from a top view where 1 corresponds to the depth being 100% filled and 0 is no fillers through the coating profile

The estimation of REV was based on the average relative permeability, the standard deviation of the relative permeability, and the number of fillers in evaluated coatings. Different coating

sizes were evaluated and the results compared. For this, the length (J) and width (M) of the coating were assumed to be the same and, for both, the analysis was carried out from 10 to 20 μm. The thickness of the coating (K) was evaluated from 2 to 6 μm. Figure 6.5 shows the variation of the predictions in terms of average relative permeability, relative permeability standard deviation, and the number of fillers required for different sized coatings. As the thickness of the coating increases, the lower relative permeability predicted, until a balance was reached at coating thickness equal or larger than 4 μm. The variation on the prediction is reduced if the length, width and thickness of the coating increase; however, it also increased the required number of fillers. In terms of modelling, coatings with a large number of fillers are in general more complex to resolve. Thus, the geometry has to be as small as possible to minimise the number of fillers, and reduce computational difficulty. Based on this, the REV for modelling of barrier performance of dispersion coating was defined by sizes equal to $12 \times 12 \times 5\ \mu m^3$.

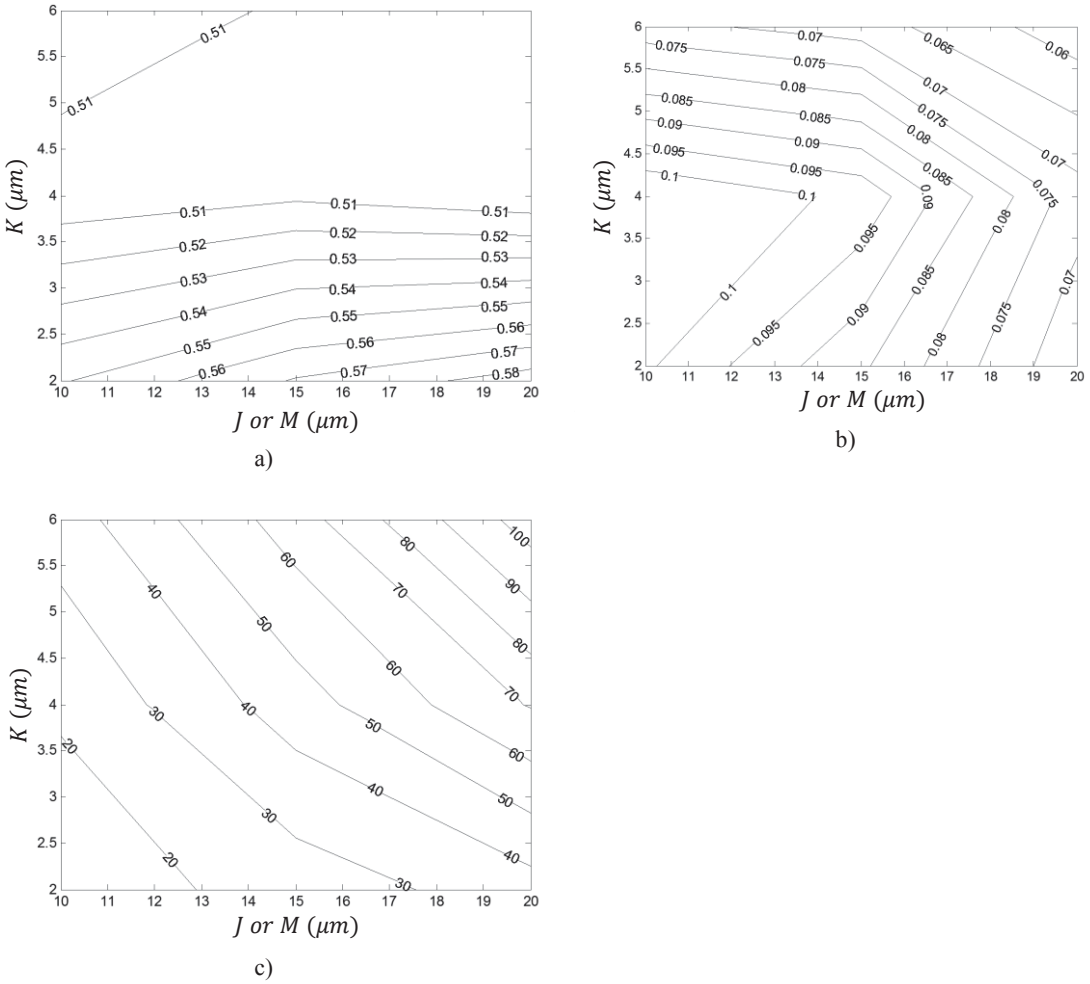

Figure 6.5 Effect of the barrier dispersion coating size on a) average relative permeability, b) standard deviation and c) number of fillers require for coating formulation based on Clay A at 4.9% of volume fraction of fillers

The primary estimation of REV established a coating size of $10 \times 10 \times 2\ \mu^3$ (Section 5.6 in Chapter 5). Because the REV estimated in this section was larger than that proposed in Chapter 5, the geometries of the coatings were sized at $12 \times 12 \times 5\ \mu m^3$ ($J \times M \times K$ respectively). This geometry was thinner than the thinnest coating studied in Chapter 4 Section 4.2 (8.88 μm thick of coatings formulated with Clay B at 28.6% of volume fraction). Also, the length and width of the REV were smaller than the average distance between peaks (16.2 μm) of the coating profile (Section 4.2 in Chapter 4). It is important to note that the complete coating thickness is not required for simulation of the performance of dispersion coatings. Similarly to the concentration of permeant on the coating surfaces, the thickness of the coating is cancelled during calculation of the relative permeability. However, to use a value of thickness based on the REV ensures an adequate representation of the fillers dispersion in the coating binder.

It is important to note that these dimensions present a slightly higher variability (relative permeability equal to 0.51, standard deviation equal to 0.085, and number of fillers equal to 37) than expected for the other combinations. As an example, $20 \times 20 \times 5\ \mu m^3$ presents a relative permeability equal to 0.51, standard deviation equal to 0.070, and number of fillers equal to 85. To resolve larger volumes stretches computing resources for minimal gain, particularly at high volume fraction of fillers.

6.4 Model validation

The purpose of the model validation was to analyse predictions by comparison with experimental observations to gain an indication of the model performance. The experiments conducted and presented in Chapter 4 were used to determine the level of agreement. The predictions of relative permeability for different coating formulations (Equation 5.8) were compared with observed relative permeability. The relative permeability was calculated as the ratio of the WVTR measured for barrier dispersion coatings with different filler volume fraction and the WVTR of unfilled barrier dispersion coatings at the same coating thickness level (prepared with the same rod) (Equation 6.11).

$$RP_{obs} = \frac{WVTR_{filled}}{WVTR_{unfilled}} \tag{6.11}$$

where

RP_{obs}: Relative permeability of analysed barrier dispersion coatings

$WVTR_{filled}$: Normalised water vapour transmission rate of barrier dispersion coatings filled at different volume fraction of filler

$WVTR_{unfilled}$: Normalised water vapour transmission rate of unfilled barrier dispersion coatings

The geometrical characterisation of fillers presented in Chapter 3 was used to define the distribution of the parameter of distribution of length, elongation, and thickness for all the selected filler types. The size of the coatings was based on the estimation of REV presented in the previous section.

A summary of all the system inputs required to run the model are presented in Tables 6.1 to 6.6.

Table 6.1 Summary of the system inputs related to coating geometry and properties

Parameter description	Symbol	Unit	Value
Length	J	μm	12
Width	M	μm	12
Thickness	K	μm	5
Glass transition temperature of the coating	T_g	$°C$	2

Table 6.2 Condition for definition of grid of coating geometry

Parameter description	Symbol	Value
Initial grid division in x-axis	nx_i	5
Initial grid division in y-axis	ny_i	5
Initial grid division in z-axis	nz_i	5

Table 6.3 Summary of the system inputs related to fillers

Parameter description	Symbol	Clay A	Clay B	Clay C
Average of the logarithm of the length	μ_{length}	0.733	0.727	0.570
Standard deviation of the logarithm of the length	σ_{length}	0.731	0.746	0.781
Average of the logarithm of the thickness	$\mu_{thickness}$	-2.055	-1.968	-2.222
Standard deviation of the logarithm of the thickness	$\sigma_{thickness}$	0.231	0.154	0.227
Location parameter of elongation	$\mu_{elongation}$	0.275	0.303	0.268
Scale parameter of elongation	$\sigma_{elongation}$	0.206	0.225	0.193
Shape parameter of elongation	$k_{elongation}$	1.273	1.278	1.262
Maximum limit of length	Max_{length}	22.83	19.34	14.49
Maximum limit of thickness	$Max_{thickness}$	0.200	0.200	0.179
Maximum limit of elongation	$Max_{elongation}$	6.670	5.100	6.200
Minimum limit of length	Min_{length}	0.550	0.550	0.550
Minimum limit of thickness	$Min_{thickness}$	0.070	0.080	0.050
Minimum limit of elongation	$Min_{elongation}$	1.000	1.000	1.000

Table 6.4 Condition of exposure of the dispersion coating

	Parameter description	Symbol	Unit	Value
Top coating surface	Temperature	θ	$°C$	23
	Relative humidity	RH	%	50
Bottom coating surface	Temperature	θ	$°C$	23
	Relative humidity	RH	%	0

Table 6.5 Summary of the system inputs related to permeability parameters

Parameter description	Symbol	Unit	Value	
			Oxygen	Water vapour
Lennard-Jones temperature	$\frac{\varepsilon}{k}$	K	93	809
Ratio of the collision diameter of the permeant and nitrogen	$\left(\frac{\sigma_x}{\sigma_{N_2}}\right)^2$		0.83	0.48

Table 6.6 Constants used for simulations

Parameter description	Symbol	Units	Value
Calculation of partial pressure of air (Equation 5.14)	C_8		$-5.800\,220\,6 \times 10^{3}$
Calculation of partial pressure of air (Equation 5.14)	C_9		$1.391\,499\,3$
Calculation of partial pressure of air (Equation 5.14)	C_{10}		$-4.864\,023\,9 \times 10^{-2}$
Calculation of partial pressure of air (Equation 5.14)	C_{11}		$-4.176\,476\,8 \times 10^{-5}$
Calculation of partial pressure of air (Equation 5.14)	C_{12}		$-1.445\,209\,3 \times 10^{-8}$
Calculation of partial pressure of air (Equation 5.14)	C_{13}		$-6.545\,967\,3$
Ideal gas constant	R	$J \cdot mol^{-1} \cdot K^{-1}$	8.314

6.4.1 Variation of the permeant concentration due to filler arrangement of barrier dispersion coatings

Figure 6.6 and Figure 6.7 show the concentration profile across the coating was affected by the distribution of fillers. Between large filler gaps, the concentration tended to change in vertical direction. In cases where parallel fillers created channels, the concentration mainly changed in a horizontal direction. It was also observed that the concentration gradients were relatively large through channels compared with other regions with no fillers around. This was due to the constriction effect around filler channels. The constriction can be divided into two components; the resistance that the slit generates itself and the resistance created when the permeant is crossing through the slit (Cussler, et al., 1988; Wakeham & Mason, 1979). If the concentration is analysed (for example at x=13.6 μm at the left boundary in Figure 6.7), it was possible to see that it changed from almost 0 $mol \cdot m^{-3}$ at y=0.5 μm to 90 $mol \cdot m^{-3}$ at y=1 μm, in part because of the small gaps between fillers at y=1 μm, and x between 16 and 18.5 μm and x between 20.5 and 24 μm. The variation of permeant concentration and the constriction of the channels affected the permeant flowrate. In Figure 6.7 the permeant flowrates at three points

were measured. Those were 6.68 $\times 10^{-9}\ mol \cdot m^{-2} \cdot s^{-1}$ followed by 1.05$\times 10^{-8}\ mol \cdot m^{-2} \cdot s^{-1}$ and 7.98$\times 10^{-5}\ mol \cdot m^{-2} \cdot s^{-1}$ for points 2, 1 and 3 respectively. These results showed that as the channel narrows, the permeant flux reduces.

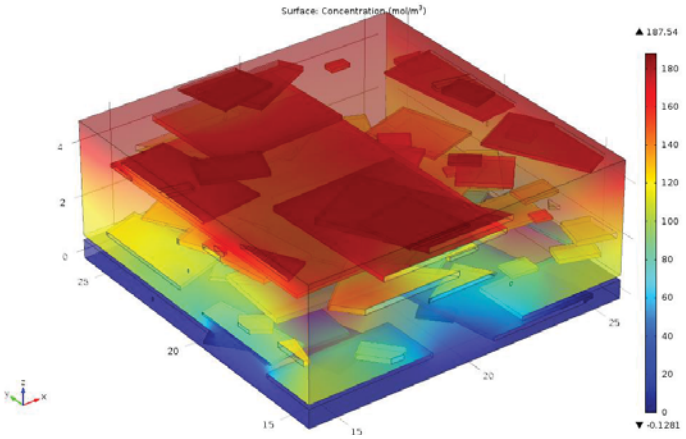

Figure 6.6 Profile of permeant concentration through a coating filled with Clay A at 10.3% of volume fraction

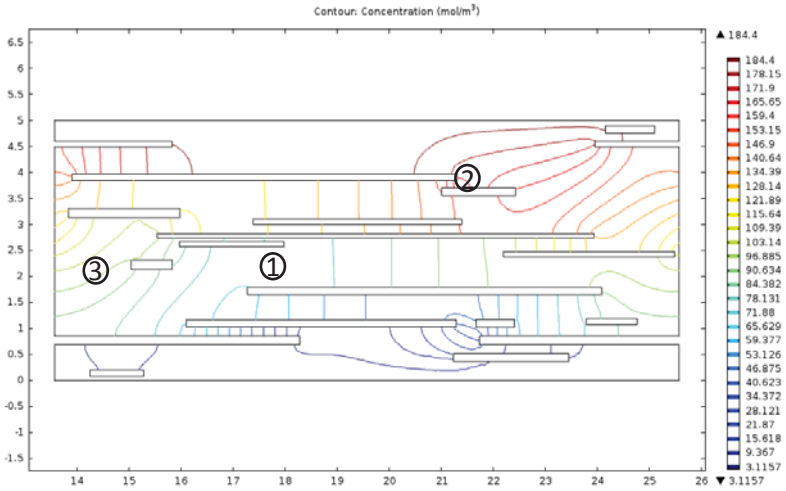

Figure 6.7 Profile of permeant concentration through a coating filled with Clay A at 10.3% filler volume fraction at $x-z$ axis view of the geometry at y=19.6 μm

6.4.2 Comparison against experimental data

Figure 6.8 shows the prediction of relative permeability as a function the volume fraction for the three selected fillers studied in previous chapters. As expected, the general trend was to reduce the relative permeability if the volume fraction of the fillers increases. The reduction of relative permeability was the most for the largest filler size (Clay A). The increase in volume fraction, particularly for large fillers, creates more intricate pathways. These pathways increased the tortuosity and constriction effects and, as a result, reduced the relative permeability. However, as the volume fraction increased, the filler size became less important in the reduction of relative permeability and the prediction tended to be similar for all selected fillers.

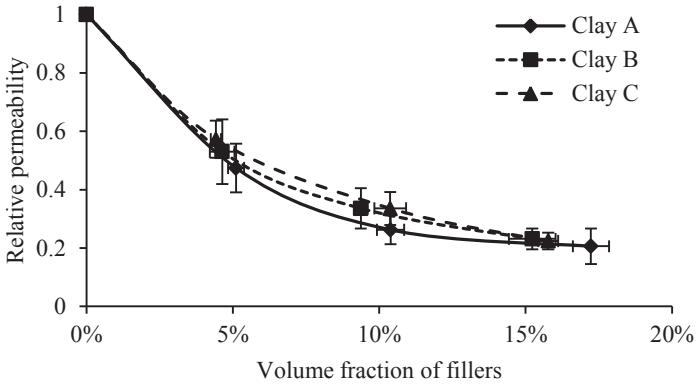

Figure 6.8 Prediction of relative permeability as a function of the volume fraction of fillers for all the selected fillers (the error bars represent standard deviation)

For example, at 4.9% volume fraction, the variation of relative permeability reached 0.05 and for larger amount of fillers the variation becomes constant at between 0.02 and 0.03 for each formulation. This means that the chance of significantly different arrangements of fillers is lower due to the large number of fillers and, as a result, most of the coating is covered with fillers. The relationship between the variation of relative permeability and the volume fraction can be seen in Figure 6.9. This figure shows the ratio between the relative permeabilities and their average as a function of the ratio between the volume fractions and their average for simulation carried out at 4.9% of filler volume fraction. As well as the predictions presented in Figure 6.8, the trend of the variation of relative permeability is inversely proportional to the fillers volume fraction.

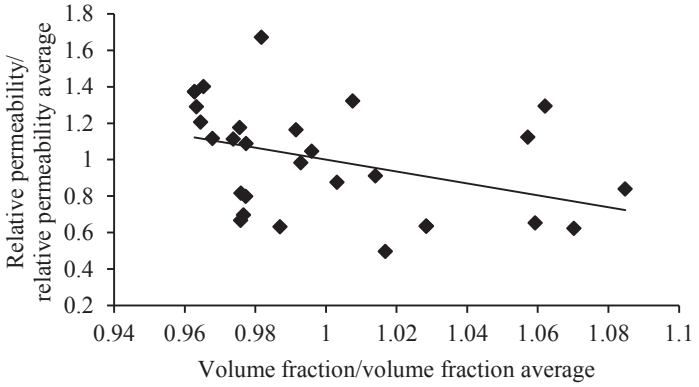

Figure 6.9 Comparison between the variation of relative and volume fraction of fillers for barrier dispersion coating formulations with Clay A at 4.9% of volume fractions (%v/dv)

Figure 6.10 shows a comparison between observed and predicted relative permeability at different volume fractions. The predictions follow the same trend as the experimental results; however, underestimations of the relative permeability for all the evaluated volume fractions

and types of fillers were found. At low volume fraction, the variability of both predictions and observations were overlapped. The differences were larger when the volume fraction increased reaching almost twice the lower predictions than the observed relative permeability for volume fraction equal to 15%.

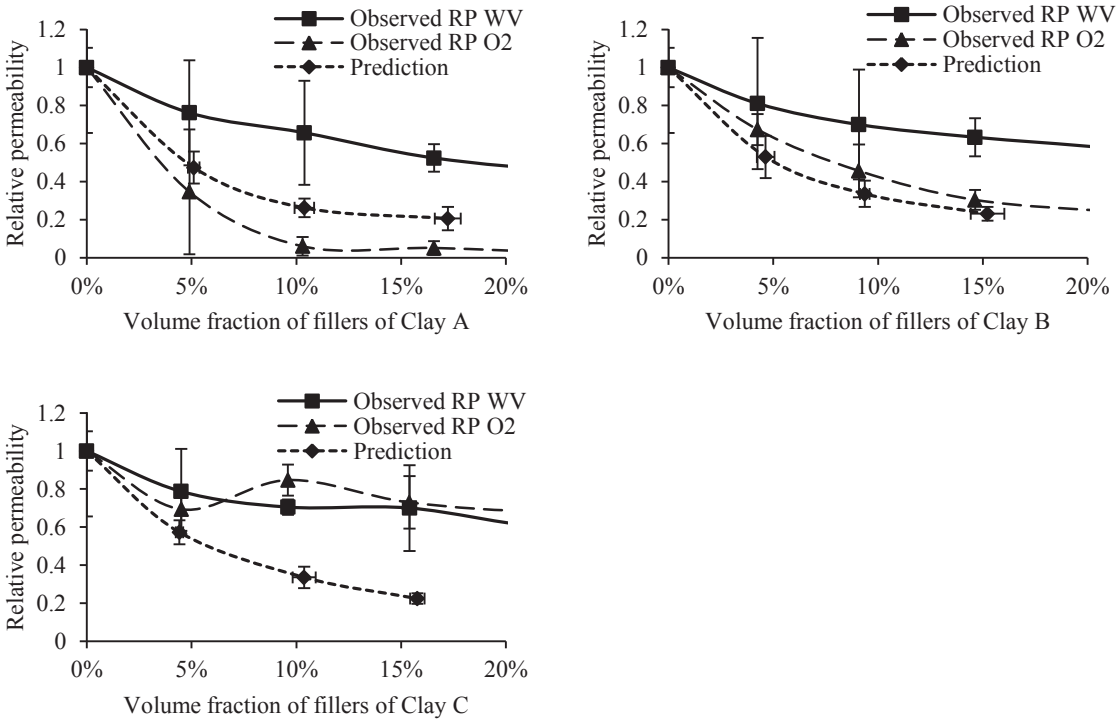

Figure 6.10 Predicted and observed relative permeability of water vapour (WV) and oxygen (O2) for coatings prepared with Clays A, B, and C (the error bars represent standard deviation)

From this point, the comparisons between experimental data and predictions were carried out only for the water vapour relative permeability. In the case of the oxygen relative permeability larger variability was observed. Other factors that were not related to the coating formulation maybe associated to large experimental variability as discussed in Section 4.3 Chapter 4.

6.5 Analysis of the difference between experimental data and predictions

The difference between the model predictions and the experiments may have two reasons: those from the experimental representation of the transmission rate of the dispersion coating trails and those related to the conceptual model. In this section both reasons were further examined.

6.5.1 Effect of the dispersion coating performance on the model validation

As was explained in Chapter 5, the relative permeability was calculated as the ratio of permeability of filled and unfilled coatings. Consequently, this estimation was very sensitive to the transmission rate of both filled and unfilled coating permeability. Figures 4.17 to 4.21

showed that the measurement of WVTR was very sensitive and important variability was observed for all the barrier dispersion formulations. If the variability of the relative permeability is included only in the performance of unfilled coating, the WVTR at 0% of volume fraction of filler has to be increased by a factor around 2 to allow a good model fit to experimental data. The results reached R^2 equal 0.95, 0.93, and 0.84 for Clay A, B, and C respectively in comparison between the prediction and adjusted experimental data (Figure 6.11). It was also noted that a lower increase in the WVTR at 0% of filler volume fraction can also improve the prediction (Figure 6.11). By increasing 1.5 times the original value of WVTR, the R^2 between the modified data and the prediction was 0.79, 0.75, and 0.60 for Clay A, B, and C respectively.

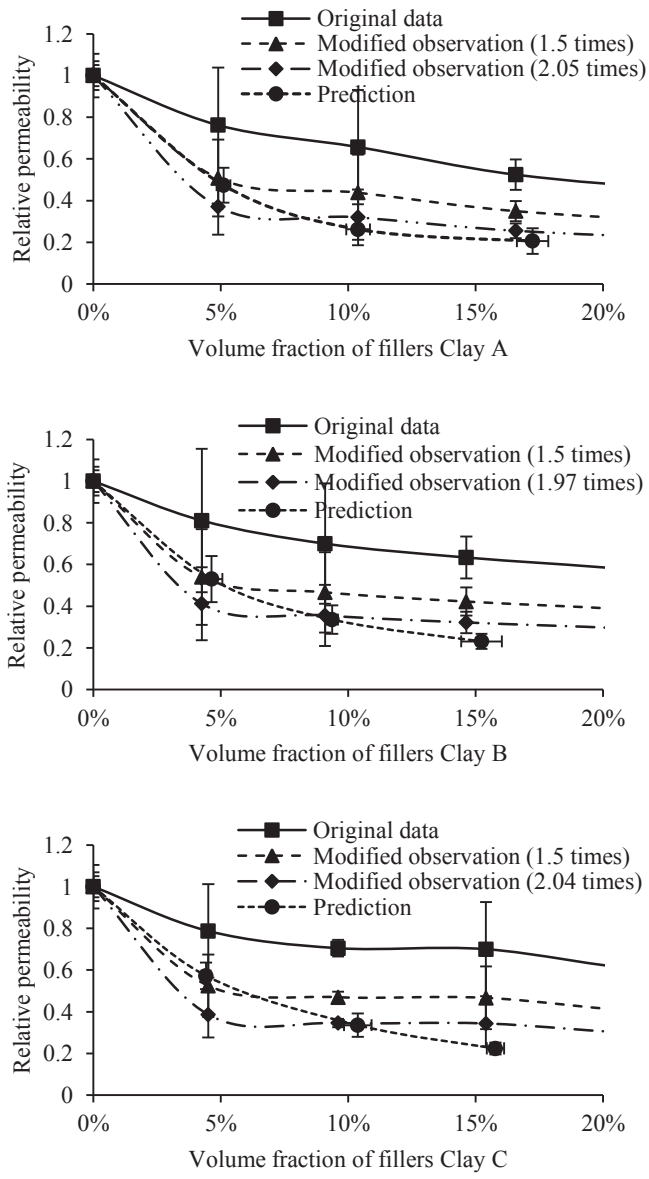

Figure 6.11 Comparison of estimated and observed relative permeability for coating filled with Clay A, Clay B, and Clay C including a modification of the value of WVTR for unfilled coatings (the error bars represent standard deviation)

It is important to note that one of the assumptions of the model was the good dispersion of the fillers in the coating. Despite the appropriate conditions where the coatings were prepared (pH and viscosity of the liquid dispersion coatings), a degree of filler agglomeration may be present. It was reported that perfect filler dispersion is difficult to achieve particularly at high volume fractions (Choudalakis & Gotsis, 2009). The agglomeration of fillers reduces their effectiveness to improve the properties of dispersion coatings. The agglomeration of two or more fillers can be considered as one thicker particle. As a result, the effective filler aspect ratio and the total surface area of the fillers available for stopping the permeant are reduced. From a modelling point of view, the agglomeration can be represented by increasing the filler particle thickness. This scenario has been represented in Figure 6.12. Two geometries were filled at the same volume fraction (10%) with the same type of fillers (Clay A) with normal and double filler thickness. Dispersion coatings formulated with agglomerated fillers showed larger uncovered areas that were free for direct diffusion of permeant through the coating (Figure 6.12b). In contrast, Figure 6.12a illustrated that the fillers are well dispersed and almost no empty areas are presented in the coating with thin fillers.

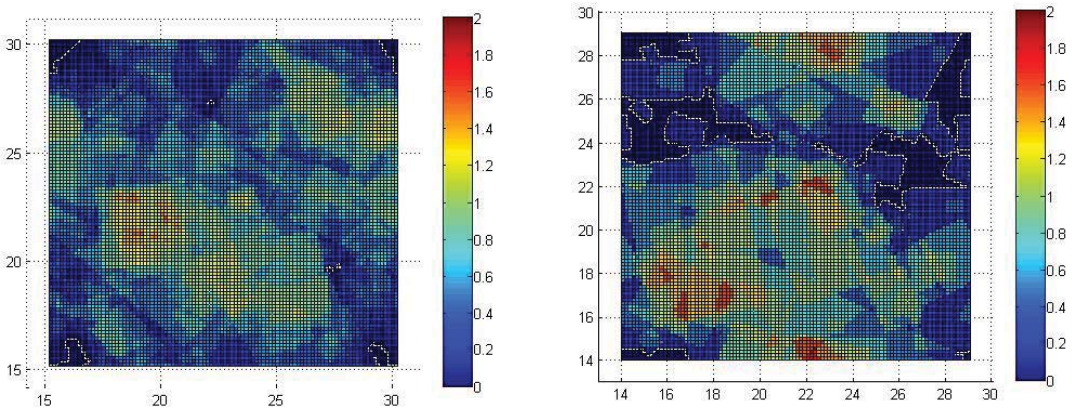

a) b)

Figure 6.12 Top view of filler distribution of coatings filled at 10% volume fraction of fillers (Clay A) a) normal filler thickness and b) double filler thickness

The reduction of the effective surface area of the fillers due to agglomeration of fillers was estimated in Figure 6.13. As the volume fraction increases a larger effective surface area of fillers was available for stopping the diffusive flux. However, minimum increase of filler thickness (agglomeration) can significantly reduce the availability of filler surface area. The reduction in the effective surface area was even larger for thin fillers. As an example, half the potential effective surface area at any volume fraction of fillers can be observed for filler agglomeration represented by an increase of the filler thickness from 0.05 μm to 0.1 μm.

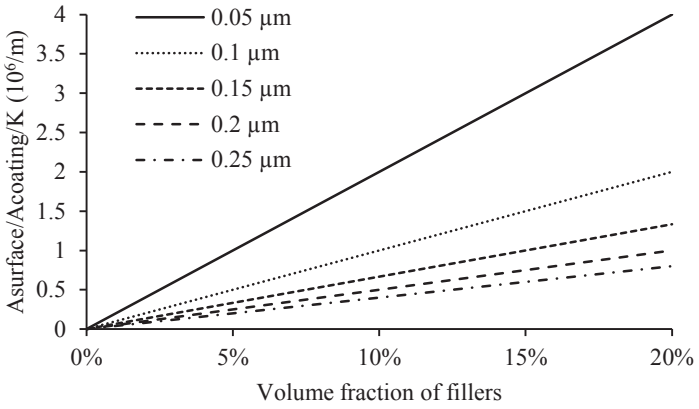

Figure 6.13 Effective surface area of fillers to stop diffusive flux through barrier dispersion coatings as a function of the volume fraction of fillers for several filler thickness

Figure 6.14 presents the relative permeability at different volume fraction for normal and agglomerated filler represented by increasing the thickness twice to the original. The differences between the prediction for normal and double filler thickness are even larger if the volume fraction increases. At 2.5% of volume fraction, the differences in prediction are less than 0.1; however, when the coatings content 10% of volume fraction the differences reached more than 0.2.

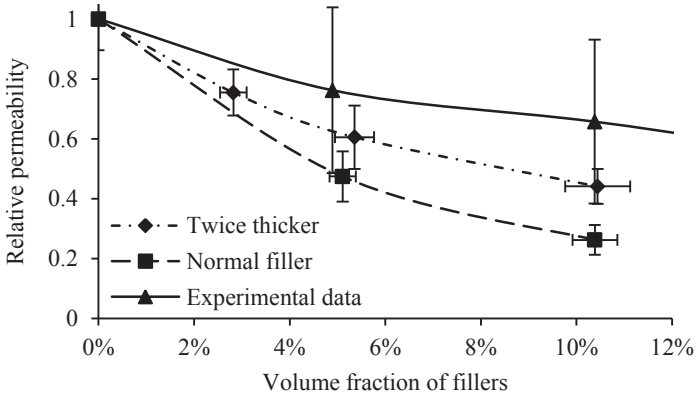

Figure 6.14 Comparison of predicted relative permeability of coatings filled with agglomerated Clay A (the error bars represent standard deviation)

In Chapter 5 Section 5.29, the surfaces of the coatings were examined to check the presence of uncoated areas. This analysis was carried out on the coating formation that is more likely to have cracks or pinholes occur. According to the observation no cracks or pinholes were observed. However, it was a chance that unobserved areas may have cracks or pinholes. It was reported that the barrier properties of dispersion coatings can be significantly affected by pinholes, cracks and other defects (Johansson, 2002; Robertson, 2013). Such areas represent an alternative path for the permeant diffusion instead the coating (Fishman, Rodov, & Ben-

Yehoshua, 1996). The permeation through pinholes occurs in air which allows faster diffusion of permeants than solid materials (Lee, et al., 2008).

The diffusion through pinholes that have a diameter that is 10 or more times smaller than the length can be represented by the Knudsen law (Geankoplis, 2003). Unlike the Fick's law, the Knudsen law describes the diffusion where the permeant interacts with the pinhole due to the collision of permeant molecules with walls (Geankoplis, 2003). The pinholes represent a parallel path to the route formed by the solid part of dispersion coatings. Thus, the total diffusive flux of dispersion coatings can be estimated as the sum of both flux through the pinhole and the solid part of the coatings (Fishman, et al., 1996). Therefore, the equation for calculation of relative permeability presented previously (Equation 5.8) can be modified as presented below

$$\left(\frac{P_f}{P_u}\right)_{pinhole} = \frac{TR_f \cdot \left(J \cdot M - \frac{\pi}{4} \cdot {d_{pinhole}}^2\right) + TR_{pinhole} \cdot \frac{\pi}{4} \cdot {d_{pinhole}}^2}{TR_u \cdot \left(J \cdot M - \frac{\pi}{4} \cdot {d_{pinhole}}^2\right) + TR_{pinhole} \cdot \frac{\pi}{4} \cdot {d_{pinhole}}^2} \tag{6.12}$$

where

$\left(\frac{P_f}{P_u}\right)_{pinhole}$: Relative permeability of coating with one representative pinhole

TR_f: Transmission rate of filled coatings $(mol \cdot m^{-2} \cdot s^{-1})$

J: Length of coating (m)

M: Width of coating (m)

$d_{pinhole}$: Diameter of the pinhole (m)

$TR_{pinhole}$: Transmission rate through the pinhole $(mol \cdot m^{-2} \cdot s^{-1})$

TR_u: Transmission rate of unfilled coatings $(mol \cdot m^{-2} \cdot s^{-1})$

And the Knudsen law can be used to defined $TR_{pinhole}$ (Geankoplis, 2003) as shown below.

$$TR_{pinhole} = \frac{48.5 \cdot d_{pinhole} \cdot (p_{top} - p_{bottom})}{R \cdot (\theta + 273.16) \cdot K} \cdot \sqrt{\frac{\theta + 273.16}{1{,}000 \cdot m_{wv}}} \tag{6.13}$$

where

θ: Temperature $(°C)$

m_{wv}: Molecular weight of the water vapour $(g \cdot mol^{-1})$

p_{top}: Partial pressure on top coating surface (Pa)

p_{bottom}: Partial pressure on bottom coating surface (Pa)

R: Ideal gas constant ($8.314\ m^3 \cdot Pa^{-1} \cdot K^{-1} \cdot mol^{-1}$)

K: Thickness of coating (m)

Figure 6.15 shows the effect of an equivalent pinhole on the relative permeability of two simulations with coating formulated with Clay A; one at 5.2% and another with 17.2% of volume fraction of filler. The results indicated that pinholes with a reduced diameter affect importantly on the relative permeability of barrier dispersion coatings. At low and high concentration of fillers, the trend showed that the effect of pinholes was relative minor for diameters up to 0.005 μm. After that range, the relative permeability became mainly governed by pinholes increasing up to a permeability equivalent to an unfilled coating when the pinhole diameter was greater than 0.03μm.

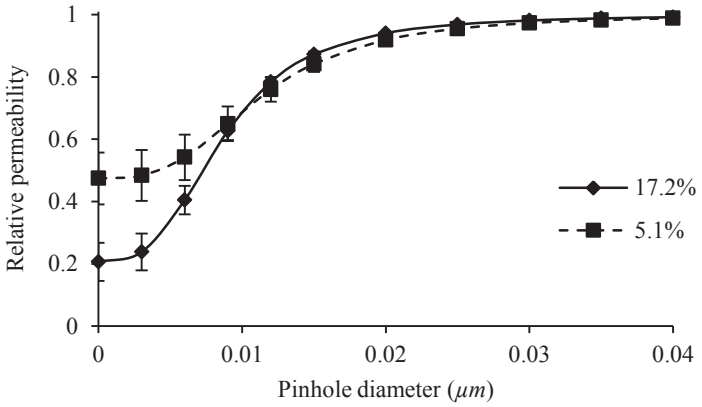

Figure 6.15 Effect of pinholes on the relative permeability of coating formulated at 17.2% and 5.2% of volume fraction of Clay A (the error bars represent standard deviation)

6.5.2 Effect of the conceptual model

The model assumed uniformity of the coating profile. This assumption allowed simplification of the coating geometry; however, irregularities on the coating profile were observed (Section 4.2 in Chapter 4). The irregularities make the area of the bottom coating surface larger than the top coating surface. This may generate permeant flux through different angles and not only in vertical directions. Also, the total permeant flux may be higher than that observed in slab shaped coatings. As a first approximation, the effect of the irregularities on the relative permeability can be estimated by assuming the coating cross section to be semi-circular (Figure 6.16). The permeant flux of this geometry has been studied in an analogous case for heat transfer through cylinder. Thus, by adaptation of that approach, the permeant flux can be estimated by the following expression.

$$J_{cyl} = \frac{D \cdot \Delta c}{ln(r_2/r_1) \cdot r_1} \tag{6.14}$$

where

J_{cyl}: Permeant flux through the coating when the cross section shape is assumed as cylinder ($mol \cdot m^{-2} \cdot s^{-1}$)

D: Diffusivity ($m^2 \cdot s^{-1}$)

Δc: Variation in concentration between surfaces ($mol \cdot m^{-3}$)

r_2: Radius of the largest distance between a coating surface and the imaginary centre of the cylinder (projection of the radius) (m)

r_1: Radius of the shortest distance between a coating surface and the imaginary centre of the cylinder (projection of the radius) (m)

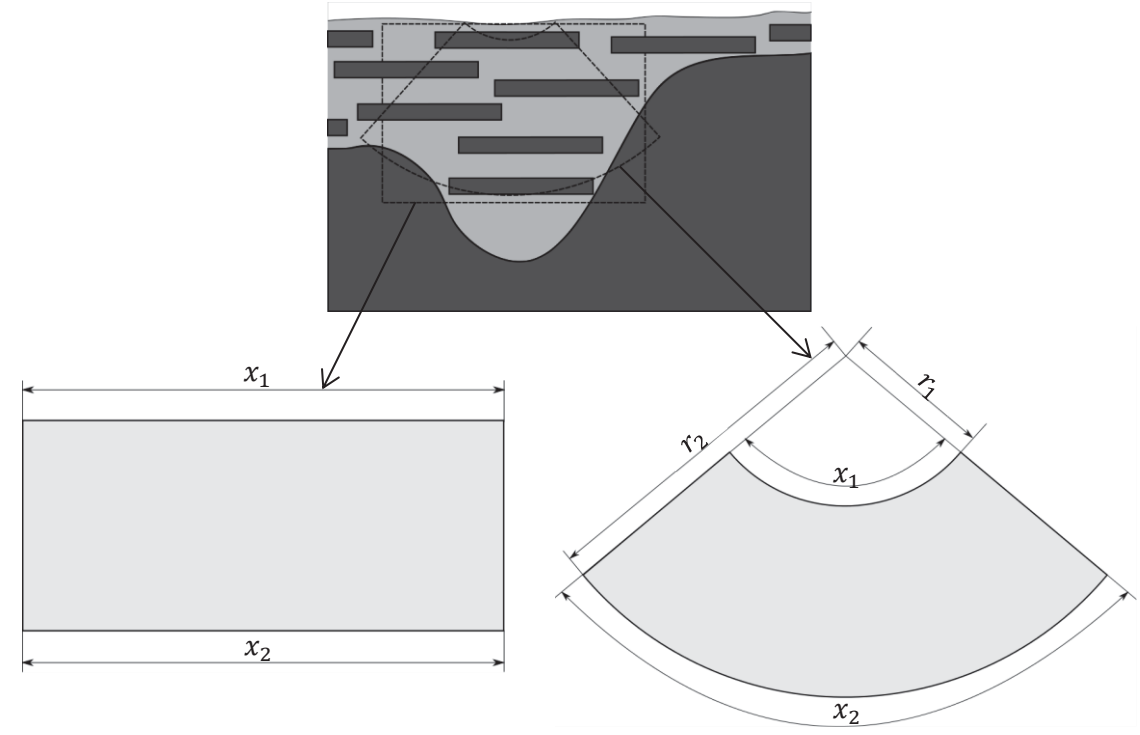

Figure 6.16 Coating cross section assuming slab (already assumed in the conceptual model) and semi cylindrical geometry where x_1 and x_2 are the length of the coating surfaces and r_1 and r_2 are the radii formed from the surfaces to the imaginary centre of the cylinder

Since the radii of the imaginary cylinder (r_1 and r_2) were not known, they were replaced by the perimeters of the semi-circles formed by the surfaces of the coating x_1 and x_2. This can be done due to the ratios of corresponding radii and perimeters are equal (Equation 6.15).

$$\frac{r_1}{r_2} = \frac{x_1}{x_2} \tag{6.15}$$

The calculation of the permeant flux through the slab geometry can be carried out by the Fick's First law presented in Equation 2.19 (Section 2.5 in Chapter 2). Thus, the ratio between the permeant flux of coatings with cylindrical and slab geometries can be estimated by the following expression.

$$\frac{J_{cyl}}{J_{slab}} = \frac{\frac{x_2}{x_1} - 1}{ln\left(\frac{x_2}{x_1}\right)} \tag{6.16}$$

Figure 6.17 shows the difference between the permeant flux through cylindrical and slab shape coatings (J_{cyl}/J_{slab}) as a function of the ratio between the largest and shortest perimeter. As the ratio of perimeters increased, larger value of the ratio between permeant fluxes results. This meant that flux through cylindrical geometry was larger than slab coatings. Thus, this higher flux may explain in part the higher measured relative permeability than that predicted. In the case of the model, x_1 and x_2 represented the top and bottom coating surface length respectively. The differences between lengths were studied in Chapter 4 Section 4.2. On average, it was estimated that x_2 was 22.3% larger than x_1. This represented a ratio x_2/x_1 equal to 1.29. The ratio of permeant fluxes for that value of x_2/x_1 was 1.14, meaning the model may overestimate barrier performance by up to 14%.

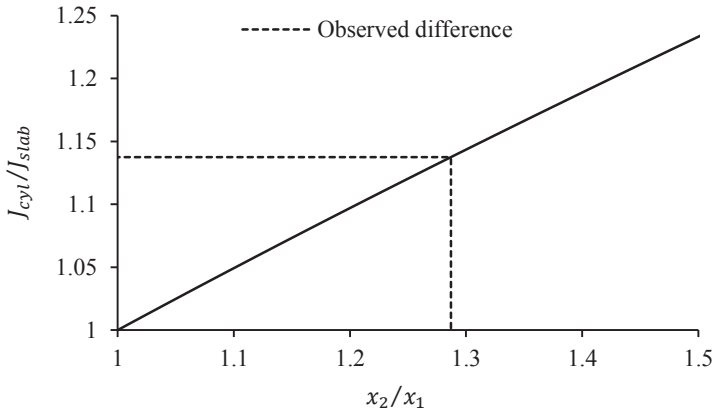

Figure 6.17 Difference between the permeant flux through cylindrical and slab shape coatings (J_{cyl}/J_{slab}) as a function of the ratio between the largest and shortest perimeter (x_2/x_1)

As was discussed in previous sections, the equation that describes the relative permeability can be simplified in several ways (Equation 5.7). Another simplification of this equation is denoted as the ratio between the diffusivity of filled and unfilled coatings. As well as previous simplifications, the same boundary conditions have to be applied in both coatings. Thus, the diffusivity of the filled coating can be estimated as:

$$D_{filled} = \frac{P_f}{P_u} \cdot D_{unfilled} \tag{6.17}$$

where

D_{filled}: Diffusivity of permeant through the filled coating ($m^2 \cdot s^{-1}$)

$\frac{P_f}{P_u}$: Relative permeability from simulation with even coating profile (normal simulations)

$D_{unfilled}$: Diffusivity of permeant through the unfilled coating ($m^2 \cdot s^{-1}$)

D_{filled} can be used to represent the diffusivity of the filled coatings in a more complex geometry. This is possible because D_{filled} includes the effect of the fillers on the diffusion of permeant. Thus, no population of filler is required to estimate the relative permeability of filled coatings. This considerably simplifies the simulation process.

By taking the section profile of one of the studied dispersion coatings and assuming anisotropic properties, the diffusivity of a coating with irregular profile at z-axis (D_z) can be assumed as D_{filled} (Figure 6.18). This assumption can be considered due to the most of the diffusion in even coating profile geometries is this direction. For x and y axes, the diffusivities (D_x and D_y) can be assumed as $D_{unfilled}$ because at these directions the fillers have a minimum effect on the reduction of the permeability.

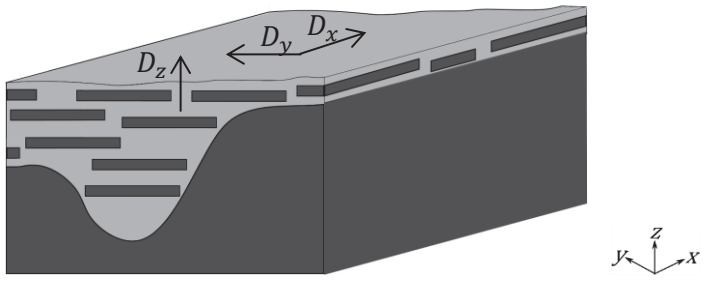

Figure 6.18 Representation of coating geometry with irregularities due to the substrate topography

Under this scenario, simulations can be developed. Figure 6.19 shows the permeant concentration profile of an irregular coating based on the relative permeability of a coating filled with Clay A at 4.9% of filler volume fraction.

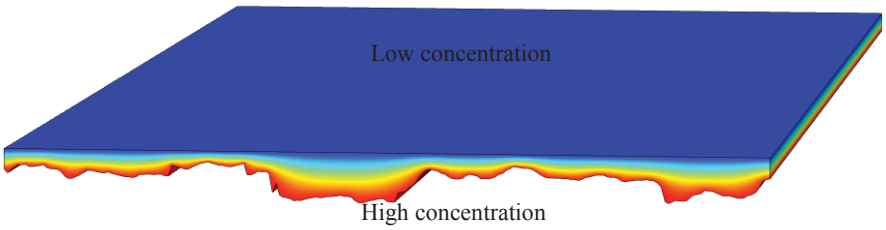

Figure 6.19 Permeant concentration of an irregular coating profile calculated from the relative permeability of a dispersion coating filled with Clay A at 4.9% of filler volume fraction

Figure 6.20 shows a comparison between simulations of even and irregular coatings based on relative permeability estimated for coating with Clay A. As was presented in previous analysis, the irregularities of coatings make the relative permeability higher than those calculated with even geometry due to the larger area for diffusion presented in the bottom coating surface. In this case, the difference between both assumptions was estimated in 21.1% average at filler volume fraction of 17.2%. It is important to note that this approach assumed the same coating profile in the x-direction. If the irregularities of the coating at this direction are included, it is expected a higher relative permeability due to the area of the bottom coating area may increase.

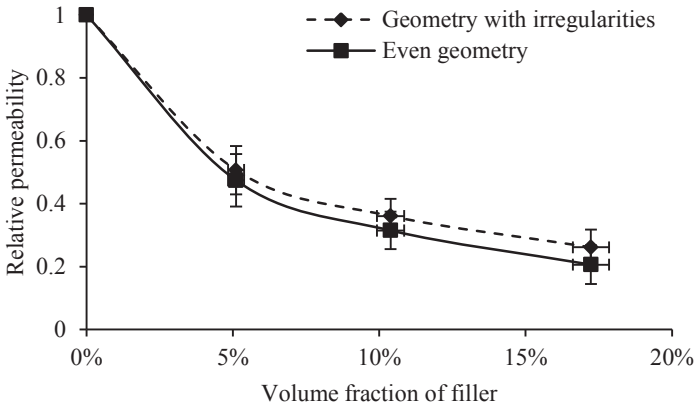

Figure 6.20 Comparison of relative permeability of coatings with even and irregular geometries based on the relative permeability estimated for even coatings geometries filled with Clay A (the error bars represent standard deviation)

As was presented in Chapter 3 Section 3.5, the shapes of the clays were found to be irregular. Approximations of the filler shape were found to be suitable to represent the filler geometries. The representation of the filler shape can be improved as the geometry assumed for this was more complex. Shapes like ellipses or the use of more complex methods such as Fourier shape descriptor were shown to be closer than the rectangular shape (which was assumed in the conceptual model). To verify whether the assumed shape of fillers affected the predictions, simulations with elliptical shaped fillers were carried out. For this, modifications in the

estimation of the number of fillers and the program were required. The number of fillers in the coating geometry was estimated by Equation 6.18. This equation included the effect of the curved shape ($\pi/4$) in the calculation of the volume of fillers. The modifications of the program were related to the method of overlapping identification. Details of modified program were presented in Appendix G**.**

$$\emptyset_F \leq \frac{1}{J \cdot M \cdot K} \cdot \sum_{i=1}^{N} \left(\frac{\pi}{4}\right) \cdot \frac{L_i^2 \cdot b_i}{E_i} \tag{6.18}$$

where

$\emptyset_F$: Volume fraction of fillers

L_i: Maximum Ferert diameter of the *i* filler (m)

b_i: Thickness of the *i* filler (m)

E_i: Elongation of the *i* filler

N: Number of fillers for coating definition

The results of the simulations showed a closer prediction to the experimental data than the rectangular shape (Figure 6.21). The relative permeability of the coating with elliptical fillers was higher than for rectangular fillers, reaching differences larger than 0.1 for volume fraction of fillers higher than 10%. A possible reason may be related to the smaller surface area of elliptical fillers compared to fillers with rectangular shape. As the surface area was reduced, less chance to stop the permeant was possible, making the pathway length for the permeant shorter. The reduction of area is equivalent to 21.5% compared with rectangular fillers defined with the same L_i and E_i.

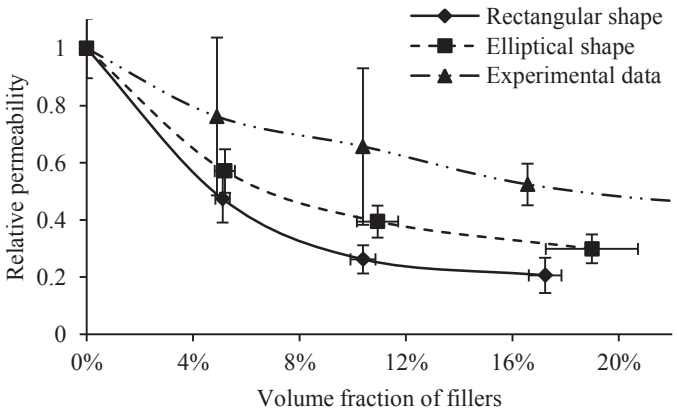

Figure 6.21 Comparison between experimental data and prediction of relative permability assuming rectangular and elliptical shaped fillers based on dispersion coatings filled with Clay A (the error bars represent standard deviation)

The curved shape of the elliptical shaped fillers may affect the length of the permeant pathways. As shown in Figure 6.22, the permeant runs across the coating binder following the contour of the fillers. The length of the permeant pathways increased in those areas where the fillers represent larger obstacles. For elliptical shapes, the largest permeant pathways were located at the major semi axis of the ellipses (x-axis in Figure 6.22). In the case of the rectangular shape, the largest permeant pathways were around the diagonal formed from the centre of the filler and the corners.

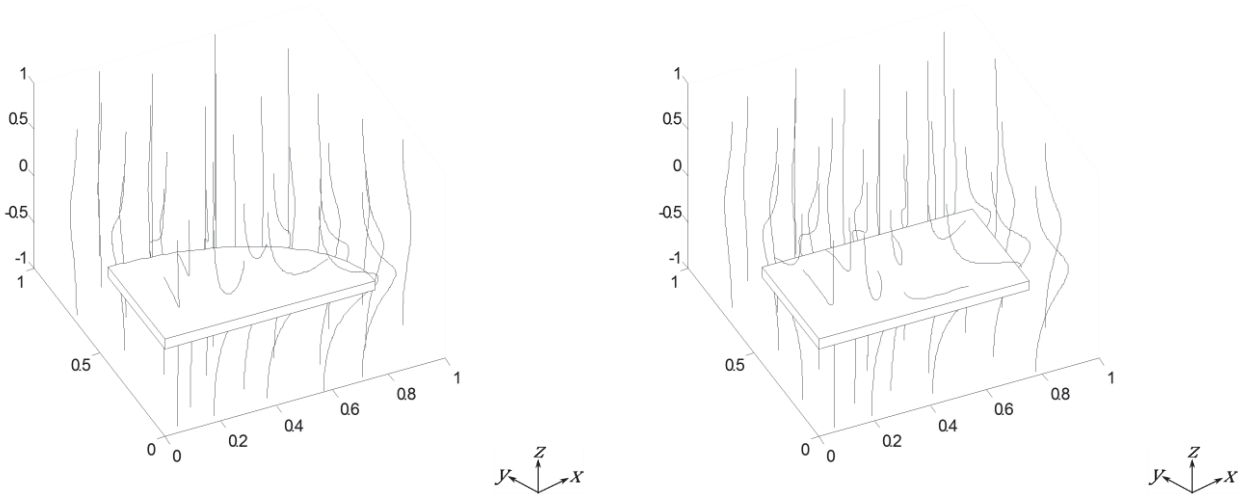

Figure 6.22 Representation of diffusive flux pathway for a quarter of elliptical and rectangular shaped fillers

The differences between the maximum length of elliptical and rectangular filler shapes can be at least 30% when the elongation was equal to one (Figure 6.23). This percentage increased as much as the difference between the major and minor semi axes of the ellipse increased. This was equivalent to increase the value of elongation.

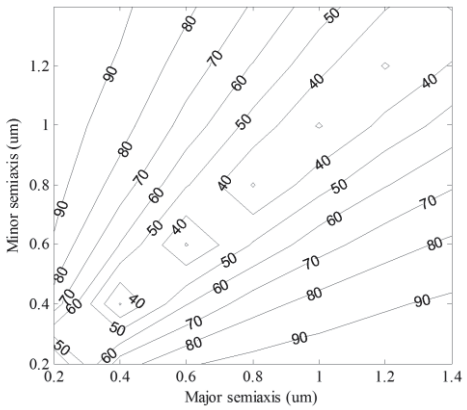

Figure 6.23 Differences (%) between maximum length of elliptical and rectangular shaped fillers

The curved shape of the elliptical fillers may also influence the occurrence of gaps between fillers increasing the permeant flux through the coatings. Figure 6.24 shows a hypothetical case

where fillers with rectangular and elliptical shapes, but the same dimensions (L and E) were placed in a way to avoid gaps. In the case of rectangular shapes, the straight contour allowed arrangement of the filler with contact through the completed border. The fitting between elliptical fillers were not continuous and they were in contact only on one point. This increases the chances for the presence of gaps. To avoid the gaps, overlap of the fillers was needed. Due to this, the effective filler surface area used to stop the permeant diffusion was reduced up to 63.4% of the original surface area of one filler or 87.7% of the total surface area.

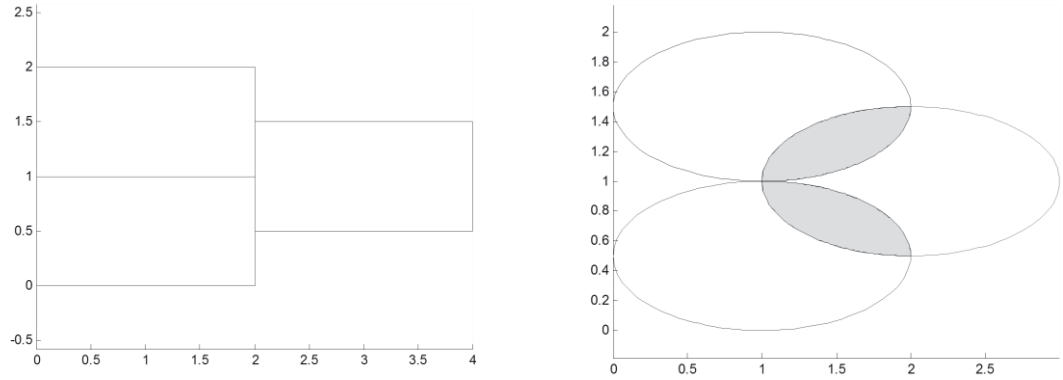

Figure 6.24 Comparison filler overlapping between rectangular and elliptical shaped fillers

It is important to mention that the reduction of surface area by assuming elliptical filler required a larger number of fillers to achieve the required volume fraction. As was presented in Section 6.3, if the number of fillers increased, better covering of filler in the coating was observed. This reduced the occurrence of direct permeant pathways through the coating. However, in terms of modelling, this was a disadvantage due to the increased complexity of coating geometry. This resulted in a larger demand of computing resources and time of simulations.

6.6 Discussion and conclusion

It was possible to solve the model under the conditions proposed in the mathematical formulation (Chapter 5). The model showed how the permeant flux moved through the dispersion coating. Also, it was possible to see the effect of the gaps between fillers on the reduction of the permeant flux. In comparison with the experimental data, the model tended to overestimate the barrier properties of the dispersion coating at any formulation. Several factors that were not included in the original conceptual model were analysed to improve the predictions. It was observed that the filler agglomeration and uncoated areas were the most significant factors that affect the potential barrier properties of the dispersion coatings. Also, other factors such the uniformity of coating profile, and filler shape were found to have an effect on the prediction. The variation of diffusivity across the coating was not studied in this analysis.

To understand the effect of this factor on the model prediction it is necessary to observe the structure of the coating and measure the variability of the latex particle packing. The particle packing has to be related with variation of the diffusivity across the coating structure. If the diffusivity significantly varies, it could be incorporated into the conceptual model.

It is important to note that in spite of the overestimation of relative permeability, the model followed the trends of the experimental measurements. This means that the model was suitable for prediction how to improve barrier performance in terms of general trends instead precise predictions. Thus, it is possible to evaluate different factors related to the barrier performance to find their best combination. For example, the model could be used to minimise the relative permeability, to minimise the amount of material to prepare dispersion coatings, or to evaluate combinations of different fillers. By including the factors that affected the calculation, the model would be suitable to accurately predict the barrier performance of dispersion coatings at different type and concentration of fillers.

Chapter 7

SENSITIVITY ANALYSIS OF THE MODEL AND ITS APPLICABILITY

As was presented in the previous chapter, despite the over prediction of the barrier performance by the model, variation of the performance of dispersion coating can be predicted. This chapter analyses how the dispersion coating can be improved to achieve better barrier properties. This was based on the sensitivity analysis of several factors that affect the barrier performance. The analysis may guide future investigations in order to detect the way to develop better dispersion coatings by simple modifications. Also, those factors that are not relevant in the development of the dispersion coatings can be identified making the process of dispersion coating development more efficient.

7.1 Sensitivity analysis of the model

The study of the dispersion coatings has indicated that the geometrical characteristics of the fillers and how they are distributed mainly governed the barrier properties of the dispersion coating. Based on this, the sensitivity analysis was focused on the effect of the fillers on the performance of dispersion coatings.

7.1.1 Settling of fillers in the dispersion coating

The model assumed even dispersion of fillers in the coating. However, the fillers can be grouped in different patterns according to the design of the coating process. For example, it is possible that the fillers can settle to the bottom part of the coating during application and drying (Figure 7.1). In terms of modelling, the settling of fillers in coatings can be represented as a barrier with two regions: a bottom region where the settled particles are present and a top region where the binder is unfilled.

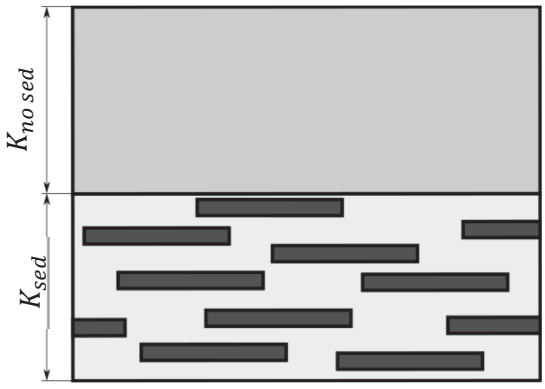

Figure 7.1 Settling of the filler in the coating profile

Under this scenario, the mechanisms of mass transfer became as in-series diffusion. The permeability of an in-series barrier has been presented in the literature as a factor of the thickness of each region (Robertson, 2013). From this, it is possible to calculate the relative permeability of the coating by modification of the in-series resistance approach resulting in the following equation.

$$RP_{settling} = \frac{K_{sed} + K_{no\ sed}}{\frac{K_{sed}}{RP_{sed}} + \frac{K_{no\ sed}}{RP_{no\ sed}}} \tag{7.1}$$

where

$RP_{settling}$: Relative permeability of a barrier dispersion coating with filler sedimentation

K_{sed}: Thickness of the settling region(m)

$K_{no\ sed}$: Thickness of the unfilled region (m)

RP_{sed}: Relative permeability of the settling region

$RP_{no\ sed}$: Relative permeability of the unfilled region

This equation can combined with the relative permeability predictions presented in Chapter 6 using the FEM model. Figure 7.2 shows a comparison of performance between a normal barrier dispersion coating and another with fillers settled in half of the coating thickness (K_{sed}=$K_{no\ sed}$=1/2).

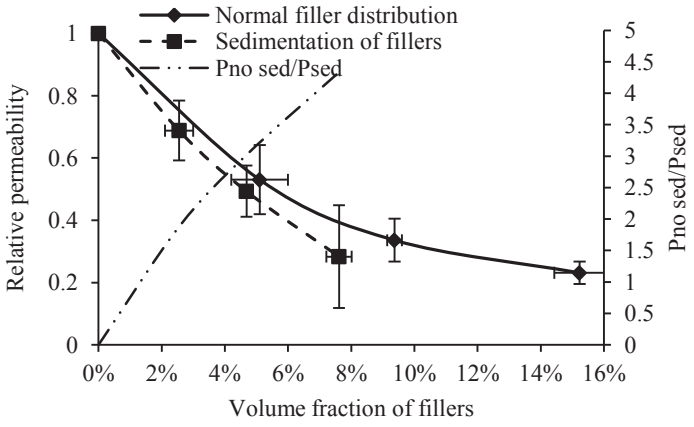

Figure 7.2 Comparison of relative permeability as a function of volume fraction of fillers between coatings with uniform distribution of fillers and sedimentation of fillers in coating. The regions have the same thickness (K_{sed}=$K_{no\ sed}$) (the error bars represent standard deviation)

A continuous reduction of the relative permeability was observed when settling was presented in the dispersion coatings. These differences were up to 0.11 of relative permeability at 7.5% filler volume fraction. The settling region acted as a thin barrier with large amount of fillers

where most of the reduction of relative permeability occurs. For coatings with high volume fraction, the fillers tended to cover all the volume of the coating binder and the available gaps for diffusion of permeant represents a reduced volume of the total coating geometry. This can also be seen by comparing the permeability through both regions. The permeability of the settled regions (P_{sed}) decreases as the volume fraction of fillers increases. As an example, the settled region reached about four times lower permeability than the unfilled region at 7.5% of volume fraction of fillers.

The above analysis was carried out in equal thickness of coating; however, this may vary in a number of combinations. To identify the best combination of region thicknesses, the relative permeability of the in-series coating was calculated as a function of the proportion of settling region thickness with respect to the total coating thickness (Equations 7.2 and 7.3).

$$RP_{settling}(\emptyset_F) = \frac{y_{settling}}{\frac{y_{settling}}{RP(\emptyset_F / y_{settling})} + (1 - y_{settling})} \tag{7.2}$$

$$y_{settling} = \frac{K_{sed}}{K_{sed} + K_{no\ sed}} \tag{7.3}$$

where

$RP_{settling}(\emptyset_F)$: Relative permeability at filler volume fraction $\emptyset_F$

$\emptyset_F$: Volume fraction of filler

$y_{settling}$: Fraction of the coating thickness where the settling occurs

Figure 7.3 shows the relative permeability as a function of $y_{settling}$. It was seen that the relative permeability at 5% of filler volume fraction was lower at $y_{settling}$ equal to 0.3. For the rest of the studied volume fraction, the relative permeability tended to be lower as the value of $y_{settling}$ increased. However, the reduction of the relative permeability was not significant for $y_{settling}$ higher than 0.6. These results may suggest that it is possible to use coating with two layers and achieve the same barrier performance. This coating structure potentially reduces the amount of filler used for coating formulation. This is because the settling region represents a thin coating, thus, it is needed less fillers to achieve the required volume fraction. In addition, the application of two coating layers may reduce the occurrence of uncoated areas on the substrate.

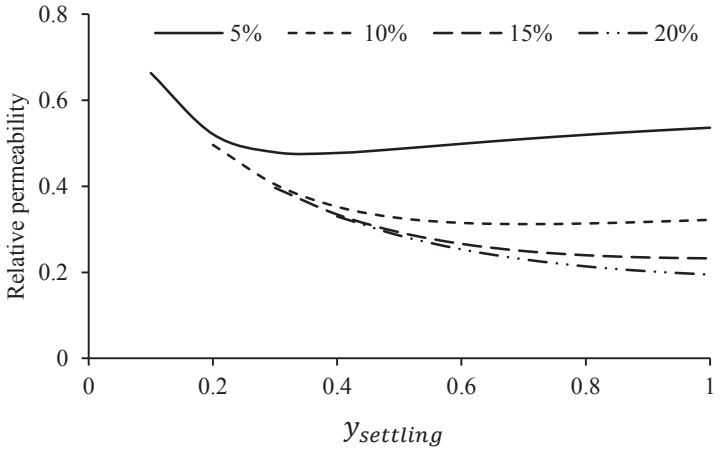

Figure 7.3 Relative permeability of two layer coatings as a function of the settled thickness fraction at four volume fractions of filler based on Clay A. The maximum volume fraction for this calculation was 50% (assuming this value as the critical pigment volume concentration)

7.1.2 Two dispersion coating layers

It is expected that the application of two coatings layers on the substrate improves the barrier performance significantly. This condition can be studied in a similar way as for the filler settling presented in the previous section. Thus, the final relative permeability of a coating with two layers can be estimated by Equation 7.4 and its overall filler volume fraction by Equation 7.5

$$RP_{two\ layers}\left(\emptyset_{F_{final}}\right) = \frac{K_{layer\ 1} + K_{layer\ 2}}{\frac{K_{layer\ 1}}{RP\left(\emptyset_{F_1}\right)} + \frac{K_{layer\ 2}}{RP\left(\emptyset_{F_2}\right)}} \tag{7.4}$$

$$\emptyset_{F_{final}} = \frac{\emptyset_{F_1} \cdot K_{layer\ 1} + \emptyset_{F_2} \cdot K_{layer\ 2}}{K_{layer\ 1} + K_{layer\ 2}} \tag{7.5}$$

Figure 7.4 shows the relative permeability for several combinations of layers and their volume fraction of fillers. It was observed that the filler volume fraction changed linearly as the fraction of the coating layer varied. However, no linear changes were observed for the final relative permeability. This may suggest that there was an optimum combination of layers to achieve the lowest relative permeability. For a given volume fraction of fillers equal to 4.9% (which was in the range of all the layers and it was highlighted with fine dotted lines in Figure 7.4), the final relative permeability of the combination of 4.9%-16.6% filler volume fraction layers was the lowest compared with the other coating formulations. In the case of the 10.4%-16.6% filler volume fraction combination, it was required to increase the volume fraction by about 2% to achieve that level of barrier properties. The 4.9%-10.4% combination was not able to reach that relative permeability. As found in the previous section, the double layer coating may reduce the amount of fillers and the potential for uncovered areas of the substrate. Some authors propose the combination of coating layers as a solution to reduce the weight of the materials used for

dispersion coatings (Kugge & Johnson, 2008). Eventually other combinations of layers may have better performance than those studied in this example. This may depend on the characteristics of the fillers and their performance for stopping the permeant flux through the coatings.

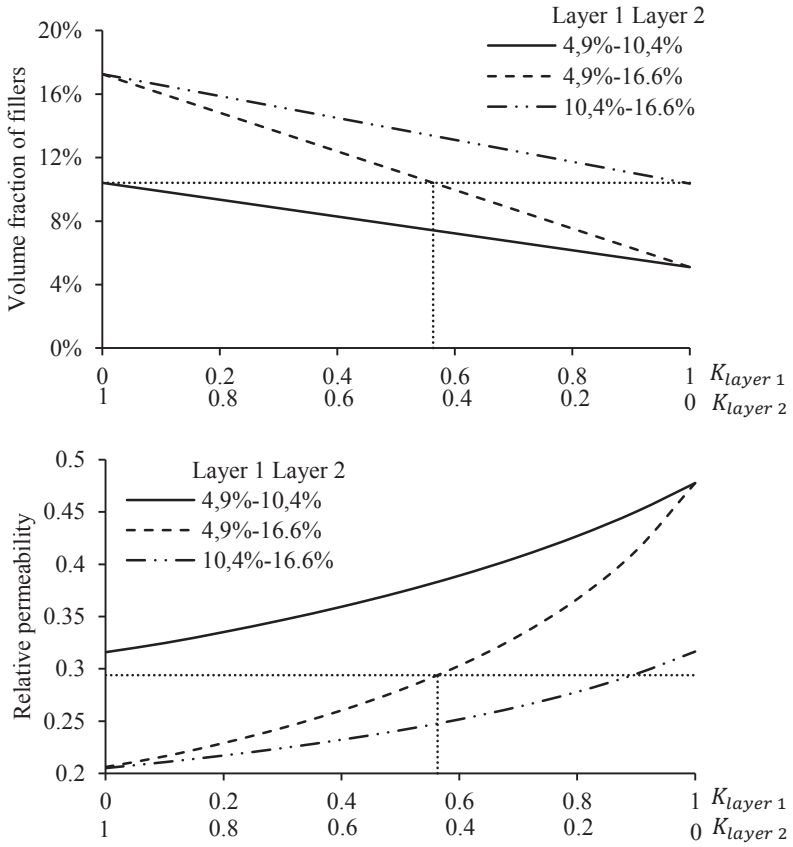

Figure 7.4 Final relative permeability and volume fraction of perfectly dispersed fillers as a function of ratio of thickness between coating layers (fine dotted lines are reference for explanations)

7.1.3 Two dispersion coating layers with presence of filler agglomeration

The above coating structure was simulated assuming perfect dispersion of fillers. However, as was explained in Chapter 6, it is likely some degree of filler agglomeration occurs in real coating trials. Based on the approach presented in the previous section, two layers with agglomerated fillers were used to define the coatings structure. The agglomeration was represented by increasing the filler thickness twice the normal during simulations. As well as the results presented in Figure 7.4, a possible optimisation of the volume fraction of filler can be achieved by the combination of layers with 2.5%-10.0% filler volume fraction (Figure 7.5). However, the improvement of the barrier properties was not as good as coatings with perfect filler dispersion. As an example, for almost the same volume fraction of fillers the relative permeability was around 25% higher for coatings with agglomerated fillers compared to coatings with the perfect dispersion of fillers.

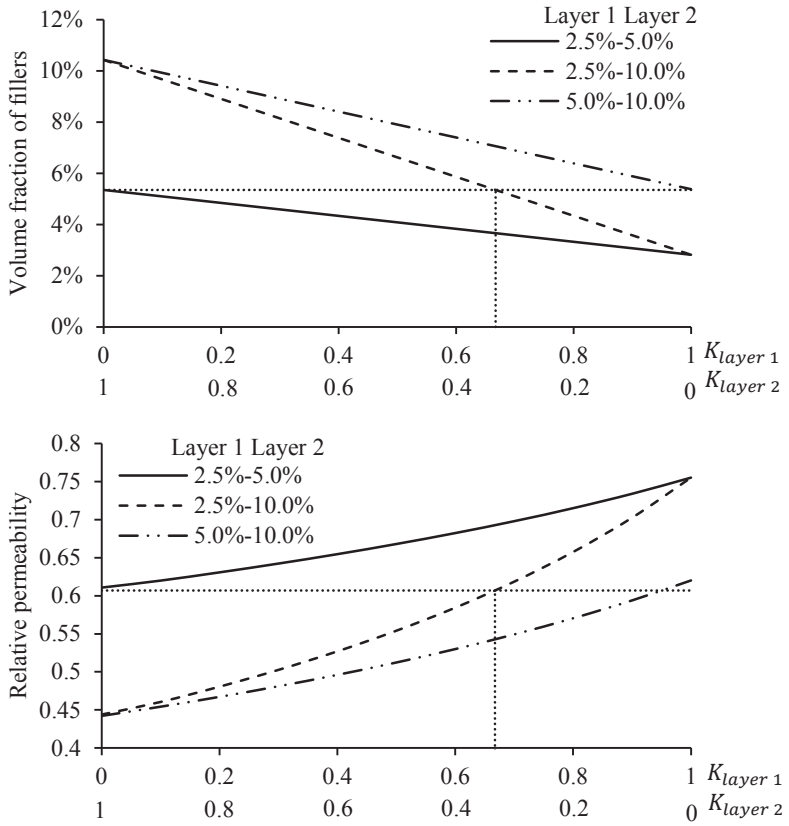

Figure 7.5 Final relative permeability and volume fraction of agglomerated fillers as a function of ratio of thickness between coating layers (fine dotted lines are reference for explanations)

7.1.4 Filler orientation ($x - y$ axis rotation)

A hypothetical analysis of how the arrangement of the fillers affect the barrier performance of the dispersion coating was presented in Section 6.5.2 in Chapter 6. This suggested that the orientation of the fillers in the $x - y$ axes may be relevant. Figure 7.6 shows a comparison of barrier performance between oriented and random angle of orientation at $x - y$ axes based on geometrical information of Clay A. At 5% filler volume fraction, the formulation with orientated fillers had 0.15 higher relative permeability than those estimated for dispersion coatings with random oriented fillers. However, as the fillers volume fraction increased, closer performances were observed between both coating formulations. For filler volume fraction greater than 11%, no differences were observed.

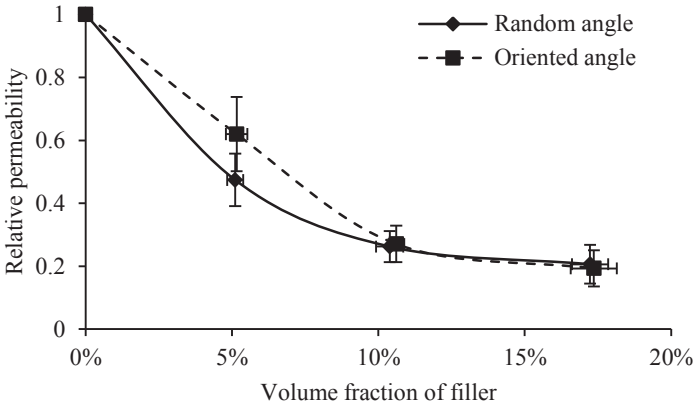

Figure 7.6 Comparison between filler arranged randomly and orientated based on Clay A (the error bars represent standard deviation)

Interestingly, at 5% of volume fraction the covering of fillers for both filler orientation was the same, reaching 31% ±18% of covering across the coating profile. However, the tortuosity (ratio between the permeant pathways and the coating thickness) at this filler volume fraction was 5.80±3.86 and 5.79±1.37 for oriented and random distribution respectively. The high variability of the tortuosity for oriented filled distribution may explain the higher relative permeability of this coating structure. Based on this, it is possible to infer that the propensity for occurrence of short or direct permeant pathways was larger in the case of oriented fillers arrangement than for dispersion coatings with random filler arrangements. The direct pathways of permeant decrease the barrier performance of coatings because only the coating binder acts as a barrier. Under these conditions, higher relative permeability is expected. However, as the fillers volume fraction increased, the gaps between fillers tended to completely cover the coatings achieving similar performance than those with random filler arrangement.

7.1.5 Filler size distribution: Combination of narrow and large length distribution

A common practice in the industry is to mix different materials to investigate their effect on the barrier performance of dispersion coatings. In this way, Figure 7.7 shows how the relative permeability changed as the volume fraction of fillers was modified at different concentrations of small and large fillers in the coating formulation. It was observed that the formulation with 100% of large fillers reached the lowest relative permeability. However, a similar level of barrier performance was achieved when the combination of small and large filler was 25% and 75% respectively. In the case of formulation with only small fillers, the relative permeability reached higher values than the other coating formulations. For this condition, the maximum difference compared with the other coating formulations was about 0.1 at 17% of filler volume fraction. There were no apparent differences in the barrier performance of coatings formulated with 50%-50% and 75%-25% mixtures of small and large fillers. Due to the arrangement of the

fillers, greater than 15% volume fraction of fillers, the relative permeability tended to remain steady reaching about 0.3 for all the coating formulations as observed for previous simulations presented in Chapter 6.

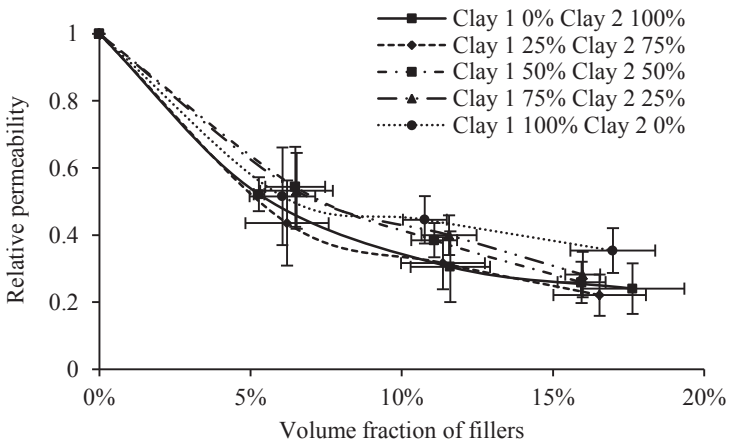

Figure 7.7 Relative permeability as a function of volume fraction of several combination of small (Clay 1) and larger (Clay 2) fillers. The filler length was defined by the lognormal distribution defined by μ=0.2 and μm σ=0.7 μm for Clay 1 and μ=1 μm and σ=0.7 μm for Clay 2 (the error bars represent standard deviation)

Figure 7.7 also shows that the performance of the dispersion coatings may be grouped into two main ranges; those formulations that have 0% or 25% of small fillers and those with larger amount of small fillers. This observation suggested that a reduced amount of small fillers does not affect the final barrier performance if the majority of the fillers were large. In contrast, deterioration of the barrier performance may occur if the amount small fillers was increased from 25% to 50% of the total volume fraction of filler. If the amount of small fillers was larger than 50%, the effect on the relative permeability approached that of a barrier dispersion coating completely filled with small fillers.

The performance of the barrier dispersion coating was also affected by how the distribution of the filler length was defined. This was studied assuming two distributions with the same mean and different standard deviation ($\mu = 1 \ \ \mu m \ \ \sigma = 0.7 \ \ \mu m$ and $\mu = 1 \, \mu m \ \ \sigma = 0.2 \ \ \mu m$ respectively). Table 7.1 shows the results of this calculation.

Table 7.1 Relative permeability (RP) of dispersion coatings formulated with two sizes of fillers, their final average volume fraction ($\emptyset_f$), and their normalisations (RP_n) against the average filler volume fraction of all simulations (5.91 %)

Distribution	RP	$\emptyset_f$ (%)	RP_n
$\boldsymbol{\mu = 1 \, \mu m \ \sigma = 0.2 \, \mu m}$	0.558 ± 0.105	5.46 ± 0.29	0.516 ± 0.096
$\boldsymbol{\mu = 1 \, \mu m \ \sigma = 0.7 \ \mu m}$	0.456 ± 0.120	6.35 ± 1.14	0.490 ± 0.129

It was observed that barrier dispersion coatings with broad filler length distribution ($\mu = 1\ \mu m$ $\sigma = 0.7\ \mu m$) achieved lower relative permeability than those with narrow filler length distribution ($\mu = 1\ \mu m\ \sigma = 0.2\ \mu m$). Under this condition, the occurrence of large fillers is higher. The large fillers can increase significantly the length of permeant pathway and as a result reduce the relative permeability.

It was noted from the above results presented in Figure 7.7 and Table 7.1 that the improvement of the barrier performance of dispersion coatings in terms of fillers is mostly dependent on the length of the fillers. The variability of the filler size may not play a relevant role; however, as shown in Figure 7.7, the variability has to be small enough to keep the majority of the fillers with large dimensions.

7.2 Optimisation of dispersion coating performance based on the modelling and simulations

The information presented in Chapter 5, 6 and 7 can guide the exploration of new coating formulations to optimise their barrier properties. In this way, the results indicated that the agglomeration of the filler may be the most relevant factor that reduces the barrier performance of dispersion coatings. The analyses presented in the previous section and in Chapter 6 demonstrated the sensitivity of the coating to filler agglomeration. Thus, future investigations may focus on this aspect. Coating preparation and application may play an important role for the reduction of filler agglomeration. In Chapter 4, optimum conditions to disperse fillers were introduced; however, the addition of other practices during coating formulation, preparation, or application may help. It is important to note that the modification of the coating formulation may consider the avoidance of pinholes. The pinholes, cracks or uncoated areas also have a large negative effect on the barrier properties (Figure 6.15 in Chapter 6, Section 6.5.1). They may be from air bubbles produced during coating preparation and consolidation, high viscosity of the liquid dispersion coating, or by damage from the substrate fibres (Johansson, 2002).

It was observed that the size of the fillers affect the barrier performance. As the filler size increases, lower relative permeability is expected. The distribution of the fillers size also influences the barrier properties. As the filler size distribution becomes broad, the relative permeability tends to be lower; however, this may be related to the occurrence of large fillers. As shown in Figure 7.7, to keep low relative permeability, the fillers size has to be large. Thus, the optimum dispersion coatings have to be formulated based on large fillers with a narrow variation of size. It is important to note that fillers with these characteristics may reduce the number of filler particles in coatings. Thus, if agglomeration occurs, the effectivity of the fillers to stop the permeant flux may be significantly reduced.

According to the simulations, two coating layers achieved better barrier performance that normal single layer coatings with the same equivalent volume fraction. The application of two layers may also improve the covering of the coating on the substrate and the potential reduction of the materials of the coating formulation. Improvements were observed even when one of the layers was unfilled. It is important to study the compatibility between coating layers. This may guide what combination of coating layers is suitable. The applicability of two layers may also influence the parallel orientation of the fillers in the top coating layer. This may increase the length of the permeant pathway in the coating layers, improving its barrier properties.

7.3 Recommendations for the application of the model

In order to use the proposed model, some considerations have to be taken into account. One is related to the nomenclature used in this model. This point covers aspects from the units used to quantify measurements to the definitions of parameters. For example, the units for the transmission rate may vary according to the permeant and the standard. The WVTR and O_2TR are normally expressed in different terms ($g \cdot m^{-2} \cdot day^{-1}$ and $mL \cdot m^{-2} \cdot day^{-1}$ respectively). In this project, the units were based on SI units, thus they correspond to $mol \cdot m^{-2} \cdot s^{-1}$ for both permeants. This becomes important when comparisons between experimental data and predictions are required. To avoid confusion, Table 7.2 presents the conversion between SI units and several other unit combinations.

Table 7.2 Conversion factor of permeability and transmission rate of water vapour and oxygen from the SI units to several combinations of the units where m_{perm} is the molecular mass of the permeant ($g \cdot mol^{-1}$), p_{tot} is the total pressure of the system (Pa) and θ temperature ($°C$)

Variable	Original Unit	Conversion Factor	Ref
Permeability ($mol \cdot m \cdot m^{-2} \cdot s^{-1} \cdot Pa^{-1}$)	$mmol \cdot cm \cdot cm^{-2} \cdot h^{-1} \cdot kPa^{-1}$	2.778×10^{-8}	a
	$g \cdot mil \cdot m^{-2} \cdot day^{-1} \cdot mmHg^{-1}$	$2.205 \times 10^{-12}/m_{perm}$	a
	$mL \cdot mil \cdot m^{-2} \cdot day^{-1} \cdot atm^{-1}$	$3.492 \times 10^{-22} \cdot p_{tot}/(\theta + 273)$	a
	$mL \cdot mil \cdot cm^{-2} \cdot day^{-1} \cdot atm^{-1}$	$3.492 \times 10^{-18} \cdot p_{tot}/(\theta + 273)$	a
	$mL \cdot mil \cdot cm^{-2} \cdot h^{-1} \cdot atm^{-1}$	$3.297 \times 10^{-14} \cdot p_{tot}/(\theta + 273)$	a
	$mL \cdot mil \cdot cm^{-2} \cdot s^{-1} \cdot atm^{-1}$	$1.187 \times 10^{-10} \cdot p_{tot}/(\theta + 273)$	a
	$mL \cdot mil \cdot cm^{-2} \cdot s^{-1} \cdot Pa^{-1}$	$1.203 \times 10^{-5} \cdot p_{tot}/(\theta + 273)$	a
	$mL \cdot mil \cdot cm^{-2} \cdot s^{-1} \cdot cmHg^{-1}$	$9.023 \times 10^{-9} \cdot p_{tot}/(\theta + 273)$	a
	$cm(STP) \cdot mm \cdot m^{-2} \cdot s^{-1} \cdot Pa^{-1}$	2.241×10^{7}	b
	$cm(STP) \cdot mm \cdot m^{-2} \cdot day^{-1} \cdot atm^{-1}$	1.962×10^{17}	b
	$cc \cdot mil \cdot 100in^{-2} \cdot day^{-1} \cdot atm^{-1}$	4.984×10^{17}	b
	$Barrer$	2.990×10^{15}	b
Transmission rate ($mol \cdot m^{-2} \cdot s^{-1}$)	$g \cdot m^{-2} \cdot day^{-1}$	$1.157 \times 10^{-5}/m_{perm}$	c
	$mL \cdot m^{-2} \cdot day^{-1}$	$1.392 \times 10^{-12} \cdot p_{tot}/(\theta + 273)$	c

a: Banks, Cleland, Cameron, Beaudry, & Kader (1995); b: Solovyov & Goldman (2008); c: Kruger (2011)

To formulate dispersion coatings from simulations it is required to express the amount of filler in terms of mass or mass fraction. The model was designed to quantify the fillers in terms of the volume fraction with respect to the total volume of dispersion coating. The method of how to convert the amount of fillers into volume fraction was presented in the Chapter 2 Section 2.2. Thus, this method can be used in the backward direction to calculate the mass fraction and the total mass of fillers and latex required.

The model expresses the length of the fillers in terms of maximum Feret diameter. For this reason, it is recommended to verify whether the length data that are going to be used in the model correspond to this concept. Details of this parameter were presented in Chapter 3. In the same way, if information is derived from parameters such as aspect ratio or elongation of fillers, it is essential to check how those parameters were defined and compare them with the definition used in the model. As an example, the aspect ratio of filler may be calculated as the ratio between the length or a half of the length (maximum Feret diameter, equivalent diameter, or other reference length) over the thickness of fillers. Also, the similarities of the concept of some parameters may generate confusion due to their potential ambiguous definitions. For example, the aspect ratio and the elongation represent ratio between two lengths of the fillers. Thus, depending in the reference that is used to observe the fillers, care must be taken as to how those parameters were defined.

7.4 Discussion and conclusion

The sensitivity analysis showed that it is possible to use a model to evaluate different formulation of coatings. From this information, it is possible to optimise coating formulations to achieve required relative permeability. In this way, it was found that settling of the fillers in the coating or two coating layers represented an advantage in the reduction of relative permeability. This technique may reduce the material used for coating preparation and the occurrence of uncoated areas. In addition, the analysis indicated that the most important factor that affects the barrier properties of dispersion coating was the agglomeration of fillers. This observation was based on coatings with no uncoated areas. Future studies should be carried out to improve the dispersion of the fillers in the coating. The applicability of the model to optimise coating formulation must consider the definitions of the concepts used in the model in order to apply the correct information for running simulations.

Chapter 8

CONCLUSIONS AND RECOMMENDATIONS

8.1 General discussion and conclusions

The efforts of this study were focused on the understanding of how dispersion coatings behave with different types and quantities of fillers, in order to develop a permeability model specifically for this type of barrier. This challenge required the characterisation of both fillers and dispersion coatings to assist in conceptual model development, to provide input data for simulations and to have reference data for model validation.

The geometry of fillers was characterised based on image processing and analysis. This method was suitable to collect information related to fillers sizes and shape. This information is essential for both understanding the effect of the fillers on the barrier properties of dispersion coatings and when reconstruction of a filler population is required for development of model geometry. It was observed that average values of filler size and shape descriptors are not enough for this purpose. Instead, more complex methods have to be utilised. Dimensions such as maximum Feret diameter, elongation, and thickness of fillers can be represented by distribution curves. In the case of the filler shape, the representation can be based on either regular shapes or mathematical descriptions. The regular shapes provide a simple and representative way to define the shape. The mathematical description such as the Fourier series allows more accurate representation of the shape of fillers. When the focus is on modelling and simulation, the selection of the method to define the filler shape has to be based on the available computing resources. As more complex characterisations are applied, the required computer resources to achieve geometry meshing and solution become larger. In this project, regular rectangular and elliptical plates were selected to represent the fillers.

The geometry of the dispersion coatings were studied based on image processing and analysis. The coating thickness was measured on cross section images captured by SEM. The thickness depends on the coating process and the coating formulation. The coater rod gives only an indication of thickness. The measurements indicated that the final thickness is a function of the solid content in the wet coating. The thickness of coating can also be fitted to distribution curves. The characterisation of thickness by distribution allows representation of the coating irregularities. The irregularities of the coating were shown to be governed by the substrate (bottom coating surface), in this case linerboard paper. This is because the distribution of

cellulosic fibres that constitute the linerboard structure provides a very uneven surface for coating application. The observation of coating profile by SEM offers high accuracy in the measurement; however, a larger number of images are needed to gain a representative thickness profile. Routines based on programming may help to evaluate the large number of required images. This technique can also be expensive and high level of knowledge and experience in the operation of the instrument is required. A less accurate, but cheaper and easy to accomplish option is the use of transmitted light microscope for image capture (sometimes called reflected or incident light microscope).

The formulation of dispersion coatings plays an important role in their barrier performance. As the volume fraction of fillers increases, the transmission rate of both water vapour and oxygen decreases. The reduction in the transmission rate was higher for those coatings formulated with larger fillers. The fillers had a greater influence in the improvement of barrier properties in the case of thin coatings. In the cases of thicker dispersion coatings, the improvement of barrier properties is related to the increase of the permeant pathway length created by the coating itself and not for the fillers geometry.

The model differentiates the effect of volume fraction and size of fillers on the relative permeability of dispersion coatings. Compared with the experimental data, the model overestimated the barrier properties of dispersion coatings. The differences may be related to the natural variability of the experimental data and the more ideal conditions that the model represents. However, despite those differences, the model followed the trends observed in the experiments. This allows comparison in terms of general variation between coating formulations instead of accurate predictions for particular conditions. The predictions can be improved by including better representation of filler shape and irregularities of the coating profile.

Despite the understanding of the diffusion process through barriers, it was a challenge to develop the model. The difficulties were related to the definition of the geometries and the mathematical solution process. The generation of dispersion coating geometries requires the random placement of a population of fillers into a representative elemental volume (REV) of the binder. During this process, the likelihood of overlapping between fillers is very high. This is particularly manifested when the volume of fraction of filler is large. In three dimensions, the techniques to avoid fillers overlapping are computationally and mathematically demanding. The definition of filler shape also affects the meshing of the coating geometries. For more intricate shapes, the fillers have to be discretised into more parts. This increases the number of elements of the mesh and, as a result, the number of calculations required to be solved the simulations. In

general, the process of simulation has to be carried out with a balance between the accuracy in the coatings/filler description, accuracy of the prediction, and the available computing resources. The use of regular shapes of the filler can help to simplify this process. According to the method used to populate fillers into the coating binder, it is practical to simulate dispersion coatings with up to 20% of volume fraction of clay particles. This represents about 40% of fillers on a mass fraction basis.

The model represents an advance in the understanding of how dispersion coatings work. Because the model allows prediction of barrier properties, it is possible to infer how coating formulations can be improved to achieve better barrier performance. This makes possible the application of the models in the industry to add value to products. Due to the advances of computing technology, improvement in capabilities for simulation and the reduction processing time, more complex models and simulations are expected in the soon future. Thus, this study could be used as a basis for the next investigations in order to create closer representations of the diffusion through barrier dispersion coatings.

8.2 Recommendation for further studies

Due to this study being the first time that a predictive model has been developed to estimate the barrier properties of dispersion coatings, several aspects were not fully explored in this study. Some of them are related to description of dispersion coating, fillers, or modelling. A list of potential future research is presented below:

- Improve the characterisation of filler geometry. In particular, develop a method to ensure no filler agglomeration in samples to be observed. This may also help to characterise the smallest fillers.

- Study how fillers are distributed in the coating binder. Factors such as orientation of fillers in the coating or settling may help in the definition of the geometries for simulation. However, this characterisation is difficult. The common techniques for observation of fillers distributed in coatings are based on SEM images of the coating profile. Thus, this only allows examination of a few points of view (i.e. machine direction, cross machine direction, or top coating surface). Other techniques such as attenuated total reflectance infrared analysis (ATR-IR) or X-ray diffraction have been used to explore the alignment of fillers in the dispersion coatings. However, the given information from these techniques describes the orientation of the fillers in a general way. Thus, reconstruction of coating geometries seems to be not possible. A potential good technique is the X-ray microtomography (XMT); however, the achievable

magnification of the instrument is closer to the thickness of clays. This may limit its application for only description of the coating geometry and not for characterisation of fillers dispersion.

- Understand how the coating behaves from application to consolidation on the substrate, in order to understand how the filler arrangement is developed during the coating process. This information together with the understanding developed in this work may help in the physical generation of geometries with larger volume fraction of fillers. Also, study of the latex particle packing after coating consolidation can help in the identification of potential variation of diffusivity across coating binder. As a result, the model can be modified including anisotropic diffusivity as part of the conceptual model.

- Incorporation of irregularities of the bottom coating surface in the simulations. This study proposed an approximation of this. However, the effect of the irregularities of the bottom coating surface on the orientation of fillers was not considered. It is expected that the irregularities force the fillers to be parallel to the bottom surface. Because the bottom surface is irregular, the fillers will be diagonally oriented reducing their capability to stop permeants.

- Eventual incorporation of the Fourier shape descriptor to define of filler shapes. This may improve the prediction of the model. It is expected that modelling with such complexity will be practical to simulate in the near future.

- Analysis and incorporation in the model of other factors related to the performance of dispersion coatings. For example, the effect on barrier performance of additives used in commercial coatings such as wax, small spheres, and others.

Chapter 9

REFERENCES

Alava, M., & Niskanen, K. (2006). The physics of paper. *Reports on Progress in Physics, 69*(3), 669-723. doi: 10.1088/0034-4885/69/3/R03

Allem, R. (1998). Characterization of paper coatings by scanning electron microscopy and image analysis. *Journal of Pulp and Paper Science, 24*(10), 329-336.

Allen, T. (1997). *Particle size measurement: Powder sampling and particle size measurement* (Vol. 1). Padstow, England: Chapman & Hall.

Andersson, C. (2008). New ways to enhance the functionality of paperboard by surface treatment: A review. *Packaging Technology and Science, 21*(6), 339-373. doi: 10.1002/pts.823

Andersson, C., Ernstsson, M., & Järnström, L. (2002). Barrier properties and heat sealability/failure mechanisms of dispersion-coated paperboard. *Packaging Technology and Science, 15*(4), 209-224. doi: 10.1002/pts.590

Andrady, A. L. (2008). *Science and technology of polymer nanofibres*. Hoboken, NJ: John Wiley & Sons.

Aris, R. (1986). On a problem in hindered diffusion. *Archive for Rational Mechanics and Analysis, 95*(2), 83-91.

Arora, A., & Padua, G. D. (2010). Review: Nanocomposites in Food Packaging. Journal of Food Science. *Journal of Food Science, 75*(1), 43-49. doi: 10.1111/j.1750-3841.2009.01456.x

Asbeck, W. K., & Van Loo, M. (1949). Critical pigment volume relationships. *Industrial and Engineering Chemistry, 41*(7), 1470-1475. doi: 10.1021/ie50475a042

ASHRAE. (2013). *ASHRAE Handbook: Fundamentals*. Atlanta, GA: American Society of Heting, Refrigerating and Air-Conditioning Engineers.

ASTM standard D3985-05. (2010). Oxygen Gas Transmission Rate Through Plastic Film and Sheeting Using a Coulometric Sensor. ASTM International, West Conshohocken, PA, 2010. doi: 10.1520/D3985-05R10E01

ASTM standard E96-95. (1995). Standard Test Methods for Water Vapor Transmission of Materials. ASTM International, Philadelphia, PA, 1995

ASTM standard F1927-07. (2007). Determination of Oxygen Gas Transmission Rate, Permeability and Permeance at Controlled Relative Humidity Through Barrier

Materials Using a Coulometric Detector. ASTM International, West Conshohocken, PA, 2007. doi: 10.1520/F1927-07

ASTM standard F2476-05. (2006). Determination of Carbon Dioxide Gas Transmission Rate (Co_2TR) Through Barrier Materials Using An Infrared Detector. ASTM International, West Conshohocken, PA, 2006. doi: 10.1520/F2476-05

ASTM standard F2622-08. (2008). Oxygen Gas Transmission Rate Through Plastic Film and Sheeting Using Various Sensors. ASTM International, West Conshohocken, PA, 2008. doi: 10.1520/F2622-08E01

Ayyub, B. M., & McCuen, R. H. (2011). *Probability, Statistics, and Reliability for, Engineers and Scientists* (3rd ed.). Boca Raton, FL: CRC Press.

Banks, N. H., Cleland, C. J., Cameron, A. C., Beaudry, R. M., & Kader, A. (1995). Proposal for a rationalized system of units for postharvest research in gas exchange. *HortScience, 30*(6), 1129-1131.

Baranau, V., Hlushkou, D., Khirevich, S., & Tallarek, U. (2013). Pore-size entropy of random hard-sphere packings. *Soft Matter, 9*, 3361-3372. doi: 10 .1039/c3sm2737 4a

Bergaya, F., & Lagaly, G. (2013). General introduction: Clays, clay minerals, and clay science. In F. Bergaya & G. Lagaly (Eds.), *Hanbook of Clay Science Part A: Fundamentals* (2nd ed.). Amsterdam, The Netherlands: Elsevier.

Bernstein, O., & Shapiro, M. (1994). Direct determination of the orientation distribution function of cylindrical particles immersed in laminar andturbulent shear flows. *Journal of Aerosol Science, 25*(1), 113–136.

Bertrand, F., Gange, T., Desaulniers, E., Vidal, D., & Hayes, R. E. (2004). Simulation of the consolidation of paper coating structures: Probabilistic versus deterministic models. *Computer and Chemical Engineering, 28*(12), 2595-2604. doi: 10.1016/j.compchemeng.2004.07.004

Bharadwaj, R. K. (2001). Notes: Modeling the barrier properties of polymer-layered silicate nanocomposites. *Macromolecules, 34*(26), 9138-9192. doi: 10.1021/ma010780b

Biermann, C. J. (1996). *Handbook of Pulping and Papermaking* (2nd ed.). San Diego, CA: Academic press.

Bollström, R., Nyqvist, R., Preston, J., Salminen, P., & Toivakke, M. (2013). Barrier properties created by dispersion coating. *Tappi Journal, 12*(4), 45-51.

Bowman, E. T., Soga, K., & Drummond, W. (2001). Particle shape characterisation using Fourier descriptor analysis. *Géotechnique, 51*(6), 545-554.

Braunshausen, R. H., Baltrus, R. A., & De Bolt, L. (1992). A review of methods of CPVC determination (critical pigment volume concentration). *Journal of Coatings Technology, 64*, 51-55.

Bristow, A. (2009). The surface of paper. In G. Henriksson, G. Gellerstedt & M. Ek (Eds.), Pulp and Paper Chemistry and Technology: Paper Products Physics and Technology (Vol. 4). Berlin, Germany: Walter de Gruyter Gmb & Co.

Bundy, W. M., & Ishley, J. N. (1991). Kaolin in paper filling and coating. *Apply Clay Science, 5*(5-6), 397-420.

Chandrupatla, T. R., & Belegundu, A. D. (2012). *Introduction to finite elements in enginering* (4th ed.). Harlow, England: Pearson Education.

Chinga, G., Helle, T., & Johnse, P. O. (2000). *Characterization of pigment coating layer structure using SEM and digital image*. Paper presented at the Tappi Conference and Trade Fair.

Choudalakis, G., & Gotsis, A. D. (2009). Permeability of polymer/clay nanocomposites: A review. *European Polymer Journal, 45*(4), 967-984. doi: 10.1016/j.eurpolymj.2009.01.027.

Comsol. (2013). *Comsol multiphysics reference manual version 4.3b.* Retrieved April 3, 2014, from http://www.comsol.com/shared/downloads/4.3b/ReleaseNotes.pdf

Comyn, J. (Ed.). (1985). *Polymer Permeability*. London: Elsevier Applied Science.

Crank, J. (1956). *The mathematics of diffusion*. Oxford: Clarendon Press.

Cussler, E. L., Hughes, S. E., Ward, W. J., & Aris, R. (1988). Barrier membranes. *Journal of Membrane Science, 38*(2), 161-174.

Dan, B., Irvin, G. C., & Pasquali, M. (2009). Continuous and scalable fabrication of transparent conducting carbon nanotube films. *ACS Nano, 3*(4), 835-843. doi: 10.1021/nn8008307

de Azeredo, H. M. C. (2009). Nanocomposites for food packaging applications. *Food research international, 42*(9), 1240-1253. doi: 10.1016/j.foodres.2009.03.019

Deng, X., & Chawla, N. (2006). Modeling the effect of particle clustering on the mechanical behavior of SiC particle reinforced Al matrix composites. *Journal of Materials Science, 41*(17), 5731-5734. doi: 10.1007/s10853-006-0100-1

Djamarani, K. M., & Clark, I. M. (1997). Characterization of particle size based on fine and coarse fractions. *Powder Technology, 93*(2), 101-108.

Drage, G., & Tamms, O. (2000). Kaolin. In E. Lethinen (Ed.), *Pigment coating and surface sizing of paper*. Helskinki, Finland: Gummerus Printing.

Drugan, W. J., & Willis, J. R. (1996). A micromechanics-based nonlocal constitutive equation and estimates of representative volume element size for elastic composites. *Journal of the Mechanics and Physics of Solids, 44*(4), 497–524.

Echlin, P. (2009). *Handbook of sample preparation for scanning electron microscopy and X-ray microanalysis*. London: UK: Springer.

Ehrlich, R., & Weinberg, B. (1970). An exact method for characterization of grain shape. *Journal of Sedimentary Research, 40*(1), 205-212.

Eksi, G., & Bousfield, D. W. (1997). Modeling of coating structure development. *Tappi Journal, 80*(2), 125-135.

Embrechts, P., Klüppelberg, C., & Mikosch, T. (1997). *Modelling extremal events for insurance and finance*. New York, NY: Springer.

Euston, S. R., Costello, G., Naser, M. A., & Nicolasai, M. L. (2007). Modelling and computer simulation of food structures. In I. D. J. McClements (Ed.), *Understanding and controlling the microstructure of complex food* (pp. 334-386). Cambrige, England: Woodhead Publishing Limited.

Fagan, M. J. (1992). *Finite element analysis: Theory and practice*. New York, NY: John Wiley & Sons.

Falla, W. R., Mulski, M., & Cussler, E. L. (1996). Estimating diffusion through flake-filled membranes. *Journal of Membrane Science, 119*(1), 129-138.

Fang, Q., & Zhang, J. (2014). 3D numerical modeling of projectile penetration into rock-rubble overlays accounting for random distribution of rock-rubble. *International Journal of Impact Engineering, 63*, 118-128. doi: 10.1016/j.ijimpeng.2013.08.010

Fellers, C. (2009). The structure of paper and its modelling. In M. Ek, G. Gellerstedt & G. Henriksson (Eds.), Pulp and Paper Chemistry and Technology: Paper Products Physics and Technology (Vol. 4). Berlin, Germany: Walter de Gruyter Gmb & Co..

Finnigan, B. (2009). Barrier polymers. In K. L. Yam (Ed.), *The Wiley Encyclopedia of Packaging Technology* (3rd ed.). New York, NY: John Wiley & Sons.

Fisher, R. B., Breckon, T. P., Dawson-Howe, K., Fitzgibbon, A., Robertson, C., Trucco, E., & Williams, C. K. I. (2014). *Dictionary of Computer Vision and Image Processing* (2nd ed.). Chichester, West Sussex: John Wiley & Sons Inc.

Fishman, S., Rodov, V., & Ben-Yehoshua, S. (1996). Mathematical model for perforation effect on oxygen and water vapor dynamics in modefifed-atmosphere packages. *Journal of Food Science, 61*(5), 956-961.

Fitzgibbon, A., Pilu, M., & Fisher, R. B. (1999). Direct least square fitting of ellipses. *Pattern Analysis and Machine 21*(5), 476-480. doi: 10.1109/34.765658

Fredickson, G. H., & Bicerano, J. (1999). Barrier properties of oriented disk composites. *Journal of Chemical Physics, 110*(4), 2181-2188.

Gander, W., Golub, G. H., & Strebel, R. (1994). Least-Squares Fitting of Circles and Ellipses. *BIT Numerical Mathematics, 34*(4), 558-578.

Geankoplis, C. J. (2003). *Transport processes and separation process principles (Includes Unit Operations)* (4th ed.). New Jersey: Prentice Hall.

Gelinas, D., & Vidal, D. (2010). Determination of particle shape distribution of clay using an automated AFM image analysis method. *Powder Technology, 203*(2), 254-264. doi: 10.1016/j.powtec.2010.05.016

Goodyer, C. E., & Bunge, A. L. (2009). Comparison of numerical simulations of barrier membranes with impermeable flakes. *Journal of Membranes Science, 329*(1-2), 209-218.

Grim, R. E. (1968). *Clay Mineralogy* (2nd ed.). New York, NZ: McGraw-Hill.

Gusev, A. A., & Guseva, O. (2007). Rapid Mass Transport in Mixed Matrix Nanotube/Polymer Membranes. *Advanced Materials, 19*(18), 2672-2676. doi: 10.1002/adma.200602018

Gusev, A. A., & Lusti, H. R. (2001). Rational design of nanocomposites for barrier applications. *Advanced Materials, 13*(21), 1641-1643.

Hawkins, A. E. (1990). Characterizing the single particles. In M. J. Rhodes (Ed.), *Principles of powder technology*. Chichester, England: John Willey & Sons.

Hentschel, M. L., & Page, N. W. (2003). Selection of descriptors for particle shape characterization. *Particle and Particle Systems Characterization, 20*(1), 25-38. doi: 10.1002/ppsc.200390002

Holik, H. (Ed.). (2006). *Handbook of paper and board*. Weinheim, Germany: Wiley-VCH. .

Hosking, J. R. M., Wallis, J. R., & Wood, E. F. (1985). Estimation of the generalized extreme-vale distribution by the method of probability-weifhted moments. *Technometrics, 27*(3), 251-261.

Hubbe, M. A. (2005). Paper. In: (Ed.), Kirk-Othmer Encyclopedia of Chemical Technology. New York, NY: John Wiley and Sons. doi: 10.1002/0471238961

Hussain, F., & Mehdi, H. (2006). Review article: Polymer-matrix nanocomposites, processing, manufacturing, and application: An overview. *Journal of Composite Materials, 40*(17), 1511-1575. doi: 10.1177/0021998306067321

Jianzhong, L., Weifeng, Z., & Zhaosheng, Y. (2004). Numerical research on the orientation distribution of fibers immersed in laminar and turbulent pipe flows. *Aerosol Science, 35*(1), 63 – 82. doi: 10.1016/S0021-8502(03)00388-4

Johansson, C. (2002). *Interactions between Polymers in Dispersion Coating and Surface Sizing of Paper and Board.* (Doctoral thesis), Karlstad University, Karlstad, Sweden.

Kanit, T., Forest, S., Galliet, I., Mounoury, V., & Jeulin, D. (2003). Determination of the size of the representative volume element for random composites: Statistical and numerical approach. *Int. J. Solids Struct., 40*, 3647-3679. doi: 10.1016/S0020-7683(03)00143-4

Keddie, J. L. (1997). Film formation of latex *Materials Science and Engineering: R: Reports, 21*(3), 101-170. doi: 10.1016/S0927-796X(97)00011-9

Khwaldia, K., Arab-Tehrany, E., & Desobry, S. (2010). Biopolymer coatings on paper packaging materials. *Comprehensive Reviews in Food Science and Food Safety, 9*(1), 82-90. doi: 10.1111/j.1541-4337.2009.00095.x

Kimpimäki, T., & Savolainen, A. V. (1997). Barrier dispersion coating of paper and board In J. Brander & I. Thorn (Eds.), *Surface Application of Paper Chemicals* (pp. 208-228).

Kirwan, M. J. (Ed.). (2005). *Paper and paperboard: Packaging technology*. Oxford,UK: Blackwell Publishing.

Krochta, J. M. (2010). Packaging: Permeability. In D. R. Heldman & C. I. Moraru (Eds.), *Encyclopedia of Agricultural, Food, and Biological Engineering* (2nd ed.). Boca Raton, FL: Taylor & Francis.

Kruger, J. (2011). *Mathematical modelling of mass transfer in food packaging systems.* (Master's thesis), Massey University, Palmerston North, New Zealand.

Kugge, C., Craig, V. S. J., & Daicic, J. (2004). A scanning electron microscope study of the surface structure of mineral pigments, latices and thickeners used for paper coating on non-absorbent substrates. *Colloids and Surfaces A: Physicochemical and Engineering Aspects, 238*(1-3), 1-11. doi: 10.1016/j.colsurfa.2004.02.029

Kugge, C., & Johnson, B. (2008). Improved barrier properties of double dispersion coated liner. *Progress in Organic Coatings, 62*(4), 430-435. doi: 10.1016/j.porgcoat.2008.03.006

Kwon, O., Zumbrunnen, D. A. (2003). Production of barrier films by chaotic mixing of plastics. *Polymer Engineering and Science, 43*(8), 1443-1459.

Lange, J., & Wyser, Y. (2003). Recent innovations in barrier technologies for plastic packaging: A review. *Packaging Technology and Science, 16*(4), 146-157. doi: 10.1002/pts.621

Lape, N. K., Nuxoll, E. E., & Cussler, E. L. (2004). Polydisperse flakes in barrier films. *Journal of Membrane Science, 234*(1-2), 29-37. doi: 10.1016/j.memsci.2003.12.026

LeBaron, P. C., Wang, Z., & Pinnivaia, T. J. (1999). Polymer-layered silicate nanocomposites: An overview. *Applied Clay Science, 15*(1-2), 11-29. doi: 10.1016/S0169-1317(99)00017-4

Lee, D. S., Yam, K. L., & Piergiovanni, L. (2008). *Food packaging science and technology*. Boca Raton, FL: CRC Press.

Lehtinen, E. (2000a). Coating binders - general. In E. Lehtinen (Ed.), *Pigment coating and surface sizing of paper*. Helskinki, Finland: Gummerus Printing.

Lehtinen, E. (2000b). Coating pigments - general. In E. Lehtinen (Ed.), *Pigment coating and surface sizing of paper*. Helskinki, Finland: Gummerus Printing.

Lehtinen, E. (2000c). Introduction to pigment coating of paper. In E. Lehtinen (Ed.), *Pigment coating and surface sizing of paper*. Helskinki, Finland: Gummerus Printing.

Lehtinen, E. (Ed.). (2000d). *Pigment coating and surface sizing of paper*. Helskinki, Finland: Gummerus Printing.

Leonard, M. W. (2009). Barrier and overprint coatings. In K. L. Yam (Ed.), *The Wiley Encyclopedia of Packaging Technology* (3rd ed.). New York, NY: John Wiley & Sons.

Lepoutre, P. (1989). The structure of paper coating: An update. *Progress in Organic Coatings, 17*(2), 89-106.

Li, Y., & He, B. (2012). Study on coating surface topography and properties of coated paper related to pigment. *Advanced Materials Research, 466-467*, 504-507. doi: 10.4028/www.scientific.net/AMR.466-467.504

Li, Z., Yang, J., Xu., X., Xu, X., Yu, W., Yue, X., & Sun, C. (2002). Particle shape characterization of fluidized catalytic cracking catalyst powders using the mean value and distributuon of shape factors. *Advanced Powder Technology, 13*(3), 249-263. doi: 10.1163/156855202320252435

Linnonmaa, J., & Trefz, M. (2000). Pigment coating techniques. In E. Lehtinen (Ed.), *Pigment coating and surface sizing of paper*. Helsinki, Finland: Gummerus Printing.

Liu, G. R., & Quek, S. S. (2013). *The finite element method: A practical course* (2nd ed.). Oxford, UK: Elsevier.

Lu, C., & Mai, Y.-W. (2007). Permeability modelling of polymer-layered silicate nanocomposites. *Composites Science and Technology, 67*(14), 2895-2902. doi: 10.1016/j.compscitech.2007.05.008

Lu, M., & McDowell, G. R. (2007). The importance of modelling ballast particle shape in the discrete element method. *Granular Matter, 9*(1-2), 69-80. doi: 10.1007/s10035-006-0021-3

Luo, J. J., & Daniel, I. M. (2003). Characterization and modeling of mechanical behavior of polymer/clay nanocomposites. *Composites Science and Technology, 63*(11), 1607–1616. doi: 10.1016/S0266-3538(03)00060-5

Masuda, H., Higashitani, K., & Yoshida, H. (Eds.). (2006). *Powder Technology Handbook* (3th ed.). Boca Raton, FL: Taylor & Francis.

Matteucci, S., Yampolskii, Y., Freeman, B. D., & Pinnau, I. (2006). Transport of Gases and Vapors in Glassy and Rubbery Polymers. In Y. Yampolskii, I. Pinnau & B. Freeman (Eds.), *Materials Science of Membranes for Gas and Vapor Separation* Chichester, UK: John Wiley & Sons, Ltd.

Mesic, B., Kugge, C., & Järnström, L. (2010). Superhydrophobic paper coating containing nonconventional clay. *Tappi Journal, 9*(11), 33-40.

Michaels, A. S., & Bixler, H. J. (1961). Solubility of gases in polyethilene. *Journal of Polymer Science, 50*(144), 393–412. doi: 10.1002/pol.1961.1205015411

Michler, G. H. (2008). *Electron microscopy of polymer*. Berlin, Germany: Springer.

Mills, A. (1997). Optical oxygen sensors: Utilising the limunescence of platinum metals complexes. *Platinum Metals Review, 41*(3), 115-127.

Minelli, M., Baschetti, M. G., & Doghieri, F. (2011). A comprehensive model for mass transport properties in nanocomposites. *Journal of Membranes Science, 381*(1-2), 10-20. doi: 10.1016/j.memsci.2011.06.036

Moggridge, G. D., Lape, N. K., Yang, C., & Cussler, E. L. (2003). Barrier films using flakes and reactive additives. *Process in Organic Coatings, 46*(4), 231-240. doi: 10.1016/S0300-9440(02)00180-7

Nagy, T. F., & Duxbury, P. M. (2002). Permeability and conductivity of platelet-reinforced membranes and composites. *Physical Review E, E66*(020802(R)), 1-4. doi: 10.1103/PhysRevE.66.020802

Nazarenko, S., Meneghetti, P., Julmon, P., Olson, B. G., & Qutubuddin, S. (2007). Gas barrier of polystyrene montmorillonite clay nanocomposites: Effect of mineral layer aggregation. *Journal of Polymer Science: Part B: Polymer Physics, 45*(13), 1733-1753. doi: 10.1002/polb.21181

Nielsen, L. E. (1967). Models for the permeability of filled polymer systems. *Journal of Macromolecular Science: Part A - Chemistry, 1*(5), 929-942. doi: 10.1080/10601326708053745

Nolan, G. T., & Kavanagh, P. E. (1995). Random packing of nonspherical particles *Powder Technology, 84*(3), 199-205. doi: 10.1016/0032-5910(95)98237-S

Osborn, K. R., & Jenkins, W. R. (1992). *Plastic films: Technology and packaging applications*. Lancaster, PA: Technomic Publishing Company.

Pal, R. (2008). Permeation models for mixed matrix membranes. *Journal of Colloid and Interface Science, 314*(1), 191-198. doi: 10.1016/j.jcis.2007.09.032

Park, H. M., Lee, W. K., Park, C. Y., Cho, W. J., & Ha, C. S. (2003). Environmentally friendly polymer hybrids: Part I Mechanical, thermal, and barrier properties of thermoplastic starch/clay nanocomposites. *Journal of Materials Science, 38*, 909-915.

Podczeck, F. (1997). A shape factor to assess the shape of particles using image analysis. *Powder Technology, 93*(1), 47-53. doi: 10.1016/S0032-5910(97)03257-9

Pöhler, T., Juvonen, K., & Sneck, A. (2006). *Coating layer microstructure and location of bidner: Result from SEM analysis*. Paper presented at the Advanced Coating Fundamentas Symposium, Turki, Finland.

Pratt, V. (1987). Direct least-squares fitting of algebraic surfaces. *Computer Graphics, 21*(4), 145-152.

Pryor, R. W. (2012). *Multiphysics modeling using Comsol® 4: A first principles approoach*. Boston, Mass.: Mercury Learning and Information.

Reddy, J. N., & Gartling, D. K. (2010). *The finite element method in heat transfer and fluid dynamics* (3rd ed.). Boca Raton, Fl: Taylor & Francis Group.

Riegel, C. A. (1974). Comments on " A simple but accurate formula for the saturation vapor pressure over liquid water. *Journal of Applied Meteorology, 13*, 606-607.

Rissa, K., Lepisto, T., Vaha-Nissi, M., & Savolainen, A. (2000). Orientation of talc fillers in dispersion coatings. *Nordic Pulp and Paper Journal, 15*(5), 357-361.

Rissa, K., Lepistö, T., & Yrjölä, K. (2006). Effect of kaolin content on structure and functional properties of water-based coatings. *Progress in Organic Coatings, 55*(2), 137-141. doi: 10.1016/j.porgcoat.2005.09.009

Robertson, G. L. (2013). *Food packaging: Principles and practice* (3rd ed.). Boca Raton, Fl: CRC Press.

Russ, J. C. (1990). *Computer assisted microscopy: The measurement and analysis of images*. New York, NY: Plenum Press.

Russ, J. C. (2011). *The image processing handbook* (6th ed.). Boca Raton, FL: Taylor and Francis Group.

Samyn, P., Deconinck, M., Schoukens, G., Stanssens, D., Vonck, L., & Van den Abbeele, H. (2010). Modifications of paper and paperboard surfaces with a nanostructured polymer coating. *Progress in Organic Coatings, 69*(4), 442-454. doi: 10.1016/j.porgcoat.2010.08.008

Schatten, H. (2013). The role of scanning electron microscopy in cell and molecular biology: SEM basics, past accomplishments, and new frontiers. In H. Schatten (Ed.), *Scanning electron microscopy for the life sciences*. Cambridge, NY: Cambridge University Press.

Schuman, T., Adolfsson, B., Wikström, M., & Rigdahl, M. (2005). Surface treatment and printing properties of dispersion-coated paperboard. *Progress in Organic Coatings, 54*(3), 188-197. doi: 10.1016/j.porgcoat.2005.06.010

Schuman, T., Karlsson, A., Larsson, J., Wikström, M., & M., R. (2005). Characteristics of pigment-filled polymer coatings on paperboard. *Progress in Organic Coatings, 54*(1), 360-371. doi: 10.1016/j.porgcoat.2005.06.017

Schuman, T., Wikström, M., & Rigdahl, M. (2004a). Dispersion coating with carboxylated and cross-linked styrene-butadiene latices 1. Effect of some polymer characteristics on film properties. *Progress in Organic Coatings, 51*(3), 220-227. doi: 10.1016/j.porgcoat.2004.07.015

Schuman, T., Wikström, M., & Rigdahl, M. (2004b). Dispersion coating with carboxylated and cross-linked styrene-butadiene latices 2. Effects of substrate and polymer characteristics on the properties of coated paperboard. *Progress in Organic Coatings, 51*(3), 228-237. doi: 10.1016/j.porgcoat.2004.07.016

Shen, H., & Lissenden, C. J. (2002). 3D finite element analysis of particle-reinforced aluminum. *Materials Science and Engineering: A, 338*(1-2), 271-281. doi: 10.1016/S0921-5093(02)00094-1

Sinha Ray, S., & Okamoto, M. (2003). Polymer/layered silicate nanocomposites: A review from preparation to processing. *Progress in Polymer Science, 28*(11), 1539-1641. doi: 10.1016/j.progpolymsci.2003.08.002

Smook, G. A. (1982). *Handbook for Pulp and Paper Technologists*. Canada: Joint Texbook Comittee of the Paper Industry.

Solovyov, S., & Goldman, A. (2008). *Mass Transport and Reactive Barriers in Packaging: Theory, applications and design*. Lancaster, PA: DEStech Publications.

Sun, L., Boo, W. J., Clearfield, A., Sue, H.-J., & Pham, H. Q. (2008). Barrier properties of model epoxy nanocomposites. *Journal of Membrane Science, 318*(1-2), 129-136. doi: 10.1016/j.memsci.2008.02.041

TAPPI standard T 448 om-97. (1997).Water vapor transmission rate of paper and paperboard at 23°C and 50% RH. Technical Association of the Pulp and Paper Industry, 1997.

TAPPI standard T 448 om-09. (2009).Water vapor transmission rate of paper and paperboard at 23°C and 50% RH. Technical Association of the Pulp and Paper Industry, 2009.

TAPPI/ANSI standard T464 om-12. (2012).Water vapor transmission rate of paper and paperboard at high temperature and humidity. Technical Association of the Pulp and Paper Industry, 2012.

Thomopoulos, N. T. (2013). *Essentials of Monte Carlo Simulation*. New York: NY: Springer.

Tsvetkov, V. N. (1942). Molecular ordering in the anisotropic liquid. *Acta Physicochimica U.R.S.S, 16*, 132-147.

Vähä-Nissi, M., Kervinen, K., Savolainen, A., Egolf, S., & Lau, W. (2006). Hydrophobic polymers as barrier dispersion coatings. *Journal of Applied Polymer Science, 101*(3), 1958-1962. doi: 10.1002/app.23687

van Krevelen, D. W., & te Nijenhuis, K. (2009). *Properties of poylmers: Their correlation with chemical structure; their numerical estimation and prediction from additive group contributions* (4th ed.). Oxford, UK: Elsevier Science.

Vaz, C. M. P., Herrmann, P. S. P., & Crestana, S. (2002). Thickness and size distribution of clay-sized soil particles measured through atomic from atomic force microscopy. *Powder Technology, 126*(1), 51-58. doi: 10.1016/S0032-5910(02)00037-2

Velde, B. (1995). Composition and minerology of clay minerals. In B. Velde (Ed.), *Origin and minerology of clays: Clays and the enviroment*. New York: NY: Springer.

Vernhes, P., Dubé, M., & Bloch, J. F. (2010). Effect of calendering on paper surface properties. *Applied Surface Science, 256*(22), 6923–6927. doi: 10.1016/j.apsusc.2010.05.004

Waack, R., Alex, N. H., Frisch, H. L., Stannett, V., & Szwarc, M. (1955). Permeability of polymer films to gases and vapors. *Industrial and Engineering Chemistry, 47*(12), 2524-2527.

Wakeham, W. A., & Mason, E. A. (1979). Diffusion through multiperforate laminae. *Industrial and Engineering Chemistry Fundamentals, 18*(4), 301-305.

Wang, Z. F., Wang, B., Qi, N., Zhang, H. F., & Zhang, L. Q. (2005). Influence of filler on free volume and gas barrier properties in styrene-butadiene rubber studied by positrons. *Polymer, 46*(3), 719-724. doi: 10.1016/j.polymer.2004.12.002

Wilhelm, L. R. (1976). Numerical calculation of psychrometric properties in SI units. *Transaction of the ASAE, 19*(2), 318-321.

Wu, G., Zhang, Q., Yang, X., & Huang, X. (2014). Effects of particle/matrix interface and strengthening mechanisms on the mechanical properties of metal matrix composites. *Composite Interfaces, 21*(5), 415-429. doi: 10.1080/15685543.2014.872914

Zeng, Q. H., Yu, A. B., & Lu, G. Q. (2008). Multiscale modeling anf simulation of polymer nanocomposite. *Process Modelling and Simulations with Finite Element Methods, 33*(2), 191-269. doi: 10.1016/j.progpolymsci.2007.09.002

Zhu, Y. D., Allen, G. C., Adams, J. M., Gittins, D. I., Hooper, J. J., & Skuse, D. R. (2013). Barrier properties of latex/kaolin coatings. *Polymer Chemistry, 4*(16), 4386-4395. doi: 10.1039/C3PY00376K

Zienkiewicz, O. C., Taylor, R. L., & Zhu, J. Z. (2005). *The finite element method : Its basis and fundamentals* (6th ed.). Oxford ; Boston Elsevier Butterworth-Heinemann.

Zimmerman, W. J. (2004). *Process modelling and simulation with Finite Element Methods* (Vol. 15). London, England: World Scientific Publishing Co. Pte. Ltd.

Zwon, O., & Zumbrunnen, A. (2003). Production of barrier films by chaotic mixing of plastic. *Polymer Engineering and Science, 43*(8), 1443-1459. doi: 10.1002/pen.10122

Appendix A

PROGRAMS TO CALCULATE THE FOURIER SHAPE DESCRIPTOR

The estimation of the Fourier parameters was divided into two programs; the generation of filler radii and the estimation of the parameters to define the Fourier descriptors. These programs were developed in both ImageJ and Matlab. Below is a description of the codes for each program:

A.1Program 1: Identification of fillers and definition of radius

The images captured from light microscopy were made binaries by Image J (Figure A.1). From these images, the program identifies the fillers and labels them with a number. It is important to indicate that digital images are discretised in pixels. Each pixel has a value in terms of the colour. Thus, an image can be represented as a matrix. On the captured images, the fillers (white areas) have a value 1 and the black background is equal to 0. From this understanding, the filler can be identified where the value of the pixels is 1 and the edges where the values change from 1 to 0.

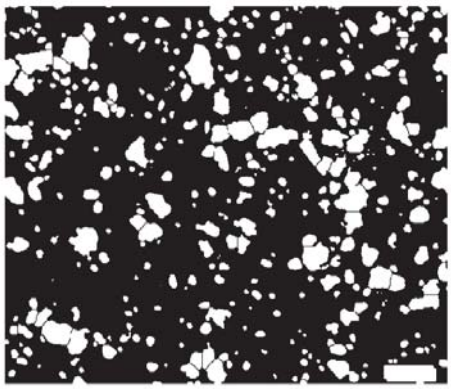

Figure A.1 Binary image of a filler sample taken by light microscopy

Fillers which are not complete such as those at the image border were not considered in the analysis. This can be carried out by checking the value of the pixel at the border. If the value of a pixel is equal to 1 (white area) at the border, the filler that the pixel is identified as not completed and it is rejected. Once the fillers were detected, the radii were defined ($R(\theta)$ in Equation 2.16). The first step is to identify the largest radius because this is the basis for the angle of rotation for the identification of the rest of the radii. For this, the extreme pixels of the

fillers were identified and from them the distance to the centre of gravity calculated (Figure A.2a). The largest distance defined the largest radius.

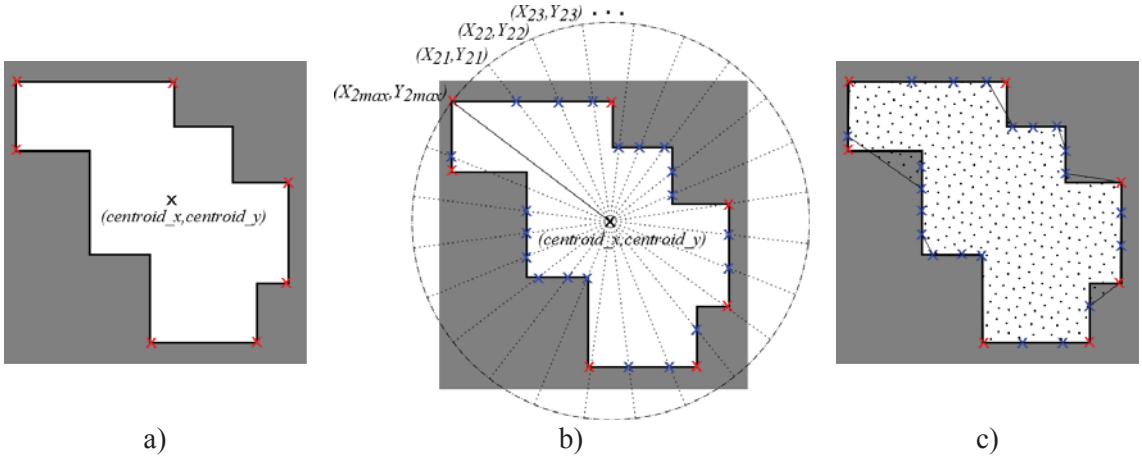

Figure A.2 Discretised filler by pixels and a) identification of the centre (black x) and the extreme pixel at the filler edges (red x), b) definition of the largest radius (continuous line) and spots of filler edges (blue x), and c) the predicted filler shape (hatched area)

A circle centred at the filler centroid with a radius equal to the largest radius was drawn as reference to project the rest of the radii (Figure 4.2b). Because the rest of radii are shorter than the radius of the circle, all the projected radii cross the filler edges. Thus, the length between the filler centre of gravity and the filler edge through the projected radii can be determined by identification of the changes in the colour of the pixels from 1 (white area) to 0 (black area) (blue x in Figure 4.2b). These lengths represent $R(\theta)$. Figure A.2c shows the final representation of the filler according the presented method. The lengths were expressed relatively by the ratio between the radius length and the largest radius length. The program exports the information into Excel files and presents the relative length at different angle of rotation for each observed filler sorter from the largest to the smallest predicted area. Figure A.3 shows the identified fillers with drawn relative radii included the discarded fillers at the image edges.

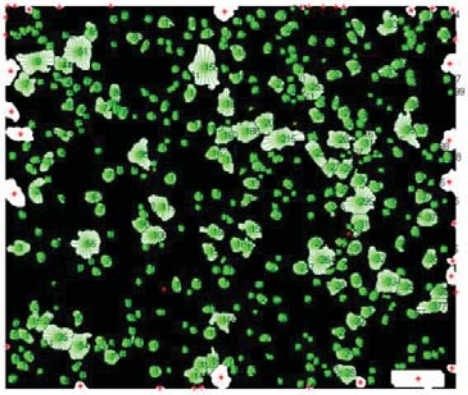

Figure A.3 Identification of the fillers and generation of radii for a sample binary image

In order to run the program, open `identification_of_filler_and_max_radius.m` in Maltab from the folder "Appendix A". The program will analyse an example image saved in the folder "Image sample". The results will be saved in the folder "Results" with the name "Radius vs Angle.xlsx". The name of the sheet will indicate the name of analysed image. This file contains the relative length of each filler at 15° (not including the rejected fillers).

A.2 Program 2: Calculation of Fourier descriptor parameters

Once the file with the relative radii was generated, the Fourier shape descriptor parameters can be determined. For this, the program extracts the data from the file. Then the calculation of a_0, a_n, and b_n are calculated based on Equation 2.16, 3.1, 3.2, and 3.3. a_0 is estimated by the mean of the relative radii. The corresponding integrals of a_n, and b_n, are calculated for each harmonic and then all the results are summed. After estimation of the Fourier shape descriptor parameters, the program predicts the shape of the fillers by estimation of the relative radii to check the number of harmonics was properly defined. As was discussed in Chapter 3, an appropriate number of harmonics was 7. A selected list of a_0, a_n, and b_n are presented in Appendix B. An example of the experimental data curve and the prediction are shown in Figure A.4.

The program exports the data of a_0, a_n, b_n, and the predicted relative radii into the same file generated in the previous program. The name of the program is `estimation_of_Fourier_parameters.m` and is available in the folder "Appendix A". Due to both programs use a common file to save the data, it is important to run first Program 1.

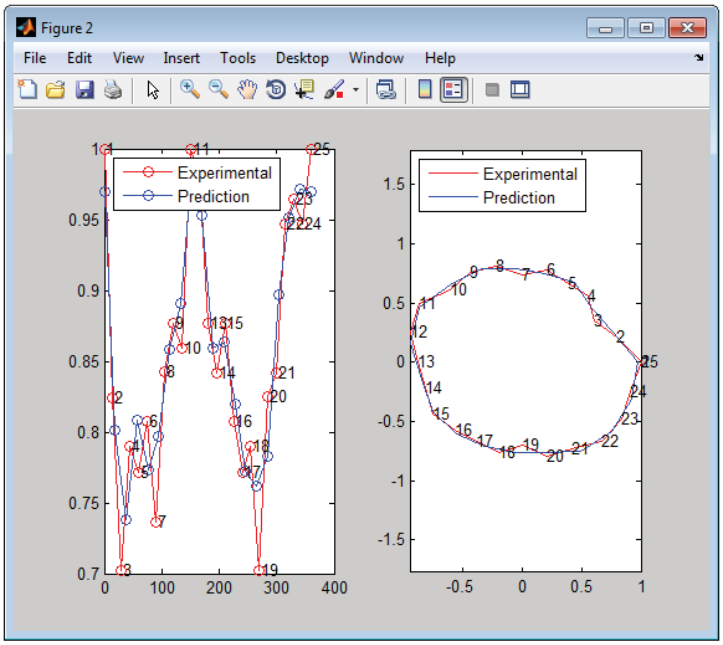

Figure A.4 Comparison between experimental and prediction of shape by Fourier shape descriptor of a sample filler

Appendix B

FOURIER SHAPE DESCRIPTOR PARAMETERS OF CLAY A, B, AND C

Table B.1 Fourier shape descriptor (a_0, a_n, and b_n) for 50 Clay A fillers

Filler	a_0	a_1	a_2	a_3	a_4	a_5	a_6	a_7	b_1	b_2	b_3	b_4	b_5	b_6	b_7
1	0.7668	0.0275	0.1292	0.0419	0.0290	-0.0125	0.0137	0.0038	0.0072	0.0373	-0.0235	0.0078	0.0080	-0.0092	-0.0132
2	0.7688	0.0276	0.0937	-0.0034	0.0612	0.0012	0.0023	0.0114	0.0021	0.0429	-0.0366	0.0212	-0.0154	0.0011	0.0121
3	0.6400	0.0091	0.2619	-0.0471	0.0264	0.0265	0.0160	0.0187	-0.0026	-0.0645	0.0112	0.0011	0.0225	0.0034	-0.0037
4	0.7668	-0.0065	0.1075	0.0164	0.0058	0.0362	0.0183	0.0134	0.0011	-0.1029	-0.0423	0.0257	0.0015	0.0000	0.0047
5	0.7014	-0.0113	0.1612	-0.0046	0.0452	0.0110	0.0163	0.0146	0.0085	-0.0423	-0.0380	-0.0397	-0.0230	-0.0058	-0.0007
6	0.8554	-0.0065	0.0707	0.0056	-0.0047	0.0162	0.0107	0.0219	-0.0034	-0.0703	-0.0208	-0.0266	0.0025	-0.0083	0.0104
7	0.7919	0.0001	0.1324	0.0160	0.0348	0.0249	-0.0057	-0.0069	0.0025	-0.0201	0.0307	-0.0134	0.0025	-0.0229	-0.0139
8	0.8154	-0.0209	0.0423	0.0643	0.0193	-0.0084	-0.0024	0.0122	-0.0075	-0.0183	0.0119	0.0312	0.0321	-0.0083	0.0058
9	0.8393	-0.0049	0.0489	0.0619	-0.0118	0.0204	-0.0012	-0.0123	0.0053	-0.0547	-0.0512	0.0613	0.0109	0.0140	0.0180
10	0.7665	-0.0226	0.1033	0.0682	0.0283	0.0297	0.0037	0.0063	0.0177	0.0871	-0.0308	0.0395	-0.0342	-0.0197	-0.0145
11	0.7938	0.0081	0.1251	0.0212	0.0177	0.0072	-0.0023	-0.0040	0.0052	0.1294	-0.0328	-0.0034	-0.0076	-0.0035	-0.0159
12	0.8828	0.0001	0.0524	0.0028	-0.0187	0.0222	0.0095	-0.0134	-0.0003	0.0047	0.0017	-0.0046	0.0269	-0.0107	-0.0159
13	0.8545	0.0016	0.0564	0.0400	-0.0131	0.0187	-0.0082	0.0111	-0.0020	0.1154	0.0277	-0.0159	0.0046	0.0163	-0.0118
14	0.6653	-0.0296	0.1908	0.0728	0.0253	0.0417	0.0036	0.0202	0.0216	-0.0636	-0.0734	0.0208	0.0007	-0.0024	-0.0041
15	0.7081	0.0025	0.2123	-0.0379	0.0560	0.0486	-0.0178	0.0078	0.0159	-0.0022	-0.0646	0.0069	-0.0140	-0.0083	0.0066
16	0.8467	-0.0144	0.0357	0.0537	0.0239	0.0008	0.0188	0.0185	-0.0110	-0.0814	0.0048	-0.0097	-0.0016	-0.0175	-0.0022
17	0.8063	0.0002	-0.0334	0.0789	0.0180	0.0229	0.0000	0.0007	0.0000	0.0193	-0.0789	-0.0312	-0.0855	-0.0640	0.0025
18	0.6542	0.0065	0.2402	-0.0156	0.0560	0.0124	0.0034	0.0098	0.0199	-0.0703	-0.0280	-0.0480	-0.0324	0.0057	-0.0161
19	0.6861	-0.0217	0.1166	0.0071	0.0805	0.0483	0.0343	0.0212	0.0057	-0.0368	-0.0174	-0.0301	-0.0209	-0.0126	-0.0123
20	0.8207	0.0041	0.1020	-0.0114	0.0151	0.0335	0.0105	0.0093	0.0123	-0.0421	-0.0446	0.0170	-0.0067	-0.0082	0.0114
21	0.7763	-0.0121	0.1140	0.0565	0.0245	0.0168	-0.0080	0.0107	-0.0019	0.0330	0.0106	-0.0022	0.0035	-0.0057	-0.0012
22	0.6945	-0.0010	0.0920	0.1603	0.0525	0.0474	0.0000	-0.0109	-0.0037	-0.0531	0.1603	-0.0909	0.0127	-0.0246	0.0029
23	0.6542	0.0065	0.2402	-0.0156	0.0560	0.0124	0.0034	0.0098	0.0199	-0.0703	-0.0280	-0.0480	-0.0324	0.0057	-0.0161

Continuation Table B.1

Filler	a_0	a_1	a_2	a_3	a_4	a_5	a_6	a_7	b_1	b_2	b_3	b_4	b_5	b_6	b_7
24	0.7151	-0.0059	0.1908	0.0294	0.0440	0.0070	0.0142	-0.0090	0.0011	-0.0572	-0.0203	0.0369	0.0014	0.0142	0.0026
25	0.8234	0.0105	0.0635	0.0116	0.0445	0.0305	-0.0140	0.0120	0.0146	0.0349	0.0326	0.0000	-0.0197	-0.0023	0.0174
26	0.6926	0.0053	0.1850	0.0341	0.0507	0.0130	0.0332	0.0043	0.0044	0.1571	0.0014	0.0000	-0.0101	-0.0119	-0.0052
27	0.8228	-0.0087	0.0380	0.0529	0.0249	0.0332	0.0012	0.0119	0.0057	0.0039	-0.0050	0.0250	0.0367	0.0116	-0.0028
28	0.7986	0.0066	0.0368	0.0034	0.0157	0.0316	0.0280	0.0273	-0.0181	-0.0115	0.0585	-0.0227	-0.0064	-0.0070	-0.0081
29	0.8229	-0.0073	0.1154	0.0609	-0.0068	-0.0108	0.0084	-0.0012	-0.0151	-0.0462	0.0254	-0.0329	0.0183	0.0133	-0.0079
30	0.8200	-0.0115	0.1355	0.0265	0.0326	0.0076	0.0060	-0.0058	-0.0094	-0.0389	0.0215	0.0000	0.0027	-0.0084	0.0018
31	0.8200	-0.0115	0.1355	0.0265	0.0326	0.0076	0.0060	-0.0058	-0.0094	-0.0389	0.0215	0.0000	0.0027	-0.0084	0.0018
32	0.6639	-0.0183	0.2553	0.0527	0.0293	0.0006	0.0154	-0.0090	-0.0038	-0.0537	-0.0079	-0.0162	0.0117	0.0095	-0.0007
33	0.8786	-0.0042	-0.0110	0.0528	0.0340	0.0233	-0.0166	0.0007	0.0069	0.0387	-0.0029	-0.0012	0.0348	0.0059	0.0070
34	0.8982	-0.0023	0.0084	0.0393	0.0546	-0.0111	0.0246	0.0081	-0.0208	-0.0134	-0.0003	0.0012	0.0133	-0.0074	0.0161
35	0.7455	-0.0004	0.1598	0.0671	0.0511	-0.0362	0.0093	0.0120	-0.0095	0.0141	-0.0586	0.0363	0.0237	-0.0408	0.0214
36	0.8554	-0.0065	0.0707	0.0056	-0.0047	0.0162	0.0107	0.0219	-0.0034	-0.0703	-0.0208	-0.0266	0.0025	-0.0083	0.0104
37	0.8172	-0.0121	0.1419	0.0313	0.0066	0.0309	-0.0151	-0.0040	0.0053	-0.0398	-0.0250	0.0272	-0.0073	0.0023	-0.0006
38	0.8000	0.0000	0.0479	0.0000	0.0970	0.0000	0.1141	0.0000	0.0000	0.0000	0.0000	0.0000	0.0000	0.0000	0.0000
39	0.7771	-0.0131	0.1575	0.0607	0.0088	0.0239	-0.0133	-0.0063	-0.0009	0.0524	0.0155	-0.0223	-0.0068	0.0036	0.0230
40	0.7903	0.0000	0.0000	0.0000	0.1336	0.0000	0.0000	0.0000	0.0000	0.0000	0.0000	-0.2315	0.0000	0.0000	0.0000
41	0.8317	-0.0105	0.1021	0.0284	0.0039	0.0003	0.0000	-0.0020	0.0000	0.0000	0.0000	0.0000	0.0000	0.0000	0.0000
42	0.7634	-0.0140	0.0729	-0.0027	0.0576	0.0232	0.0280	0.0259	-0.0078	0.0411	0.0795	-0.0204	0.0285	0.0291	0.0073
43	0.7414	-0.0017	-0.0711	0.0814	0.0367	0.0616	0.0419	0.0069	0.0167	0.1371	-0.0339	-0.0363	0.0129	-0.0012	0.0030
44	0.6903	0.0071	0.2052	-0.0251	0.0675	0.0292	0.0186	0.0039	0.0073	-0.1037	-0.0064	-0.0125	0.0119	-0.0105	-0.0071
45	0.8186	-0.0101	0.0808	0.0783	0.0156	0.0010	-0.0036	-0.0050	-0.0055	-0.0517	-0.0213	-0.0035	0.0157	0.0109	0.0211
46	0.7444	-0.0110	0.1348	0.0770	0.0380	0.0004	0.0023	0.0243	0.0118	0.0261	0.0236	-0.0033	-0.0083	-0.0149	0.0133
47	0.7464	0.0063	0.1575	0.0174	-0.0156	0.0279	0.0012	0.0270	0.0015	-0.0489	0.0216	-0.0247	-0.0166	0.0096	-0.0073
48	0.6117	-0.0037	0.2167	0.0247	0.0504	0.0296	0.0116	0.0220	0.0189	-0.0960	-0.0413	-0.0125	-0.0085	0.0245	0.0042
49	0.7621	0.0080	0.1574	0.0082	0.0300	0.0093	0.0107	-0.0050	-0.0068	-0.0208	-0.0118	-0.0173	-0.0210	0.0024	-0.0045
50	0.8498	-0.0136	0.0460	0.0618	0.0353	-0.0021	-0.0012	0.0094	0.0035	-0.0398	-0.1011	0.0219	-0.0040	0.0178	0.0025

Table B.2 Fourier shape descriptor (a_0, a_n, and b_n) for 50 Clay B fillers

Filler	a_0	a_1	a_2	a_3	a_4	a_5	a_6	a_7	b_1	b_2	b_3	b_4	b_5	b_6	b_7
1	0.8671	-0.0027	-0.0027	-0.0027	-0.0027	-0.0027	-0.0027	0.0038	0.0096	0.0546	-0.0395	0.0012	0.0046	-0.0096	-0.0043
2	0.8054	0.0002	0.0002	0.0002	0.0002	0.0002	0.0002	-0.0011	-0.0008	0.0069	0.0008	-0.0022	-0.0085	0.0114	-0.0005
3	0.7641	-0.0272	-0.0272	-0.0272	-0.0272	-0.0272	-0.0272	-0.0134	0.0224	-0.0273	-0.0361	-0.0034	-0.0148	-0.0070	0.0142
4	0.8807	-0.0015	-0.0015	-0.0015	-0.0015	-0.0015	-0.0015	0.0144	0.0018	-0.0424	0.0217	0.0094	0.0030	0.0133	-0.0195
5	0.6917	-0.0300	-0.0300	-0.0300	-0.0300	-0.0300	-0.0300	0.0120	-0.0182	-0.0228	-0.0265	0.0079	-0.0045	-0.0012	0.0021
6	0.8766	-0.0005	-0.0005	-0.0005	-0.0005	-0.0005	-0.0005	0.0064	-0.0008	-0.0027	0.0000	-0.0257	0.0172	0.0000	-0.0045
7	0.6449	-0.0276	-0.0276	-0.0276	-0.0276	-0.0276	-0.0276	0.0112	0.0167	0.0688	-0.0208	0.0323	0.0102	-0.0012	0.0044
8	0.8483	-0.0008	-0.0008	-0.0008	-0.0008	-0.0008	-0.0008	0.0261	0.0121	-0.0460	0.0120	0.0352	0.0039	-0.0105	0.0101
9	0.7249	-0.0188	-0.0188	-0.0188	-0.0188	-0.0188	-0.0188	0.0153	0.0075	-0.0366	0.0229	0.0046	-0.0215	-0.0237	-0.0053
10	0.8607	0.0033	0.0033	0.0033	0.0033	0.0033	0.0033	-0.0073	0.0116	0.0821	-0.0186	-0.0091	-0.0304	0.0012	0.0001
11	0.8393	-0.0058	-0.0058	-0.0058	-0.0058	-0.0058	-0.0058	0.0270	0.0094	-0.0381	-0.0015	0.0023	-0.0012	-0.0105	-0.0206
12	0.8102	0.0098	0.0098	0.0098	0.0098	0.0098	0.0098	0.0016	-0.0005	0.0062	-0.0072	0.0100	-0.0082	0.0103	-0.0113
13	0.7912	-0.0067	-0.0067	-0.0067	-0.0067	-0.0067	-0.0067	0.0098	-0.0037	-0.0236	-0.0114	0.0100	0.0148	0.0195	0.0017
14	0.8488	0.0023	0.0023	0.0023	0.0023	0.0023	0.0023	0.0161	0.0008	-0.0351	-0.0107	0.0290	-0.0093	0.0103	0.0193
15	0.7502	-0.0160	-0.0160	-0.0160	-0.0160	-0.0160	-0.0160	0.0074	0.0060	-0.0736	-0.0118	0.0647	-0.0072	0.0000	0.0140
16	0.7850	-0.0125	-0.0125	-0.0125	-0.0125	-0.0125	-0.0125	0.0173	-0.0068	-0.0088	0.0024	-0.0411	-0.0358	-0.0157	-0.0076
17	0.5710	-0.0359	-0.0359	-0.0359	-0.0359	-0.0359	-0.0359	-0.0101	-0.0725	-0.0840	0.0804	0.0091	0.0326	0.0151	-0.0009
18	0.8498	-0.0005	-0.0005	-0.0005	-0.0005	-0.0005	-0.0005	0.0131	0.0020	0.0360	-0.0421	0.0485	0.0113	0.0142	0.0040
19	0.9024	0.0038	0.0038	0.0038	0.0038	0.0038	0.0038	0.0062	-0.0013	-0.0019	0.0004	-0.0067	0.0002	-0.0011	0.0004
20	0.8102	0.0098	0.0098	0.0098	0.0098	0.0098	0.0098	0.0016	-0.0005	0.0062	-0.0072	0.0100	-0.0082	0.0103	-0.0113
21	0.8379	0.0051	0.0051	0.0051	0.0051	0.0051	0.0051	0.0179	-0.0057	0.0129	0.0641	-0.0364	-0.0178	0.0145	-0.0037
22	0.7431	-0.0181	-0.0181	-0.0181	-0.0181	-0.0181	-0.0181	0.0064	0.0034	-0.0074	0.0303	-0.0234	-0.0126	0.0149	-0.0077
23	0.8014	-0.0040	-0.0040	-0.0040	-0.0040	-0.0040	-0.0040	0.0177	0.0087	-0.0393	0.0110	-0.0212	-0.0037	-0.0084	-0.0047
24	0.8653	0.0034	0.0034	0.0034	0.0034	0.0034	0.0034	0.0033	-0.0001	0.0378	-0.0168	0.0231	-0.0134	0.0119	-0.0122
25	0.8679	0.0118	0.0118	0.0118	0.0118	0.0118	0.0118	0.0116	-0.0025	0.0139	-0.0167	0.0000	-0.0180	0.0084	-0.0003
26	0.8793	0.0051	0.0051	0.0051	0.0051	0.0051	0.0051	-0.0095	-0.0056	-0.0672	-0.0126	0.0104	-0.0082	0.0024	0.0196
27	0.9004	-0.0009	-0.0009	-0.0009	-0.0009	-0.0009	-0.0009	0.0202	-0.0016	-0.0522	0.0000	0.0275	0.0068	0.0000	0.0271
28	0.6114	-0.0202	-0.0202	-0.0202	-0.0202	-0.0202	-0.0202	-0.0016	0.0512	0.0966	-0.0609	-0.0247	-0.0430	-0.0060	-0.0063
29	0.7436	-0.0098	-0.0098	-0.0098	-0.0098	-0.0098	-0.0098	-0.0050	0.0027	-0.0385	0.0182	0.0129	-0.0076	-0.0060	0.0073
30	0.7557	-0.0231	-0.0231	-0.0231	-0.0231	-0.0231	-0.0231	0.0063	0.0013	0.0569	0.0305	-0.0129	0.0341	-0.0133	-0.0024
31	0.8495	0.0133	0.0133	0.0133	0.0133	0.0133	0.0133	0.0161	0.0024	-0.0070	-0.0461	0.0112	-0.0024	0.0080	-0.0105

Continuation Table B.2

Filler	a_0	a_1	a_2	a_3	a_4	a_5	a_6	a_7	b_1	b_2	b_3	b_4	b_5	b_6	b_7
32	0.8169	0.0023	0.0023	0.0023	0.0023	0.0023	0.0023	0.0098	-0.0074	-0.0338	-0.0107	0.0089	-0.0031	0.0149	0.0032
33	0.6745	-0.0062	-0.0062	-0.0062	-0.0062	-0.0062	-0.0062	0.0000	-0.0041	-0.0463	0.0219	-0.0068	-0.0003	0.0070	-0.0147
34	0.7829	-0.0131	-0.0131	-0.0131	-0.0131	-0.0131	-0.0131	-0.0050	-0.0074	-0.0013	0.0639	-0.0341	-0.0012	0.0000	0.0153
35	0.8850	0.0076	0.0076	0.0076	0.0076	0.0076	0.0076	0.0207	-0.0137	0.0529	0.0311	0.0035	0.0068	-0.0181	0.0000
36	0.7745	-0.0201	-0.0201	-0.0201	-0.0201	-0.0201	-0.0201	0.0029	-0.0069	0.0247	0.0329	0.0048	0.0226	-0.0172	0.0180
37	0.7703	0.0018	0.0018	0.0018	0.0018	0.0018	0.0018	0.0000	-0.0041	0.0549	-0.0083	-0.0068	0.0025	-0.0070	-0.0059
38	0.8264	-0.0095	-0.0095	-0.0095	-0.0095	-0.0095	-0.0095	-0.0129	-0.0029	0.0057	-0.0268	-0.0201	0.0164	0.0034	-0.0054
39	0.8251	-0.0022	-0.0022	-0.0022	-0.0022	-0.0022	-0.0022	-0.0109	-0.0024	0.0183	0.0184	-0.0201	-0.0012	-0.0034	-0.0021
40	0.8241	-0.0091	-0.0091	-0.0091	-0.0091	-0.0091	-0.0091	0.0197	-0.0041	-0.0080	0.0019	0.0125	-0.0026	0.0012	0.0068
41	0.8828	0.0062	0.0062	0.0062	0.0062	0.0062	0.0062	0.0058	0.0007	-0.0179	0.0006	-0.0427	0.0058	-0.0071	-0.0081
42	0.7546	0.0013	0.0013	0.0013	0.0013	0.0013	0.0013	0.0000	-0.0012	-0.0431	-0.0065	0.0402	-0.0044	0.0309	0.0136
43	0.8671	-0.0027	-0.0027	-0.0027	-0.0027	-0.0027	-0.0027	0.0038	0.0096	0.0546	-0.0395	0.0012	0.0046	-0.0096	-0.0043
44	0.8088	-0.0008	-0.0008	-0.0008	-0.0008	-0.0008	-0.0008	0.0313	-0.0034	0.0682	0.0073	0.0402	-0.0216	0.0126	-0.0094
45	0.8766	-0.0005	-0.0005	-0.0005	-0.0005	-0.0005	-0.0005	0.0064	-0.0008	-0.0027	0.0000	-0.0257	0.0172	0.0000	-0.0045
46	0.7942	0.0057	0.0057	0.0057	0.0057	0.0057	0.0057	0.0187	0.0034	0.0431	-0.1223	0.0048	0.0038	0.0123	-0.0120
47	0.7923	0.0000	0.0000	0.0000	0.0000	0.0000	0.0000	0.0000	0.0000	-0.1595	0.0000	0.0508	0.0000	0.0000	0.0000
48	0.7881	-0.0029	-0.0029	-0.0029	-0.0029	-0.0029	-0.0029	-0.0088	0.0121	0.0157	-0.0258	0.0104	-0.0332	-0.0249	-0.0189
49	0.8483	-0.0008	-0.0008	-0.0008	-0.0008	-0.0008	-0.0008	0.0261	0.0121	-0.0460	0.0120	0.0352	0.0039	-0.0105	0.0101
50	0.7558	-0.0126	-0.0126	-0.0126	-0.0126	-0.0126	-0.0126	-0.0095	0.0140	-0.0065	-0.0192	-0.0323	-0.0156	0.0071	-0.0146

Table B.3 Fourier shape descriptor (a_0, a_n, and b_n) for 50 Clay C fillers

Filler	a_0	a_1	a_2	a_3	a_4	a_5	a_6	a_7	b_1	b_2	b_3	b_4	b_5	b_6	b_7
1	0.6338	-0.0349	-0.0349	-0.0349	-0.0349	-0.0349	-0.0349	0.0068	-0.0264	-0.0895	0.0196	0.0045	0.0112	0.0175	-0.0032
2	0.8856	-0.0091	-0.0091	-0.0091	-0.0091	-0.0091	-0.0091	0.0037	0.0054	-0.0743	0.0160	0.0000	-0.0152	-0.0012	-0.0026
3	0.6421	-0.0036	-0.0036	-0.0036	-0.0036	-0.0036	-0.0036	0.0056	-0.0005	0.0661	0.0069	0.0381	-0.0117	0.0000	-0.0109
4	0.6421	-0.0036	-0.0036	-0.0036	-0.0036	-0.0036	-0.0036	0.0056	-0.0005	0.0661	0.0069	0.0381	-0.0117	0.0000	-0.0109
5	0.7607	0.0121	0.0121	0.0121	0.0121	0.0121	0.0121	0.0238	0.0018	0.0985	-0.0563	0.0284	0.0565	0.0035	-0.0209
6	0.8090	-0.0143	-0.0143	-0.0143	-0.0143	-0.0143	-0.0143	-0.0127	0.0075	0.0035	-0.0004	0.0011	0.0109	0.0058	-0.0105
7	0.7630	-0.0226	-0.0226	-0.0226	-0.0226	-0.0226	-0.0226	0.0112	0.0045	-0.1386	-0.0408	0.0329	0.0096	0.0088	0.0164
8	0.7156	-0.0372	-0.0372	-0.0372	-0.0372	-0.0372	-0.0372	0.0190	-0.0176	-0.0282	0.0029	-0.0156	0.0036	0.0049	0.0057
9	0.7726	-0.0108	-0.0108	-0.0108	-0.0108	-0.0108	-0.0108	0.0058	-0.0263	0.0222	0.0190	-0.0058	0.0221	-0.0178	-0.0282
10	0.6933	-0.0271	-0.0271	-0.0271	-0.0271	-0.0271	-0.0271	-0.0007	0.0004	-0.0264	0.0010	-0.0406	0.0078	0.0394	-0.0088
11	0.6676	-0.0204	-0.0204	-0.0204	-0.0204	-0.0204	-0.0204	-0.0024	0.0006	0.0479	-0.0120	0.0251	-0.0033	0.0086	-0.0113
12	0.8856	-0.0045	-0.0045	-0.0045	-0.0045	-0.0045	-0.0045	0.0181	0.0069	-0.0148	0.0163	0.0185	0.0033	0.0237	-0.0092
13	0.9284	0.0025	0.0025	0.0025	0.0025	0.0025	0.0025	0.0216	0.0070	0.0027	0.0130	0.0219	0.0070	0.0059	0.0066
14	0.6929	-0.0258	-0.0258	-0.0258	-0.0258	-0.0258	-0.0258	0.0063	0.0963	0.1007	-0.1485	-0.0082	0.0038	-0.0096	0.0017
15	0.7675	-0.0421	-0.0421	-0.0421	-0.0421	-0.0421	-0.0421	-0.0048	-0.0077	-0.0857	-0.1161	-0.0413	0.0150	-0.0126	0.0198
16	0.7676	-0.0069	-0.0069	-0.0069	-0.0069	-0.0069	-0.0069	-0.0025	0.0122	0.0138	-0.0276	-0.0635	0.0131	-0.0012	-0.0101
17	0.9302	0.0000	0.0000	0.0000	0.0000	0.0000	0.0000	0.0000	0.0000	0.0000	0.0000	-0.0862	0.0000	0.0000	0.0000
18	0.8630	-0.0036	-0.0036	-0.0036	-0.0036	-0.0036	-0.0036	0.0007	-0.0031	0.0324	0.0406	-0.0171	0.0069	-0.0125	0.0134
19	0.7953	0.0014	0.0014	0.0014	0.0014	0.0014	0.0014	0.0010	0.0000	0.0000	0.0000	0.0000	0.0000	0.0000	0.0000
20	0.8063	0.0002	0.0002	0.0002	0.0002	0.0002	0.0002	0.0007	0.0000	0.0193	-0.0789	-0.0312	-0.0855	-0.0640	0.0025
21	0.7779	-0.0055	-0.0055	-0.0055	-0.0055	-0.0055	-0.0055	-0.0024	-0.0013	0.0984	0.0598	-0.0284	0.0097	-0.0058	-0.0031
22	0.7193	-0.0172	-0.0172	-0.0172	-0.0172	-0.0172	-0.0172	-0.0054	0.0040	-0.0508	0.0109	0.0000	-0.0347	0.0082	0.0090
23	0.5294	-0.0932	-0.0932	-0.0932	-0.0932	-0.0932	-0.0932	0.0377	-0.0385	-0.0277	0.0239	0.0465	0.0385	0.0397	0.0400
24	0.8667	0.0000	0.0000	0.0000	0.0000	0.0000	0.0000	0.0000	0.0000	-0.0329	0.0000	-0.0300	0.0000	-0.0593	0.0000
25	0.7512	-0.0122	-0.0122	-0.0122	-0.0122	-0.0122	-0.0122	0.0202	0.0141	0.1115	0.0315	-0.0190	-0.0091	0.0343	0.0058
26	0.8443	0.0168	0.0168	0.0168	0.0168	0.0168	0.0168	0.0187	0.0086	0.0164	-0.0204	0.0165	0.0011	0.0012	-0.0024
27	0.8563	-0.0029	-0.0029	-0.0029	-0.0029	-0.0029	-0.0029	0.0070	-0.0045	-0.0583	-0.0321	0.0012	0.0021	-0.0125	-0.0071
28	0.8443	0.0168	0.0168	0.0168	0.0168	0.0168	0.0168	0.0187	0.0086	0.0164	-0.0204	0.0165	0.0011	0.0012	-0.0024
29	0.8883	0.0031	0.0031	0.0031	0.0031	0.0031	0.0031	0.0047	0.0044	0.0004	-0.0220	0.0159	0.0201	0.0047	0.0080
30	0.7953	0.0014	0.0014	0.0014	0.0014	0.0014	0.0014	0.0010	0.0000	0.0000	0.0000	0.0000	0.0000	0.0000	0.0000
31	0.7779	-0.0055	-0.0055	-0.0055	-0.0055	-0.0055	-0.0055	-0.0024	-0.0013	0.0984	0.0598	-0.0284	0.0097	-0.0058	-0.0031

Continuation Table B.3

Filler	a_0	a_1	a_2	a_3	a_4	a_5	a_6	a_7	b_1	b_2	b_3	b_4	b_5	b_6	b_7
32	0.7462	-0.0256	-0.0256	-0.0256	-0.0256	-0.0256	-0.0256	0.0019	-0.0006	-0.0293	-0.0061	0.0060	-0.0273	0.0000	-0.0095
33	0.7523	0.0008	0.0008	0.0008	0.0008	0.0008	0.0008	-0.0010	-0.0060	0.1620	0.0044	0.0035	0.0128	0.0095	-0.0049
34	0.8448	-0.0119	-0.0119	-0.0119	-0.0119	-0.0119	-0.0119	-0.0042	-0.0013	-0.0421	-0.0011	0.0465	0.0263	-0.0186	0.0011
35	0.7726	0.0026	0.0026	0.0026	0.0026	0.0026	0.0026	0.0307	-0.0226	-0.1352	0.0386	0.0475	-0.0029	-0.0038	0.0469
36	0.8710	-0.0064	-0.0064	-0.0064	-0.0064	-0.0064	-0.0064	0.0061	-0.0155	0.0109	-0.0545	-0.0170	0.0120	0.0000	0.0185
37	0.5340	-0.0589	-0.0589	-0.0589	-0.0589	-0.0589	-0.0589	0.0057	0.0442	-0.1897	-0.1688	-0.0681	-0.0143	-0.0225	-0.0096
38	0.6915	-0.0100	-0.0100	-0.0100	-0.0100	-0.0100	-0.0100	0.0173	-0.0083	-0.0227	0.0303	-0.0212	0.0057	-0.0080	0.0050
39	0.7855	0.0053	0.0053	0.0053	0.0053	0.0053	0.0053	0.0302	0.0015	-0.0318	-0.0320	0.0136	0.0110	-0.0012	-0.0164
40	0.7158	-0.0150	-0.0150	-0.0150	-0.0150	-0.0150	-0.0150	0.0148	0.0241	-0.0010	-0.0687	-0.0046	0.0126	0.0130	0.0090
41	0.8610	-0.0063	-0.0063	-0.0063	-0.0063	-0.0063	-0.0063	-0.0023	0.0004	-0.0146	-0.0314	0.0000	-0.0111	0.0034	0.0102
42	0.7722	0.0019	0.0019	0.0019	0.0019	0.0019	0.0019	0.0053	0.0000	0.0000	0.0000	0.0000	0.0000	0.0000	0.0000
43	0.8400	0.0001	0.0001	0.0001	0.0001	0.0001	0.0001	-0.0179	0.0045	0.0029	-0.0299	-0.0078	0.0177	-0.0034	0.0122
44	0.8400	0.0001	0.0001	0.0001	0.0001	0.0001	0.0001	-0.0179	0.0045	0.0029	-0.0299	-0.0078	0.0177	-0.0034	0.0122
45	0.7729	0.0034	0.0034	0.0034	0.0034	0.0034	0.0034	0.0130	-0.0124	0.0148	-0.0443	0.0323	0.0383	-0.0011	-0.0002
46	0.7234	-0.0349	-0.0349	-0.0349	-0.0349	-0.0349	-0.0349	0.0267	-0.0246	-0.1209	-0.0716	-0.0178	-0.0396	-0.0126	0.0028
47	0.8136	-0.0011	-0.0011	-0.0011	-0.0011	-0.0011	-0.0011	0.0193	0.0010	-0.0225	-0.0492	0.0156	0.0210	-0.0126	0.0069
48	0.7512	-0.0122	-0.0122	-0.0122	-0.0122	-0.0122	-0.0122	0.0202	0.0141	0.1115	0.0315	-0.0190	-0.0091	0.0343	0.0058
49	0.6854	-0.0172	-0.0172	-0.0172	-0.0172	-0.0172	-0.0172	0.0310	0.0122	0.1322	0.0250	0.0323	0.0030	0.0011	-0.0119
50	0.5393	-0.0737	-0.0737	-0.0737	-0.0737	-0.0737	-0.0737	0.0022	0.0601	0.1798	0.0003	0.1182	0.0530	0.0175	0.0323

Appendix C

CALCULATION OF THE ANGLE OF ROTATION FOR DEFINITION OF FOURIER DESCRIPTOR PARAMETERS

The Fourier descriptor introduced in Chapter 3 requires the definition of radii to estimate parameters of shape description. These radii can be drawn at any particular angle of rotation. At a large angle of rotation, a reduced number of radii was drawn and vice versa. However, a reduced number of radii can oversimplify the shapes due the omission of details of filler contours. Thus, to find an appropriate angle of rotation, the surface area of predicted and measured fillers was compared. The surface area of the fillers was selected as a parameter of comparison because it is one of the main characteristics of the filler related to the improvement of barrier performance of dispersion coatings. The calculation was carried out by the programs presented in Appendix A. The surface areas of two clays (Clay A and B) were predicted and then compared with the measured surface area. The predictions were based on calculation of the filler shape varying the angle of the radii from 5° to 90°. This represented a number of radii from 4 to 72. Figure C.1 shows the error in the prediction of filler surface area by predicted shape at different angles of orientation for Clay A and B.

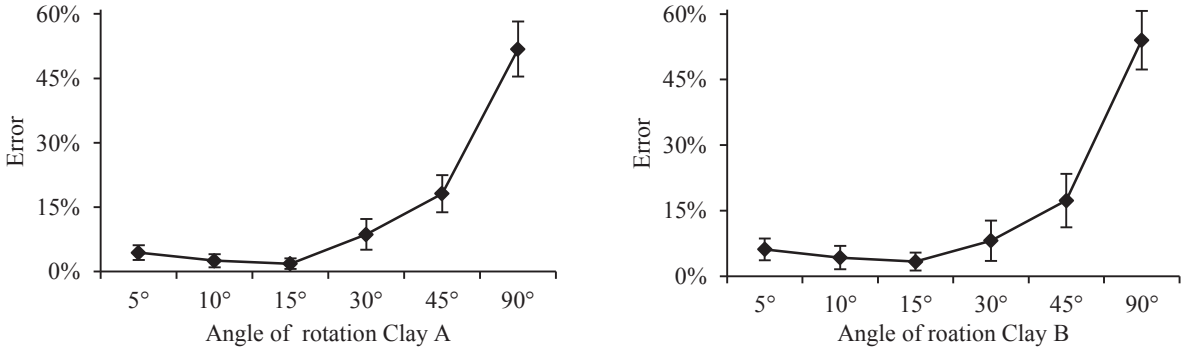

Figure C.1 Error in the estimation of area of filler from Fourier descriptor based on the measurement of radius at different angles of rotation for Clay A and Clay B

The error was observed to be lower than 5% for clay analysed at angle of rotation equal to 15º. This represented a number of radii equal to 24. For angles larger than this, the error increased up to about 50% for an angle of orientation equal to 90°. Interestingly the error increased at angle of rotation lower than 15°. This observation was due to the discretisation of the filler shape by pixels.

Appendix D

PROGRAM TO CALCULATE THICKNESS OF BARRIER DISPERSION COATINGS

This program estimates the thickness of cross section of barrier dispersion coating based on scanning electron microscopy images. An example of these images was presented in Figure 4.7 in Chapter 4. The program was developed in Matlab in a graphical user interface (GUI) to facilitate the process of measurement. Figure D.1 shows the user interface and the sections of the program.

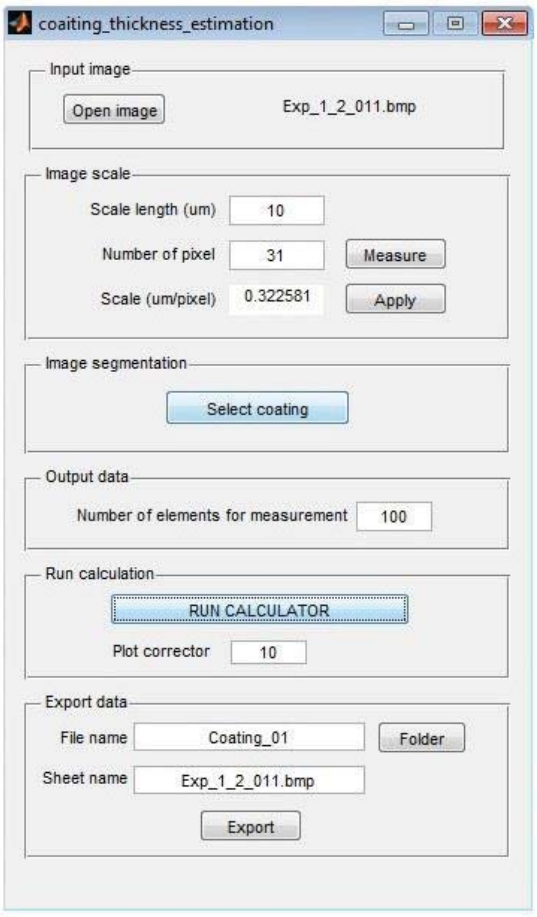

Selection of the image

Length of the scale (μm)

Measurement of the number of pixels in the scale

Scale ($\mu m/pixel$)

Selection of the coating on the image

Number of points where the thickness is measured

Run calculation

Correction of coating thickness measurement

Export data into Excel format

Figure D.1 Graphical user interface of the program for measurement of barrier dispersion coating thickness

To measure the thickness of the barrier dispersion coatings it is required to know the scale of the microscopic image. The scale is measured by counting the pixels in the scale bar in the horizontal direction. From this, the number of pixels can be associated to the length of the scale in terms of μm (Figure D.2). The measurement is carried out by counting the white pixel area where the scale bar is (Figure D.2). This area is selected by the mouse.

Figure D.2 Selection of the scale bar section

Once the scale is calculated, the measurement of the coating thickness can occur. This calculation begins with selecting the area where the coating is presented. Due to the similarity of the colour between the coating, paper, and embedding, the selection of this area is executed by mouse. From the selection area, both top and bottom coating surfaces are delineated by the mouse. Figure D.3 shows the selected coating sections and the coating detection.

a)

b)

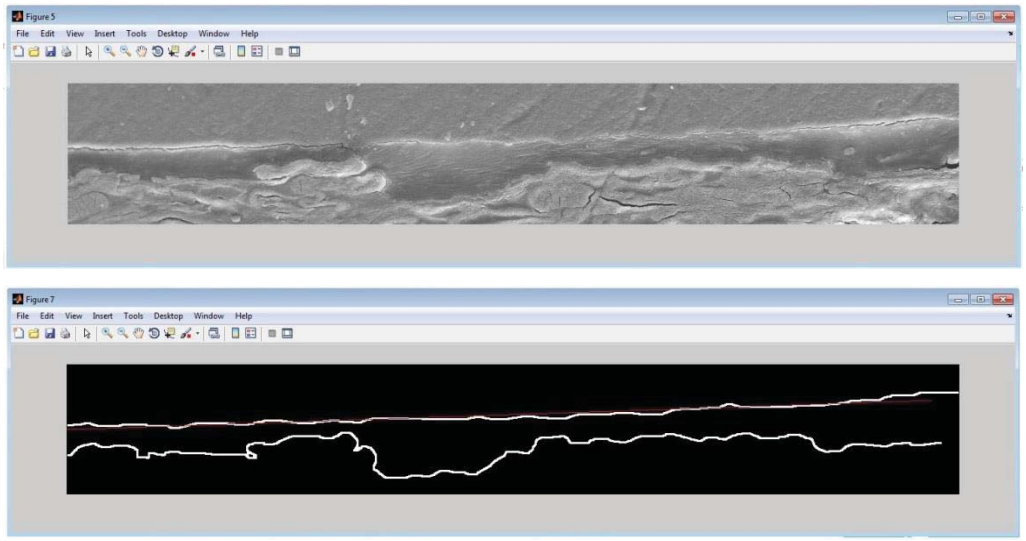

Figure D.3 a) Selected section of coating b) Detected coating surfaces

On the top surface of the coating, a reference line is defined by a linear regression of all the pixels in the line (Figure D.3b). Once the reference line was established, it was displaced to include all the points in the top surface (for more details see Figure 4.8). From the shifted reference line, perpendicular lines were demarcated and the distance between the dispersion coating surfaces across the perpendicular lines were measured. The spots where the thickness is measured were equally spaced according to the required number of measurements. The measurement of the thickness is based on the value of the pixel colour through the perpendicular lines. Thus, by checking each pixel through the perpendicular and identifying where pixels are equal 1 it is possible to calculate the thickness. Through the perpendicular line should be only two white pixels; one at the top surface intersection and one at the bottom surface intersection (Figure D.4). Using the coordinates of those pixels, the thickness at a particular spot can be determined by the Euclidean distance equation (Equation D.1).

$$M_i = \sqrt{\left(x_{top_i} - x_{bottom_i}\right)^2 + \left(y_{top_i} - y_{bottom_i}\right)^2} \quad \text{(D.1)}$$

where

M_i : Coating thickness measured at a particular spot

(x_{top_i}, y_{top_i}): Coordinates at the interception on the top surface

$(x_{bottom_i}, y_{bottom_i})$: Coordinates at the interception on the top surface

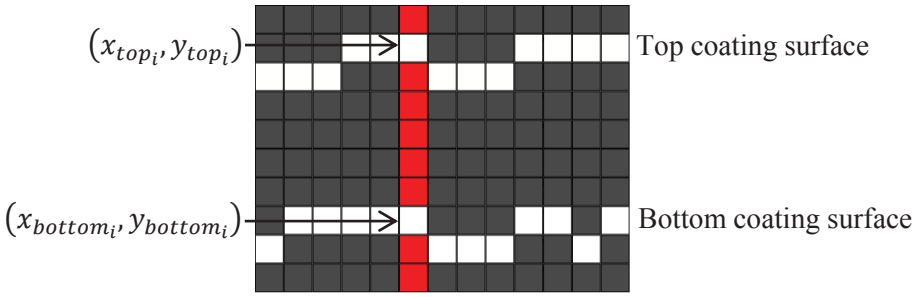

Figure D.4 Diagram of identification of interception between perpendicular line and top/bottom coating surfaces

In some cases, due to the curvature of the surfaces there is more than one pixel that intercepts the perpendicular lines. Under this scenario, it is required to adjust the calculation by finding more than two pixels through the perpendicular lines ("plot corrector" in the user interface). When the distance is estimated, the value is transformed into μm using the scale ratio previously estimated. Figure D.5 shows the thickness profile through the cross section of the coating. For further analysis the data is saved in Excel files.

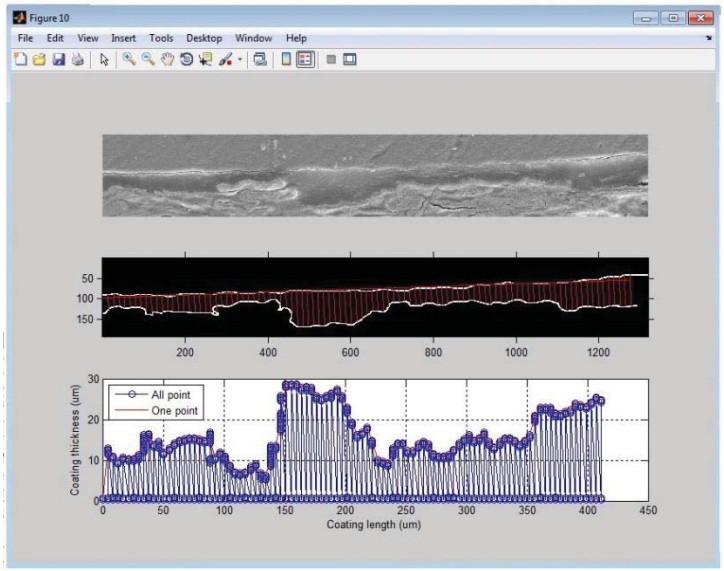

Figure D.5 Final results of the coating thickness calculation

The name of the program is `coaiting_thickness_estimation.fig` for the graphical user interface and `coaiting_thickness_estimation.m` for the programming code. Both programs have been saved in the folder “Appendix D”.

Appendix E

CALCULATION OF ERROR IN THE MEASUREMENT OF COATING THICKNESS

The measurement of coating thickness was based on observations of the cross section of coated samples. The observation and capture of images first required the embedding of the samples into epoxy resin blocks. During this process, the samples may potentially lose their perpendicular orientation (Figure E.1). The effect of this factor on the measurement of coating thickness can be estimated by the following geometrical consideration

$$K_m = \frac{K_r}{sin(\alpha)} \tag{A.1}$$

where

K_m : Measured thickness

K_r: Real thickness

α : Angle formed between the coating sample and the surface of the block

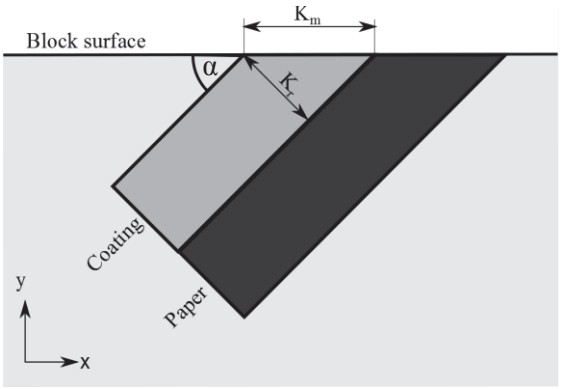

Figure E.1 Diagram of embedded coating sample with no perpendicular orientation

Figure E.2 shows the ratio between the real and the measured coating thickness. The results indicated that level of error is relatively low even if the angle formed between the block surface and the coating samples is high (i.e. 70°). This ensures the suitability of the method to measure coating thickness

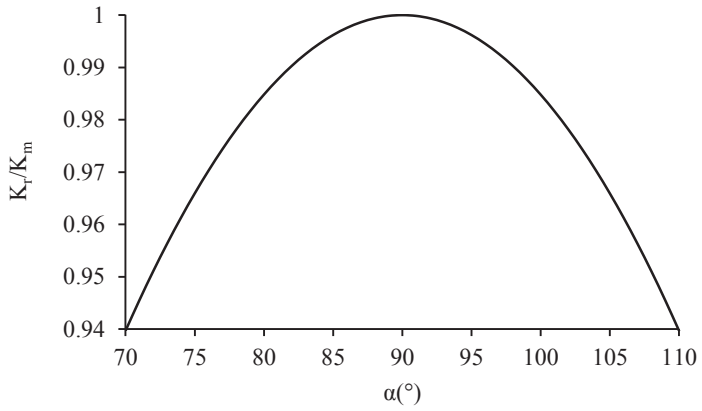

Figure E.2 Ratio between the real and the measured coating thickness (K_r/K_m) as a function of the angle formed between the coating sample and the block surface (α)

Appendix F

PROGRAM TO CALCULATE RELATIVE PERMEABILITY ON BARRIER DISPERSION COATINGS: RECTANGULAR FILLER SHAPE

This program has been developed to calculate the relative permeability of barrier dispersion coatings at particular values of volume fraction of filler, filler dimensions, and coating dimensions. The program groups a number of subprograms or "functions" according to the different stages of the simulations. These stages are: reading of the system inputs; calculation of number of fillers into the coating with their length, thickness and elongation; definition of the coating and its grid; location of the fillers into the coating grid; checking for filler overlapping; saving of the geometrical characteristics of the final coating; model solution; and data analysis. All of these stages are integrated into a main code. To run the program, "Matlab R2012a", "Comsol 4.3b", and "Comsol 4.3b with Matlab" are required. Explanations of each stage of the program are presented below:

F.1 The main code (`COATING_GEOMETRY_GENERATION_MAIN_CODE.m`)

The main code involves all the functions required for estimation of the relative permeability. In this part it is possible to define the size of the coating (`J,M,K`), the exposure conditions (`T_top ,RH_top,T_bottom,RH_bottom`), and definition of the clay used for coating formulation (`name_filler`). In addition, it is possible to set some parameters to facilitate the generation of the geometry and the mathematical formulation such as the smallest element on the edges of coating to facilitate meshing (`edges_tolerance`), minimum space between fillers (`fillers_tolerance`), or an increment of filler thickness for further analysis such as agglomeration (`increase_thickness`). It is also possible to set the number of geometries required to represent a particular coating formulation (`number_geometries`).

F.2 Reading of the system inputs (`data_filler_parameters_function.m`)

The function contains all the information regarding filler geometry. Also includes the density of all the studied clays. For using the function it is only required to outline the name of the filler (`name_filler`). The output information that the functions provides is indicated in Table F.1.

Table F.1 Output information of the functions to generate geometrical information of fillers for coating formulation

Output information
Filler length μ of lognormal distribution (`mu_length`)
Filler length σ of lognormal distribution (`sigma_length`)
Maximum filler length (`max_length`)
Minimum filler length (`min_length`)
Filler elongation *k* of generalised extreme value distribution (`k_elongation`)
Filler elongation σ of generalised extreme value distribution (`sigma_elongation`)
Filler elongation μ of generalised extreme value distribution (`mu_elongation`)
Maximum filler elongation (`max_elongation`)
Minimum filler elongation (`min_elongation`)
Filler thickness μ of lognormal distribution (`mu_b`)
Filler thickness σ of lognormal distribution (`sigma_b`)
Maximum filler thickness (`max_b`)
Minimum filler thickness (`min_b`)
Filler area μ of lognormal distribution (`mu_area`)
Filler area σ of lognormal distribution (`sigma_area`)
Maximum filler area (`max_area`)
Minimum filler area (`min_area`)
Filler aspect ratio μ of lognormal distribution (`mu_AR`)
Filler aspect ratio σ of lognormal distribution (`sigma_AR`)
Maximum filler aspect ratio (`min_AR`)
Minimum filler aspect ratio (`max_AR`)
Average true density of the clay (`average_density`)
Standard deviation of the true density of the clay (`std_density`)

F.3 Calculation of number of fillers into the coating with theirs length, thickness and elongation (`number_filler_calculation_function.m`)

20,000 values of length, thickness, and elongation of fillers are estimated based on the distribution parameters presented in Chapter 6. Each of these parameters was calculated by estimation of the corresponded inversed distribution at random probabilities from 0 to 1. Then, taking one by one value length, thickness and elongation, fillers are defined and calculation of their volume is carried out. The number of fillers has to be enough to reach the required volume fraction (Equation 5.17). Finally, the values of the length, thickness and elongation of the fillers are sorted from the largest to the smallest filler volume and exported into the main code.

The name of the required sub-functions are presented below.

Sub-functions: `b_distribution_function.m`
`elongation_distribution_function.m`
`max_Feret_distribution_function.m`

The required information to run the functions is presented in Table F.2.

Table F.2 Required information to run the main and sub functions for calculation of number, length, thickness, and elongation of fillers into the barrier dispersion coating. The names of the variables used in the program are presented in brackets

Required information	Data from*
Increment of filler thickness (default =1meaning no increasing) (`increase_thickness`)	F.2
Maximum filler length (`max_length`)	F.2
Minimum filler length (`min_length`)	F.2
Filler length μ of lognormal distribution (`mu_length`)	F.2
Filler length σ of lognormal distribution (`sigma_length`)	F.2
Maximum filler thickness (`max_b`)	F.2
Minimum filler thickness (`min_b`)	F.2
Maximum filler elongation (`max_elongation`)	F.2
Minimum filler elongation (`min_elongation`)	F.2
Filler elongation *k* of generalised extreme value distribution (`k_elongation`)	F.2
Filler elongation μ of generalised extreme value distribution (`mu_elongation`)	F.2
Filler elongation σ of generalised extreme value distribution (`sigma_elongation`)	F.2
Filler thickness μ of lognormal distribution (`mu_b`)	F.2
Filler thickness σ of lognormal distribution (`sigma_b`)	F.2
Required filler volume fraction (`Real_Vol_Fraction`)	S.I.
Length of the coating (`J`)	S.I.
Width of the coating (`M`)	S.I.

*: SI: System input, F.2: Section F.23

The outputs of the main function are presented in Table F.3.

Table F.3 Output information from the main and sub functions for calculation of number, length, thickness, and elongation of fillers into the barrier dispersion coating. The names of the variables used in the program are presented in brackets

Output information
Final filler volume fraction (`final_vol_fraction`)
Number of fillers into the coating (`nfibres`)
Filler length (`length_FINAL`)
Filler thickness (`b_FINAL`)
Filler elongation (`E_FINAL`)

F.4 Definition of the coating and its grid (`definition_of_grid_function.m`)

This stage defines the coating binder dimension based on the length, width, and thickness of the coating required in section F.2. To ensure that the coordinates of all the fillers are positive, a minimum distance between the origin of the axis ($x = 0\ y = 0\ z = 0$) and the closest coating

border is defined based on the largest filler. Before distribution of fillers into the coating, the coating binder is divided into small elements forming a grid. In each element one filler is located. For this, the number of elements has to be at least the same of the number of filler (Equation 5.20 in Chapter 5). For this, an initial number of elements is assigned based on the division of the coating in equally spaced segments through each axis (Figure F.1). If the initial number of elements is lower than the number of fillers, the number of elements in the x and y axes was increased one by one unit until the number of elements is equal or larger than the number of fillers. It is possible that the number of elements was larger than the number of fillers. In this case, the elements were randomly chosen, leaving the remaining grid element with no fillers. The chosen and empty elements are labelled for distribution of fillers introduced in the following section.

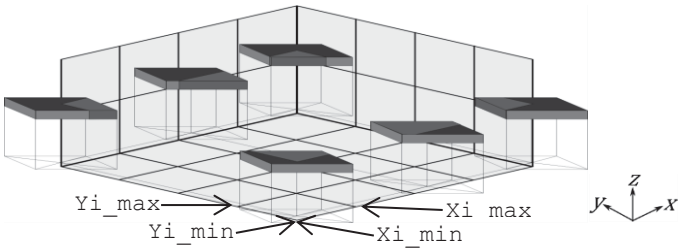

Figure F.1 Nomenclature of the side of the elements of the grid with `nx=4, ny=4,` and `nz=2`

The required information to run the function are presented in Table F.4 and the outputs of the function in Table F.5

Table F.4 Required information to run the main function to define the coating geometry and its grid. The names of the variables used in the program are presented in brackets

Required information	Data from*
Initial number of element in length direction of the coating (`nx`)	S.I.
Initial number of element in width direction of the coating (`ny`)	S.I.
Initial number of element in height direction of the coating (`nz`)	S.I.
Increment of the number of grid element (default=1 meaning no increase) (`increment`)	S.I.
Number of fillers into the coating (`nfibres`)	F.4
Minimum distance between the origin of the axis and the closest coating border of it (`limit_max`)	F.4
Length of the coating (`J`)	S.I.
Width of the coating (`M`)	S.I.
Thickness of the coating (`K`)	S.I.

*: SI: System input, F.4: Section F.4

Table F.5 Output information from the main function to define the coating geometry and its grid. The names of the variables used in the program are presented in brackets.

Output information
Coordinate of the left limit of elements at the length direction (`Xi_min`)
Coordinate of the right limit of elements at the length direction (`Xi_max`)
Coordinate of the front limit of elements at the width direction (`Yi_min`)
Coordinate of the behind limit of elements at the width direction (`Yi_max`)
Coordinate of the bottom limit of elements at the height direction (`Zi_min`)
Coordinate of the top limit of elements at the height direction (`Zi_max`)
Final number of element in length direction of the coating (`nx`)
Final number of element in width direction of the coating (`ny`)
Final number of element in height direction of the coating (`nz`)
Label of the chosen element of the grid (`coord`)
Label of the empty element of the grid (`emp_pos`)

F.5 Location of the fillers into the coating grid (`filler_arrangement_function.m`)

In this stage, fillers are assigned to each chosen element. Also, the minor filler length is estimated by the ratio of the major length and the elongation. It is possible to include a tolerance for the space between fillers (`tolerance_space`). This defines a minimum distance between fillers. The default case is a tolerance equal 0.

The required information to run the function are presented in Table F.6 and the outputs of the function in Table F.7

Table F.6 Required information to run the function to locate fillers in the coating geometry. The names of the variables used in the program are presented in brackets

Required information	Data from*
Final number of element in length direction of the coating (`nx`)	F.4
Final number of element in width direction of the coating (`ny`)	F.4
Final number of element in height direction of the coating (`nz`)	F.4
Filler length (`length_FINAL`)	F.3
Filler thickness (`b_FINAL`)	F.3
Label of the empty element of the grid (`emp_pos`)	F.4
Filler elongation (`E_FINAL`)	F.3

*: F.3: Section F.3, F.4: Section F.4

Table F.7 Output information from the function to locate fillers in the coating geometry. The names of the variables used in the program are presented in brackets.

Output information
Major filler length (`Lx`)
Minor filler length (`Ly`)
Filler thickness (`b`)

The fillers have to be located into the designated elements. For this, the centre of gravity of the fillers is placed inside the element. The coordinates for the centre of gravity of the fillers are `Xc, Yc,` and `Zc`. The coordinates of the centre of gravity have to be inside the element limits (`Xi_min, Xi_max, Yi_min, Yi_max, Zi_min, Zi_max`). Then, the filler is placed in the element and rotated at $x - y$ axes on its centre of gravity in a random angle (`alpha`). Once the filler is placed and rotated, the coordinates of the filler corners are estimated (`XR1` to `XR8, YR1` to `YR8, ZR1` to `ZR8`). In some cases the location of filler at the coating corners can place more than one part outside of the coating (Figure F.2). To simplify the programming process, above case was avoided.

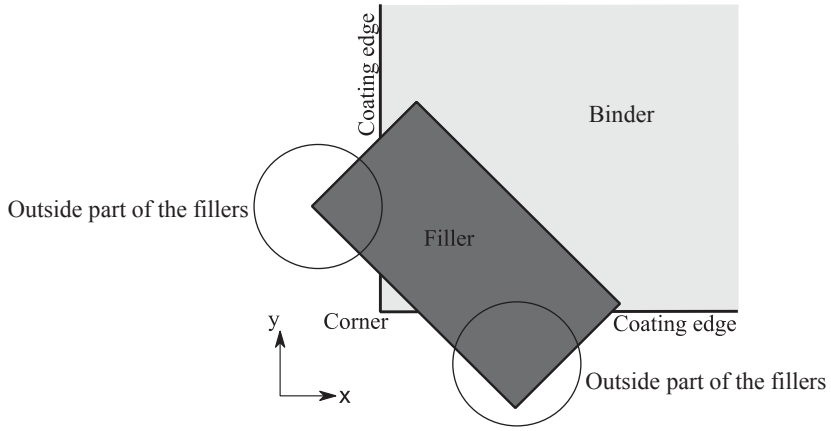

Figure F.2 Location of a filler with more than one part outside of the coating

To prove that the filler is correctly located in corners, the coating corner must be among of the fillers corners. The function presented in this section was developed to repeat the filler location if above conditions was not achieved (`check_corners` =1). To identify if the coating corners is in between all the filler corners, a Matlab function called `inpolygon` was used. This function identifies point inside a polygonal region. In this case, the point is the coating corner and the polygonal region the four corners of the filler.

To reduce problems with meshing for small parts such as fillers corners that are slightly out of the coating edges, this function also can be set to have a minimum element size at the coating

edges (`dist`). In addition, the function gives information of the gaps between fillers for further analysis of the coating geometry (`distance_filler`)

Main function: `filler_corner_coordinates_function.m`

Sub-functions: `free_space_function.m`

`tolerance_edges_function.m`

`distance_between_fillers_function.m`

The required information to run the function are presented in Table F.8 and the outputs of the function in Table F.9.

Table F.8 Required information to run the function to locate fillers in coating corners. The names of the variables used in the program are presented in brackets

Required information	Data from*
Coordinate of the left limit of elements at the length direction (`Xi_min`)	F.4
Coordinate of the right limit of elements at the length direction (`Xi_max`)	F.4
Coordinate of the front limit of elements at the width direction (`Yi_min`)	F.4
Coordinate of the behind limit of elements at the width direction (`Yi_max`)	F.4
Coordinate of the bottom limit of elements at the height direction (`Zi_min`)	F.4
Coordinate of the top limit of elements at the height direction (`Zi_max`)	F.4
Major filler length (`Lx`)	F.5
Minor filler length (`Ly`)	F.5
Minimum distance between the origin of the axis and the closest coating border of it (`limit_max`)	F.4
Label of the chosen element (`i`)	S.C.
Filler thickness (`b`)	F.6
Length of the coating (`J`)	S.I.
Width of the coating (`M`)	S.I.
Chosen element of the grid (`coord`)	F.4
Arrangement of x-axis filler corners including the extra filler due to periodic boundary conditions (`X`)	F.1
Arrangement of y-axis filler corners including the extra filler due to periodic boundary conditions (`Y`)	F.1
Arrangement of z-axis filler corners including the extra filler due to periodic boundary conditions (`Z`)	F.1
Thickness of the coating (`K`)	S.I.

*: F.1: Section F.1, F.4: Section F.4, F.5: Section F.5, F.6: Section F.6, S.C.: simulation condition, S.I.: System input

Table F.9 Output information from the function to locate fillers in coating corners. The names of the variables used in the program are presented in brackets.

Output information
Centre of filler coordinates (`Xc, Yc, Zc`)
Coordinates of the filler corners at x-axis (`XR1, XR2, XR3, XR4, XR5, XR6, XR7, XR8`)
Coordinates of the filler corners at y-axis (`YR1, YR2, YR3, YR4, YR5, YR6, YR7, YR8`)
Coordinates of the filler corners at z-axis (`ZR1, ZR2, ZR3, ZR4, ZR5, ZR6, ZR7, ZR8`)
Instruction to repeat filler location due location at coating corners (`check_corners`)
Angle of orientation of the filler (`alpha`)
Distance between the filers and the coating borders (`dist`)
Distance between fillers (`distance_filler`)

It is important to note that the location of the fillers is repeated if part of fillers is beyond the coating dimension plus the limit area, part of fillers is under the minimum distance to the edge (`dist`), or the fillers is closer to others than the allowed limit (`distance_filler`).

As explained in Chapter 5, one of the assumptions of the model is related to periodic boundary conditions. If part of filler crosses the edge of the coating, the external part is included in the opposite edge. In the cases of fillers that are at the corner of the coating, the fillers are repeated three times and located into the other three corners. This condition does not include condition showed in Figure F.2.

This function identifies the fillers that are at the coating edges or corners. By adding or subtraction the length (`J`) or width (`M`) of the filler coordinates, the new copied fillers are defined. The Z-axis coordinates are maintained for the copied fillers. An example of location of copied filler is presented in Figure F.3. The function gives information of the coordinates and the centre for all the copied fillers. The new coordinates are named including a suffix ; i.e. `XR1a – XR8a` are the x- axis coordinates of a filler copied once, `XR1a – XR8a, XR1b – XR8b`, and `XR1c – XR8c` are the x- axis coordinates of a filler copied three times. These new fillers are then included in the original list of fillers that was defined in previous section.

The name of this function is `periodic_boundary_condition_filler_function.m`. The required information to run this function is presented in Table F.10 and the outputs of the function in Table F.11.

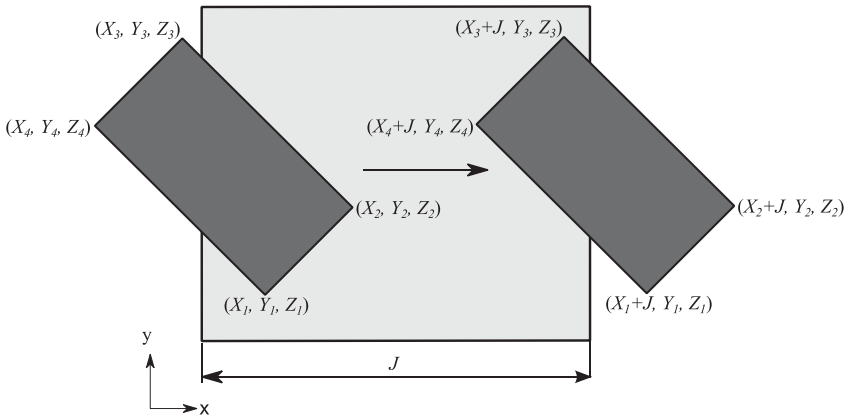

Figure F.3 Example of location of copied filler

Table F.10 Required information to run the function to repeat filler due to periodic boundary conditions. The names of the variables used in the program are presented in brackets

Required information	Data from*
Centre of filler coordinates (`Xc, Yc, Zc`)	F.5
Coordinates of the filler corners at x-axis (`XR1, XR2, XR3, XR4, XR5, XR6, XR7, XR8`)	F.5
Coordinates of the filler corners at y-axis (`YR1, YR2, YR3, YR4, YR5, YR6, YR7, YR8`)	F.5
Coordinates of the filler corners at z-axis (`ZR1, ZR2, ZR3, ZR4, ZR5, ZR6, ZR7, ZR8`)	F.5
Length of the coating (`J`)	S.I.
Width of the coating (`M`)	S.I.
Minimum distance between the origin of the axis and the closest coating border of it (`limit_max`)	F.4

*: S.I.: System input, F.4: Section F.4, F.5: Section F.5

Table F.11 Output information from the function to repeat filler due to periodic boundary conditions. The names of the variables used in the program are presented in brackets.

Output information
Coordinates of the new fillers including the extra filler due to periodic boundary conditions (`XR,YR,ZR`)
Coordinates of the fillers centre of the first extra filler due to periodic boundary conditions (`Xca,Yca,Zca`)
Coordinates of the fillers centre of the second extra filler due to periodic boundary conditions (`Xcb,Ycb,Zcb`)
Coordinates of the fillers centre of the third extra filler due to periodic boundary conditions (`Xcc,Ycc,Zcc`)

F.6 Checking of filler overlapping (`filler_overlapping_checking_function.m`)

The identification of filler overlapping is based on a Matlab function called `inpolygon`. This function detects points inside a given polygon. As shown in Figure 5.8, the edges of the fillers were discretised as group of points in each projection at $x-y$, $x-z$, and $y-z$ axes. The corners of the fillers projection of were used as the required polygon and then they were compared with the discretised edges, one by one filler, to detect overlapping. The function evaluates the overlapping for each projection labelling the results as `check_YZ_sum`,

`check_XZ_sum`, and `check_XY_sum`. If the projection labels are equal to 1, there are overlapping between two projections. This process is carried out for all the projection of all the fillers. To communicate the results with the main code, the function exports the variable `check` to indicate overlapping. If `check` is 1, overlapping has been detected at least between two fillers. The required information to run this function is presented in Table F.10 and the outputs of the function in Table F.13.

Table F.12 Required information to run the function to detect overlapping of fillers. The names of the variables used in the program are presented in brackets

Required information	Data from*
Extra filler due to periodic boundary conditions in the current iteration (`hola`)	S.C.
Extra filler due to periodic boundary conditions in the all the iterations (`m`)	S.C.
Arrangement of x-axis filler corners including the extra filler due to periodic boundary conditions (`X`)	F.1
Arrangement of y-axis filler corners including the extra filler due to periodic boundary conditions (`Y`)	F.1
Arrangement of z-axis filler corners including the extra filler due to periodic boundary conditions (`Z`)	F.1
Number of element of the discretisation of the filler edge (`range`)	S.I.
Record of overlapping checking at $y-z$ axis of all the fillers (`check_YZ`)	F.6
Record of overlapping checking at $x-z$ axis of all the fillers (`check_XZ`)	F.6
Record of overlapping checking at $x-y$ axis of all the fillers (`check_XY`)	F.6

*: S.I.: System input, F.6: Section F.6, S.C.: simulation condition

Table F.13 Output information from the function to detect overlapping of fillers. The names of the variables used in the program are presented in brackets.

Output information
Instruction to the main code to repeat the location of the filler (`check`)

If overlapping is detected (`check` is equal to 1), the filler is relocated in the same grid element. The relocation of the fillers includes all the steps and considerations explained previously (section F.5 and F.6). If overlapping is detected for more than 20 times in the same element, the filler is relocated into another empty element. After location of all the fillers, the program sorts the information for data exportation into Comsol Multiphysics.

F.7 Saving of the geometrical characteristics of the final coating

(`saving_geometry_data_function.m`)

To export the information into Comsol Multiphysics, it is required to save the geometrical data of the coating. In this way, the information regarding filler dimension, coating dimensions, angle of orientation of the fillers, exposure condition of the coating are saved in "`.mat`" files. The name of the files indicates the variable and the label of the fillers. For example, the file

"angle_of_orientation_24.mat" content information about variable angle of orientation of the filler number 24. The required information to run this function is presented in Table F.14. The information is saved in a folder called according to the volume fraction of fillers (i.e. "10%") in a main folder called "Geometries".

Table F.14 Required information to run the function to detect overlapping of fillers. The names of the variables used in the program are presented in brackets

Saved information	Data from*
Lennard-Jones temperature (e_k)	S.I.
Ratio of the collision diameter of the permeant and nitrogen (tx_tN2)	S.I.
Glass transition temperature of the coating (Tg)	S.I.
Distance between filler (distance)	S.C.
Arrangement of x-axis filler corners including the extra filler due to periodic boundary conditions (X)	F.6
Arrangement of y-axis filler corners including the extra filler due to periodic boundary conditions (Y)	F.6
Arrangement of z-axis filler corners including the extra filler due to periodic boundary conditions (Z)	F.6
Minimum distance between filler (minimum_distance)	S.C.
Length of the coating (J)	S.I.
Width of the coating (M)	S.I.
Thickness of the coating (K)	S.I.
Major filler length (Lx)	F.5
Minor filler length (Ly)	F.5
Filler thickness (b)	F.5
Rearrangement of the centre of fillers (centre_of_pigment)	F.1
Rearrangement of the angle of orientation of fillers (angle_of_orientation)	F.1
Minimum distance between the origin of the axis and the closest coating border of it (limit_max)	F.1
Temperature at the top coating surface (T_top)	S.I.
Relative humidity at the top surface (RH_top)	S.I.
Relative humidity at the bottom surface (RH_bottom)	S.I.
Temperature at the bottom coating surface (T_bottom)	S.I.
Molar weight of the water vapour (nw)	S.I.
Number of geometry (iteration)	S.C.
Final volume fraction of the filler in the coating after filler definition (final_vol_fraction)	F.3

*: S.I.: System input, F.1: Section F.1, F.3: Section F.3, F.5: Section F.5, F.6: Section F.6, S.C.: simulation condition

F.8 Model solution (COMSOL_SOLUTION.m)

The data presented in Table F.14 are the basis of the definition of the model solution. The function opens that information and imports it into Comsol Multiphysics. This software is controlled by Matlab scripting environment by Comsol 4.3b with Matlab. The transport of diluted species for three dimensional geometries under stationary studies is set for model solution. The coating dimensions are measured in μm and the angle of rotation in radians.

The function defines the geometry of the dispersion coating drawing the fillers across the coating binder, which is represented by a block. The fillers are defined by `Lx`, `Ly`, `b`, `centre_of_pigment`, and `angle_of_orientation`. The block is defined by `J`, `M`, and `K` and the corner of the origin of the block is (`2*limit_max`, `2*limit_max`, `0`). By a Boolean operation of subtraction between the binder and the fillers, the domain for further calculations is created.

The surfaces of the domain have to be identified to specify the boundary conditions. The top and bottom surfaces are defined at different permeant concentrations to allow diffusive flux through the coating. The concentration of permeant is a function of the exposure condition of the dispersion coating. The relationship between the exposure and the permeant concentration are detailed in Chapter 5 and 6. The lateral edges of the coating are defined by periodic boundary conditions.

The mesh is defined in two parts; free triangular meshing for all the surfaces and free tetrahedral meshing for the rest of the binder. The initial mesh has a minimum element size of 0.0001 μm and a maximum element size of 1 μm with growing rate of 1.2. The mesh is refined to reduce the element size in 5 times.

The model calculates the concentration of permeant through the coating by solving Equation 5.1. The diffusive flux is calculated by surface integral of the top and bottom coating surfaces. The program saves each simulation as a Comsol file in the same folder where the information was collected with the name "`comsol_geometry_1.mph`". The prefix 1 represents the name of the coating geometry. Thus, the data can be extracted by opening each file and copying and pasting the information. The analysis of the data is carried out in Excel spreadsheets. Figure F.4 shown the user interface windows of Comsol after simulation.

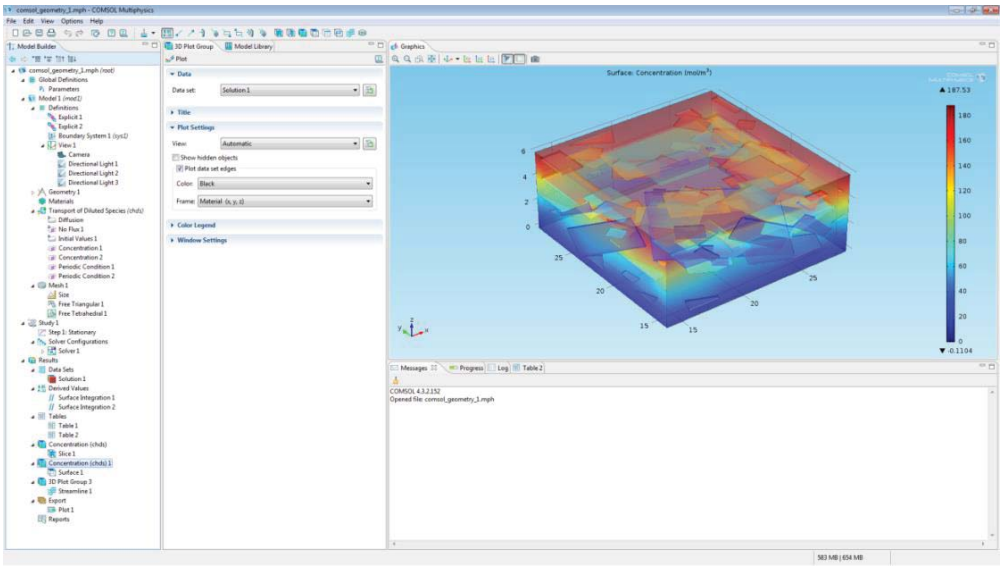

Figure F.4 User interface windows of Comsol after simulation for coating filled with rectangular fillers

The name of the main function is `COMSOL_SOLUTION.m`, and the functions are `comsol_solving_function.m` and `calculation_of_vapor_concentration_function.m`.

A summary of all the functions required to run simulations for coating with rectangular shaped fillers was presented in Table F.15.

Table F.15 List of functions and sub-functions required to run the main codes for simulation of dispersion coatings filled with rectangular particles

Main code	Functions	Sub functions
COATING_GEOMETRY_ GENERATION_MAIN_CODE	1. data_filler_parameters_function	
	2. number_filler_calculation_function	2.1. b_distribution_function
		2.2. elongation_distribution_function
		2.3. max_Feret_distribution_function
	3. definition_of_grid_function	
	4. filler_arrangement_function	
	5. filler_corner_coordinates_function	5.1. free_space_function
		5.2. tolerance_edges_function
		5.3. distance_between_fillers_function
	6. periodic_boundary_condition_filler_function	
	7. filler_overlapping_checking_function	
	8. analysis_distance_between_fillers_function	
	9. drawing_coating_geometry_function	
	10. saving_geometry_data_function	
COMSOL_SOLUTION	1. comsol_solving_function	1.1. calculation_of_vapor_concentration_function

Appendix G

PROGRAM TO CALCULATE RELATIVE PERMEABILITY ON BARRIER DISPERSION COATINGS: ELLIPTICAL FILLER SHAPE

To improve the predictions from the proposed model, the effect of the fillers are evaluated assuming elliptical shapes. Thus, adaptation of the program presented in Appendix F is required. It is important to note that no changes were made to the conceptual model, mathematical formulation, assumptions, and mathematical solution beyond those related to the filler shape.

G.1 The main code (`COATING_GEOMETRY_GENERATION_ELLIPSE_MAIN_CODE.m`)

The main code presented in Appendix F is the same for this modification; however, some functions were modified.

G.2 Reading of the system inputs (`data_filler_parameters_function.m`)

The same presented in Appendix F, Section F.2.

G.3 Calculation of number of fillers into the coating with theirs length, thickness and elongation (`number_filler_ellipse_function.m`)

This function is based on the same ideas of the function presented in Section F.3 Appendix F. The difference is related to the way of final volume fraction calculation. Due to the elliptical shape, the surface area is reduced by the factor $\pi/4$ (Equation 6.18 in Chapter 6). For this function, the same sub function required in Section F.3 are used to define L, b and E.

G.4 Definition of the coating and its grid (`definition_of_grid_function.m`)

The same presented in Appendix F, Section F.4.

G.5 Location of the fillers into the coating grid

The definition of the grid and the elements is the same presented in Appendix F, Section F.5 (`filler_arrangement_function.m`). However, the function for location of the fillers was modified (`coordinate_ellipse_function.m`). Once the filler centre was located into a grid element as was defined in Appendix F, Section F.5, the coordinates of the edges have to be defined. In the case of the rectangular shaped fillers, it was required to identify the corners after rotation; however, for elliptical fillers the shape has to be transformed into a polygon. This is

required for filler overlapping detection. For this, the edge was discretised in 360 points by calculation of the radius at angle of $r(\theta)$ from 0° to ° to 360°. (Figure G.1a). Then, the angle of rotation was applied and the final position of the filler was established (Figure G.1b). The transformation of the elliptical filler shape into rotated polygon is based on Equations G.1, G.2, and G.3. Those equations allow calculation of the coordinates of each corner of the polygon (dots in Figure G.1b).

a)

b)

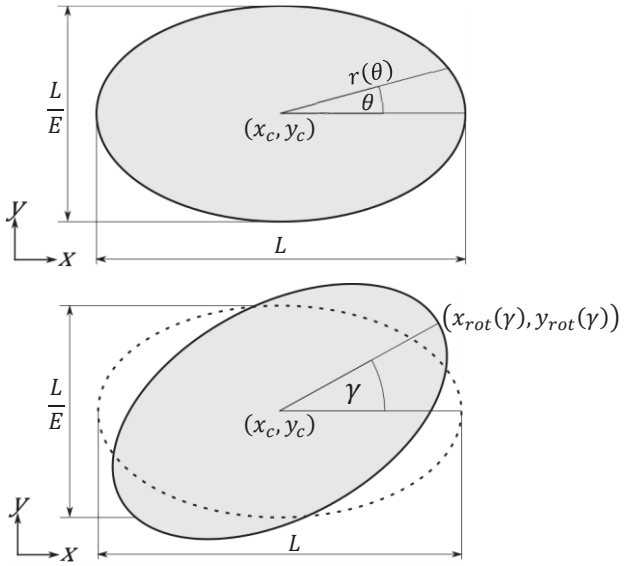

Figure G.1 Radius of the corner of discretised ellipse as a function of the angle of orientation and rotation

$$r(\theta) = \left(2 \cdot \sqrt{\frac{cos^2\theta}{L^2} + \frac{sin^2\theta}{(L/E)^2}} \right)^{-1} \quad \text{(G.1)}$$

$$x_{rot}(\gamma) = x_c + r(\theta) \cdot cos(\theta) \cdot cos(\gamma) - r(\theta) \cdot sin(\theta) \cdot sin(\gamma) \quad \text{(G.2)}$$

$$y_{rot}(\gamma) = y_c + r(\theta) \cdot cos(\theta) \cdot sin(\gamma) + r(\theta) \cdot sin(\theta) \cdot cos(\gamma) \quad \text{(G.3)}$$

where

$r(\theta)$: Radius of the non-rotated filler at an angle θ

L: Filler length (major semi axis equivalent to the length of the rectangular shaped filler)

$\frac{L}{E}$: Filler width (minor semi axis equivalent to the width of the rectangular shaped filler)

x_c: Centre of the filler at x-axis

y_c: Centre of the filler at y-axis

$x_{rot}(\gamma)$: Coordinate of an spot at the rotated filler at x-axis

$y_{rot}(\gamma)$: Coordinate of an spot at the rotated filler at y-axis

γ: Angle of the rotation of the filler

The required information to run the function is presented in Table G.1 and the output data are in Table G.2.

Table G.1 Required information to run the function to calculate the coordinate of the elliptical fillers. The names of the variables used in the program are presented in brackets

Saved information	Data from*
Limit of the angle of rotation (`rot_limit`)	S.I.
Coordinate of the left limit of elements at the length direction (`Xi_min`)	G.4
Coordinate of the right limit of elements at the length direction (`Xi_max`)	G.4
Coordinate of the front limit of elements at the width direction (`Yi_min`)	G.4
Coordinate of the behind limit of elements at the width direction (`Yi_max`)	G.4
Coordinate of the bottom limit of elements at the height direction (`Zi_min`)	G.4
Coordinate of the top limit of elements at the height direction (`Zi_max`)	G.4
Major filler length (`Lx`)	G.5
Minor filler length (`Ly`)	G.5
Label of the chosen element (`i`)	S.C.
Filler thickness (`b`)	G.6
Length of the coating (`J`)	S.I.
Width of the coating (`M`)	S.I.
Chosen element of the grid (`coord`)	G.4
Arrangement of x-axis filler corners including the extra filler due to periodic boundary conditions (`X`)	G.1
Arrangement of y-axis filler corners including the extra filler due to periodic boundary conditions (`Y`)	G.1
Arrangement of z-axis filler corners including the extra filler due to periodic boundary conditions (`Z`)	G.1

*: SI: System input, G.1: Section G.1, G.4: Section G.4, G.5: Section G.5, G.6: Section G.6

Table G.2 Output information from the function to calculate the coordinate of the elliptical fillers. The names of the variables used in the program are presented in brackets.

Output information
Centre of filler coordinates (`Xc, Yc, Zc`)
Rotated corners of the discretisation of the filler (polygon) (`x_rot, y_rot, z_rot`)
Angle of rotation of each filler (`rotation`)

The rest of the considerations required in this section are the same as those presented in Section F.5.

G.6 Checking of filler overlapping

(`filler_ellipse_overlapping_checking_function.m`)

The process of detection of filler overlapping is based on the method presented in Section E.6. However, the required polygon to detect the overlapping corresponds to the discretisation of the ellipses presented in Section G.5. Thus, the points that form the polygon (Section G.5) are

compared with the points from the other fillers. If at least one point is inside the polygon, then overlapping occurs. A representation of how the function detects filler overlapping was presented in Figure G.2.

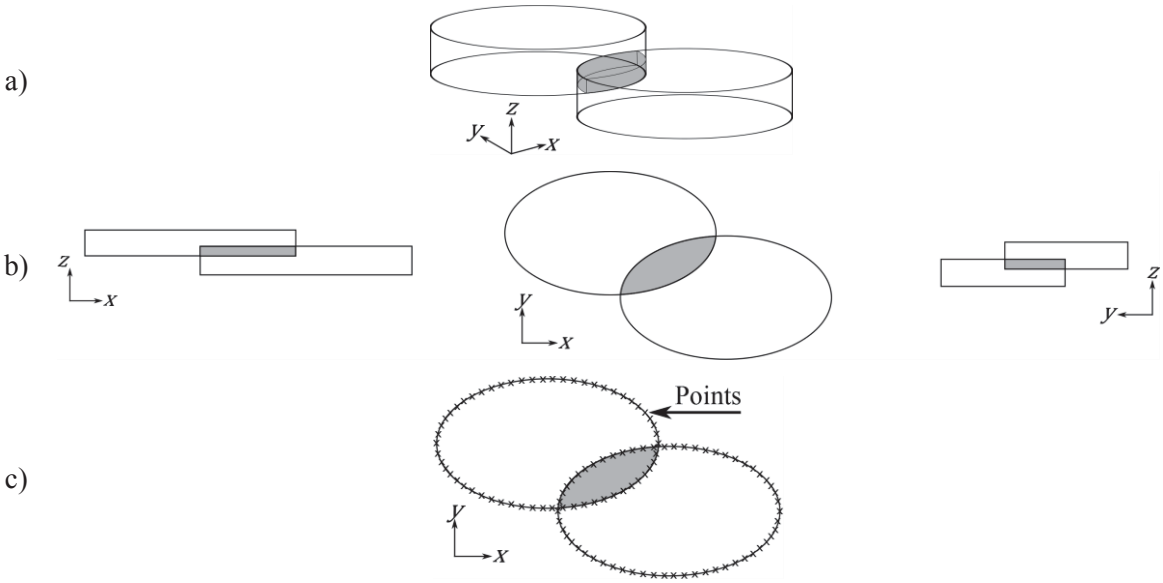

Figure G.2 Detection of overlapping by analysis of the discretisation of fillers where a) is a three dimensional view, b) are lateral views, and c) is the discretisation of the edges seen from the top view.

The required information to run the function is presented in Table G.3 and the output data are in Table G.4.

Table G.3 Required information to run the function to detect overlapping of elliptical fillers. The names of the variables used in the program are presented in brackets

Saved information	Data from*
Extra filler due to periodic boundary conditions in the current iteration (`hola`)	S.C.
Extra filler due to periodic boundary conditions in the all the iterations (`m`)	S.C.
Arrangement of x-axis filler corners including the extra filler due to periodic boundary conditions (`X`)	G.1
Arrangement of y-axis filler corners including the extra filler due to periodic boundary conditions (`Y`)	G.1
Arrangement of z-axis filler corners including the extra filler due to periodic boundary conditions (`Z`)	G.1
Number of element of the discretisation of the filler edge (`range`)	S.I.
Record of overlapping checking at $y-z$ axis of all the fillers (`check_YZ`)	G.6
Record of overlapping checking at $x-z$ axis of all the fillers (`check_XZ`)	G.6
Record of overlapping checking at $x-y$ axis of all the fillers (`check_XY`)	G.6
Thickness of the fillers (`filler_thickeness`)	G.2

*: SI: System input, G.1: Section G.1, G.2: Section G.2, G.6: Section G.6

Table G.4 Output information from the function to detect overlapping of elliptical fillers. The names of the variables used in the program are presented in brackets.

Output information
Instruction to the main code to repeat the location of the filler (`check`)

G.7 Saving of the geometrical characteristics of the final coating

The same presented in Appendix F, Section F.7.

G.8 Model solution (`COMSOL_SOLUTION_ELLIPSE.m`)

As well as Section E.8, the information of coating geometries is collected and the simulation is created in Comsol. The main difference between this section and Section E.8 is related to the way how to draw the fillers. For this, ellipses are drawn in two dimensions and then extruded transforming the fillers in three dimensional geometries. Figure G.3 shows the user interface windows of Comsol after simulation based on elliptical shaped fillers.

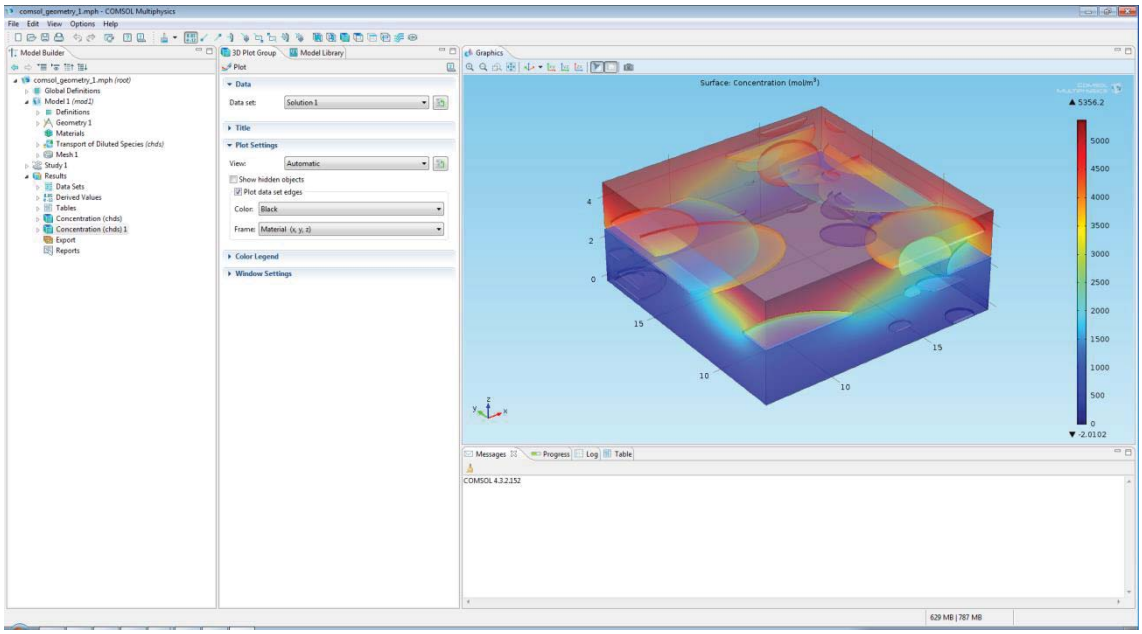

Figure G.3 User interface windows of Comsol after simulation for coating filled with elliptical fillers

The name of the main function is `COMSOL_SOLUTION_ELLIPSE.m`, and the functions are `comsol_solving_ellipse_function.m` and `calculation_of_vapor_concentration_function.m`.

A summary of all the functions required to run simulations for coating with elliptical shaped fillers was presented in Table G.5.

Table G.5 List of functions and sub-functions required to run the main codes for simulation of dispersion coatings filled with elliptical particles

Main code	Functions	Sub functions
COATING_GEOMETRY_GENERATION_ELLIPSE_MAIN_CODE	1. data_filler_parameters_function	
	2. number_filler_ellipse_function	2.1. b_distribution_function
		2.2. elongation_distribution_function
		2.3. max_Feret_distribution_function
	3. definition_of_grid_function	
	4. filler_arrangement_function	
	5. coordinates_ellipse_function	5.1. free_space_function
	6. periodic_boundary_condition_filler_ellipse_function	
	7. filler_ellipse_overlapping_checking_function	
	8. saving_geometric_data_ellipse_function	
COMSOL_SOLUTION_ELLIPSE	1. comsol_solving_ellipse_function	1.1. calculation_of_vapor_concentration_function